

SANDIA REPORT

SAND2020-10223

Printed September 22, 2020



Arctic Coastal Erosion: Modeling and Experimentation

PI

Diana Bull (SNL)

Team Members

Oceanographic Modeling: Chris Flanary (Integral Consulting), Craig Jones (Integral Consulting)

Terrestrial Modeling: Jennifer Frederick* (SNL), Alejandro Mota* (SNL), Irina Tezaur (SNL)

Oceanographic Field Work: Jeremy Kasper (UAF), Eloise Brown (UAF)

Terrestrial Field Work: Benjamin Jones (UAF), Melissa Ward Jones (UAF)

Permafrost Material Analyses: Emily Bristol (UTA), Charles Choens (SNL), Craig Connolly (UTA), James McClelland (UTA)

**equal contributors*

Contributors (listed alphabetically)

Mike Angelopolous (AWI), Chris Arp (USGS), Katherine Barnhart (USGS), Allen Bondurant (UAF), Richard Buzard (DGGS AK), Chris Chartrand (SNL), John Crews (Helicopter Pilot), Paul Duvoy (UAF), Li Erikson (USGS), William K Eymold (SNL), Louise Farquharson (UAF), Mike Fleming (R/V Ukpik Captain), Guido Grosse (AWI), Anastasia G. Ilgen (SNL), Go Iwahana (UAF), Stephanie Jump (UAF), Misha Kenevskiy (UAF), Nick Konefal (UAF), Thomas D. Lorenson (USGS), Siddharth Namachivayam, Kylea Parchert (SNL), Bruce M. Richmond (USGS), Erik Rogers (NRL), Robert Spencer (FSU), Matt Thomas (USGS), Jim Thomson (UW), Jim Webster (Floatplane Pilot), Dongmei Ye (SNL)

Recommended Citation:

Bull, D.L., E. M. Bristol, E. Brown, R. C. Choens, C. T. Connolly, C. Flanary, J. M. Frederick, B. M. Jones, C. A. Jones, M. Ward Jones, J. W. McClelland, A. Mota, I. Tezaur (2020). Arctic Coastal Erosion: Modeling and Experimentation, SAND2020-10223, Sandia National Laboratories, NM.

Prepared by
Sandia National Laboratories
Albuquerque, New Mexico
87185 and Livermore,
California 94550

Issued by Sandia National Laboratories, operated for the United States Department of Energy by National Technology & Engineering Solutions of Sandia, LLC.

NOTICE: This report was prepared as an account of work sponsored by an agency of the United States Government. Neither the United States Government, nor any agency thereof, nor any of their employees, nor any of their contractors, subcontractors, or their employees, make any warranty, express or implied, or assume any legal liability or responsibility for the accuracy, completeness, or usefulness of any information, apparatus, product, or process disclosed, or represent that its use would not infringe privately owned rights. Reference herein to any specific commercial product, process, or service by trade name, trademark, manufacturer, or otherwise, does not necessarily constitute or imply its endorsement, recommendation, or favoring by the United States Government, any agency thereof, or any of their contractors or subcontractors. The views and opinions expressed herein do not necessarily state or reflect those of the United States Government, any agency thereof, or any of their contractors.

Printed in the United States of America. This report has been reproduced directly from the best available copy.

Available to DOE and DOE contractors from

U.S. Department of Energy
Office of Scientific and Technical Information
P.O. Box 62
Oak Ridge, TN 37831

Telephone: (865) 576-8401
Facsimile: (865) 576-5728
E-Mail: reports@osti.gov
Online ordering: <http://www.osti.gov/scitech>

Available to the public from

U.S. Department of Commerce
National Technical Information Service
5301 Shawnee Rd
Alexandria, VA 22312

Telephone: (800) 553-6847
Facsimile: (703) 605-6900
E-Mail: orders@ntis.gov
Online order: <https://classic.ntis.gov/help/order-methods/>



ABSTRACT

Increasing Arctic coastal erosion rates have put critical infrastructure and native communities at risk while also mobilizing ancient organic carbon into modern carbon cycles. Although the Arctic comprises one-third of the global coastline and has some of the fastest eroding coasts, current tools for quantifying permafrost erosion are unable to explain the episodic, storm-driven erosion events. Our approach, mechanistically coupling oceanographic predictions with a terrestrial model to capture the thermo-mechanical dynamics of erosion, enables this much needed treatment of transient erosion events. The Arctic Coastal Erosion Model consists of oceanographic and atmospheric boundary conditions that force a coastal terrestrial permafrost environment in Albany (a multi-physics based finite element model). An oceanographic modeling suite (consisting of WAVEWATCH III, Delft3D-FLOW, and Delft3D-WAVE) produced time-dependent surge and run-up boundary conditions for the terrestrial model. In the terrestrial model, a coupling framework unites the mechanical and thermal aspects of erosion. 3D stress/strain fields develop in response to a plasticity model of the permafrost that is controlled by the frozen water content determined by modeling 3D heat conduction and solid-liquid phase change. This modeling approach enables failure from any allowable deformation (block failure, slumping, etc.). Extensive experimental work has underpinned the ACE Model development including field campaigns to measure in situ ocean and erosion processes, strength properties derived from thermally driven geomechanical experiments, as well as extensive physical composition and geochemical analyses. Combined, this work offers the most comprehensive and physically grounded treatment of Arctic coastal erosion available in the literature. The ACE model and experimental results can be used to inform scientific understanding of coastal erosion processes, contribute to estimates of geochemical and sediment land-to-ocean fluxes, and facilitate infrastructure susceptibility assessments.

ACKNOWLEDGEMENTS

Throughout the document we attempt to capture the main author of each section as well as the contributors who helped make the section possible thus interspersing acknowledgements throughout the document. These contributors are also listed on the cover page.

In addition to the interspersed acknowledgements, there are a few contributions to be more fully recognized:

Matt Thomas (USGS Geologic Hazards Science Center) has been a team member since the inception of the project and the original scoping of problem (Frederick et al. 2016). Matt has, unfortunately, had to turn his attention towards other projects, but has continued to act as an advisor as we have moved forward. We all still view him as a central team member.

Li Erikson, Thomas Lorenson, and Bruce Richmond (USGS Pacific Coastal and Marine Science Center) have all been important collaborators on this project. Li has worked with us on the development of the oceanographic modeling suite and has contributed water level boundary conditions for historical and projected conditions along the North Slope. She was integral to the WW3 assessment with industry data (Section 5.2.2). Tom and Bruce contributed to the geochemical analyses of the permafrost cores (Section 3.2.1).

Jim Thomson (University of Washington) kindly provided ocean measurements from two locations along the North Shore for oceanographic model comparison (www.apl.uw.edu/coda).

Katherine Barnhart (USGS Landslide Hazards) provided oceanographic data for nearshore oceanographic model comparison.

Erik Rogers (NRL) provided a polar stereographic, curvilinear WW3 grid.

Mike Angelopolous (AWI) & Guido Grosse (AWI) shared their nearshore bathymetric data.

There were two summer interns who contributed to this work. Richard Buzard worked with Ben Jones on AUV and time-lapse camera processing Section 2.2.1. Siddharth Namachivayam worked to develop down-core models of permafrost material properties Section 3.3.

Lori Parrott (SNL), program manager of this project, worked tirelessly to promote our work and inform potential customers of our progress. She helped shepherd this diverse team and put technical decisions within programmatic frameworks.

We received extensive formatting on the whole document from Mary Ann Cordova (SNL). Additionally, William Eymold (SNL) helped with comprehensive edits to Section 2.3.1.

Project authors were supported by the Laboratory Directed Research and Development program at Sandia National Laboratories.

CONTENTS

1. Motivation.....	20
1.1. Permafrost.....	21
1.2. Environmental Drivers	22
1.3. Erosion Mechanisms	25
1.4. Proposed Mechanistic Modeling Approach.....	27
2. Field Work	29
2.1. Drew Point.....	30
2.2. Terrestrial Field Campaigns.....	33
2.2.1. Terrestrial Measurement Details	33
2.2.1.1. USGS Weather Station (1998-2020)	33
2.2.1.2. Telemetered Time Lapse Cameras (2018)	34
2.2.1.3. Horizontal Thermistor (2018)	35
2.2.1.4. Vertical Thermistor (2018)	36
2.2.1.5. 2-D Thermistor Array (2019).....	36
2.2.1.6. Tilt Sensors (2019)	40
2.2.1.7. Niche Geometry Measurement (2019)	42
2.2.2. Erosion Measurements.....	43
2.3. Oceanographic Field Campaign.....	52
2.3.1. Oceanographic Measurement Details	53
2.3.1.1. Ikpikuk Delta Pressure Sensor (2011-2018)	53
2.3.1.2. Drew Point Spit Pressure Sensor (2018-2019)	54
2.3.1.3. RBR TDWave Sensor (2018-2019)	55
2.3.1.4. Smith Bay Mooring (2018-2019)	55
2.3.1.5. Multi-Beam Bathymetry (2018).....	57
2.3.1.6. Nearshore Single-Beam Bathymetry (2018).....	58
2.3.1.7. Water Samples (2018).....	58
2.3.1.8. Conductivity Temperature and Depth (2018)	60
2.3.1.9. Bottom Grabs (2018)	62
2.3.2. Analysis of Wave Environment	64
2.3.3. Analysis of Water Levels	66
2.3.4. Analysis of Wind	67
2.3.4.1. USGS Weather Station.....	68
2.3.4.2. ARM Mobile Facility Located at Oliktok Point	68
3. Permafrost Material Analyses.....	70
3.1. Coring Campaign	70
3.2. Permafrost Geochemical Analyses.....	75
3.2.1. Synopsis: Geochemistry and Erosional Organic Carbon and Nitrogen Fluxes.....	75
3.2.2. Decomposition of Organic Carbon.....	77
3.3. Physical Composition.....	79
3.4. Thermal Properties	89
3.4.1. Ancient Drained Thermokarst Lake Basin.....	90
3.4.2. Young Drained Thermokarst Lake Basin.....	94
3.4.3. Primary Material	97
3.5. Physical Strength Properties.....	101
3.5.1. Introduction	101

3.5.2.	Methods	102
3.5.3.	Experimental Results	107
3.5.3.1.	Compressive Tests	110
3.5.3.2.	Extension (Tensile) Tests	112
3.5.4.	Discussion of Mechanical Results.....	114
3.5.5.	Development of a Strength Model.....	116
3.5.5.1.	Failure Strength Using Volumetric Content of Ice in Frozen Soil Approach.....	117
3.5.5.2.	Failure Strength Using an Ice Adhesion in Frozen Soil Approach	118
3.5.5.3.	Elastic Moduli.....	119
3.5.6.	Conclusions.....	120
4.	Model Development.....	121
4.1.	Boundary Condition Sources	121
4.1.1.	Atmospheric Boundary Conditions.....	121
4.1.2.	Oceanographic Boundary Conditions.....	123
4.2.	Oceanographic Modeling Suite.....	126
4.2.1.	WAVEWATCH III Wave Model Setup.....	127
4.2.1.1.	WW3 Model Grid and Bathymetry	127
4.2.1.2.	WW3 Boundary Conditions	128
4.2.2.	Delft3D-FLOW/WAVE Model Setup.....	130
4.2.2.1.	Delft3D-FLOW	130
4.2.2.1.1.	Delft3D-FLOW Grid and Bathymetry	130
4.2.2.1.2.	Delft3D-FLOW Boundary Conditions	133
4.2.2.1.3.	Delft3D-FLOW Initial Conditions	134
4.2.2.2.	Delft3D-WAVE.....	134
4.2.2.2.1.	Delft3D-WAVE Grid and Bathymetry.....	134
4.2.2.2.2.	Delft3D-WAVE Boundary Conditions	135
4.2.3.	Delft3D-FLOW/WAVE Model Simulations	136
4.2.4.	WW3 and Delft3D-FLOW/WAVE Simulations.....	138
4.3.	Terrestrial Model – Albany.....	139
4.3.1.	Thermal Model	139
4.3.1.1.	Strong Form	139
4.3.1.2.	Thermal Model Variational Form	140
4.3.1.3.	Salinity Enhanced Melting.....	140
4.3.2.	Mechanical Model	141
4.3.2.1.	Mechanical Model Variational Form	141
4.3.2.2.	Dynamic Wave Pressure	142
4.3.3.	Material Model.....	144
4.3.3.1.	Mechanical Material Model	144
4.3.3.2.	Thermal Mixture Models	144
4.3.4.	Thermo-mechanical Coupling and Implementation.....	150
4.3.4.1.	Sequential Thermo-Mechanical Coupling Algorithm.....	150
4.3.4.2.	Implementation in Albany LCM Code.....	152
4.4.	Vertical Datum.....	153
5.	Model Execution.....	156
5.1.	Boundary Condition Implementation.....	156
5.1.1.	Atmospheric Inputs	156

5.1.2.	Oceanographic Inputs	157
5.1.3.	Exposure Time / Grid Spacing.....	158
5.1.4.	Storm Identification.....	163
5.1.5.	Geothermal Heat Flux Input.....	164
5.2.	Oceanographic Validation	166
5.2.1.	Bathymetry Comparison	167
5.2.2.	WW3 – BOEM Buoy Comparison	170
5.2.2.1.	Arctic Atmospheric Reanalysis Data.....	170
5.2.2.2.	Output Stations	171
5.2.2.3.	Results.....	172
5.2.3.	WW3 – UW CODA Buoy Comparison	179
5.2.4.	SWAN – Barnhart Nearshore Comparison	183
5.2.5.	SWAN – 2018 2019 Field Data Comparison.....	185
5.2.6.	Nearshore Water Level Comparison.....	188
5.2.7.	Future Steps	193
5.2.8.	Oceanographic Modeling Conclusions	194
5.3.	Erosion Model Demonstration.....	194
5.3.1.	Field Data	195
5.3.2.	Oceanographic Conditions	197
5.3.3.	Erosion Model Performance	199
5.3.3.1.	Model Set-up	199
5.3.3.2.	Model Demonstration.....	205
5.3.3.3.	Future Modeling Work	211
6.	Accomplishments.....	212
6.1.	Follow-on Work.....	212
6.1.1.	InterFACE	212
6.1.2.	Air Force Reviewer	212
6.2.	Publications.....	212
6.2.1.	Journal.....	213
6.2.1.1.	Published or Submitted.....	213
6.2.1.2.	In Preparation.....	213
6.2.2.	Invited Presentations	213
6.2.3.	Conference Presentations	214
6.2.4.	Lectures Series Presentations	214
6.2.5.	Posters.....	214
6.3.	Career Development	215
7.	Conclusions.....	217
Appendix A.	Mechanical Material Model and Adaptive Meshing for the Arctic Coastal Erosion Model.....	A-1
Appendix B.	Coring Campaign—Additional Work	B-1

LIST OF FIGURES

Figure 1.1-1. A schematic illustrating the formation of ice wedges and ice-wedge polygon landscapes. Adapted from (Martin et al., 2009).	22
Figure 1.2-1. Scatterplots of mean erosion between 2007 and 2016 and potential environmental forcing factors. Open water days derived from NSIDC, storms, storm power, thawing degree day (TDD) sums, and near surface permafrost temperature (1.2 m depth) derived from the Drew Point Meteorological Station, and sea surface temperature derived from NOAA OISST V2 data. All plots show coefficient of determination and linear regression lines (dashed). Adapted from Jones et al. 2018.	24
Figure 1.3-1. Conceptual cross section of patterns of stress based on elastic geomechanical simulation. Adapted from Thomas et al. 2020.	26
Figure 1.3-2. Boxplots showing the impact of variability in geometric (i.e., erosional niche, permafrost block, and ice wedge) characteristics and ice/permafrost material properties (i.e., bulk density, Young’s Modulus, and Poisson’s Ratio) on the (a) location and (b) magnitude of the simulated maximum tensile stress (σ_{Tmax}). Adapted from Thomas et al. 2020.	27
Figure 2.1-1. The Drew Point study area, Alaska Beaufort Sea Coast (ABSC). (a) The overlapping footprint of remotely sensed imagery used in this study is outlined with the red rectangle. The location of the meteorological station is shown with the yellow dot. (b) The location of Drew Point along the ABSC. Historic erosion rates from Gibbs and Richmond (2017) are shown for the period 1947 to 2010.	31
Figure 2.1-2. Field photographs documenting aspects of the permafrost bluff and erosion mechanisms at Drew Point, AK. Photos from the coast show: aspects of the permafrost bluff stratigraphy, a well-developed niche geometry with measured dimensions overlaid, and the lower two photos document thermo-denudation and block failure.	32
Figure 2.2-1. Components of a typical U.S. Department of the Interior/Global Terrestrial Network for Permafrost (DOI/GTN-P) climate monitoring station. (cm, centimeter). Adapted from Urban and Clow 2018.	34
Figure 2.2-2. Field photo showing the installation of the 4-channel data logger (inside gold circle) and thermistor strings in the bluff face at Drew Point.	36
Figure 2.2-3. Temperature records from initial installation in 5-10hour increments up to 56-65 hours after installation in the bottom (A), middle (B), and upper (C) horizontal boreholes and in the vertical (D) borehole. Initial installation times: 08/13/19 05:28:38 PM bottom, 08/13/19 05:55:13 PM middle, 08/13/19 06:49:43 PM upper, and 08/13/19 07:19:10 PM vertical.	38
Figure 2.2-4. Collage of 2-D thermistor array measurements. The picture shows the location of the thermistor strings and the thermal denudation measurements, the 2-D bluff temperature in Fahrenheit on evening of August 14 2019 is shown in the center with the pink circles indicating the temperature probe locations, and a thermal image of the bluff face taken on August 14th 2019 shows the relative temperatures of the ocean, bluff face, and ice wedge the bottom and middle thermistor string can be seen in the thermal image.	39
Figure 2.2-5. Photograph of the Drew Point coastline (A) before and (B) after a toppling-mode permafrost block failure. (C) Multi-day time series of tilt sensor measurements. Negative degrees indicate oceanward tilting. Thick red line corresponds to the location shown in (A-B), whereas the orange and blue lines correspond to another nearby coastal bluff and inland control location, respectively.	41

Figure 2.2-6. Profile measurements of M4, M5, and M9 with associated pictures. Orange squares are not measured values, they are guesses indicating the height of a “vertical” bluff face. The white and orange scale held by Jennifer Frederick in the photos is 2m in length.	42
Figure 2.2-7. Experimental correlation between niche depth and height using the data presented in Table 2.2-4. Best fit shown in dotted blue line: $y=3.2991*x-1.2533$. Orange and blue dashed lines give bounding fits for the highest and lowest data points assuming the same y-intercept. The slope could be as high as 4.49 (orange dashed) or as low as 1.85 (grey dashed). .	43
Figure 2.2-8. Long-term decadal-scale erosion rates for Drew Point, 9km, section of coast.....	44
Figure 2.2-9. Annual open-water period erosion for Drew Point, 9 km, section of coast between 2007 and 2019.....	45
Figure 2.2-10. Overview of the dense time series of imagery that we have compiled for providing for model inputs.....	45
Figure 2.2-11. UAV surveys conducted in 2018 and 2019.	46
Figure 2.2-12. Assessing the horizontal and vertical quality of the UAV datasets.....	46
Figure 2.2-13. UAV data collection, image processing, bluff extraction, and erosion determination workflow.....	47
Figure 2.2-14. Example of the detail that you can resolve in the UAV time series.	48
Figure 2.2-15. Example of the entire UAV time series and the mapped erosion between for each time period.	48
Figure 2.2-16. Example of partitioning erosion happening during a specific time period based on erosional process.	49
Figure 2.2-17. Example of output from DSAS tool showing variability in erosion for the 1.5 km section of study coast at Drew Point between the first and last UAV survey.	49
Figure 2.2-18. Mean erosion along 1.5 km study coast for each UAV time period.....	50
Figure 2.2-19. Mean erosion by block failure.	50
Figure 2.2-20. Mean erosion by thaw slumping.	51
Figure 2.2-21. Manual mapping of thermo-erosional niche heights from UAV survey data.	51
Figure 2.2-22. Compilation of histograms of niche heights resolved in each UAV survey.....	52
Figure 2.3-1. Navigation track logged by GPS.	53
Figure 2.3-2. Location of the Drew Point RBR Duo TDWave and “Spit” HOBO sensors, Lagoon and Bluff.	54
Figure 2.3-3. The oceanographic mooring as it entered the water for deployment on the sea floor. .	56
Figure 2.3-4. Smith Bay mooring deployment location.....	56
Figure 2.3-5. Prior to deployment of the mooring the multibeam sonar was used to confirm the presence of a ridge to deploy the mooring behind. The ridge appears on chart data from the region that dates to the 1950s and appears to be a persistent relic ice scour. The presence of the ridge was first noted by J. Kasper in 2005 during a previous mooring deployment.	57
Figure 2.3-6. Drew Point multibeam derived bathymetry referenced to WGS84.....	58
Figure 2.3-7. Seabird water sample cast locations.....	59
Figure 2.3-8. Stable Oxygen isotope results ($\delta^{18}O$, %).	60
Figure 2.3-9. AML cast locations.....	61
Figure 2.3-10. AML CTD and Turbidity cast from station 51. Yellow line turbidity, red line temperature, and green line salinity.	62
Figure 2.3-11. Bottom grab collections locations.....	63
Figure 2.3-12. D50 values of bottom sediments from the Ponar Bottom Grab samples.....	63

Figure 2.3-13. 2018 RBR Data. Top: Significant Wave Height (m) followed by Peak Period (s), Water Level referenced to WGS84 (m), Temperature (deg. C), Atm. Pressure (mbar) from the HOBO “spit” atm. pressure sensor and Atm. Pressure Oliktok (mbar). All are versus time.	64
Figure 2.3-14. 2019 RBR Data. Top: Significant Wave Height (m) followed by Peak Period (s), Water Level referenced to WGS84 (m), Temperature (deg. C), Atm. Pressure (mbar) from the HOBO “spit” atm. pressure sensor and Atm. Pressure Oliktok (mbar). All are versus time.	65
Figure 2.3-15. 2018 total water level referenced to WGS84 (m, water level plus significant wave height, Hs).....	65
Figure 2.3-16. 2019 total water level referenced to WGS84 (m, water level plus significant wave height, Hs).....	66
Figure 2.3-17. Timeseries of atmospheric pressure (mbar), air temperature (C°) (top panel); water depth (m) and water temperature (C°) (bottom panel) at Drew Point, Alaska from May 1, 2018 – August 15, 2019.....	67
Figure 2.3-18. Histogram of wind speed and direction at Drew Point, Alaska from August 1998-February 2020, showing wind speeds (m/s) and direction (clockwise from 0° due north). Wind speeds range from 0-21.79 m/s and are binned according to the Beaufort wind scale shown below. Note, wind speeds within the Beaufort scales 0-1 and 7-9 were binned together, and no winds were recorded above severe gale speeds. Based on Drew Point wind data obtained from Frank Urban and described above (USGS met station at Drew Point).....	68
Figure 2.3-19. Histogram of wind speed and direction at Oliktok Point, Alaska during the open water season (OWS) from March 1 – October 31 in 2018 and 2019, showing wind speeds (m/s) and direction (clockwise from 0° due north). Wind speeds range from 0-12.9 m/s and are binned according to the Beaufort wind scale shown below. Note, wind speeds within the Beaufort scales 0-1 and 7-9 were binned together, and no winds were recorded above a strong breeze.....	69
Figure 3.1-1. Collage of photos taken while SIPRE coring.....	70
Figure 3.1-2. Collage of photos taken while JiPRO coring (taken by Misha).....	71
Figure 3.1-3. From left to right, photographs of landscape classified as Primary Surface, Ancient DTLB (drained ~5 kyr BP), and Young DTLB (most recent drainage occurred ~0.5 kyr BP).....	71
Figure 3.1-4. Map of our 9 km study coastline denoting coastline lost from 1955 (bold black line) and 2018 (bold red line), locations where permafrost was cored (DP1, DP2, PM), and terrain classifications. White lines show bluff line position for timesteps between 1955 and 2018.....	72
Figure 3.1-5. Sandia scientists examine core sections for geomechanical and geochemical analysis. .	74
Figure 3.2-1. Soil total organic carbon (TOC; wt %), total nitrogen (TN; wt %), soil organic carbon to nitrogen molar ratio (C:N), and d ¹³ C-TOC (‰) profiles for three permafrost cores. Colors and symbols indicate the terrain classification each core was sampled from. The black horizontal lines indicate mean sea level.	76
Figure 3.2-2. Estimation of total organic carbon fluxes to the ocean (metric tons TOC yr ⁻¹) from the 9 km study section over four time steps from 1955 to 2018 and over annual time steps from 2008 to 2018. The error bar shows standard error.	76
Figure 3.2-3. The figure shows the average percent loss of dissolved organic carbon (DOC) leached from active layer soils, organic-rich permafrost, and relict marine sediments over a 90-day incubation.	78
Figure 3.3-1. Down core profiles of frozen bulk density, dry bulk density, gravimetric water content, soil water content, and estimated porosity. Color and symbol indicate the terrain classification of the sample. One sample that was mostly ice is not shown in the gravimetric water content plot due to its high value (37,350 %).	80

Figure 3.3-2. Comparison of modeled and measured frozen bulk density values. Data points represent core sections that had both water content and volume measurements. The color of the data points represents the elevation (m) of the sample, and the symbols represent the terrain unit. The black line is the modeled frozen bulk density as a function of gravimetric water content (i.e. wet mass and dry mass).	81
Figure 3.3-3. Porosity (%) as a function of gravimetric water content (%). Data points indicate the measured porosity for samples with a volume measurement. Data point shape indicates the terrain classification and the color scale indicates the elevation (m) of the sample. The first model method, which uses the particle bulk density of soil/sediment to estimate porosity, is shown as a solid line. The second model method, which fits a power curve to the data points, is shown as a dashed line.	82
Figure 3.3-4. Porosity as a function of elevation for data above sea level. Solid lines show modeled porosity using a second order polynomial. The high porosity value in the Young DTLB figure was a sample that was nearly completely ice. Dashed lines show third order polynomial fits for the Primary Surface and Ancient DTLB, and a linear fit for DP2 that were used in initial model runs to assess model skill (Section 5.3.3).	83
Figure 3.3-5. Porosity as a function of elevation, for permafrost above sea level and below a depth of 0.5 m. All models are linear fits. The high porosity value in the Young DTLB figure was a sample that was nearly completely ice.	84
Figure 3.3-6. Downcore profiles of sand, silt, and clay fractions (%). Color and symbols indicate the terrain classification of the sample.	85
Figure 3.3-7. Linear models of grain fraction by elevation for data above sea level, in each of the terrain classifications.	86
Figure 3.3-8. Peat fraction modeled as a function of elevation for each terrain classification. Points represent measured data, and lines represent the peat model. Peat (% by weight) was assumed to be twice the total organic carbon content (% by weight).	88
Figure 3.3-9. Salinity as a function of elevation. Measured porewater salinity is represented by data points, coded by color and shape to indicate terrain classification.	89
Figure 3.4-1. Measured sediment constituent fraction in the Ancient DTLB as a function of elevation with overlaying high-order fit for: a) sand, b) silt, and c) clay.	90
Figure 3.4-2. Model of soil constituents in the Ancient DTLB as a function of elevation, including peat.	91
Figure 3.4-3. Measured porosity in the Ancient DTLB as a function of elevation with overlaying high-order fit. (fit details given in Table 3.3-1).	91
Figure 3.4-4. Model of frozen bulk density, at -20C, constructed from the model of soil constituents (Figure 3.4-2) and porosity (Figure 3.4-3.) overlaid on top of the experimentally obtained values. Visually, the models of underlying constituents are working very well as the solid line bisects the experimental data.	92
Figure 3.4-5. Model of fully frozen Ancient DTLB permafrost soil's specific heat capacity at -20C.	93
Figure 3.4-6. Model of fully frozen Ancient DTLB permafrost soil's thermal conductivity at -20C.	93
Figure 3.4-7Figure 3.4-8 Measured sediment constituent fraction in the Young DTLB as a function of elevation with overlaying high-order fit for: a) sand, b) silt, and c) clay.	94
Figure 3.4-9. Model of soil constituents in the Young DTLB as a function of elevation, including peat.	94
Figure 3.4-10. Measured porosity in the Young DTLB as a function of elevation with overlaying high-order fit. (fit details given in Table 3.3-1).	95

Figure 3.4-11. Model of frozen bulk density, at -20C, in the Young DTLB constructed from the model of soil constituents (Figure 3.4-2) and porosity (Figure 3.4-3.) overlaid on top of the experimentally obtained values. Visually, the models of underlying constituents are working very well as the solid line bisects the experimental data.....	96
Figure 3.4-12. Model of fully frozen Young DTLB permafrost soil's specific heat capacity at -20C.	96
Figure 3.4-13. Model of fully frozen Young DTLB permafrost soil's thermal conductivity at -20C..	97
Figure 3.4-14. Measured sediment constituent fraction in the Primary Material as a function of elevation with overlaying high-order fit for: a) sand, b) silt, and c) clay.	97
Figure 3.4-15. Model of soil constituents in the Primary Material as a function of elevation, including peat.....	98
Figure 3.4-16. Measured porosity in the Primary Material as a function of elevation with overlaying high-order fit. (fit details given in Table 3.3-1).....	99
Figure 3.4-17. Model of frozen bulk density, at -20C, in the Primary Material constructed from the model of soil constituents (Figure 3.4-2) and porosity (Figure 3.4-3.) overlaid on top of the experimentally obtained values.....	100
Figure 3.4-18. Model of fully frozen Primary Material permafrost soil's specific heat capacity at -20C.	100
Figure 3.4-19. Model of fully frozen Primary Material permafrost soil's thermal conductivity at -20C.	101
Figure 3.5-1. Experimental setup for the different types of testing. a) Prepared UCS geometry on sample PM1-1 303-310. b) Deformed UCS experiment on sample PM 1-1 303-310. c) Prepared DT geometry on sample PM1-3 512-522. d) Deformed DT experiment on sample PM1-1 213-232.5. e) BTS experiment on DP 1-1 356-371.	105
Figure 3.5-2. a) Measured density of frozen soil samples used for geomechanics testing. Lower bound for Density axis is set at the density of ice for comparison. b) Measured porosity of frozen soil samples used for geomechanics testing. c) Calculated volumetric fraction of ice at test temperatures.	108
Figure 3.5-3. a) Axial stress versus axial, lateral, and volume strain for visibly high ice content samples for temperatures of -6.4, -2.3, and -2.3°C. b) Axial stress versus axial, lateral, and volume strain for visibly medium ice content samples for temperatures of -6.2 and -2.33°C. Samples are listed by core and top depth of sample interval.....	111
Figure 3.5-4. Mechanical properties for visibly high ice content (orange circles) and visibly medium ice content (blue circles) samples. a) Failure strength versus temperature. b) Young's modulus versus temperature. c) Poisson's ratio versus temperature. d) Failure strength versus ice volume fraction for all UCS tests. e) Young's modulus versus ice volume fraction for all UCS tests. f) Poisson's ratio versus ice volume fraction for all UCS tests.....	111
Figure 3.5-5. a) Axial stress versus axial, lateral, and volume strain for visibly high ice content samples for temperatures of -6.1, -3.2, and -1.2°C. b) Axial stress versus axial, lateral, and volume strain for low ice content samples for temperatures of -6.1, -5.4, -3.2, and -1.0°C. Samples are listed by core and top depth of sample interval.....	113
Figure 3.5-6. Mechanical properties for visibly high ice content (orange) and visibly low ice content (blue); results from DT tests (circles) and BTS (squares). a) Failure strength versus temperature. Error bars represent one standard deviation from the mean BTS value for a given condition. b) Young's modulus and Poisson's ratio versus temperature c) Failure strength versus ice volume fraction for all tensile samples. Error bars represent one standard	

deviation from the mean BTS value for a given condition. d) Young’s modulus and Poisson’s ratio versus ice volume fraction.	114
Figure 3.5-7. Failure strength versus ice volume fraction for UCS experiments. Blue line is linear best fit relationship to the experimental results. The dashed red line is a theoretical fit assuming 5 MPa for the strength of pure ice. The dashed green line shows the linear relationship based on the tensile strength observed in BTS samples.....	118
Figure 3.5-8. Failure strength versus ice saturation for UCS experiments. Blue line is linear best fit relationship to the experimental results. The dashed red line represents an upper bound to the data, and the dashed green line represents a lower bound to the data. a) Bounding curves assume different soil strength. b) Bounding curves assume different ice strength.	119
Figure 3.5-9. Elastic moduli versus ice volume fraction for UCS experiments. Blue line is linear best fit relationship to the experimental results. a) Young’s modulus and b) Poisson’s ratio. ...	120
Figure 4.1-1. ASR Grid Spacing At Drew Point, AK Project Area.....	121
Figure 4.1-2. ERA5 Grid Spacing At Drew Point, AK Project Area.....	122
Figure 4.1-3. Time Series Comparison of Measured Water Level at Prudhoe Bay, AK To GOFS 3.1 Extracted Water Level Predictions at Prudhoe Bay and Drew Point, AK.	124
Figure 4.1-4. GOFS 3.1 HYCOM Grid Spacing At Drew Point, AK Project Area.....	125
Figure 4.1-5. CanESM2 GCM Grid Spacing At Drew Point, AK Project Area.	126
Figure 4.2-1. Arctic WW3 Model Grid Extents With ETOPO 1 Bathymetry.	128
Figure 4.2-2. Sea Ice Coverage From ASRv2 Data Used in the Arctic WW3 Model.....	129
Figure 4.2-3. Delft3D-FLOW Grid in comparison to the Drew Point, AK 2007 and 2018 Shorelines.	131
Figure 4.2-4. Delft3D-FLOW Nearshore Circulation Grid.	132
Figure 4.2-5. Delft3D-FLOW Bottom elevations Defined from ARDEMv2.	133
Figure 4.2-6. Delft3D-WAVE Nearshore Spectral Wave Grid.	135
Figure 4.2-7. Final Output Locations For Delft3D-FLOW/WAVE Simulations and Delft3D- FLOW/WAVE Grid Outline.	136
Figure 4.2-8. Final Output Locations For Delft3D-FLOW/WAVE Simulations and Delft3D- FLOW Grid in the Drew Point, AK Nearshore Region.....	137
Figure 4.2-9. Arctic coastal Erosion Oceanographic Modeling Suite Workflow.	138
Figure 4.3-1. Diagram of dynamic pressure distribution along a vertical coastal structure as a result of surge and wave action (Partensky 1989).	144
Figure 4.3-2. Soil freezing curve for a 70/20/10 sand/silt/clay mix.	147
Figure 4.3-3. Soil freezing curve for a 50/25/25 sand/silt/clay mix.	148
Figure 4.3-4. Soil freezing curve for a 30/30/40 sand/silt/clay mix.	148
Figure 4.3-5. Soil freezing curve for a 10/20/70 sand/silt/clay mix.	149
Figure 4.3-6. Schematic depicting sequential thermo-mechanical coupling.....	151
Figure 4.4-1. Example analysis within AUV survey data to obtain bluff toe elevation in WGS84 Ellipsoid.....	154
Figure 4.4-2. Conceptual Model of Vertical Datum Reference Frames for the Cliff Toe and the Modeled Water Surface Elevation.	155
Figure 5.1-1. 2007 skin temperature for the month of August from ASR (red dot) with piecewise cubic interpolation to 60sec (dashed green line).	156
Figure 5.1-2. Map indicating the output locations for skin temperature.	157
Figure 5.1-3. Example 2019 oceanographic model output that forms the basis of the terrestrial model inputs. The water contact record is established by combining water level and spectral properties.....	158

Figure 5.1-4. Illustration of the effect of the vertical resolution of the terrestrial grid (0.02m, 0.08m, 0.1m, and 0.2m) on the total duration of water contact with each slice for a 0.5Hz time history. A randomly selected hour, 93, in 2019 is used to show the effect on the binning of the water contact history with distinct vertical resolutions. As the vertical resolution increases from 0.2m, the peak duration of exposure decreases as previously excluded water contact levels become populated.	159
Figure 5.1-5. Illustration of the effect of the minimum simulation time step on a 0.1m vertical resolution grid. A randomly selected hour, 93, in 2019 is used to show the effect of the minimum simulation time step on the simulated exposure used by the terrestrial model. As the simulation time step increases the exposure magnitude (water contact height on bluff face) and duration become coarser.....	160
Figure 5.1-6. Temperature boundary condition at 0.0m for a vertical resolution of 0.1m and a simulation time step of 10min over the 2019 summer in which the ocean water temperatures are shown as blue dots when the water is in contact with the identified vertical layer.....	161
Figure 5.1-7. Temperature boundary condition at 0.2m for a vertical resolution of 0.1m and a simulation time step of 10min over the 2019 summer in which the ocean water temperatures are shown as blue dots when the water is in contact with the identified vertical layer.....	161
Figure 5.1-8. Temperature boundary condition at 0.4m for a vertical resolution of 0.1m and a simulation time step of 10min over the 2019 summer in which the ocean water temperatures are shown as blue dots when the water is in contact with the identified vertical layer.....	161
Figure 5.1-9. Temperature boundary condition at 0.8m for a vertical resolution of 0.1m and a simulation time step of 10min over the 2019 summer in which the ocean water temperatures are shown as blue dots when the water is in contact with the identified vertical layer.....	162
Figure 5.1-10. Percentage of time between successive AUV surveys that water is in contact with a particular height up the permafrost cliff face; the time spent below the cliff face is given in the legend.	162
Figure 5.1-11. Salinity history over the 2019 summer. Original in blue and exposure calculated using a simulation time step of 60sec and a vertical resolution of 0.02m shown as green dots. Only time periods in which water is in contact with any portion of the permafrost bluff face is shown in green.....	163
Figure 5.1-12. Identification of time periods for which a vertical level of 0.4m is in contact with ocean water for at least 6 consecutive hours in 2019; establishing these time periods as illustrative storms. Water contact history has been established using a simulation time step of 2sec and a vertical resolution of 0.02m.....	164
Figure 5.1-13. Temperature records at the Drew Point deep borehole, used to determine the value of the geothermal heat flux boundary condition. Adapted from Clow (2014).....	165
Figure 5.2-1. Spatial Comparison of ARDEM/IBCAO depths to the Drew Point Nearshore Single Beam and Multibeam Depths.	168
Figure 5.2-2. Scatter Plot Comparison of ARDEM/IBCAO depths to the Drew Point Nearshore Single Beam Survey Depths.....	169
Figure 5.2-3. Scatter Plot Comparison of ARDEM/IBCAO depths to the Drew Point Multibeam Survey Depths.	169
Figure 5.2-4. WW3 model grid centers and selected industry wave measurement stations around Drew Point, Alaska. Industry wave measurement stations made available through the BOEM project Jeremy Kasper is PI on.	171
Figure 5.2-5. 2011 MOB2 comparison of simulated and measured significant wave height (left) and peak wave period (right) for the Arctic WW3 model forced by ERAI-WRF, ASR, and	

NARR. The gray symbols are a direct comparison of simulated and measured data. The colored symbols are quantile-quantile values.	173
Figure 5.2-6. 2012 ShellHB comparison of simulated and measured significant wave height (left) and peak wave period (right) for the Arctic WW3 model forced by ERAI-WRF, ASR, and NARR. The gray symbols are a direct comparison of simulated and measured data. The colored symbols are quantile-quantile values.	174
Figure 5.2-7. 2012 MOB103 comparison of simulated and measured significant wave height (left) and peak wave period (right) for the Arctic WW3 model forced by ERAI-WRF, ASR, and NARR. The gray symbols are a direct comparison of simulated and measured data. The colored symbols are quantile-quantile values.	175
Figure 5.2-8. 2013 ShellHB comparison of simulated and measured significant wave height (left) and peak wave period (right) for the Arctic WW3 model forced by ERAI-WRF, ASR, and NARR. The gray symbols are a direct comparison of simulated and measured data. The colored symbols are quantile-quantile values.	176
Figure 5.2-9. 2014 MOB101 comparison of simulated and measured significant wave height (left) and peak wave period (right) for the Arctic WW3 model forced by ERAI-WRF, ASR, and NARR. The gray symbols are a direct comparison of simulated and measured data. The colored symbols are quantile-quantile values.	177
Figure 5.2-10. 2015 MOB102 comparison of simulated and measured significant wave height (left) and peak wave period (right) for the Arctic WW3 model forced by ERAI-WRF and ASR. The gray symbols are a direct comparison of simulated and measured data. The colored symbols are quantile-quantile values.	178
Figure 5.2-11. University of Washington RBR Measurement Locations along the North Slope of Alaska.	180
Figure 5.2-12. Comparison of the Arctic Ocean WW3 Predicted Significant Wave Height and Peak Wave Period to the UW Measured Data at Location S2-P1.	181
Figure 5.2-13. Comparison of the Arctic Ocean WW3 Predicted Significant Wave Height and Peak Wave Period to the UW Measured Data at Location S3-P1.	182
Figure 5.2-14. Comparison of NOAA Prudhoe Bay, AK Station Wind Speeds with ERA5 Predicted Wind Speeds.	183
Figure 5.2-15. Location of Wave Logger 2 Measurement Station from Barnhart et al. 2014b.	184
Figure 5.2-16. Comparison of the Delft3D-FLOW/WAVE Predicted Significant Wave Height and Peak Wave Period to the Barnhart et al. 2014b Wave Logger 2 Measurement Station.	185
Figure 5.2-17. Location of 2018 and 2019 Drew Point RBRs.	186
Figure 5.2-18. Comparison of the Delft3D-FLOW/WAVE Predicted Water Level, Significant Wave Height, and Peak Wave Period to the Drew Point 2018 RBR Measurement Station.	187
Figure 5.2-19. Comparison of the Delft3D-FLOW/WAVE Predicted Water Level, Significant Wave Height, and Peak Wave Period to the Drew Point 2019 RBR Measurement Station.	188
Figure 5.2-20. Delft3D-FLOW/WAVE Output Locations for Comparison to Nearshore Water Level Sensors.	189
Figure 5.2-21. Comparison of the Delft3D-FLOW/WAVE Predicted Water Level to the 2011 Data from the Ikpikpuk Delta Water Inundation Station. The Established Cliff Toe Height is shown as the Red Line.	190
Figure 5.2-22. Comparison of the Delft3D-FLOW/WAVE Predicted Water Level to the 2012 Data from the Ikpikpuk Delta Water Inundation Station. The Established Cliff Toe Height is shown as the Red Line.	191

Figure 5.2-23. Comparison of the Delft3D-FLOW/WAVE Predicted Water Level to the 2018 Data from the Ikpikpuk Delta Water Inundation Station. The Established Cliff Toe Height is shown as the Red Line.	192
Figure 5.2-24. Comparison of the Delft3D-FLOW/WAVE Predicted Water Level to the 2018 Data from the Drew Point, AK Spit Water Level Station.	193
Figure 5.2-25. Comparison of the Delft3D-FLOW/WAVE Predicted Water Level to the 2019 Data from the Drew Point, AK Spit Water Level Station.	193
Figure 5.3-1. Image of vertical thermistor location with dimensions overlaid of the polygon size and ice wedge width on August 3 rd 2018. The following dimensions correspond with the lines identified in the plot: 1. 2.62m, 2. 6.5m, 3. 10.8m, 4. 5.65m, and 5. 3.0m.....	196
Figure 5.3-2. Permafrost borehole temperature profile showing niche development and block collapse paired with time lapse camera images. The bluff toe is at -5.2 m depth. Initial niche development occurred between 15 Aug and 20 Aug. Secondary niche development that led to block failure commenced on 29 Aug. Niche height grew to ~1.8 m between 29 August and 01 September prior to block failure. (times given in UTC).	197
Figure 5.3-3. Water contact history from closest oceanographic grid cell with permafrost bluff over the time period in which the niche developed and the block broke (August 15 th – September 3 rd 2018). Raw file processed with a simulation time step of 2sec and a vertical resolution of 0.02m. Area between red lines indicate a water contact level of 0.4m up the bluff face has occurred for at least 12 consecutive hours; the number of consecutive hours is given above the arrows.....	198
Figure 5.3-4. Distribution of the water contact history with the bluff face from closest oceanographic grid cell with the location of the vertical thermistor in 2018. Duration of exposure has been normalized by the total time between surveys. The percentage of time where the ocean did not contact the bluff is given in the legend.	198
Figure 5.3-5. Quasi-2D finite element grid used to compare with the vertical thermistor field data. The location of the vertical thermistor is shown with the silver arrow. Red grid cells represent ice wedge material while gray cells represent permafrost material.....	199
Figure 5.3-6. Subset of temperature boundary conditions applied in the terrestrial model for comparison with the vertical thermistor data; applicable vertical level identified in top left-hand corner of each temperature B.C. time history.....	201
Figure 5.3-7. Ocean water contact time history processed with a simulation time step of 2min and a vertical resolution of 0.02m. This time history is used in the terrestrial model to determine both the height of salinity enhanced melting and dynamic pressure from the ocean on the bluff face.....	201
Figure 5.3-8. Ocean salinity time history processed with a simulation time step of 2min and a vertical resolution of 0.02m. Cyan values indicate some level of the bluff is in contact with the ocean water, water contact history given in Figure 5.3-7, and that salinity enhanced melting is thus occurring in the model calculation.....	202
Figure 5.3-9 Initial temperature field [K] in the computational domain. The top of the bluff is warmer than the bottom due to surface warming and a geothermal gradient. The bluff face is also above freezing due to contact with the air or ocean.	203
Figure 5.3-10 Initial ice saturation field in the computational domain. The ice wedge and permafrost material can be distinguished visually by the difference in ice content. The top surface of the bluff is completely thawed, as well as the face of the bluff.	204
Figure 5.3-11 Niche formation progression on the quasi-2D grid. Niche formation progresses from the top to the bottom in the column of figures. Left-hand column shows the ice saturation field (blue represents 100% ice and red represents 0% ice), and the right-hand	

column shows the failure state of each grid cell (blue represents 0 failed integration points, white represents 4 failed integration points (indicating the element will be removed), and red indicates 8 failed integration).....	206
Figure 5.3-12 Ice saturation (blue, 100% and red, 0%) and niche geometry at the time step immediately preceding block collapse. Two potential regions for tension fracture formation can be seen at the surface, ~ 2/3 rd s of the distance inland from the bluff face and at the ice wedge-permafrost polygon boundary.	207
Figure 5.3-13 Grid cell failure state and niche geometry at the time step immediately preceding block collapse. The grid cells with the highest failure state are located in the regions of maximal tension (near the bluff surface behind the niche) and maximal compression (at the back wall of the niche).....	208
Figure 5.3-14 Conceptual cross section of a bluff with a prescribed niche, showing regions of maximal tensile stress and maximal compressive stress. Adapted from Thomas et al. 2020.	209
Figure 5.3-15 Bluff salinity field and niche geometry at the time step immediately preceding block collapse. Grid cells that have been exposed to the ocean experience enhanced thaw and diffusion of salt into the permafrost.	210
Figure 5.3-16 Bluff displacement and niche geometry at the time step immediately preceding block collapse. Red indicates larger values of displacement, or slumping/rotation as the weight of the bluff and niche incision creates a bending moment.	211

LIST OF TABLES

Table 2.2-1. Details of the 3 telemetered time lapse cameras.	35
Table 2.2-2. Raw thermal denudation measurements. Top, Middle and Bottom refer to the horizontal location of the thermistor strings. Method of measurement changed on 08/14/2029 from the end of the pipe to the number of 10cm marks shown from face of bluff.....	39
Table 2.2-3. Summary of tilt sensor installation locations.	41
Table 2.2-4. Details of the 9 niche measurements made with laser finder. The max niche height is estimated from the full measurement profiles.	42
Table 2.3-1. Ikpikpuk Pressure sensor deployment details.....	53
Table 2.3-2. Drew Point Spit pressure sensor deployment details.	54
Table 2.3-3. 2018 & 2019 Temporary Wave/Water Level RBR Deployment Details.	55
Table 2.3-4. Mooring locations.	56
Table 2.3-5. Multibeam offset settings.....	57
Table 2.3-6. Water sampling plus CTD (Seabird Electronics 25+CTD with SBE 55 water sampler).	59
Table 2.3-7. Oxygen stable isotope values ($\delta^{18}\text{O}$, %).	60
Table 2.3-8. AML Probe Data (AML Oceanographic MinosX CTD).	61
Table 2.3-9. Bottom grab collections details and sediment grain size distribution analysis.....	62
Table 2.3-10. Beaufort Wind Scale.	67
Table 3.1-1. Detailed information on each core collected. Above Sea Level = ASL and Below Sea Level = BSL.	73
Table 3.3-1. Model coefficients for models shown in Figure 3.3-4 (above). In form $y = a + bx + cx^2 + dx^3$, where x is elevation (m) and y is porosity (%).	83
Table 3.3-2. Model coefficients for models shown in Figure 3.3-5 (above). Equations are in the form $y = a + bx$ where x is elevation (m) and y is porosity (%).	84

Table 3.3-3. Coefficients for linear models of grain fraction. Equations are in the form $y = a + bx$ where x is elevation (m) and y is the grain fraction (%).	87
Table 3.5-1. Frozen soil samples prepared for FY19 testing.	106
Table 3.5-2. Material Properties of Frozen Soil Samples.	109
Table 3.5-3. Results for compressive tests on frozen soil.	110
Table 3.5-4. Results for tensile testing on frozen soil.	112
Table 4.1-1. Variables of Interest From Atmospheric Reanalysis and Projection Datasets.	123
Table 4.2-1. WW3 Mean Wave Parameter Output Variables For All Output Stations.	129
Table 4.2-2. Descriptive Information about WW3 and Delft3D-FLOW/WAVE Models in the Oceanographic Modeling Suite.	139
Table 4.3-1. Overview of dynamic wave pressure variables.	143
Table 4.3-2. Density values for each permafrost constituent.	145
Table 4.3-3. Specific heat values for each permafrost constituent (Robertson 1988).	145
Table 4.3-4. Thermal conductivity values for each permafrost constituent (Robertson 1988; O'Connor et al. 2020).	146
Table 4.4-1. Experimental data used to establish vertical datum conversion between terrestrial and oceanographic products.	154
Table 5.2-1. Model Skill Performance Metrics.	166
Table 5.2-2. Arctic Atmospheric Reanalysis Data Sets used for WW3 Forcing.	170
Table 5.2-3. Selected Industry Wave Measurement Station Summary.	172
Table 5.2-4. WW3 Significant Wave Height / Peak Wave Period Performance Metrics at 2011 MOB2 Site for the Arctic Reanalysis Data Sets.	173
Table 5.2-5. WW3 Significant Wave Height / Peak Wave Period Performance Metrics at 2012 ShellHB Site for the Arctic Reanalysis Data Sets.	174
Table 5.2-6. WW3 Significant Wave Height / Peak Wave Period Performance Metrics at 2012 MOB103 Site for the Arctic Reanalysis Data Sets.	175
Table 5.2-7. WW3 Significant Wave Height / Peak Wave Period Performance Metrics at 2013 ShellHB Site for the Arctic Reanalysis Data Sets.	176
Table 5.2-8. WW3 Significant Wave Height / Peak Wave Period Performance Metrics at 2014 MOB101 Site for the Arctic Reanalysis Data Sets.	177
Table 5.2-9. WW3 Significant Wave Height / Peak Wave Period Performance Metrics at 2015 MOB102 Site for the Arctic Reanalysis Data Sets.	178
Table 5.2-10. Average WW3 Significant Wave Height / Peak Wave Period Performance Metrics for the Six Selected Stations for the Arctic Reanalysis Data Sets.	179
Table 5.2-11. WW3 Significant Wave Height / Peak Wave Period Performance Metrics at UW CODA S2-P1 Site.	181
Table 5.2-12. WW3 Significant Wave Height / Peak Wave Period Performance Metrics at UW CODA S3-P1 Site.	182
Table 5.2-13. Delft3D-FLOW/WAVE Significant Wave Height / Peak Wave Period Performance Metrics at Barnhart et al. 2014b Wave Logger 2 (2009) Site.	185
Table 5.2-14. Delft3D-FLOW/WAVE Water Level / Significant Wave Height / Peak Wave Period Performance Metrics at 2018 RBR Site.	187
Table 5.2-15. Delft3D-FLOW/WAVE Water Level / Significant Wave Height / Peak Wave Period Performance Metrics at 2019 RBR Site.	188
Table 5.3-1. Summary of locations and distance between them.	195
Table 5.3-2. Model parameters used for the niche formation demonstration simulation.	204

This page left blank

1. MOTIVATION

Arctic coastlines, which make up roughly one third of the global coastline extent, are retreating at an average rate of 0.5 m yr^{-1} (Lantuit et al. 2012). The long-term mean annual erosion rate (1940s – 2000s) of Alaska’s 1,957 km of Beaufort Sea coastline is 1.7 m yr^{-1} (Gibbs and Richmond 2015). Although these values may seem innocuous and low, the variability of magnitude and trend in rates is quite astounding. Some sections of the Alaska Beaufort Sea coast retreat more than 22 m in a single year, making them some of the fastest eroding coasts in the world (Gibbs and Richmond 2015, Jones et al. 2009a, 2018). And there is accumulating evidence indicating multiple Arctic coastal sites have experienced increased erosion of permafrost coastal bluffs during the 21st Century. Jones et al. (2018) showed that mean annual erosion for the 2007 to 2016 decade at Drew Point AK was 17.2 m yr^{-1} , which is 2.5 times faster than historic rates. “Tweedie et al. (2012) documented recent annual erosion trends of 1 to 4 m yr^{-1} between 2003 and 2011, which is 2 to 4 times higher than historic rates reported for their ~11-km study coast in Elson Lagoon in the western Alaskan Beaufort Sea (Brown et al., 2003). Along the eastern Alaskan Beaufort Sea, Gibbs et al. (2018) report that erosion along permafrost coastal bluffs at Barter Island increased from 1.6 m yr^{-1} (1979 to 2003) to 5.5 m yr^{-1} (2003-2017), a 3.4-fold increase. Irrgang et al. (2018) report that decadal-scale erosion measured along a 210 km reach of the Yukon Territory mainland Canadian Beaufort Sea increased from 0.5 m yr^{-1} (1970 to 1990) to 1.3 m yr^{-1} (1990 to 2011), a 2.6-fold increase. And lastly, observations from coastlines backed by syngenetic permafrost in the Laptev Sea region in Siberia also indicate erosion rates 1.5 to 3 times higher in the early 2000s relative to the period between 1950 and 2000 (Günther et al., 2013, 2015).” (verbatim from Jones et al. 2018)

In the Arctic people and infrastructure are concentrated near the coastline and along rivers due to the lack of all-season roads, hence erosion along coastlines has an outsized influence on the economic activities of the Arctic. These eroding coastlines are compromising infrastructure, destroying cultural sites, and threatening traditional practices including hunting and fishing (Jones, 2008). More than 30 native coastal villages in Alaska are facing relocation, at huge economic and cultural expense, due to erosion (USGAO 2004, 2009). Active U.S. Department of Defense (DOD) Long Range Radar Sites in the North Warning System (NWS) are experiencing higher-than-expected rates of bluff retreat requiring remediation efforts to secure them (Hughes 2016). The DOD has explicitly noted impacts from increasing storm intensity and associated storm surge with resulting mission vulnerabilities including: “disruption of military operations, increased cost of infrastructure modification, impacts to future land availability, and siting of new construction” (USGAO, 2014). And, the financial impact of coastal erosion will likely be further exacerbated by emerging economic incentives requiring the development of new infrastructure, including the discovery of natural resources (oil and gas (Bird et al. 2008), and minerals (Borgerson 2013)) and the opening of new shipping routes (Humpert and Raspotnik 2012) in the Arctic.

“Erosion also delivers sediment, organic matter, and inorganic nutrients to the Arctic Ocean (Ping et al. 2011; Lantuit et al. 2012). Soils in northern Alaska contain ~40 to 150 kg total organic carbon (TOC) m^{-2} in the top 3 m (Hugelius et al. 2014, Schuur et al. 2015, Strauss et al. 2013; Fuchs et al. 2019). Most of this TOC is sequestered in permafrost. However, coastal erosion can rapidly liberate large quantities of frozen organic matter to the coastal ocean (Fritz et al 2017; Stein and MacDonald 2004; Vonk et al. 2012; Vonk and Gustafsson 2013). An estimated 5-41 Tg of soil TOC is released to the Arctic Ocean each year from coastal erosion, similar in magnitude to river-borne particulate organic carbon (POC) export to the Arctic Ocean (McClelland et al. 2016; Wegner et al. 2015).” (verbatim from Bristol et al. Submitted) At Drew Point AK, erosional fluxes of TOC along a 9km stretch averaged 12,849 metric tons C/yr (12.8 Gg C/yr) during the 21st century (2002-2018), nearly

double the average for historical fluxes (1955-2002) (Bristol et al. Submitted). “Eroded material may be deposited in nearshore marine sediments, resuspended in the water column as POC, or leached to dissolved organic carbon (DOC) (Dou et al. 2008, Fritz et al. 2017, Vonk et al. 2012). Previous work has shown that coastal permafrost soils along Herschel Island, Canada are rapidly decomposed by bacteria in seawater, thereby creating a significant source of carbon dioxide from microbial metabolism (Tanski et al. 2019). In addition to heterotrophic bacteria, higher organisms in nearshore marine food webs also utilize watershed-derived organic matter along the Beaufort Sea coast (Bell et al. 2016, Dunton et al. 2012, Harris et al. 2018).” (verbatim from Bristol et al. Submitted)

Although the Arctic coastline comprises such a large percentage of the total coastline length, there are significant infrastructure impacts, as well as substantial ecological impacts, much of our current understanding of coastal landscape evolution is applicable to coasts that are fundamentally different than the Arctic. Ice in permafrost acts as the consolidating material, making erosion in the Arctic fundamentally a thermal-chemical-mechanical process for which models developed for the lower latitudes have limited applicability. Thermo-denudation and thermo-abrasion processes dominate Arctic coastal erosion (Are 1988a,b; Walker 1988; Günther et al. 2013). Thermo-denudation refers to the degradation of permafrost from warming air causing subsidence or slumping under gravitational forces. Thermo-abrasion refers to the combined effect of thermal and mechanical erosion of ice-rich permafrost bluffs due to ocean wave action. To date attempts to model and understand these processes have been limited in some way (as will be explored in more detail below).

In the sections that follow, details of permafrost, the environmental causes of Arctic coastal erosion, the modeling approaches to date, and the approach pursued in the rest of this document will be discussed in more detail. First characteristics of permafrost will be detailed. Next, the changing environmental conditions thought to be the cause of the increased erosion rates and correlation attempts to those drivers will be explored. Then the mechanisms of erosion and previous modeling attempts will be outlined. Finally, the approach this research is taking will be summarized before being presented in detail in the rest of the chapters (Chapters 2-4).

1.1. Permafrost

Arctic coastlines are unique in that they are composed of permafrost. “By definition, permafrost is ground (soil, rock, or sediment) that remains frozen (temperature < 0_C) for two or more consecutive years. Permafrost underlies most land surfaces in the Arctic, varying from a few meters to several hundred meters thick, depending on its thermal history. The ice content of permafrost can vary significantly. It can be ice-rich, or it can contain practically no ice at all. The surface layer, called the active layer, typically thaws and re-freezes each year.” (verbatim from Frederick et al. 2016) The vast majority of the mainland coasts in the Arctic are composed of unlithified, sedimentary deposits (Overduin et al., 2014). “Ice wedges and polygonal surface features (i.e., ice-wedge polygons) are typical of this unlithified permafrost landscape (see Figure 1.1-1). These form when thermal contraction during winter months cracks the frozen ground, much like the surface of sunbaked, dried mud. During the warmer, wetter season, water infiltrates the cracks and refreezes. Consecutive freeze-thaw cycles cause the ice wedges to grow and expand up to several meters wide, and 10s of meters deep, forming polygonal features often clearly seen on the surface. A recent survey of ground ice along the Alaskan Beaufort Sea coast found wedge ice and ice-wedge polygons nearly everywhere (Kanevskiy et al., 2013).” (verbatim from Frederick et al. 2016)

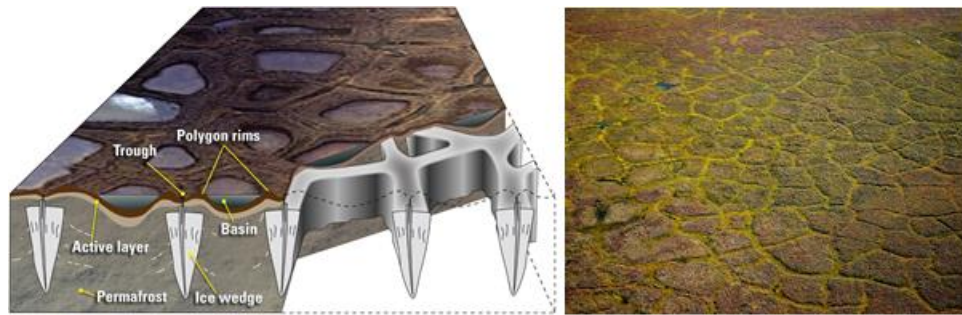


Figure 1.1-1. A schematic illustrating the formation of ice wedges and ice-wedge polygon landscapes. Adapted from (Martin et al., 2009).

The Alaskan Arctic coastline along the U.S. Chukchi and U.S. Beaufort Sea is entirely permafrost and extends more than 8,000 km from the Bering Strait to the Canadian border. Along the Beaufort Sea coastal permafrost is predominantly primary surface of the coastal plain (western and eastern regions) and drained-lake basins (Kanevskiy et al., 2013). Differences between these land surface types will be explored in more detail in the report, but importantly poorly draining soils like clays and silts common in primary surface and drained lake basins permafrost tend to have larger unfrozen water contents at temperatures well below 0°C (Kruse and Darrow 2017). Unfrozen water reduces the strength of the material, which in unlithified material derives its strength from ice, likely increasing this type of permafrost's susceptibility to thermo-abrasive erosion (Arenson et al. 2007). When thermo-abrasive processes dominate erosion for these land surface types, block failure is common. Hence erosion is largely episodic in nature and not a gradually and consistently increasing in time as is more common for thermo-denudation-based erosion. High variability in ground-ice content (effective porosity), wedge-ice content, as well as variation in erosional processes, geomorphology, lithology, coastal orientation, near shore bathymetry, and the presence of barrier islands all contribute to high variability in erosion amounts (Jorgenson and Brown, 2005; Kanevskiy et al., 2013).

1.2. Environmental Drivers

Until recent years, perennial sea-ice covered the Arctic ocean. The Arctic Report Card (ARC) highlighted that Arctic Ocean temperatures and sea ice have changed at the fastest rates in at least 1,500 years (ARC 2017). Arctic sea ice has lost 75% of its volume and 51% of its area since 1979 (Overland, 2018; ARC, 2018b). In the last 33 years, 95% of multiyear sea-ice (thicker) has vanished with the mean Arctic sea ice thickness declining from 3.64 meters in 1980 to approximately 2m in 2018 (ARC 2018; Kwok, 2018).

The Arctic is warming in all sectors. Average air temperatures are +1.7°C relative to the 1981-2010 average (ARC 2018). Increasing ocean temperatures in the Arctic (Steele and Dickinson, 2016) are not only driven through positive ice-albedo feedback (Timmermans et al. 2015) but also through both larger changes in the Atlantic and Pacific oscillations (Wantanabe & Hasumi 2009) as well as more local perturbations due to wave energy (Lincoln et al. 2016). Permafrost temperatures are also increasing (Romanovsky et al. 2010; Smith et al. 2010).

As the Arctic warms, reductions in sea-ice extent coupled with increasing duration of open water over a season are resulting in increasingly energetic waves incident upon the Alaskan coast (Stammerjohn et al. 2012; Thomson et al. 2016; Barnhart et al. 2014a). The geometry of the open water, relative to the wind magnitude and direction, as well ice-free durations determine wave

growth and energy content (Hasselmann et al. 1973; Young 1999; Pierson & Moskowitz, 1964; Thomson & Rogers 2014; Thomson et al. 2016). Historical data from satellite-derived ice concentrations show the largest changes in ice cover are occurring in the East Siberia, Chukchi, and Beaufort Seas (Stopa et al. 2016; Lee et al. 2012). With this increasing wave and temperature developments the acceleration of thermo-mechanical erosion is expected (Overeem et al. 2011; Barnhart et al. 2014b).

A preliminary step undertaken in this research was to determine the environmental drivers of erosion at Drew Point AK, the chosen field study location. In a study by Hequette & Barnes (1990) some positive correlation was observed between wave heights of over 1m and wave power with coastal retreat rates for the Canadian Beaufort Sea. Günther et al. (2015) found the two most important controls on annual erosion at Muostakh Island in the Laptev Sea were open water days and thawing degree days. Overeem et al. (2011) indicated that the duration of open water conditions could be a good first order predictor of coastal erosion based on similar increases in open water duration and erosion rates for 1979-2002 and 2002-2007 at Drew Point, Alaska. Lantuit et al. (2008a) demonstrated a weak but statistically significant relation between ground-ice content and mean retreat rate, with higher mean annual retreat rates typically corresponding to coastlines with higher ground-ice content. However, Lantuit et al. (2011) found no relation between storminess and erosion for the Bykovsky Peninsula for the years 1958-2006. And Tweedie et al. (2016) also found inconclusive evidence of correlation between erosion in Elson Lagoon with wind-driven wave activity. Employing some of the same indicators and techniques, using a high spatiotemporal erosion dataset similar questions were asked at Drew Point AK. Below highlights of the work presented in the Environmental Research Letters publication (Jones et al. 2018) undertaken during the course of this research are given.

One of the highest spatiotemporal resolution datasets of coastal permafrost erosion was investigated to determine correlation with potential environmental drivers at similar temporal resolution. High-spatial resolution (sub-meter) satellite imagery derived from optical sensors (Quickbird, IKONOS, GEOEYE, Worldview-1 and -2) documented a decade of annual open water season erosion along a 9-km segment of the Alaska Beaufort Sea Coast located near Drew Point (Figure 2.1-1). Open water season erosion was classified annually for the decade (2007-2016) making it one of the longest and highest temporally resolved erosion data sets. Possible environmental drivers included open ocean water duration, sea surface temperature, storm number, cumulative storm strength, thawing degree days, and near-surface permafrost temperatures. Descriptions of each environmental parameter are given below:

- Open water duration-- determined using the Nimbus-7 SMMR and DMSP SSM/I-SSMIS Passive Microwave Data from the National Snow and Ice Data Center (NSIDC); defined as grid cells exhibiting less than 15% sea ice concentration in a given year near Drew Point (Overeem et al. 2011)
- Sea surface temp— weekly sea surface temperature data, from the NOAA Optimum Interpolation (OI) Sea Surface Temperature (SST) V2 dataset (Reynolds et al., 2002), were averaged for the various open water periods determined with the NSIDC open water duration dataset
- Storm number-- modified the methods of Atkinson (2005) to represent winds exceeding 5 m/s from directions of 240° to 360° and 0° to 90° for a period of at least 12 hours with no lulls > 6 consecutive hours

- Cumulative storm strength-- the square of a storm's average wind velocity relative to its duration (Atkinson, 2005)
- Thawing degree days—daily means at or above on 0 °C obtained from hourly air temperature data collected by the U.S. Geological Survey meteorological station (Urban and Clow, 2016)
- Near-surface permafrost temperatures—seasonal means (June to November) from temperature data collected by the U.S. Geological Survey meteorological station (Urban and Clow, 2016).

As shown in Figure 1.2-1 multivariate analyses of the environmental data do not show significant correlations with our open water season erosion time series. The lack of significant correlations between mean annual erosion and the suite of environmental variables compiled in this study means we are likely not accurately capturing all of the environmental forcing factors at adequate resolutions or accuracies, that the system is conditioned by long-term transient effects or extreme weather events rather than annual variability, or that other not yet considered factors may be responsible for the increased erosion occurring at Drew Point.

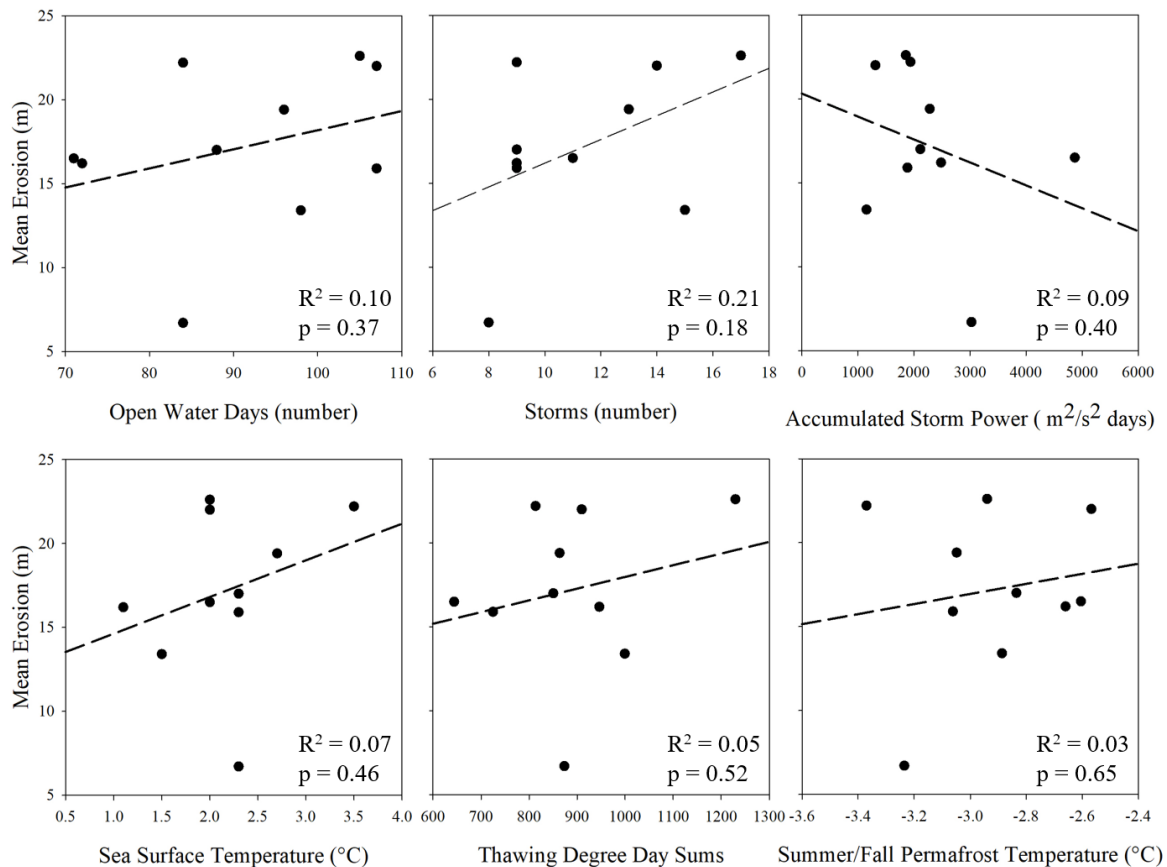


Figure 1.2-1. Scatterplots of mean erosion between 2007 and 2016 and potential environmental forcing factors. Open water days derived from NSIDC, storms, storm power, thawing degree day (TDD) sums, and near surface permafrost temperature (1.2 m depth) derived from the Drew Point Meteorological Station, and sea surface temperature derived from NOAA OISST V2 data. All plots show coefficient of determination and linear regression lines (dashed). Adapted from Jones et al. 2018.

1.3. Erosion Mechanisms

Thermo-denudation and thermo-abrasion processes dominate Arctic coastal erosion (Are, 1988a,b; Walker 1988; Günther et al. 2013). Thermo-denudation refers to atmospheric warming of permafrost, which results in subsidence or slumping of the material due to gravitational forces. Active layer detachment and retrogressive thaw slumping are two examples of slope failure associated with thermo-denudation (Lantuit & Pollard, 2008b). With a thermo-abrasive process, undercutting of a permafrost bluff to produce a niche occurs as the permafrost is first warmed by the ocean and then removed by the mechanical action of waves. The resulting over-hanging bluff then fails in a “block failure” event. The role of undercutting and the presence of massive ice and ice wedges are cited as factors affecting block failure (Walker, 1988). Although variability in ground-ice content (effective porosity), wedge-ice content, as well as variation in erosional processes, geomorphology, lithology, coastal orientation, near shore bathymetry, and the presence of barrier islands are all thought to contribute to high variability in erosion amounts (Jorgenson and Brown, 2005; Kanevskiy et al., 2013)

Focusing on block failure, it has been clear that the niche is central to the failure mechanism. The framework for modeling niche development in permafrost was pioneered by Kobayashi (1985). He developed a 1D analytical solution for heat transfer from the ocean considering water temperature, water level, and water dwell time in order to predict niche depth (Kobayashi 1985). Empirical equations originally designed to predict the melting rate of free-drifting icebergs (e.g., Russell-Head 1980; White et al. 1980) have also been the basis of niche formation predictions (Wobus et al. 2011; Barnhart et al. 2014b).

Hoque and Pollard (2009, 2016) focused on coupling niche development with block instability. Their work employs analytical relationships to explore how sliding versus toppling failure modes are influenced by geomorphological (niche depth, ice-wedge geometries, bluff heights) and geophysical (ice content, soil shear strength) properties assuming, if an ice-wedge is present, that the failure will occur along that plane (Hoque and Pollard, 2009; Hoque and Pollard, 2016). For each simulation, geotechnical properties such as cohesion, internal friction angle, and/or temperature independent tensile strength are defined for permafrost bluffs in the presence and absence of ice wedges (Hoque and Pollard, 2009). Their work expanded to developing nomograms to relate block failure potential for distinct cliff heights based on different ice wedge morphologies and permafrost rheology (Hoque and Pollard, 2016). However, their work does not address the conditions that form the niche, contribute to the small corpus of knowledge regarding temperature and ice volume dependent strength properties of permafrost, nor explore the analytical stability relationships through higher fidelity simulation.

Ravens et al. (2012) was the first model incorporating transience by focusing on the oceanographic boundary conditions in quasi-steady half-day periods that form the niche. The historical wind conditions were binned into a set of 32 classifications to determine the water levels used to populate a 1D analytical niche development model based on Kobayashi's 1985 formula. Block collapse upon attainment of a critical niche depth (10m) was assumed and the coastline was shielded until the fallen block fully degraded according to Kobayashi's 1985 erosion rate model. After calibrating their model with 24 years of bluff retreat data for the Beaufort Sea coast in Alaska, Ravens et al. (2012) calculate erosion rates for a (subsequent) seven-year period within 20% demonstrating the importance of the oceanographic boundary condition.

Barnhart et al. (2014b) combines the strengths of all of the previous approaches (e.g., Kobayashi 1985, Wobus et al. 2011, Hoque and Pollard 2009 and 2016, and Ravens et al. 2012) to use the

oceanographic conditions as a direct driver of niche formation (using Kobayashi 1985, Russell-Head 1980, and White et al. 1980) while also employing a stability model that sums the resistive and driving forces (in the spirit of Hoque and Pollard 2009 and 2016). Barnhart et al. (2014b) improves upon Ravens oceanographic treatment to increase the temporal resolution to 1 hour. Both short- and long-term model time periods are used to test the accuracy of the three niche-formation formulations expanding upon Wobus et al. (2011). This work is the first to transiently couple slope stability analyses with niche formation expanding upon Hoque and Pollard (2009, 2016). This research was, at the time, the most complete attempt to capture the full system in one model. However, this model relied upon 1D analytical and empirical formulations to form the niche, an approximation of the oceanographic conditions, an assumption of the failure plane location, and assumptions regarding the stability of an overhanging bluff.

Although the work of Hoque and Pollard (2009, 2016) explored the influence of geomorphological and geophysical properties on the failure mode, investigations into the effects of the heterogeneity of the terrestrial coastlines on failure mechanisms is in its infancy. Hence, another preliminary step undertaken as part of this research was to interrogate the geometric and material properties influence on the resulting compressive and tensile stress states in a purely mechanical finite element model of a permafrost bluff (Thomas et al. 2020). Using an elastic only simulation in Albany (an open-source implicit unstructured finite-element application (Salinger et al. 2016; Sandia National Laboratories 2017)) subject to only gravitational forces, the variations on the niche dimension, bluff height, permafrost polygon size, ice wedge geometry, bulk density, Young’s Modulus and Poisson’s ratio were evaluated for their affect on location and magnitude of simulated max tensile stress, σ_{Tmax} (Thomas et al. 2020). The σ_{Tmax} , created by a bending moment along the bluff face (Figure 1.3-1), is an important metric because it reflects a likely initiation location for toppling mode block failure.

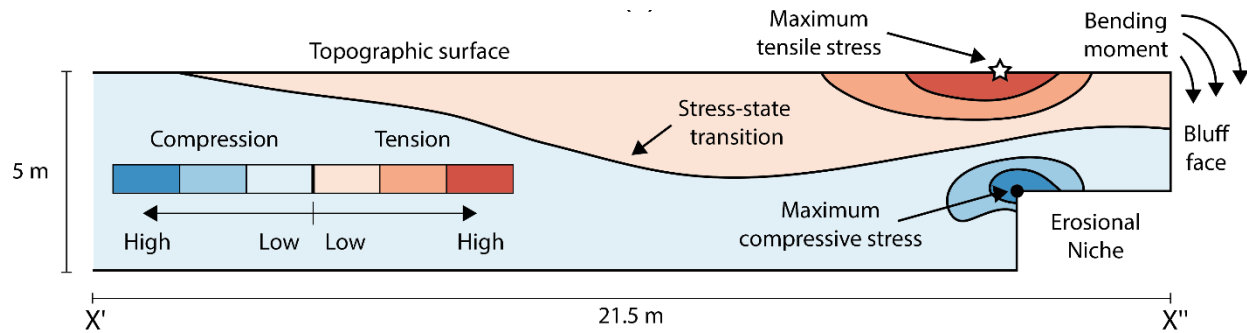


Figure 1.3-1. Conceptual cross section of patterns of stress based on elastic geomechanical simulation. Adapted from Thomas et al. 2020.

Thomas et al.’s (2020) “geometric and material property simulation ensembles indicate that niche characteristics exert the largest impact on the location and magnitude of the σ_{Tmax} (Figure 1.3-2), with the strongest gradient in simulated σ_{Tmax} following variability in niche depth (N_D). Therefore, an important implication of this work is that the location and shape of the potential failure plane could be modulated by the transient characteristics of the oceanographic forcings (e.g., wave power, water depth, and water temperature) that are delivered to a coastline. This suggests that a stability assessment approach, for which the failure plane is assumed to coincide with a constant geometric feature (e.g., a geologic discontinuity such as an ice wedge) or a particular niche depth, may not be ideal for coastlines similar to our study area. The impact of storm-based metrics (e.g., surge height, dwell time, and water temperature) on niche morphology could be examined with a physics-based

modeling approach that expands upon ours to include transient simulations of oceanographic conditions.” (verbatim from Thomas et al. 2020)

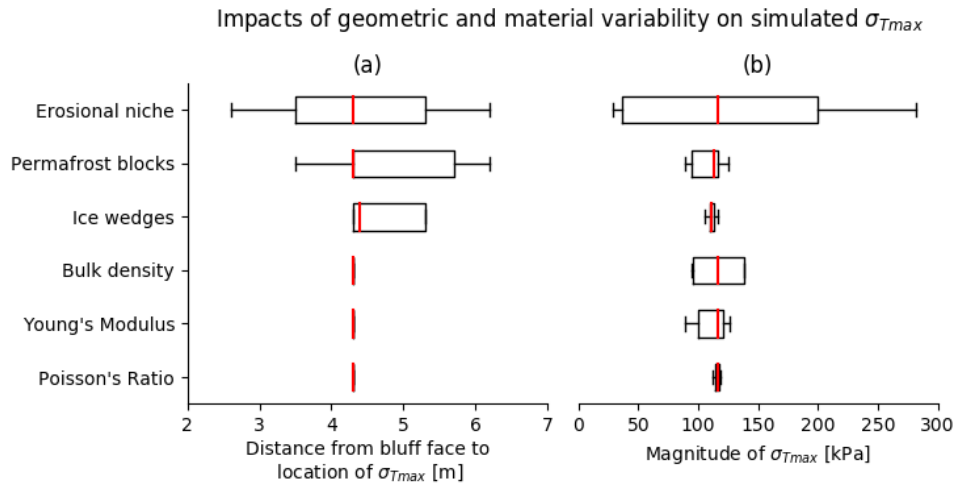


Figure 1.3-2. Boxplots showing the impact of variability in geometric (i.e., erosional niche, permafrost block, and ice wedge) characteristics and ice/permafrost material properties (i.e., bulk density, Young’s Modulus, and Poisson’s Ratio) on the (a) location and (b) magnitude of the simulated maximum tensile stress (σ_{Tmax}). Adapted from Thomas et al. 2020.

1.4. Proposed Mechanistic Modeling Approach

A few common themes emerge from the literature:

1. the permafrost thermal state, and hence ice saturation, will be a first order control on the strength of the permafrost (Arenson et al. 2007),
2. the stress state of the permafrost bluff will ultimately dictate failure (Thomas et al. 2020), and
3. the water setup on the permafrost bluff (height, duration, and temperature) will control niche formation (Barnhart et al. 2014b).

However, current Arctic erosion models have focused only on a portion of the coupled dynamics (evolving wave dynamics or the mechanical erosion process) and/or have used empirical simplifications (Hoque and Pollard 2009 & 2016; Ravens et al. 2012; Barnhart et al. 2014b). All previous approaches have also ignored the chemical process of salinity-based melting from interaction with ocean water. Further, the work of Jones et al. (2018) and Thomas et al. (2020) (pursued in during this research) combine to indicate that an understanding of the transient events that physically drive niche morphology must be developed in order to capture erosion variability and its environmental drivers.

Hence as will be detailed in the following chapters and was first proposed in Frederick et al. (2016), a physics-based model coupling high-fidelity oceanographic modeling with high-fidelity terrestrial modeling to capture the thermo-mechanical dynamics of erosion has been pursued. This local, event-based simulation framework enables testing of the hypothesis that time-varying temperature/ice contents in permafrost, controlled by time-varying boundary conditions, markedly influence the timing and degree of erosion via block failure.

In the Arctic Coastal Erosion Model, oceanographic boundary conditions are provided by a numerical modeling suite comprised of a circum-Arctic Wave Watch III model forcing a two-way coupled SWAN – Delft3D local model. Combined with atmospheric conditions, this suite produces

time-dependent surge and run-up output to force the terrestrial model developed in Albany. A major improvement offered by the Arctic Coastal Erosion Model is that the failure mechanism of the coastal permafrost is not pre-determined or empirical, but results from deformation (block erosion or slumping) found through constitutive relationships. In the multi-physics based finite element terrestrial model the 3D stress/strain fields develop according to a frozen water content dependent plasticity model which in turn is driven by the thermal evolution of the permafrost bluff via 3D heat conduction supplied from the boundary conditions. A parallel field campaign (2018 & 2019) at Drew Point, Alaska is being used to validate and calibrate the Arctic Coastal Erosion Model parameters for that rapidly eroding site.

2. FIELD WORK

Field work occurred in 2018 and 2019. Additional terrestrial field data collected over the years from 2007 through 2018 were made available to the project by Ben Jones. Additional oceanographic data compiled for the BOEM project was made available to the project by Jeremy Kasper.

In the spring of 2018, a snow machine expedition was mounted to obtain permafrost cores from land surfaces at Drew Point and is described in Section 3.1. These cores were processed to support various analyses including those discussed in Section 3.

2018 Spring Team Members: Ben Jones (UAF), Chris Arp (USGS), Allen Bondurant (UAF), Go Iwahana (UAF), and Misha Kenevskiy (UAF)

In the summer of 2018, terrestrial and oceanographic field campaigns were completed; an overview of the work is shown in Figure 2-1. The terrestrial campaign from July 22 to August 4 was led by Ben Jones and focused on UAV surveys for Structure for Motion (SfM) analysis, temperature profiles, nearshore single-beam bathymetry surveys, deployment of time-lapse cameras, and deployment of nearshore pressure sensors. The oceanographic campaign from July 28 to 29 was led by Jeremy Kasper and focused on deployment of an ADCP package, multibeam bathymetry surveys, and CTD grabs.

2018 Summer team members: Ben Jones (UAF), a team of researchers (Guido Grosse, Mike Angelopolous, Josefine Lenz, Juliane Wolter) from the Alfred Wegener Institute (AWI) in Potsdam, Germany, led by Dr. Professor Guido Grosse, Jim Webster (Floatplane Pilot), Jeremy Kasper (University of Alaska, Fairbanks), Mr. Paul Duvoy (University of Alaska, Fairbanks), Mr. Nick Konefal (University of Alaska, Fairbanks), and Mike Fleming (R/V Ukpik Captain)

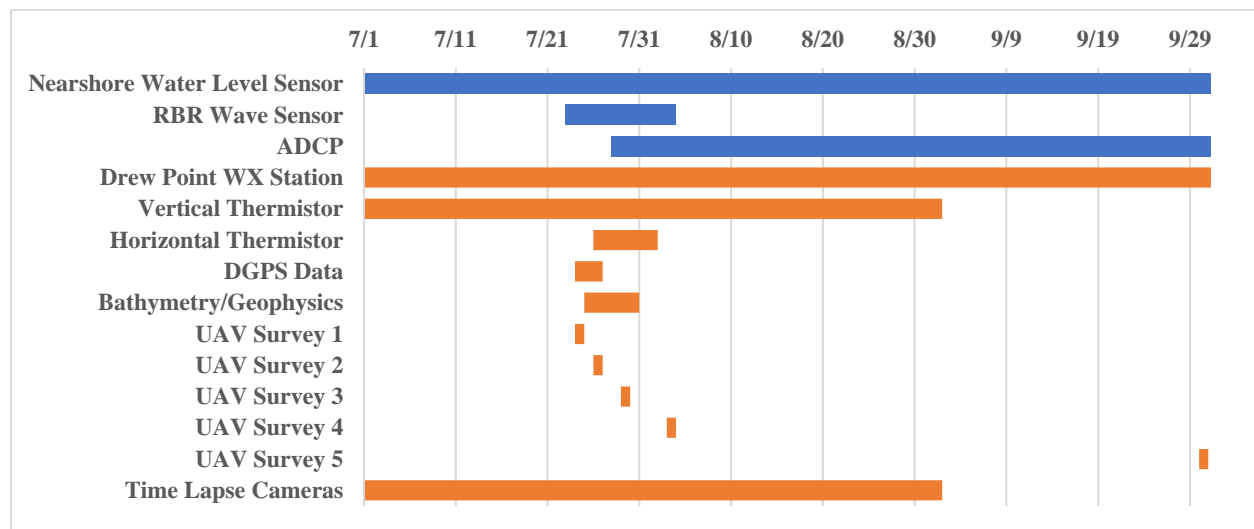


Figure 2-1. 2018 Field Campaign Gantt Chart. Oceanographic sensor deployments shown in blue and terrestrial sensor deployments shown in orange.

In the summer of 2019, terrestrial and oceanographic field campaigns were completed; an overview of the work is shown in Figure 2-2. The terrestrial campaign from August 2 to August 16 was led by Ben Jones and focused on UAV surveys for Structure for Motion (SfM) analysis, temperature profiles, tilt sensor deployment, laser measurement of niche profiles, deployment of time-lapse cameras, and deployment of nearshore pressure sensors. The oceanographic campaign from August

24 to 25 was led Jeremy Kasper and focused on collection of the Smith Bay mooring (ADCP).
 2019 Summer team members: Ben Jones (UAF), Melissa Ward Jones (UAF), Lillian Jones, Diana Bull (SNL), Jennifer Frederick (SNL), Matt Thomas (USGS), Emily Bristol (UTA), Louise Farquharson (UAF), Joan Webster (UAF), Jim Webster (Floatplane Pilot), John Crews (Helicopter Pilot), Jeremy Kasper (University of Alaska, Fairbanks), Mr. Paul Duvoy (University of Alaska, Fairbanks), Mr. Nick Konefal (University of Alaska, Fairbanks), and Mike Fleming (R/V Ukpik Captain)

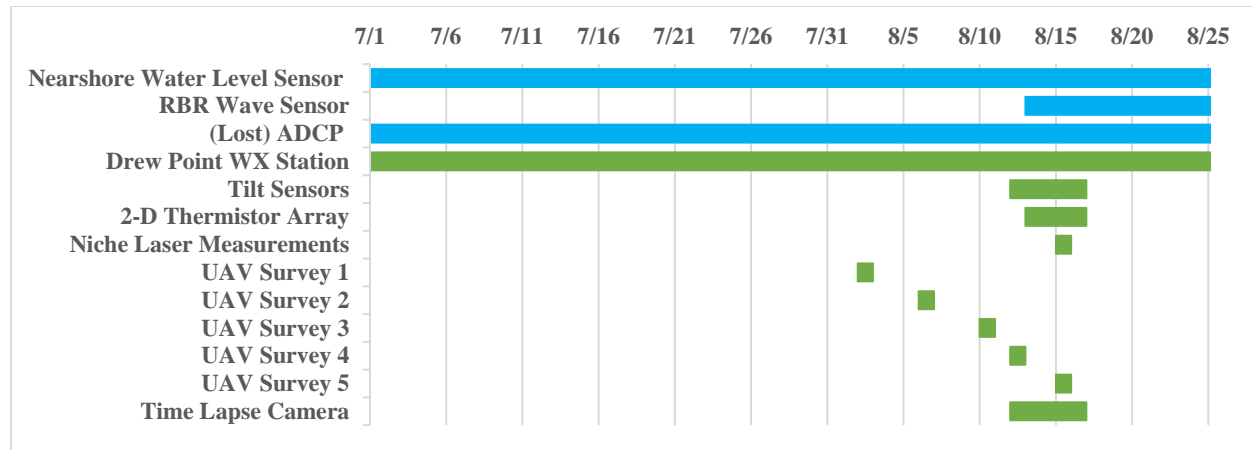


Figure 2-2. 2019 Field Campaign Gantt Chart. Oceanographic sensor deployments shown in blue and terrestrial sensor deployments shown in Green.

2.1. Drew Point

“We focus on a 9-km stretch of the Drew Point coastline located in the western region of the Alaskan Beaufort Sea Coast about 100 km east of Utqiagvik (formerly known as Barrow) and 200 km west of Prudhoe Bay (Figure 2.1-1). The dominant erosional process at Drew Point consists of thermo-abrasion (Jones et al. 2009b), although thermo-denudation also occurs here (Wobus et al., 2011) (Figure 2.1-2). Bluff height ranges from 1.6 m to 7.1 m, with a mean of 4.4 m above the mean water level during LiDAR data acquisition on 6-Aug-2011. The near surface sediments consist mainly of ice-rich Holocene-aged lacustrine silts with local peat accumulations and contain large ice wedges. Sediments underlying lacustrine silts consist of transgressed marine late Quaternary silts and clays with sandy horizons near the base of the eroding bluffs.” (verbatim from Jones et al. 2018)

The bluff stratigraphy at Drew Point (Figure 2.1-2) includes vegetative matting, an active (seasonably unfrozen) surficial layer, an organic layer, a relict marine layer, and a cyropeg (perennially unfrozen due to high salinity) (Bristol et al. Submitted). “Estimates of total volumetric ground-ice content for permafrost along these bluffs approaches 80-90 %, (Kanevskiy et al., 2013), with segregated and pore ice volumes accounting for 50 to 80 %, and wedge ice contributing nearly 30% in some locations (Wobus et al., 2011). The fine-grained composition of the bluffs means that eroded sediment is easily transported away and does not accumulate and protect the base of the bluffs as is common elsewhere. Estimates of ice-wedge polygon dimensions, range from 6 to 25 m across with a mean size of ~15 m (Wobus et al., 2011; Kanevskiy et al., 2013). Ice wedges are approximately 1 to 4 m wide near the surface and typically penetrate 3 – 5 m down from the surface. The Drew Point area is underlain by continuous permafrost with mean annual ground surface temperatures of about -9 °C (Smith et al., 2010). Permafrost at a depth of 20 m at coastal sites along the Alaskan Beaufort Sea Coast has warmed by 0.6 °C to 2.2 °C between 1989 and 2008 (Smith et al., 2010).”

(verbatim from Jones et al. 2018) These bluff height and ice-content characteristics are typical for ~25% of the Beaufort Sea coast (Barnhart et al. 2014b).

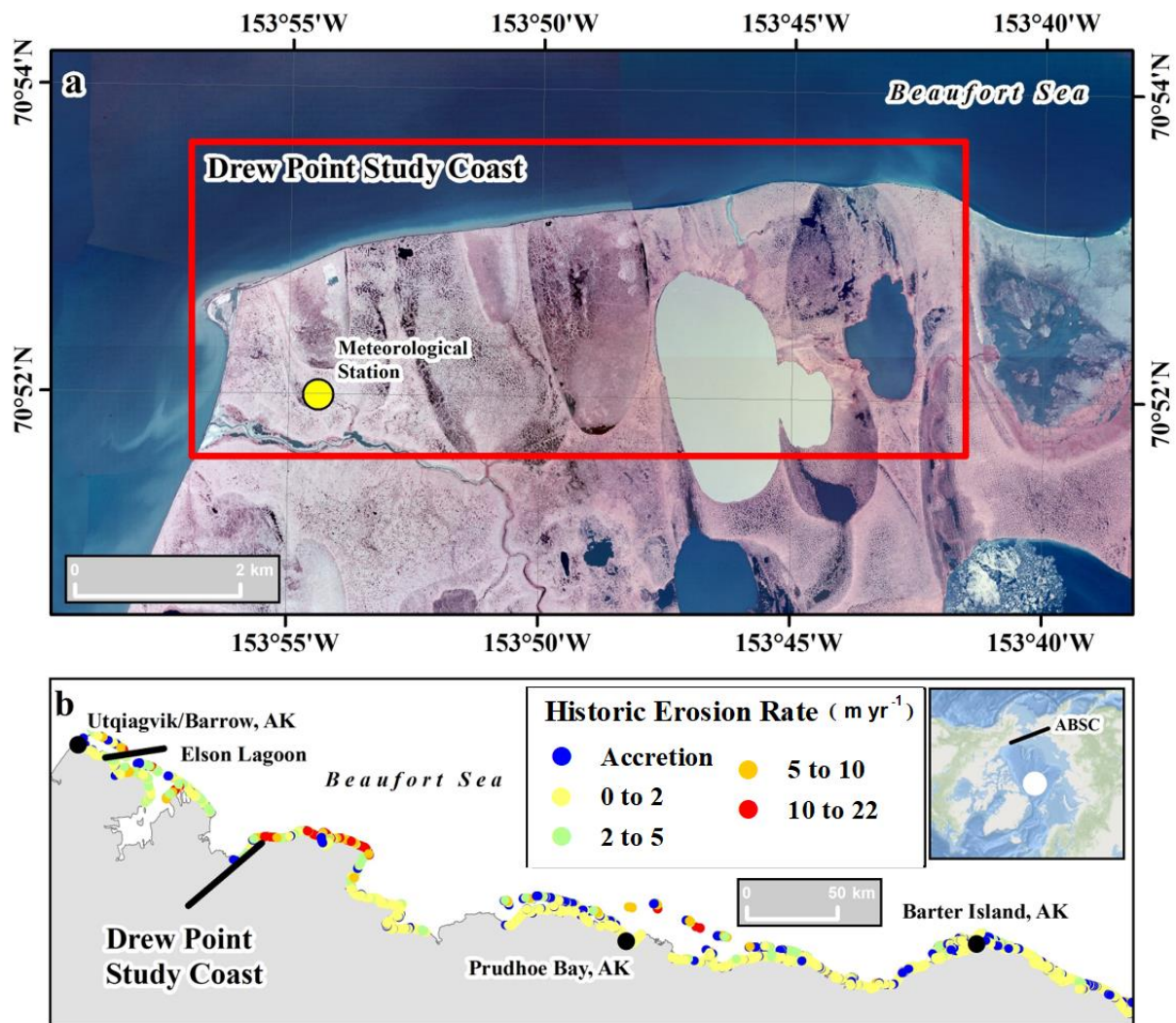


Figure 2.1-1. The Drew Point study area, Alaska Beaufort Sea Coast (ABSC). (a) The overlapping footprint of remotely sensed imagery used in this study is outlined with the red rectangle. The location of the meteorological station is shown with the yellow dot. (b) The location of Drew Point along the ABSC. Historic erosion rates from Gibbs and Richmond (2017) are shown for the period 1947 to 2010.

“Offshore, water depths are shallow, the open water season is short, and the tidal range is on average only 15 cm. Nearshore water depth is less than 2 m within a distance of 0.5 km from the shoreline and increases to 3 m at a distance of 2.0 km from the coast. The nearshore open water duration at Drew Point has more than doubled between 1979 and 2009, increasing from ~45 days to ~90 days, with a higher proportion of the increase in open water duration occurring in the fall (~0.9 days yr⁻¹) relative to the early summer (~0.7 days yr⁻¹) (Overeem et al., 2011). However, this area is prone to highly variable open water seasons and is influenced by sea-ice transport and break-up patterns from both the east and the west (Barnhart et al., 2016). Between 2007 and 2012, the Beaufort Sea experienced the lowest September sea ice extents yet observed since the late 1970s (Ballinger and Rogers, 2013) and has continued to exhibit similar patterns through 2017 (Perovich et

al., 2017). This increase in open water days has been accompanied by a warming trend in sea surface temperature (SST) in the Beaufort Sea (Steele and Dickinson, 2016). Air temperature has continued to increase in this region since 2000 as measured near Utqiagvik, AK (Wendler et al., 2012).” (verbatim from Jones et al. 2018)

“Rapid shoreline retreat rates observed along the Alaskan Beaufort Sea Coast may partially be explained by erosional processes uniquely associated with ice-rich permafrost coastal bluffs (Are, 1988; Dallimore et al., 1996). Lantuit et al. (2008a) demonstrated a weak but statistically significant relation between ground-ice content and mean retreat rate, with higher mean annual retreat rates typically corresponding to coastlines with higher ground-ice content. Block failure following undercutting caused by thermo-abrasion and thaw slump activity (thermo-denudation) are common modifiers of Arctic coastal morphology and tend to be dominant erosional processes along ice-rich permafrost bluffs (Are, 1988; Walker, 1988; Günther et al., 2012).” (verbatim from Jones et al. 2018)

Typically, the failed blocks (Figure 2.1-2) provide only short-term armoring against further retreat as they disintegrate in the nearshore environment over the course of days to weeks (Barnhart et al. 2014b; Jones et al. 2018). “Melting of ground ice is an important consideration as it can substantially reduce the volume of sediment input and cause thaw settlement in the nearshore, deepening the nearshore profile. Interestingly, observations made along this coast in 1901 (Schrader, 1904) indicate that collapsed blocks could persist for 4 to 5 years (Leffingwell, 1919). Such observations highlighting that both the formation of erosional-niches followed by block collapse have been modifying this coast for at least the last century and that the combined impacts of climatic-oceanographic-geomorphologic conditional states have changed dramatically since the early 1900s.” (verbatim from Jones et al. 2018)

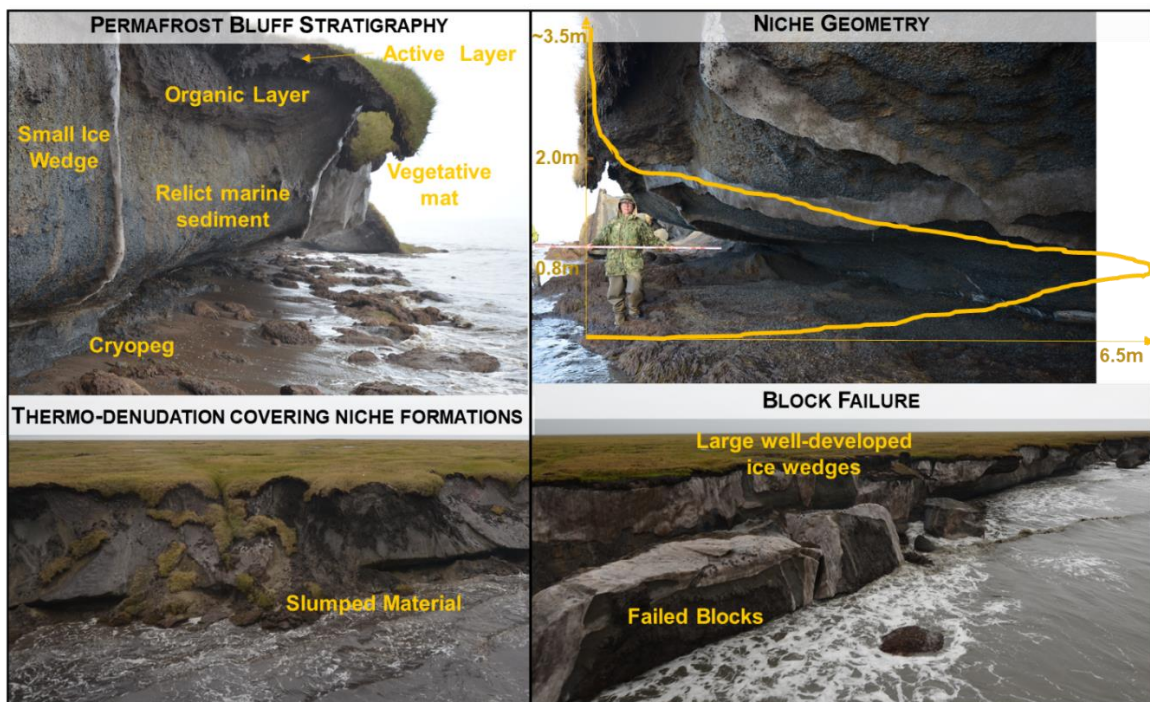


Figure 2.1-2. Field photographs documenting aspects of the permafrost bluff and erosion mechanisms at Drew Point, AK. Photos from the coast show: aspects of the permafrost bluff stratigraphy, a well-developed niche geometry with measured dimensions overlaid, and the lower two photos document thermo-denudation and block failure.

2.2. Terrestrial Field Campaigns

Team Member Author: Benjamin Jones (UAF)

Contributors: Emily Bristol (UTA), Diana Bull (SNL), Matt Thomas (USGS), Jenn Frederick (SNL), Melissa Ward Jones (UAF)

2.2.1. Terrestrial Measurement Details

2.2.1.1. USGS Weather Station (1998-2020)

INSTRUMENTATION: Multiple environmental parameters, see text.

Drew point weather station has been maintained by the USGS since 1998 and is located at 70° 51.872' N and 153° 54.405' W at an elevation of 5m above mean sea level, see Figure 2.1-1 (Urban and Clow 2018). This station monitors shallow permafrost temperature at 10 depths (5–120 centimeters), active-layer thaw depth and duration, soil moisture, air temperature and pressure, wind speed and direction, up- and downwelling shortwave radiation, surface albedo, snowpack depth and duration, and rainfall (see Figure 2.2-1 for a standard DOI monitoring station). This data can either serve as a verification of the boundary conditions obtained from other models (Section 4.1) or can be used to initialize portions of our model directly. Data through February 2020 has been made available to the project (Urban 2020).

The subject matter expertise of Ben Jones places this weather station in Primary Material land surface. During the April coring campaign (Section 3.1), two cores close to the deployed weather station were recovered and wedge ice was found 0.57-0.71m below the surface.



Figure 2.2-1. Components of a typical U.S. Department of the Interior/Global Terrestrial Network for Permafrost (DOI/GTN-P) climate monitoring station. (cm, centimeter). Adapted from Urban and Clow 2018.

2.2.1.2. Telemetered Time Lapse Cameras (2018)

INSTRUMENTATION: Buckeye cam x80 model

Three time-lapse cameras were established at Drew Point at varying times during 2018; details are given in Table 2.2-1. Camera 7 was installed on a pipe on 20 April looking westward at the BeadedStream vertical temperature array. It functioned until a block failure that occurred on 06 September, taking pictures hourly. Camera 6 was mounted to the same pipe as Camera 7 but it was pointed eastward along the bluff line and operated from 03 August until 02 September. Camera 3 was established in the beach of a large thermo-erosional gully and it pointed westward at the bluff face with the intention of document thermo-erosional niche formation. All cameras were triggered by motion as well as with the hourly time lapse function. The images were transmitted to a repeater located on the southwest corner of the old oil well pad, that was then transmitted to a repeater about 8 miles due south of Drew Point, that relayed the images back to a base station at the Teshekpuk Lake Observatory cabin and subsequently uploaded to an online server with a HughesNet satellite dish for near-real time observations and preservation of images even though all three cameras were destroyed by the vicissitudes of nature.

Table 2.2-1. Details of the 3 telemetered time lapse cameras.

	Lat (N)	Long (W)	Deployment Time range	Description
Time Lapse Cam 3	~70.880433	~153.897608		looking at niche; Mounted to a pipe in the ocean looking back at the bluff to the west of the gully near the pad
Time Lapse Cam 6	70.880585	153.889989	03 Aug – 02 Sept	Looking E from vertical thermistor
Time Lapse Cam 7	70.880585	153.889989	20 Apr – 06 Sept	Looking W towards vertical thermistor

2.2.1.3. Horizontal Thermistor (2018)

INSTRUMENTATION: 4 HOBO TMCx-HD temperature sensors of various lengths and 1 4-channel U12-008 HOBO data loggers

A horizontal thermistor string was installed in a 4-5m tall bluff-face at 70.876428°N, 153.933153°W at Drew Point in degraded¹ Primary Material on 25 July 2018 (Figure 2.2-2). A 4.5m hole was augered into the bluff face to accommodate this thermistor string. It recorded temperature values every 10minutes with a 4-channel U12-008 HOBO data logger from the 25 July to 01 August 2018. The thermistor string had 4 temperature sensors spaced at 4.5, 3.0, 1.5, and 0.5 m from the bluff face when installed.

Over the 7 days there was 0.4 m of thermal denudation as there was only 0.1m between the bluff face and the "0.5m" thermistor when the thermistor string and logger were retrieved on 1 August 2018.

¹ Noticeable ice wedge degradation, very ice rich, and more surface peat than PM1.



Figure 2.2-2. Field photo showing the installation of the 4-channel data logger (inside gold circle) and thermistor strings in the bluff face at Drew Point.

2.2.1.4. Vertical Thermistor (2018)

INSTRUMENTATION: D405 BeadedStream satellite telemetered datalogger with a 5.5 m long standard digital temperature cable

A vertical thermistor string was installed at 70.880561°N, 153.890403°W in the Ancient DTLB on the 22 April 2018 in the hole created when retrieving the DP1-1 core (see Table 3.1-1). It recorded temperature values every day from 22 April to 20 July and then hourly from 20 July until its demise on 05 September. The thermistor string had 10 temperature sensors spaced at 0.7, 1, 1.5, 2.5, 3.5, 4.5, 4.7, 5, 5.2, 5.5m below the surface of the tundra. WebCam 07, see Table 1-2, located due east of the BeadedStream datalogger on the blufftop looking westward and was configured to take hourly photos until its demise on 07 September

This thermistor string collected data until the block broke and the logger was inundated with sea water. WebCam 07 shows the block breaking between 30 August and 02 September 2018.

2.2.1.5. 2-D Thermistor Array (2019)

INSTRUMENTATION: 16 HOBO TMCx-HD temperature sensors of various lengths and 4 4-channel U12-008 HOBO data loggers

A 2-D thermistor array was installed at 70.880014 N and 153.896234 W in a 3.9m tall Young DTLB bluff over two days on the 12th and 13th of August 2019. Holes were drilled into the bluff face using a ~1.5-inch hole saw on an electric powered drill during this time period to place the thermistor strings in. The vertical borehole was created with a battery powered drill auger using a narrow core bit (5cm diameter). The array recorded temperature values from the 13th-16th of August 2019.

The 2-D thermistor array consisted of 3 arrays of horizontal thermistor strings spanning from the bluff face to a maximum/minimum depth of 2.0m/1.85m, and one vertical array located 3.0m

behind the bluff face running from an elevation of 3.9m to 0.8m above sea level. Four thermistor strings, bound so that the temperature sensors were at varying distances from the data logger, were assembled to create a single horizontal array. One array was inserted into each of the three horizontal boreholes so that the sensors were positioned at 0.06m, 0.5m, 1.0m, and 2.0m into the bluff face, with the exception of the lowest horizontal array, which was instead inserted so that the sensors were positioned at 0.35m, 0.85m, and 1.85m into the bluff face with the shortest thermistor left in the open air to measure air temperature. For the vertical thermistor, the thermistor strings were also bound so that they were varying distances from the data logger, and placed into the vertical borehole so that the sensors were positioned at depths of 0.15m, 0.9m, 2.0m, and 3.1m, although the deepest temperature sensor was probably not placed as deeply as we assumed due to complications of groundwater seeping into the borehole at depth and refreezing. The corresponding elevations of the temperature sensors were located at 3.75m, 3.0m, 1.9m, and 0.8m. The data loggers recorded temperature readings every 1 minute. Figure 2.2-3 plots the temperature profiles at each thermistor array from initial installation to a maximum of 65 hours after installation. Figure 2.2-4 illustrates all aspects of this thermistor array.

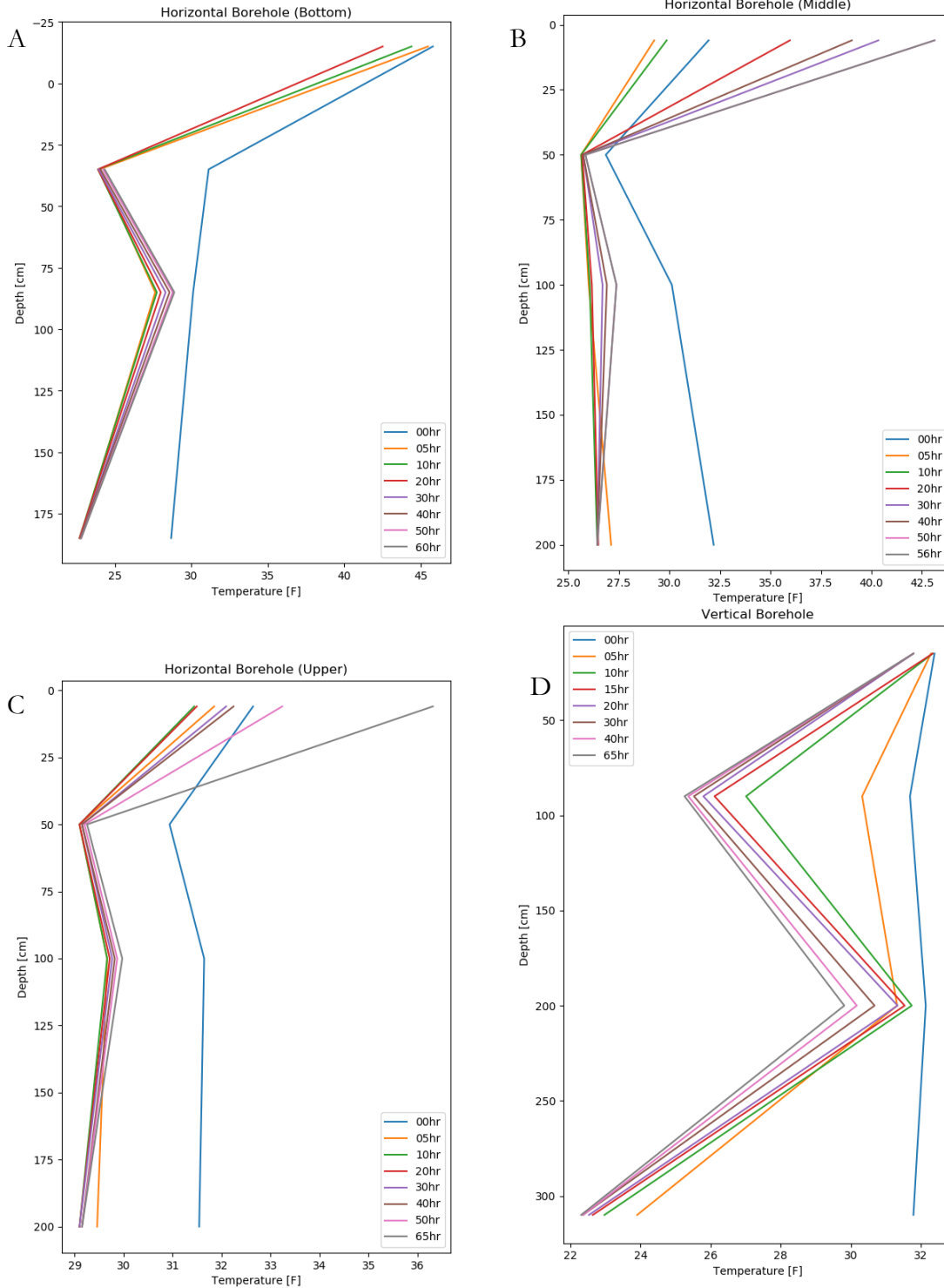


Figure 2.2-3. Temperature records from initial installation in 5-10hour increments up to 56-65 hours after installation in the bottom (A), middle (B), and upper (C) horizontal boreholes and in the vertical (D) borehole. Initial installation times: 08/13/19 05:28:38 PM bottom, 08/13/19 05:55:13 PM middle, 08/13/19 06:49:43 PM upper, and 08/13/19 07:19:10 PM vertical.

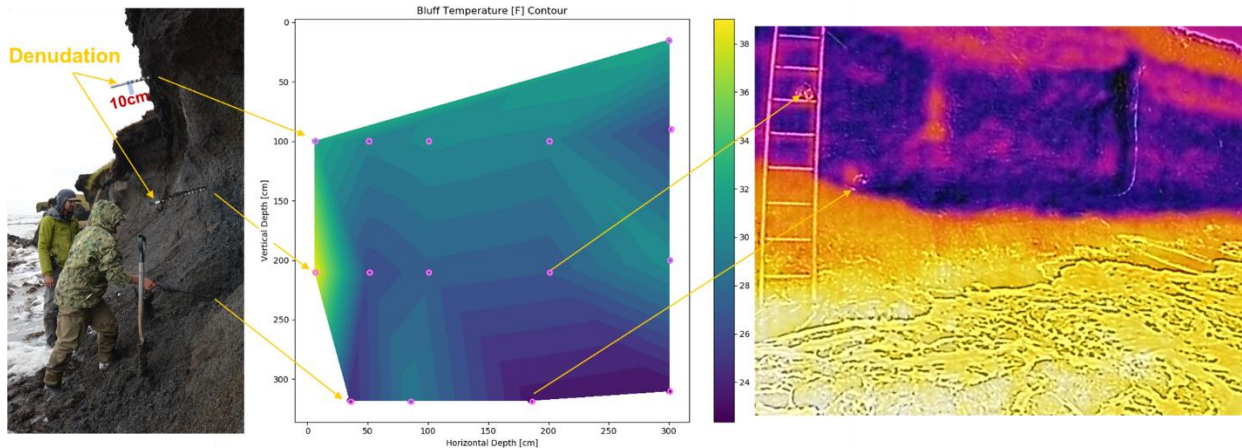


Figure 2.2-4. Collage of 2-D thermistor array measurements. The picture shows the location of the thermistor strings and the thermal denudation measurements, the 2-D bluff temperature in Fahrenheit on evening of August 14 2019 is shown in the center with the pink circles indicating the temperature probe locations, and a thermal image of the bluff face taken on August 14th 2019 shows the relative temperatures of the ocean, bluff face, and ice wedge the bottom and middle thermistor string can be seen in the thermal image.

In the horizontal holes, constructed rulers were placed to measure thermal denudation. The rulers consisted of a PVC pipe on which black electrical tape was placed every 10cm. Table 2.2-2 details the denudation measurements made over five days between the 12th – 16th of August 2019. On the 14th of August sluffed material from the permafrost bluff fully covered the lowest denudation ruler. These pipes also secured the HOBO data loggers associated with the horizontal borehole thermistor arrays.

Table 2.2-2. Raw thermal denudation measurements. Top, Middle and Bottom refer to the horizontal location of the thermistor strings. Method of measurement changed on 08/14/2029 from the end of the pipe to the number of 10cm marks shown from face of bluff.

Date	Time (akdt)	Measurement location			Denudation amount per location (cm)		
		Top	Middle	Bottom	Top	Middle	Bottom
8/12/2019	late afternoon	46cm deep		22cm deep			
8/13/2019	not recorded	43cm deep		27cm deep	3		5
8/14/2019	2:30pm	27	42				
8/15/2019	3:00pm	30	55		3	13	
8/16/2019	11:53am	32	64		2	9	

Lastly, the depth of the frostline in a failed auger hole was monitored on the 14th of August to be 1.0cm deep and on the 15th of August to be 0.5cm deep. The frostline remained relatively stable, even though the bluff face experienced denudation. The frost line was determined by measuring the depth at which humidity in the air froze onto the interior of the borehole surface, which could be distinguished visually.

2.2.1.6. Tilt Sensors (2019)

INSTRUMENTATION: Onset Hobo UA-004-64 accelerometers

We deployed 5 accelerometers along the Beaufort Sea coastline in Drew Point, AK to observe permafrost bluff deformation prior to toppling-mode block failure, a mass wasting process that is characteristic of the region. On 12 August 2019, we selected four sites located above niches formed by thermoabrasion (e.g., Figure 2.2-5A) and one inland control (Table 2.2-3). The four tilt sensors that were intended to measure bluff deformation were installed along the ground surface, approximately halfway between the bluff edge and the inland extent of 4-6 m deep niches (e.g., Figure 2.2-5A). The control point was also installed along the ground surface, but ~15 m inland from the bluff edge. At each site, we hammered approximately one-half of a 60 cm wooden stake vertically into the ground. We then attached one tilt sensor to each stake with the factory-supplied mounting bracket and wrapped the top of the stake in orange flagging to improve visibility (Figure 2.2-5A). Tilt sensor dataloggers began recording at 1-minute intervals on the afternoon of 12 August 2019.

On the morning of 15 August 2019, we observed that one of the permafrost bluffs that we had instrumented with a tilt sensor had toppled (Figure 2.2-5B). The toppled bluff had disaggregated into four sections with map-view areas ranging from ~10-25 m². The northernmost tip of the toppled bluff appeared to exhibit some buckling or back rotation, possibly associated with the block's impact with the beach or settling in the near-shore environment following failure (Figure 2.2-5B-C). Two of the four blufftop monitoring sites exhibited tilt with an appreciable deviation from the control (Figure 2.2-5C). One site (orange line; Figure 2.2-5C) showed ~5° of oceanward tilt, but did not topple. The second site (red line; Figure 2.2-5C) also accumulated small amounts of oceanward tilt until the evening of 14 August 2020, at which time the bluff appears to have abruptly toppled. We retrieved the tilt sensor from the toppled block on 15 August 2020 and the remaining tilt sensors on 16 August 2020.

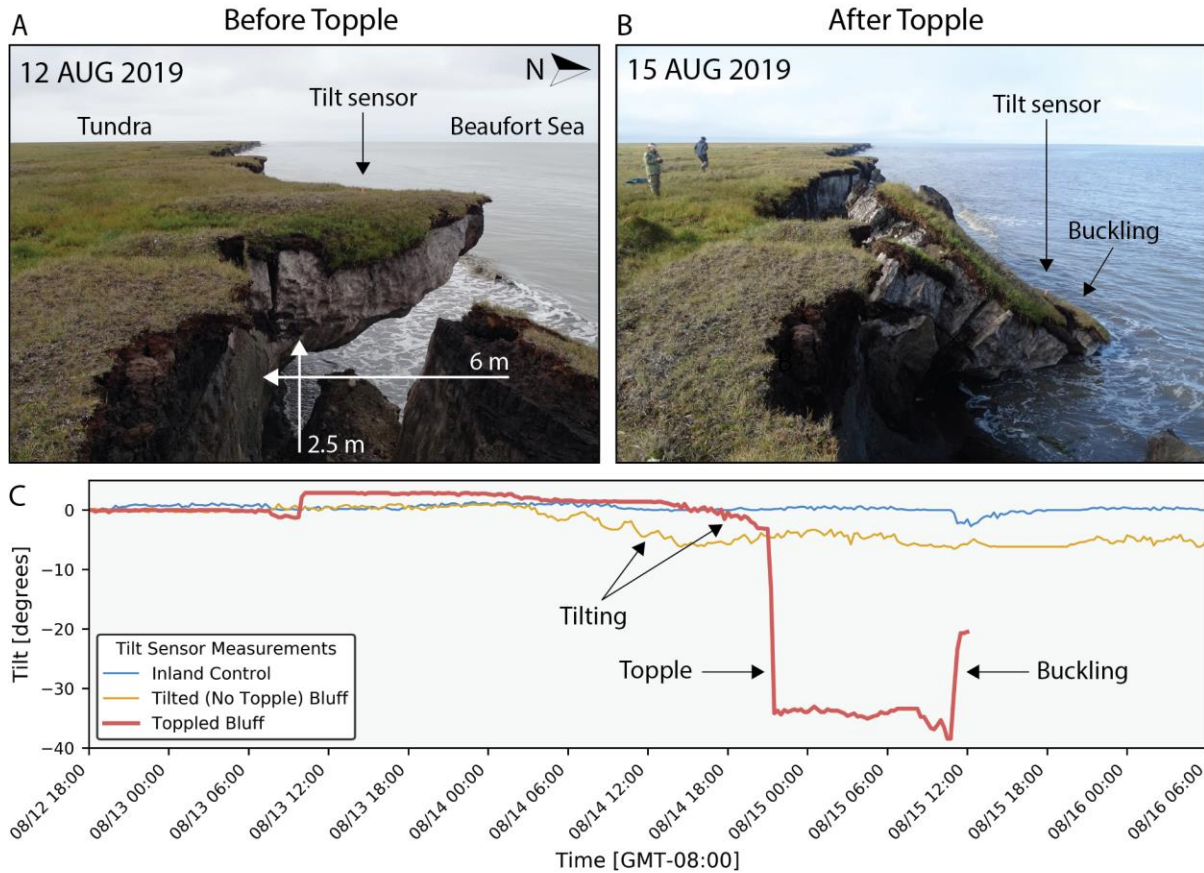


Figure 2.2-5. Photograph of the Drew Point coastline (A) before and (B) after a toppling-mode permafrost block failure. (C) Multi-day time series of tilt sensor measurements. Negative degrees indicate oceanward tilting. Thick red line corresponds to the location shown in (A-B), whereas the orange and blue lines correspond to another nearby coastal bluff and inland control location, respectively.

Table 2.2-3. Summary of tilt sensor installation locations.

Sensor ID	Lat (N) [WGS84]	Lon (W) [WGS84]	Note
20654659	70.88001	-153.89623	Tilted, no topple (orange line); niche measurement 4 (see Figure 2.2-6)
20654657	70.8806	-153.88591	Inland control (blue line)
20654658	70.88073	-153.88598	n/a
20654656	70.88016	-153.89498	n/a
20654660	70.88092	-153.88403	Toppled block (red line)

2.2.1.7. Niche Geometry Measurement (2019)

INSTRUMENTATION: Leica Disto D2 Laser Finder

On the afternoon of 08/15/2019 Diana Bull (SNL), Jennifer Frederick (SNL), and Matt Thomas (USGS) measured the dimensions of 9 niche's in two terrain units. A laser finder measured the depth of the niche as a function of height. A tape measure was used to establish the height 1m behind (by eye) the furthest outcrop of the bluff face; the depths were then decreased by 1m. A level established zero pitch in the laser finder's path at each height. Figure 2.2-6 shows representative profile measurements with associated pictures from each land surface type.

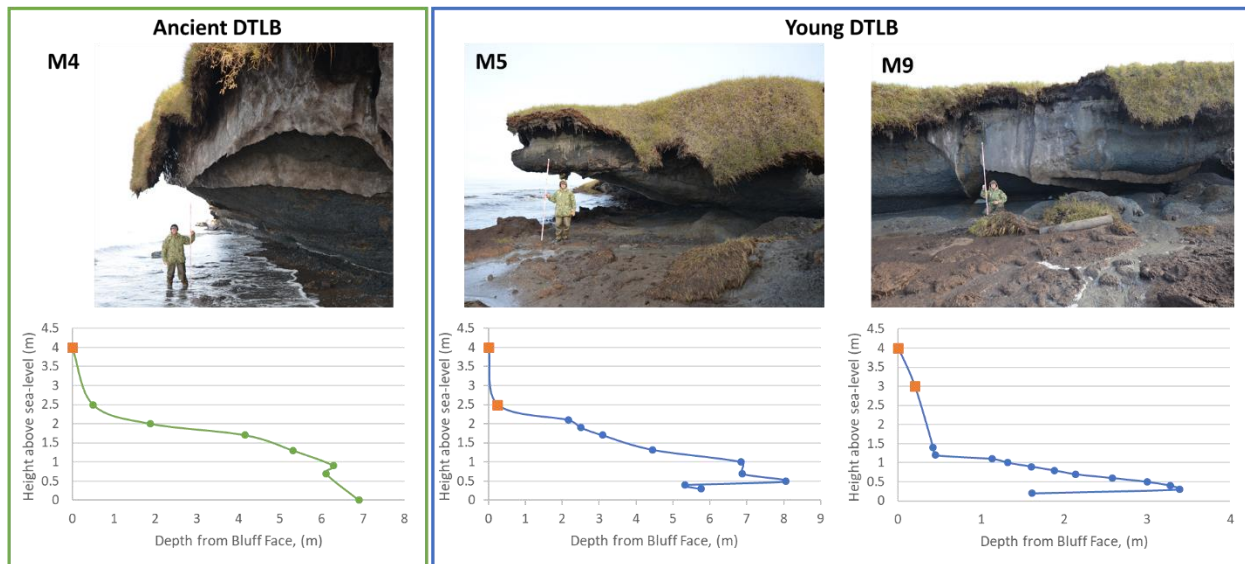


Figure 2.2-6. Profile measurements of M4, M5, and M9 with associated pictures. Orange squares are not measured values, they are guesses indicating the height of a “vertical” bluff face. The white and orange scale held by Jennifer Frederick in the photos is 2m in length.

Table 2.2-4 details the land surface type and latitude and longitude of each measurement; the maximum depth, height at maximum depth, and maximum niche height are also reported. Maximum niche height was determined by determining the height at which the bluff face returns to vertical. In some cases, there was not enough data to establish this location and the last measurement was used. An experimental correlation between niche depth and height is possible with the data presented in Table 2.2-4 and is presented in Figure 2.2-7.

Table 2.2-4. Details of the 9 niche measurements made with laser finder. The max niche height is estimated from the full measurement profiles.

Identifier	Land Surface	Lat (N)	Lon (W)	Max Depth (m)	Height at Max Depth (m)	Max Niche Height (m)
M1	Young DTLB	70 52.7899	153 53.9455	4.24	0.6	1.8
M2	Young DTLB	70 52.7875	153 53.9722	1.89	0.5	1.7
M3	Young DTLB	70 52.7919	153 53.9026	1.44	0.3	0.6

Identifier	Land Surface	Lat (N)	Lon (W)	Max Depth (m)	Height at Max Depth (m)	Max Niche Height (m)
M4	Ancient DTLB	70 52.8008	153 53.7740	6.28	0.9	2.5
M5	Young DTLB	70 52.7401	153 54.5813	8.06	0.5	2.5
M6	Young DTLB	70 52.7358	153 54.6169	5.74	0.8	2.1
M7	Young DTLB	70 52.7303	153 54.6454	6.54	0.8	2.0
M8	Young DTLB	70 52.7198	153 54.7239	6.00	0.6	2.0
M9	Young DTLB	72 52.7510	153 54.4900	3.39	0.3	1.4

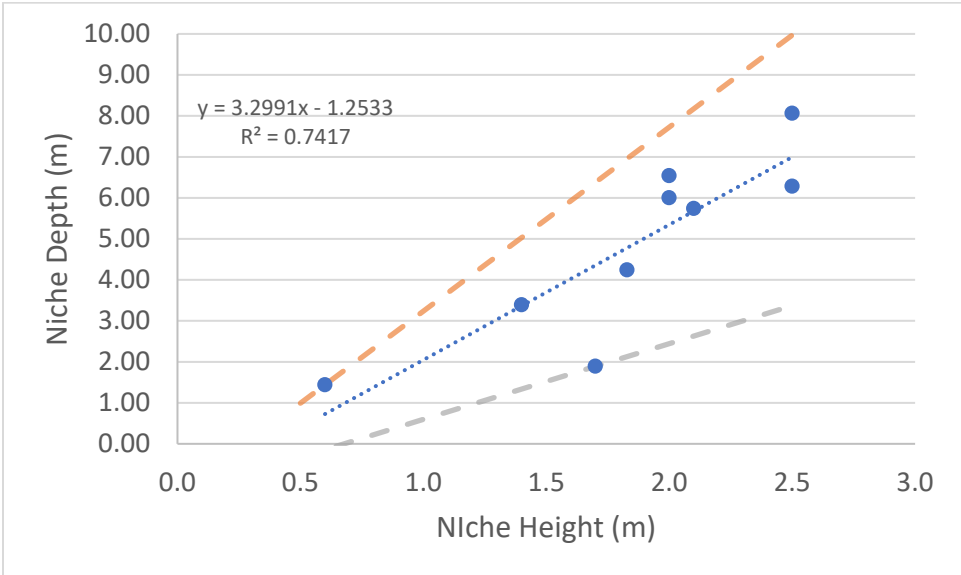


Figure 2.2-7. Experimental correlation between niche depth and height using the data presented in Table 2.2-4. Best fit shown in dotted blue line: $y=3.2991*x-1.2533$. Orange and blue dashed lines give bounding fits for the highest and lowest data points assuming the same y-intercept. The slope could be as high as 4.49 (orange dashed) or as low as 1.85 (grey dashed).

2.2.2. Erosion Measurements

We are working on a paper based on the very high spatial and temporal resolution Unmanned Aerial Vehicle (UAV), airborne, and spaceborne orthorectified image observations acquired in 2018, 2019, and 2020. A DigitalGlobe satellite image from June 2018 brackets the beginning of the 2018 erosion season. UAV images were acquired on 24 July, 29 July, 03 August, and 30 September 2018 and processed to orthophoto mosaics and digital surface models using Pix4d software and tied down to ground-control points established with the Leica dGPS. The end of the 2018 erosion season and beginning of the 2019 erosion season was bracketed by a DigitalGlobe satellite image from April 2019. Aerial photographs were acquired by the AWI team on 13 July, 23 July, and 30 July while flying surveys in the region. All images were processed out to orthomosaics and digital surface models using Pix4d and tied to the ground control points at Drew Point. Additional UAV surveys were acquired on 02 August, 06 August, 10 August, 12 August, and 15 August and processed out using the Pix4d workflow. DigitalGlobe satellite images from 26 Sept 2019 and April 2020 bracketed

the remainder of the 2019 erosion season. Our detailed analysis will allow us to quantify erosion on the time steps needed for model validation and it allows us to separate the effects of thermo-denudation and thermo-abrasion. Below we have provided an overview of the datasets acquired during the course of this project and initial observations and interpretation of the results.

Drew Point, Alaska has become one of the best sites in the Arctic in terms of documenting annual open water season erosion since the mid-2000s. Our paper published in 2018 (Jones et al. 2018), placed the recent changes occurring along a 9km stretch of coast at Drew Point into a context spanning the period 1955 to 2016. During the course of this project we continued to task and acquire high resolution satellite imagery and have updated mean-decadal scale and mean annual erosion of coastal permafrost bluffs at Drew Point through the 2019 erosion season. The mean annual erosion between 2002 and 2019 is 17.2 m/yr in comparison to a mean annual erosion rate of 8.7 m/yr between 1979 and 2002 (Figure 2.2-8).

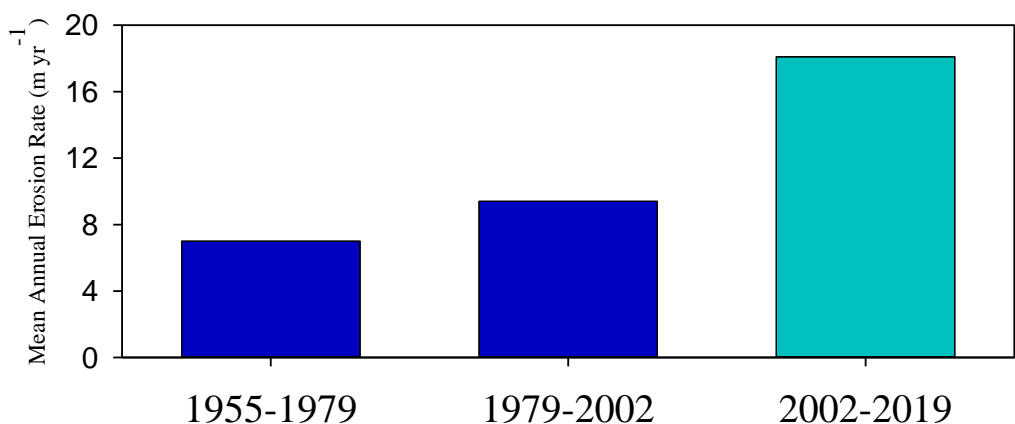


Figure 2.2-8. Long-term decadal-scale erosion rates for Drew Point, 9km, section of coast.

Since 2007, we have tabulated annual open-water season erosion to document inter-annual variability within these long-term mean erosion of the more recent time period of observation.

The variability in inter-annual erosion at Drew Point lends itself well for trying to parse out the driving and resisting forces controlling the mean erosion but also highlighted that we needed to look at finer-scales than annual mean values when it came to model inputs for the ACE model (Figure 2.2-9; Jones et al., 2018).

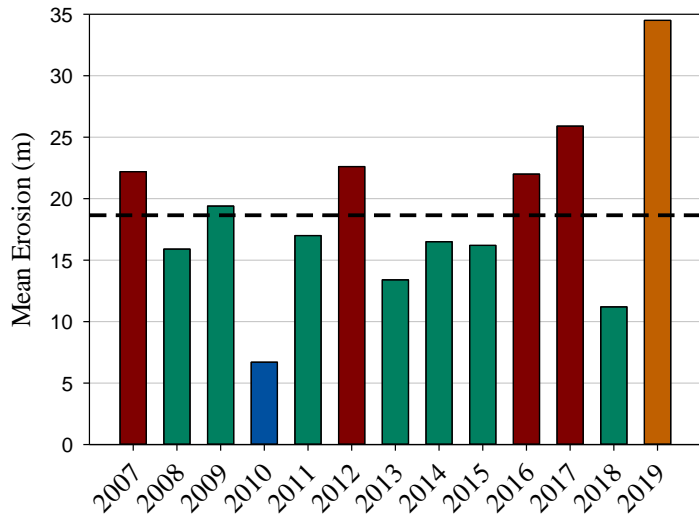


Figure 2.2-9. Annual open-water period erosion for Drew Point, 9 km, section of coast between 2007 and 2019.

To accomplish this we turned to a 1.5 km stretch of coastline at Drew Point over the years 2018 and 2019 and acquired 16 image sets combined between UAV surveys, airborne surveys conducted by collaborators from AWI, and high resolution satellite imagery available from DigitalGlobe, Inc. (Figure 2.2-10).

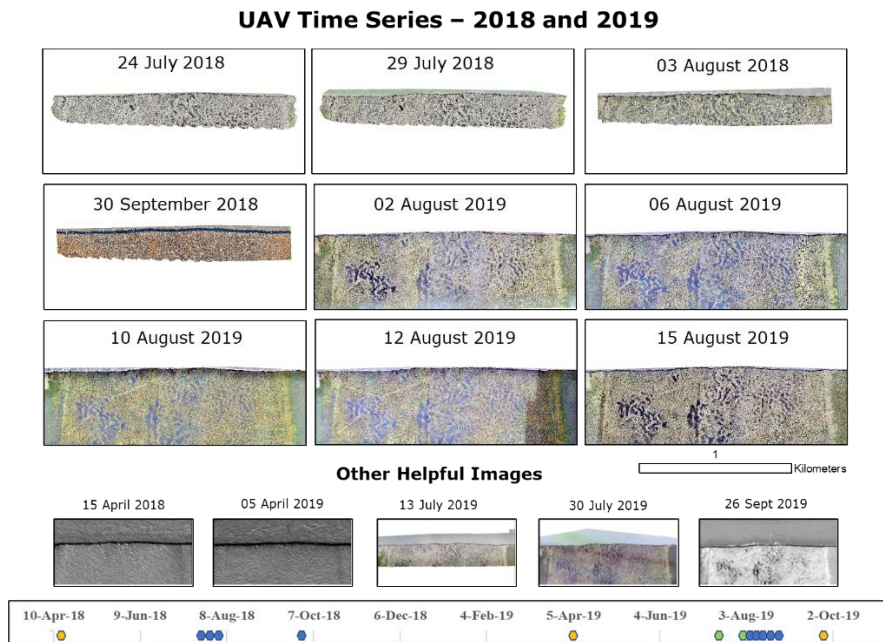


Figure 2.2-10. Overview of the dense time series of imagery that we have compiled for providing for model inputs.

The UAV imagery are the focus dataset for this analysis. The data in 2018 were acquired by a P4pro UAV and the data in 2019 were acquired by a P4RTK UAV. Images were acquired over the same 1.5 km stretch of coastline on nine different days between 2018 and 2019 to document intra-annual erosion patterns and processes. Four surveys were conducted in 2018 and five surveys were conducted in 2019 (Figure 2.2-11). Prior to image acquisition in 2018, we established 24 ground control points using a Leica differential GPS. This allowed for detailed processing of the images using Pix4d software into orthomosaics and digital surface models. We were also able to qa/qc the results of processed imagery. The average absolute horizontal error was 7cm, the average relative error was 2cm, and the average vertical error was 3cm relative to the field survey dGPS points (Figure 2.2-12).

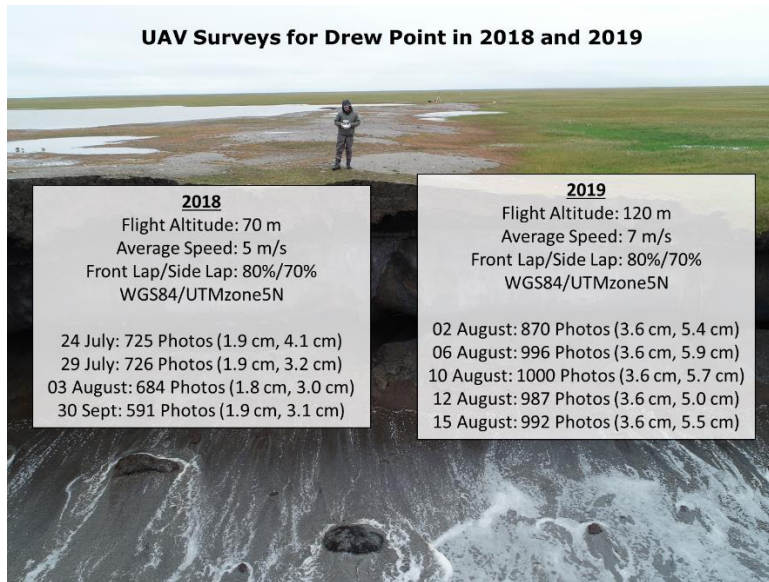


Figure 2.2-11. UAV surveys conducted in 2018 and 2019.

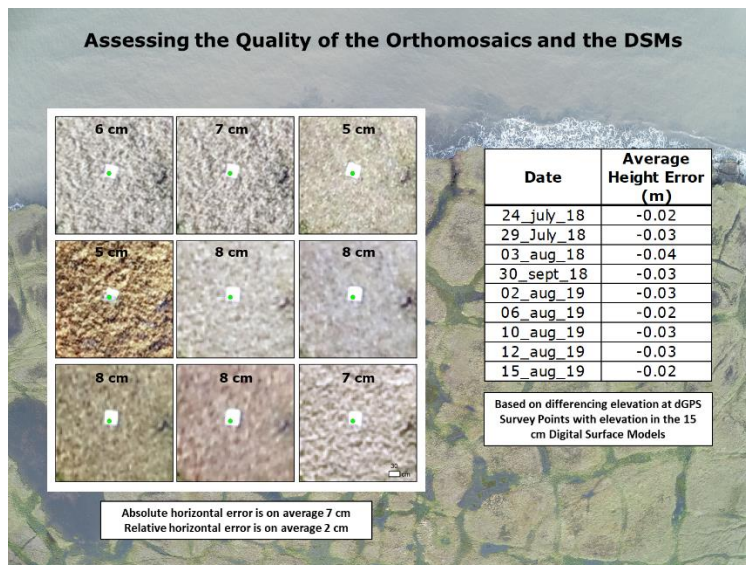


Figure 2.2-12. Assessing the horizontal and vertical quality of the UAV datasets.

We were quite happy with the performance of the UAV systems and post-processing of the images using Pix4d. We further processed the data into products that represented the bluff edge in order to determine erosion rates using the USGS DSAS tool and to clip DSMs in order to more accurately capture vertical changes associated with erosion (Figure 2.2-13 through Figure 2.2-17). We extracted the bluff edge using a 100% change in slope based on the DSM data and this vector file was manually corrected to account for any noise evident in the nearshore setting. These vector files were used to clip the DSMs. Once all of the files were clipped and cleaned up we calculated erosion rates and differentiated erosion processes (block failure vs. thaw slumping).

UAV Data Collection, Image Processing, Bluff Extraction, Erosion

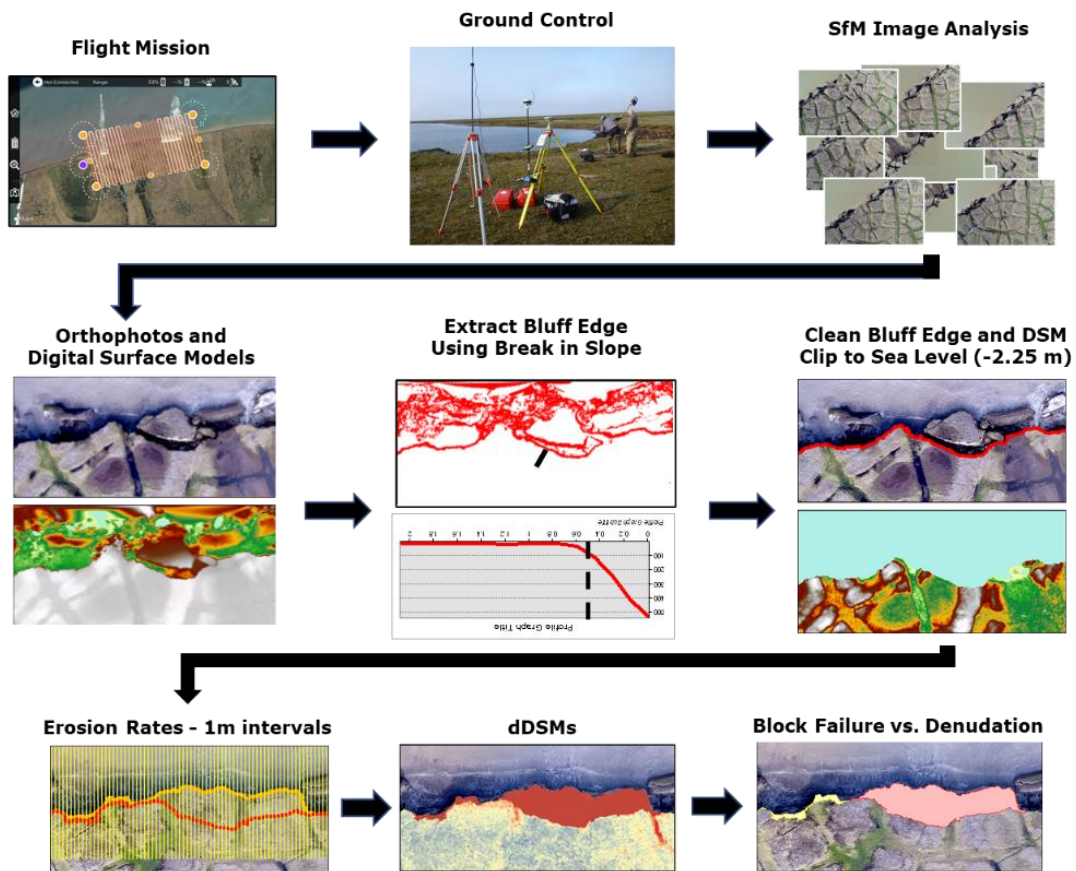


Figure 2.2-13. UAV data collection, image processing, bluff extraction, and erosion determination workflow.

Example of Bluff Erosion During 2019 Surveys

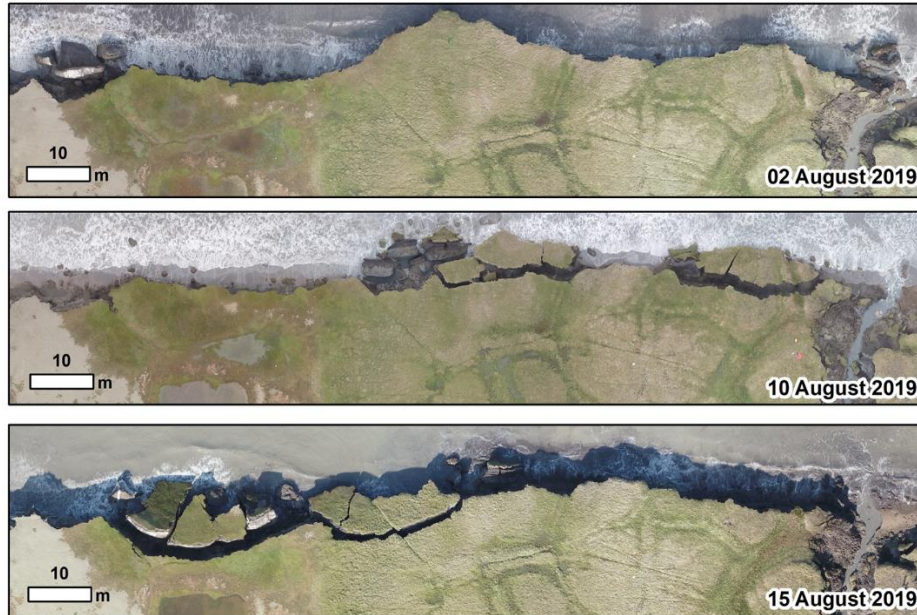


Figure 2.2-14. Example of the detail that you can resolve in the UAV time series.

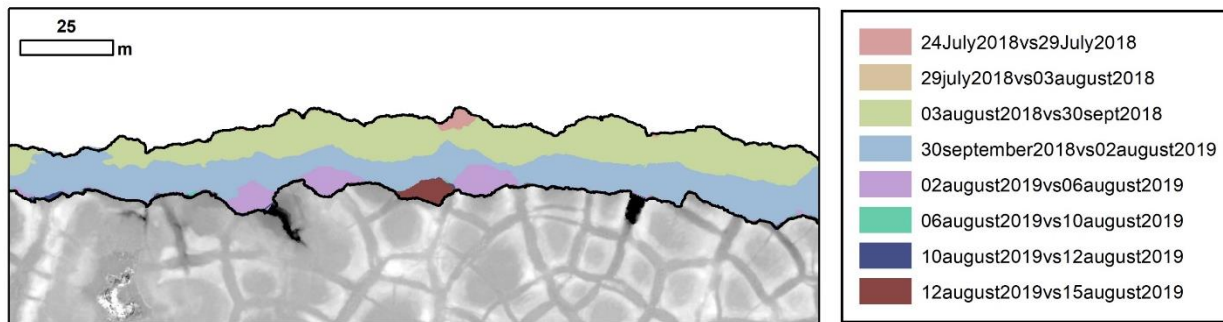


Figure 2.2-15. Example of the entire UAV time series and the mapped erosion between for each time period.

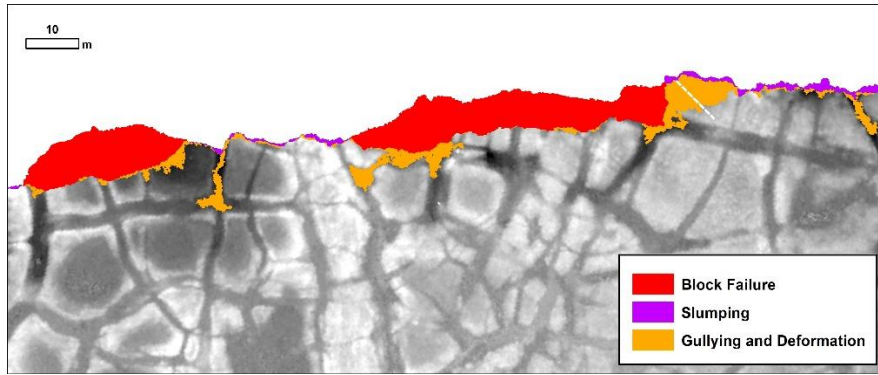


Figure 2.2-16. Example of partitioning erosion happening during a specific time period based on erosional process.

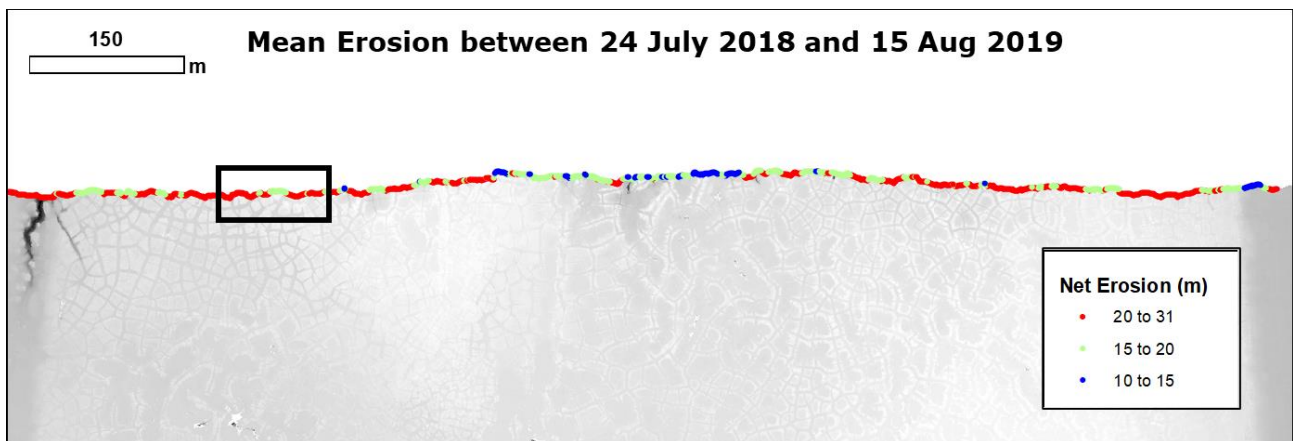


Figure 2.2-17. Example of output from DSAS tool showing variability in erosion for the 1.5 km section of study coast at Drew Point between the first and last UAV survey.

Our initial results show that erosion between the UAV surveys varied from 0.03 m/day to as high as 0.24 m/day (Figure 2.2-18). Periods of erosion that exceeded 0.10 m/day occurred during periods when elevated water levels led to erosional niche formation and block failure. We further analyzed the erosion patterns relative to whether what was being measured was a results of block failure or thaw slumping (Figure 2.2-19 and Figure 2.2-20). This shows that block failure typically resulted in 4-11 m of erosion per event (Figure 2.2-19).

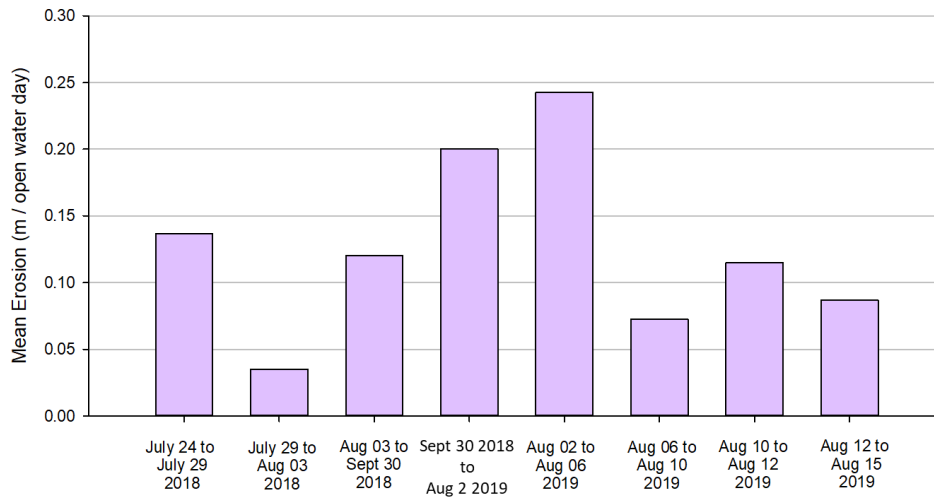


Figure 2.2-18. Mean erosion along 1.5 km study coast for each UAV time period.

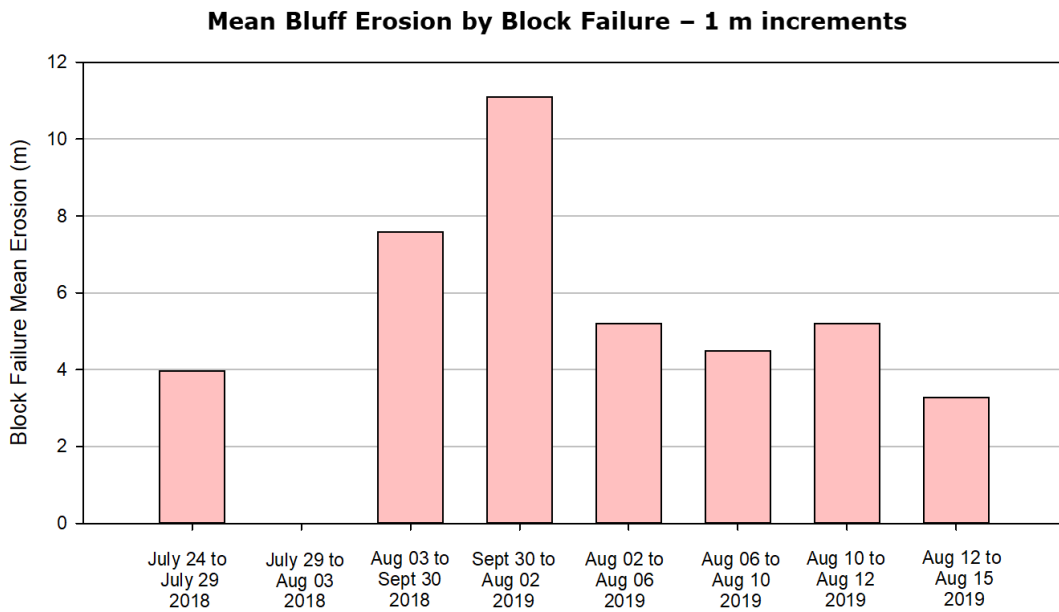


Figure 2.2-19. Mean erosion by block failure.

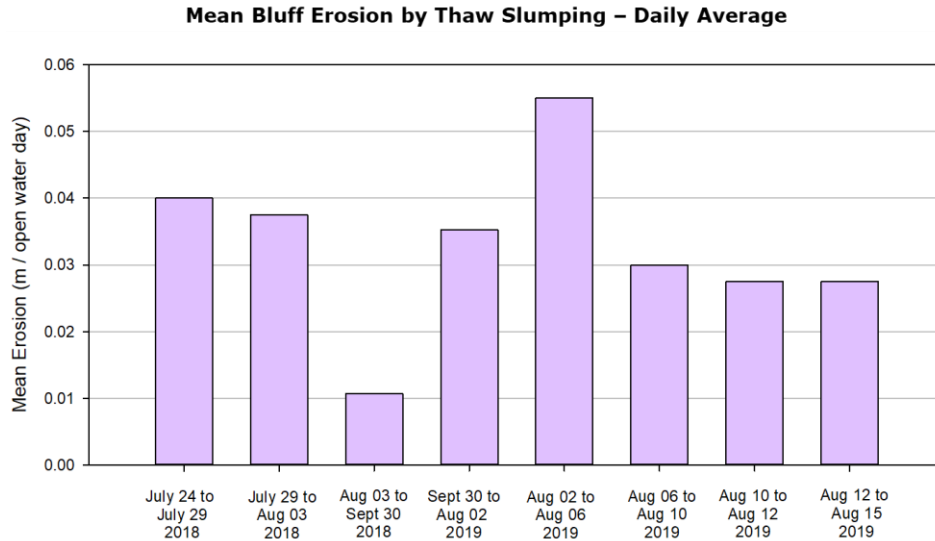


Figure 2.2-20. Mean erosion by thaw slumping.

Mean erosion by thaw slumping was also inferred from the UAV time series and showed that rates of change ranged from 0.01 m/day to as high as 0.055 m/day, with the average rate over the time series being 0.03 m/day (Figure 2.2-20). This data is extremely valuable for fine tuning this component of the ACE model.

We further analyzed the UAV data manually in an attempt to resolve the height of thermo-erosional niches across each of the UAV data collections (Figure 2.2-21). It was apparent that there were some inherent limitations in our ability to do this with the data but nonetheless we could resolve the niche heights over a subset of the survey area for each survey period.

Variability in the Ability to see the Niche

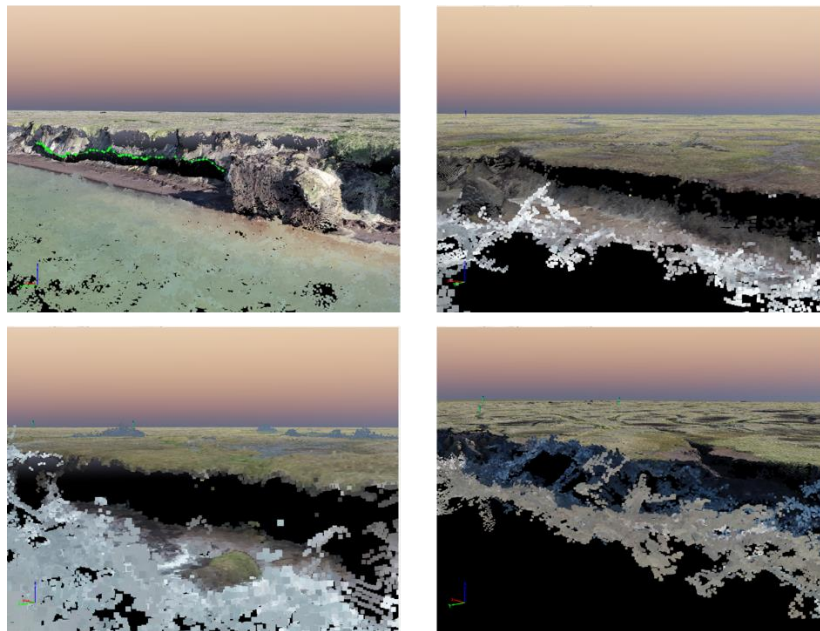


Figure 2.2-21. Manual mapping of thermo-erosional niche heights from UAV survey data.

The time series of niche height measurements allowed us to develop histograms of the change in niche heights in each UAV survey across the time series of observations (Figure 2.2-22). The data provide a fresh look at the evolution in niche heights that are being correlated to wave action and ocean energy forcing.

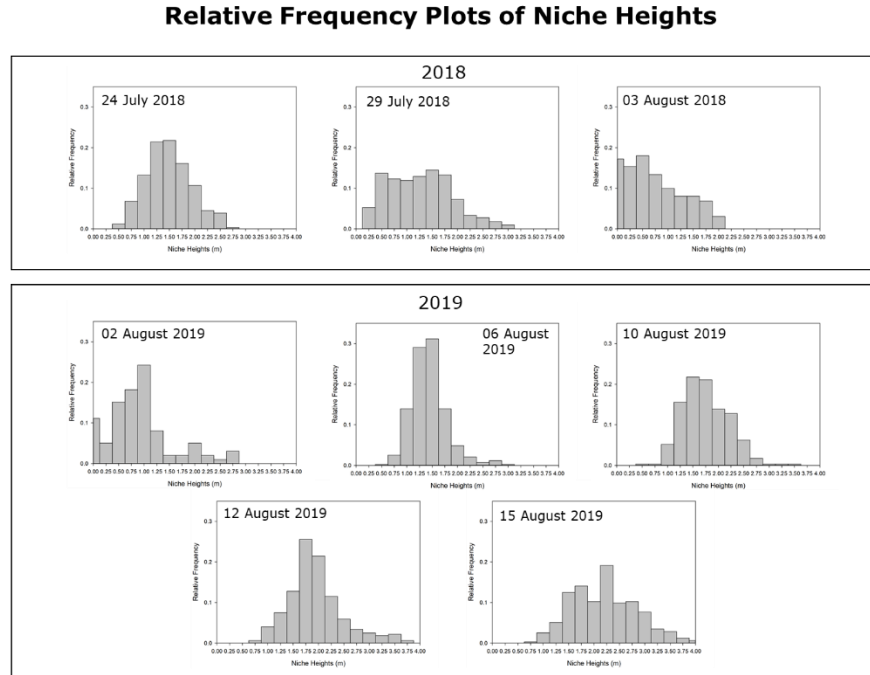


Figure 2.2-22. Compilation of histograms of niche heights resolved in each UAV survey.

2.3. Oceanographic Field Campaign

Team Member Author: Jeremy Kasper (UAF)

Contributors: Eloise Brown (UAF), Paul Duvoy (UAF), Nick Konefal (UAF), Stephanie Jump (UAF), Mike Angelopolous (AWI), Guido Grosse (AWI)

In 2018, personnel with the University of Alaska Fairbanks chartered the R/V Ukpik to complete a seafloor bathymetric survey, mooring deployment and hydrographic (acoustic Doppler current profiler and Conductivity/Temperature/Depth (CTD) profiles) and bottom grab measurements in support of the Drew Point LDRD project.

The work was carried out on July 28 and July 29, 2018; Figure 2.3-1 below shows the gps navigation track. Additional vessel days were required for staging and setting up equipment including installation of the multibeam system (MB) on the vessel, calibration of the multibeam system, configuration of the “Smith Bay” oceanographic mooring and testing and programming instruments for deployment on the mooring and for travel to and from Smith Bay offshore of Drew Point. This work was carried out in conjunction with two other projects in the same area (a Bureau of Ocean Energy Management funded project and an NSF project).

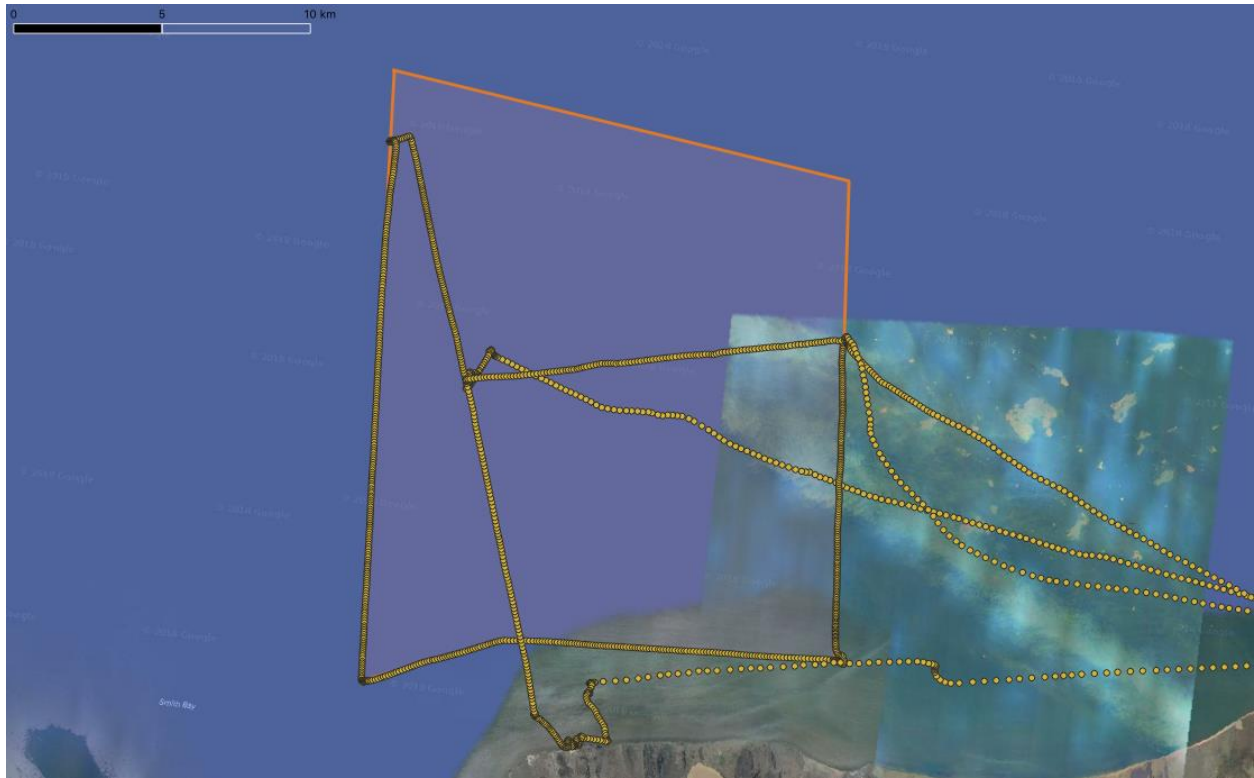


Figure 2.3-1. Navigation track logged by GPS.

In 2019 and 2020 recovery missions for the Smith Bay mooring were conducted. The Smith Bay mooring was not recovered in either year; it is believed to be lost to the vicissitudes of nature.

2.3.1. Oceanographic Measurement Details

2.3.1.1. Ikpikuk Delta Pressure Sensor (2011-2018)

INSTRUMENTATION: ONSET HOBO U20-001-01-Ti

Time series of water depth (m), water temperature (°C) were measured in the Ikpikuk Delta by an Onset Hobo pressure sensor from 2011 until present; see Table 2.3-1. The long duration of this pressure sensor is able to verify accuracy of the water level from the oceanographic data. This will only allow general comparisons for the timing of when the water surface elevation was predicted to be above the cliff toe height. Employing this sensor in this type of comparison is complicated due to river dynamics and precipitation amounts, geometry of the coast, and lack of repeat vertical reference heights.

Table 2.3-1. Ikpikuk Pressure sensor deployment details.

Sensor	Deployment	Lat & Long	WGS84 Ellipsoid Height (m)
Ikpikuk delta pressure sensor	2011 - 2020	70.81179 N 154.45998 W	-2.0266

2.3.1.2. Drew Point Spit Pressure Sensor (2018-2019)

INSTRUMENTATION: ONSET HOBO U20-001-01-Ti

Time series of water depth (m), water temperature (°C), atmospheric pressure (mbar) and air temperature (°C) were measured at Drew Point by two Onset Hobo pressure sensors from May 1, 2018-Aug 15, 2019 (water level data loggers were titanium model U20-001-01-Ti rated to 30-ft depth); see details in Table 2.3-2. Both sensors were located onshore, with one on the bluff and the second above mean sea level (MSL) in the lagoon behind the spit at an ellipsoid height of -2.00 m at Drew Point, where the ellipsoid height of MSL is -2.21m. Sampling interval for both instruments was every 10 minutes from May 1-Aug 3, 2018 and every 30 minutes from Aug 3, 2018-Aug 15, 2019. The HOBO sensors were deployed around the corner from Drew Point (Figure 2.3-2). The Bluff sensor recorded atmospheric pressure while the lagoon sensor measured absolute pressure. To derive water level, the atmospheric pressure was subtracted from the absolute pressure.

Table 2.3-2. Drew Point Spit pressure sensor deployment details.

Sensor	Deployment	Lat & Long	WGS84 Ellipsoid Height (m)
Drew Point Spit Lagoon pressure sensor	2018 - 2020	70.874732° N, 153.938711° W	-2.0000
Drew Point Spit Bluff pressure sensor	2018 - 2020	70.874747°, - 153.933054°	~1.5



Figure 2.3-2. Location of the Drew Point RBR Duo TDWave and “Spit” HOBO sensors, Lagoon and Bluff.

2.3.1.3. RBR TDWave Sensor (2018-2019)

INSTRUMENTATION: RBR Pressure Sensors (Duo TDWave)

RBR Pressure Sensors were deployed in summer 2018 and 2019 from a small inflatable boat by Ben Jones in each year. The sensors were subsequently retrieved from the R/V Ukpik. The location of the RBR pressure sensors are shown in Figure 2.3-2 and are detailed in Table 2.3-3. 2018 & 2019 Temporary Wave/Water Level RBR Deployment Details.. Nondirectional wave spectra (wave height and period), water level fluctuations and water temperature data are collected by an RBR TDWave sensor.

Table 2.3-3. 2018 & 2019 Temporary Wave/Water Level RBR Deployment Details.

RBR TDWave	Deployment Date (UTC)	Recovery Date (UTC)	Deployment Location	Average Water Depth (m) above the sensor
SN# 51091	07/25/2018 22:20	08/03/2018 23:00	70.88 N, 153.936 W	1.3 m
SN# 51091	08/13/2019 23:40	08/25/2019 21:00	70.88185 N, 153.8987 W	1.75 m

2.3.1.4. Smith Bay Mooring (2018-2019)

INSTRUMENTATION: Teledyne RD Instruments Sentivel V20 and Seabird 37 CTD mounted on a Teledyne Oceanscience sea spider fiberglass frame

The oceanographic mooring is equipped with an acoustic Doppler current profiler (ADCP), an internally logging CTD and is configured to measure directional wave spectra, water column currents, bottom temperature, conductivity and pressure for the duration of the planned 1-year deployment length. Salinity and water depth over the mooring will be derived from the latter two parameters in post processing.

The sensors were mounted on a Teledyne Oceanscience sea spider fiberglass frame. Sandia purchased a Seabird 37 (i.e. a “microcat” ctd, SN 16945, pressure sensor rated to 20 m depth) and a Teledyne RD Instruments Sentivel V20 for this project (SN 165); see Figure 2.3-3. UAF supplied a Teledyne Benthos acoustic release for retrieval of the mooring (875TD, SN 61056, Address: 31). The Sentinel V was configured to sample waves and currents once per hour. The microcat CTD was configured to sample conductivity, temperature and pressure every 300 seconds (5 minutes). All instruments were set to UTC time. Deployment location details are provided in Table 2.3-4 and Figure 2.3-5.

Note that the oceanographic mooring was not able to be retrieved in 2019. For completeness, details of the deployment are provided below but there is no data to accompany this description. A second attempt was made to locate the mooring in August 2020 using a Teledyne Blueview imaging sonar and an Edgetech sidescan sonar. There was no indication of the mooring either at the deployment site or within an area extending several kilometers in radius centered on the deployment location.

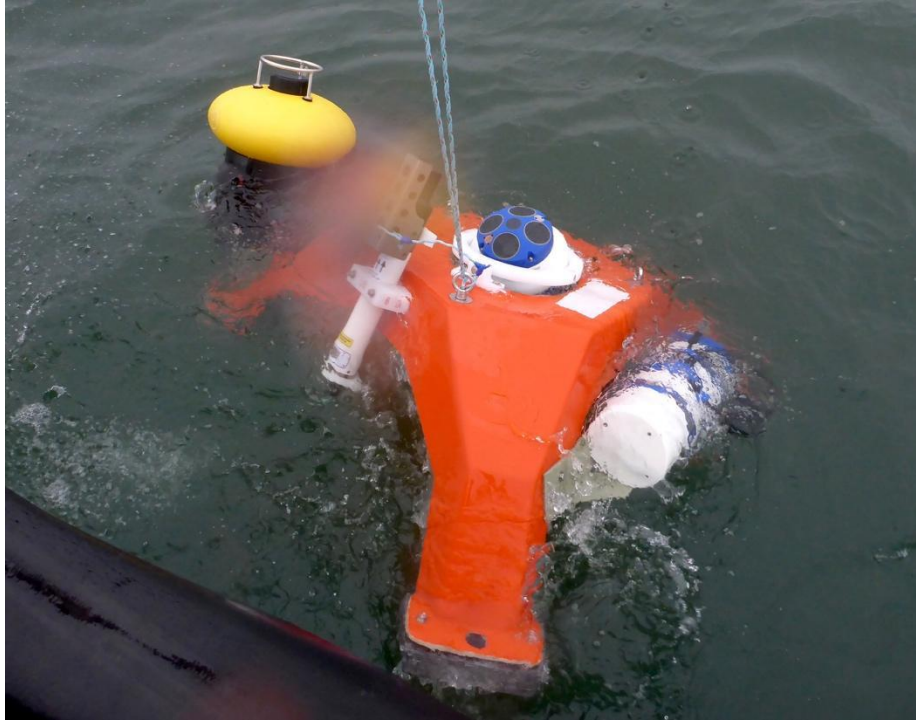


Figure 2.3-3. The oceanographic mooring as it entered the water for deployment on the sea floor.

Table 2.3-4. Mooring locations.

Name	Area	Depth [m]	Date	Time	Lat & Long
Smith Bay	Drew Point	10.12	7/27/18	10.23	70.98806333°N 154.037295°W



Figure 2.3-4. Smith Bay mooring deployment location.

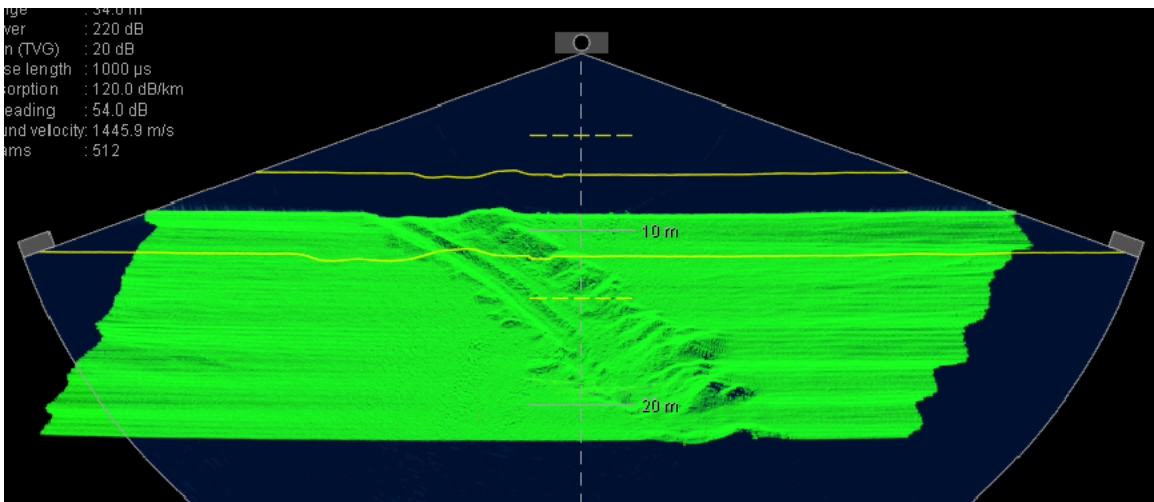


Figure 2.3-5. Prior to deployment of the mooring the multibeam sonar was used to confirm the presence of a ridge to deploy the mooring behind. The ridge appears on chart data from the region that dates to the 1950s and appears to be a persistent relic ice scour. The presence of the ridge was first noted by J. Kasper in 2005 during a previous mooring deployment.

2.3.1.5. Multi-Beam Bathymetry (2018)

INSTRUMENTATION: Reson 7125 Seabat Multibeam Echosounder and Applanix POSMV INS

A limited multibeam survey was executed in 2018 (Figure 2.3-6). Data was processed following Teledyne CARIS’ procedures using the PDS2000 and CARIS HIPS/SIPS software packages. Since both the raw and processed data files are so large, the data is only archived on an internal UAF server that is backed up the cloud. For access to the data, contact Paul Duvoy (pxduvoy@alaska.edu). A downsampled XYZ file was provided to Integral Consulting for comparing the different bathymetries used in generating the model grid. Multibeam Offsets are included below for completeness in Table 2.3-5.

Table 2.3-5. Multibeam offset settings.

PDS 2000	Reference from IMU to 7125 receiver face (z) and projector center (xy): x: -0.098 m; y: -0.18 m; z: -3.35 m (IMU: 11 cm + Pole: 309 cm + MB Head: 15 cm)
POS MV	Reference from IMU to Primary GPS Lever Arm : x: 0.762; y: -0.092 m; z: 0.056 m
From Water Surface to Bottom of MB Head	60.72 cm (to top of head 45.72 cm + MB Head: 15 cm)

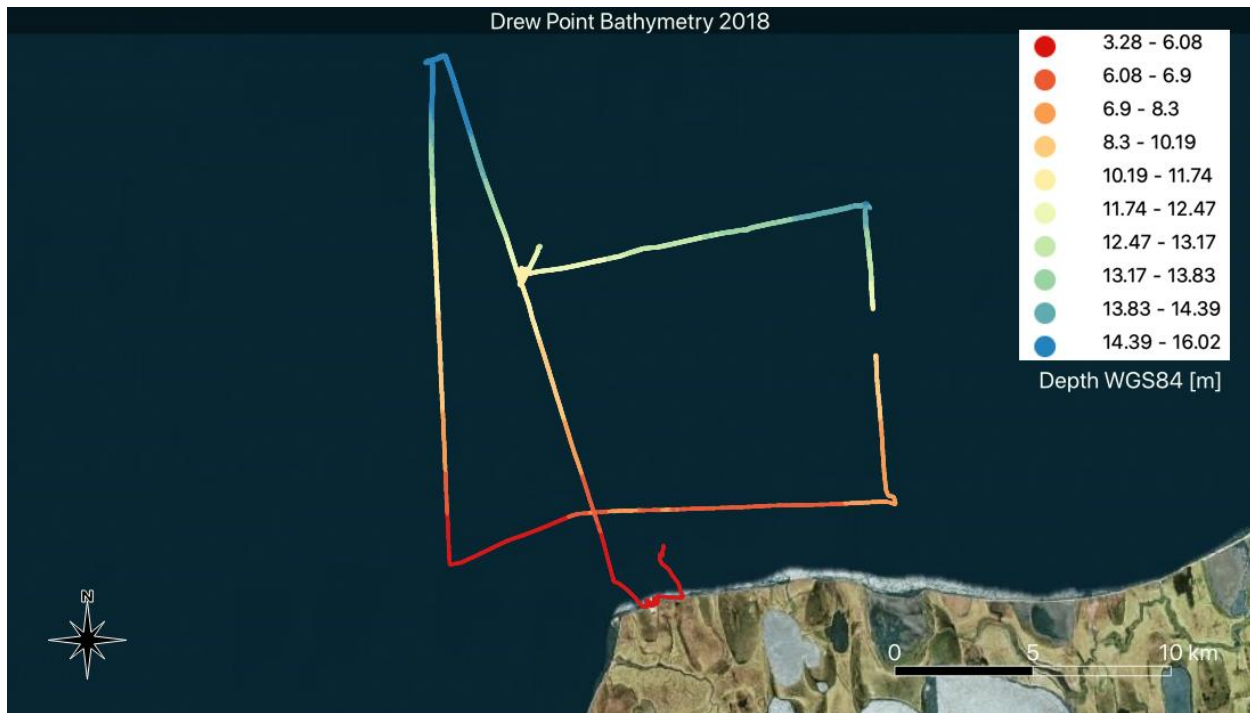


Figure 2.3-6. Drew Point multibeam derived bathymetry referenced to WGS84.

2.3.1.6. Nearshore Single-Beam Bathymetry (2018)

INSTRUMENTATION: Garmin GPSMAP 421s with Garmin sonar

AWI personnel completed 3 kilometers of bathymetry surveys in the nearshore. Survey went past the 1955 shoreline into approximately 3.5m of depth and also ran parallel to the 2002 shoreline. The sonar depth measurements were not referenced to any ellipsoid when collected. This nearshore bathymetric survey overlapped with the multi-beam bathymetric survey.

2.3.1.7. Water Samples (2018)

INSTRUMENTATION: Seabird Electronics SBE25+ CTD equipped with an SBE 55 water sampler and SBE33 deck box. The SBE25+ system was equipped with the following ancillary sensors: Teledyne Benthos Altimeter, Wetlabs FLNTUS (Fluorometer / Transmissometer), QSP2300 (PAR sensor).

A total of five locations had water samples collected using a CTD rosette equipped with Niskin bottles. Sampling times and locations are listed in Table 2.3-6 and mapped in Figure 2.3-7. Discrete water samples were taken at three depths at each station and will be analyzed for total suspended solids, trace and macro nutrients and Oxygen 18/Oxygen 16 isotope ratios. These ancillary measurements are useful for tracing water masses in the area (e.g., in distinguishing between sea ice derived water and meteoric water and ambient shelf water masses) as well as for estimating sediment fluxes in the study area.

Table 2.3-6. Water sampling plus CTD (Seabird Electronics 25+CTD with SBE 55 water sampler).

Number	Area	Date	Time	Lat & Long
13	Drew Point	7/28/2018	10:27	70.98848333°N 154.0369833°W
14	Drew Point	7/28/2018	11:36	71.05578333°N 154.1356833°W
15	Drew Point	7/28/2018	13:36	70.8933°N 154.0992667°W
16	Drew Point	7/28/2018	15:15	70.91523333°N 153.6678333°W
17	Drew Point	7/28/2018	16:41	71.01233333°N 153.6958833°W



Figure 2.3-7. Seabird water sample cast locations.

DelO18 samples were analyzed by Cornell Isotope Laboratory (COIL) in Ithaca, New York. The analysis was performed on a Thermo Delta V isotope ratio mass Spectrometer (IRMS) interfaced to a Gas Bench II. Delta values are measured in units of per mil (‰). The overall deviation for the internal DI standard 0.18 ‰ $\delta^{18}\text{O}$. Values are reported below (Figure 2.3-8) and shown in Table 2.3-7.

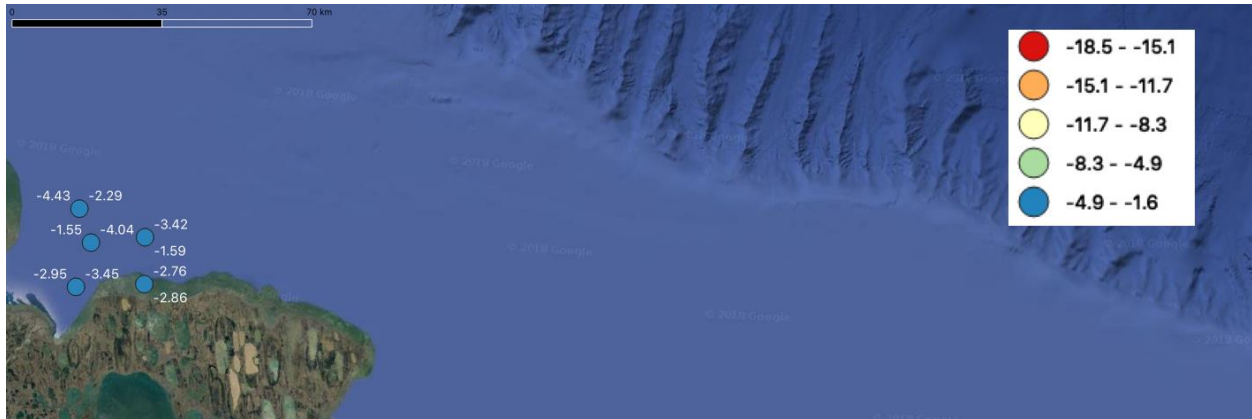


Figure 2.3-8. Stable Oxygen isotope results ($\delta^{18}\text{O}$, ‰).

Table 2.3-7. Oxygen stable isotope values ($\delta^{18}\text{O}$, ‰).

Latitude	Longitude	Delta O 18
70.9885	-154.0370	-1.55
70.9885	-154.0370	-4.04
71.0558	-154.1357	-2.29
71.0558	-154.1357	-4.43
70.8933	-154.0993	-2.95
70.8933	-154.0993	-3.45
70.9152	-153.6678	-2.86
70.9152	-153.6678	-2.76
71.0123	-153.6959	-1.59
71.0123	-153.6959	-3.42

2.3.1.8. Conductivity Temperature and Depth (2018)

INSTRUMENTATION: AML Oceanographic MinosX CTD & Seabird Electronics SBE25+ CTD

Multiple CTD measurements were made, both with the Seabird Electronics instrument (all measurements summarized in Table 2.3-7 and Figure 2.3-8 as well as with the AML instrument. Sampling times and locations for the AML instrument are listed in Table 2.3-8 and mapped in Figure 2.3-9.

Table 2.3-8. AML Probe Data (AML Oceanographic MinosX CTD).

Number	Area	Date	Time	Lat & Long
51	Drew Point	7/28/2018	10:31	70.98903611°N 154.0379167°W
52	Drew Point	7/28/2018	11:49	71.05605278°N 154.1318417°W
53	Drew Point	7/28/2018	13:32	70.89329167°N 154.1037278°W
54	Drew Point	7/28/2018	15:21	70.915075°N 153.6641278°W
55	Drew Point	7/28/2018	16:47	71.01093333°N 153.6922889°W
56	Drew Point	7/29/2018	9:07	70.88885833°N 153.9417889°W
57	Drew Point	7/29/2018	10:22	70.98712222°N 154.039625°W
58	Drew Point	7/29/2018	11:45	71.01251111°N 153.6931083°W



Figure 2.3-9. AML cast locations.

An example profile from AML Cast # 51 is shown in Figure 2.3-10. The data from these casts were used by the oceanographic modeling team to verify temperatures and salinities used in the oceanographic simulations.

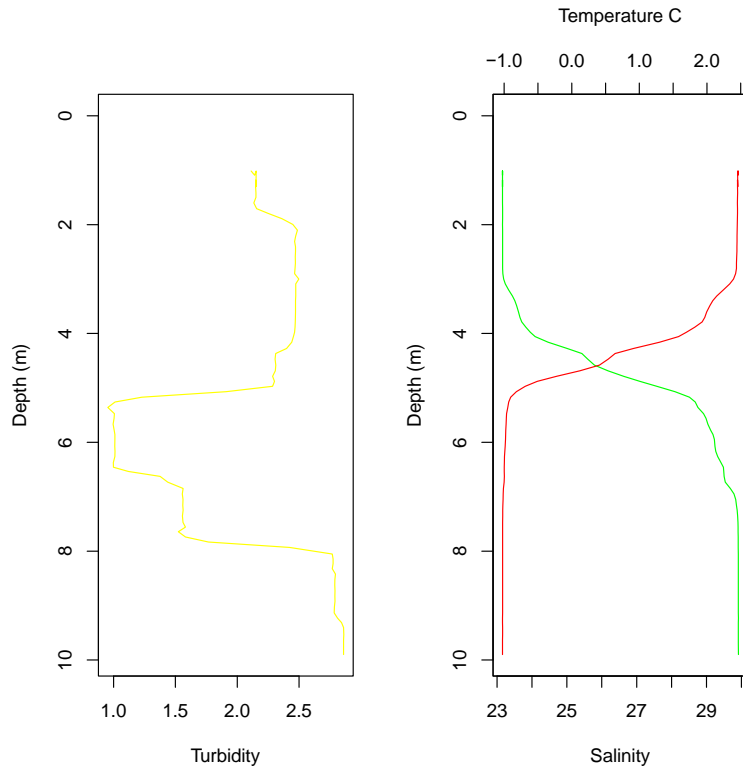


Figure 2.3-10. AML CTD and Turbidity cast from station 51. Yellow line turbidity, red line temperature, and green line salinity.

2.3.1.9. Bottom Grabs (2018)

INSTRUMENTATION: Wildco Stainless Steel Ponar Grab (0.1 m² sample area).

Bottom grabs were performed at 8 locations to determine the seafloor sediment characteristics. Table 2.3-9 and in Figure 2.3-11 detail the locations of the grabs near Drew Point.

Bottom grab samples were processed by the Oregon State University’s Central Analytical Laboratory. Samples were sieved and pipetted to determine grain size. D50 values for the samples are shown in Figure 2.3-12 and data are reported in Table 2.3-9. The full analysis is archived at UAF and is available upon request from Jeremy Kasper.

Table 2.3-9. Bottom grab collections details and sediment grain size distribution analysis.

Number	Area	Date	Time	Bottle	Lat & Long					
19	Drew Point	7/28/2018	10:33	490	70.9889°N 154.0385°W	mud	65.13	0.005248	0	0.59
20	Drew Point	7/28/2018	11:45	486	71.0560°N 154.1333°W	silt	67.6	0.005504	0	0.61
21	Drew Point	7/28/2018	13:35	500	70.8932°N 154.1010°W	silt	12.69	-0.016279	0.01	0.21
22	Drew Point	7/28/2018	14:13	463	70.9155°N 153.6708°W	silt	54.54	0.009626	0.63	1.74
23	Drew Point	7/28/2018	16:41	492	71.0109°N 153.6923°W	silt	37.31	0.001611	0.08	0.69
24	Drew Point	7/29/2018	9:08	458	70.8892°N 153.9420°W	silt	64.25	0.007527	0.2	1.55
25	Drew Point	7/29/2018	10:24	514	70.9872°N 154.0396°W	silt	9	0.022727	0.03	0.46
26	Drew Point	7/29/2018	11:46	503	71.0127°N 153.6933°W	silt	41.68	0.004095	0.56	1.74

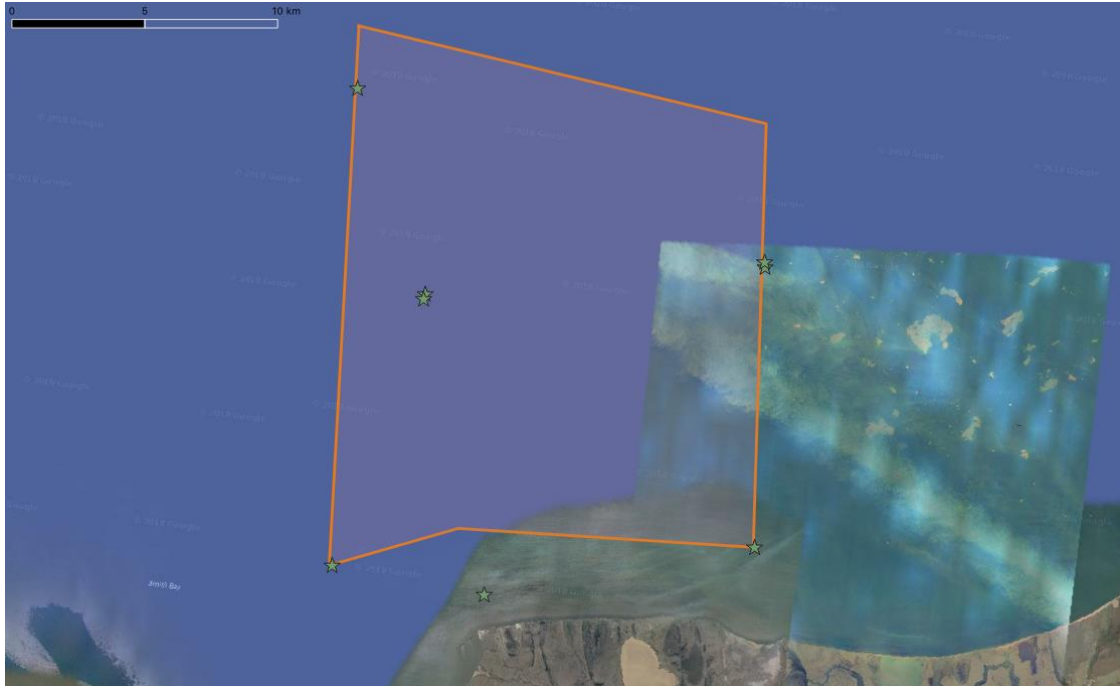


Figure 2.3-11. Bottom grab collections locations.

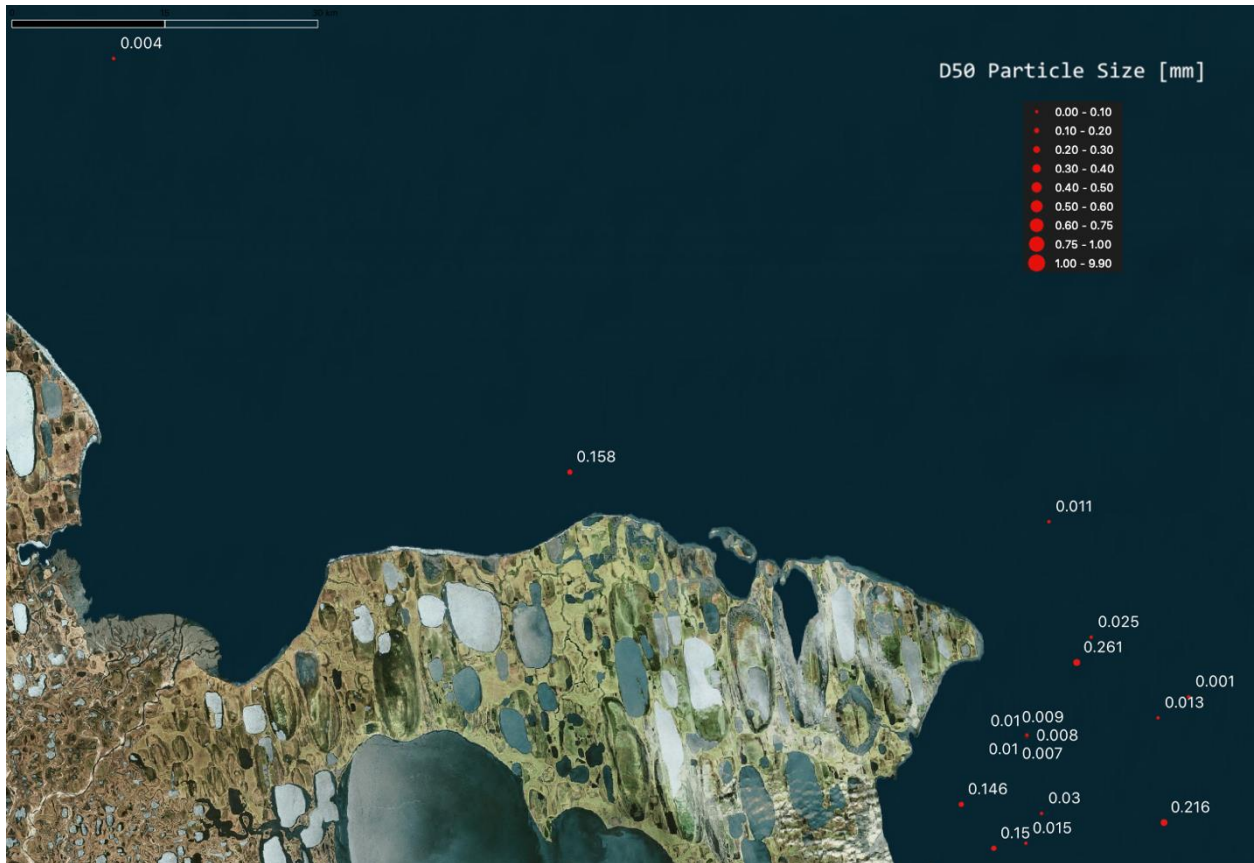


Figure 2.3-12. D50 values of bottom sediments from the Ponar Bottom Grab samples.

2.3.2. Analysis of Wave Environment

Plots of the 2018 and 2019 data sets are shown below Figure 2.3-13 and Figure 2.3-14. Measured water levels were adjusted to WGS84 using the water level survey measurements provided in Section 4.4. Based on a bluff toe height of -2 m WGS84 and the survey water levels, there is only one period in 2018 when the average water level RBR record shows average water levels exceeding the bluff toe height between ~25-Jul-2018 14:41:24 and 26-Jul-2018 01:01:24. Larger waves ($H_s > 0.2$ m) were also recorded during this episode. There are no periods in 2019 when average water levels exceed the bluff toe height though as discussed below the total water levels (average water levels plus significant wave height) do exceed the bluff toe height on several occasions noted below.

Adding the significant wave height to the average water level (Figure 2.3-15 and Figure 2.3-16 for 2018 and 2019, respectively) shows approximate total water levels exceeding the bluff toe height of -2 m several times on 7/28/2018, 7/29/2018 and 8/01/2018. 2019 is quite different with several episodes where total water level exceeds the bluff toe height on 8/15/2019, 8/17-8/18 and on 8/23. The episode on 8/15/2019 occurred despite low average water levels.

Note the water levels have not been corrected for the inverse barometer effect. This is because in this case, the total water level relative to the bluff toe height that includes the inverse barometer effect is the variable of interest. Sea level atmospheric data available from Oliktok or from the nearby USGS met-station can be used to calculate the inverse barometer effect.

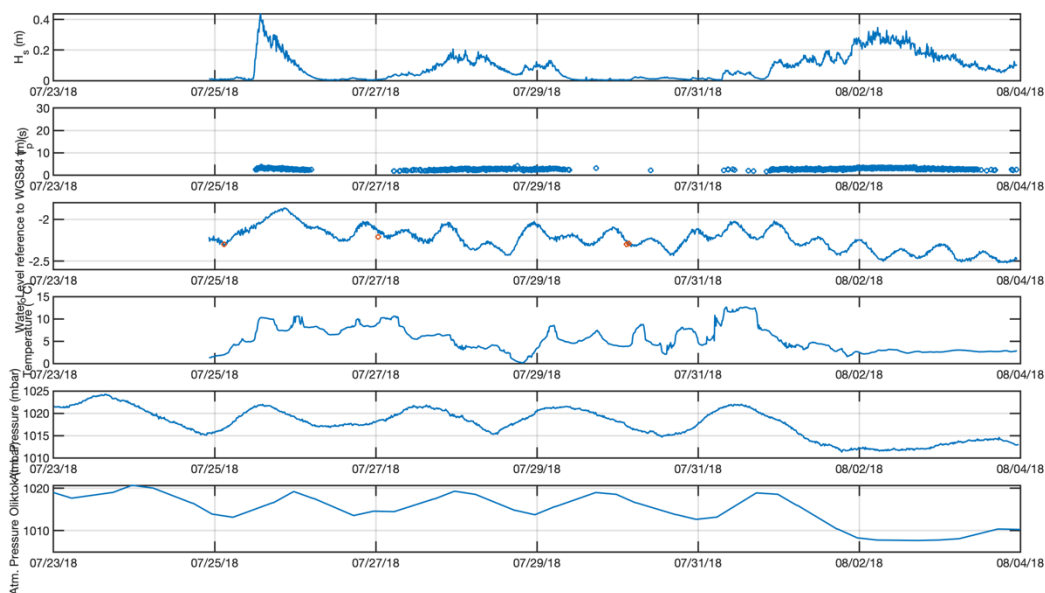


Figure 2.3-13. 2018 RBR Data. Top: Significant Wave Height (m) followed by Peak Period (s), Water Level referenced to WGS84 (m), Temperature (deg. C), Atm. Pressure (mbar) from the HOBO “spit” atm. pressure sensor and Atm. Pressure Oliktok (mbar). All are versus time.

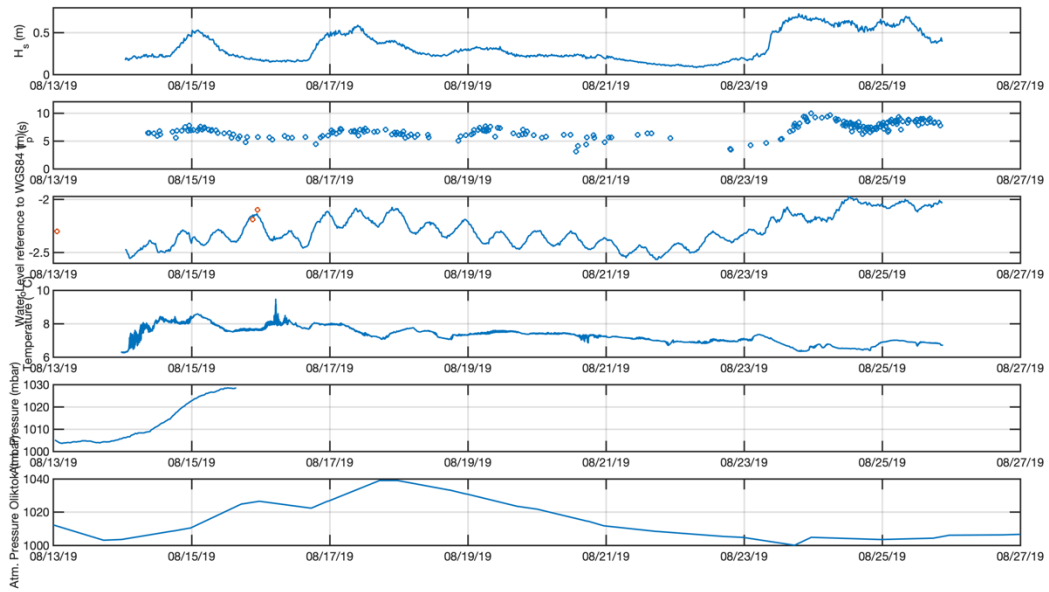


Figure 2.3-14. 2019 RBR Data. Top: Significant Wave Height (m) followed by Peak Period (s), Water Level referenced to WGS84 (m), Temperature (deg. C), Atm. Pressure (mbar) from the HOBO “spit” atm. pressure sensor and Atm. Pressure Oliktok (mbar). All are versus time.

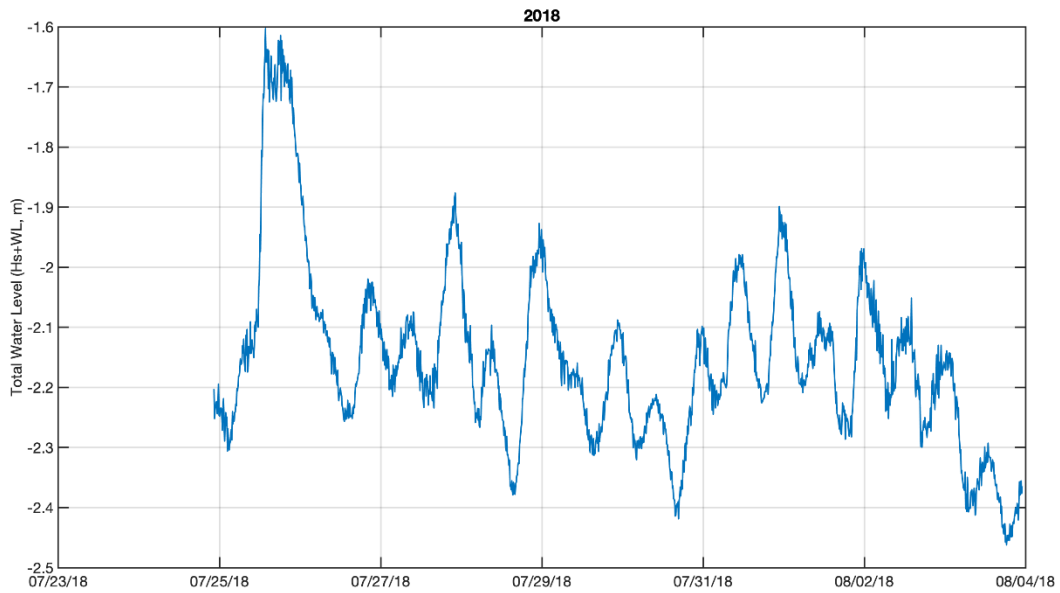


Figure 2.3-15. 2018 total water level referenced to WGS84 (m, water level plus significant wave height, Hs).

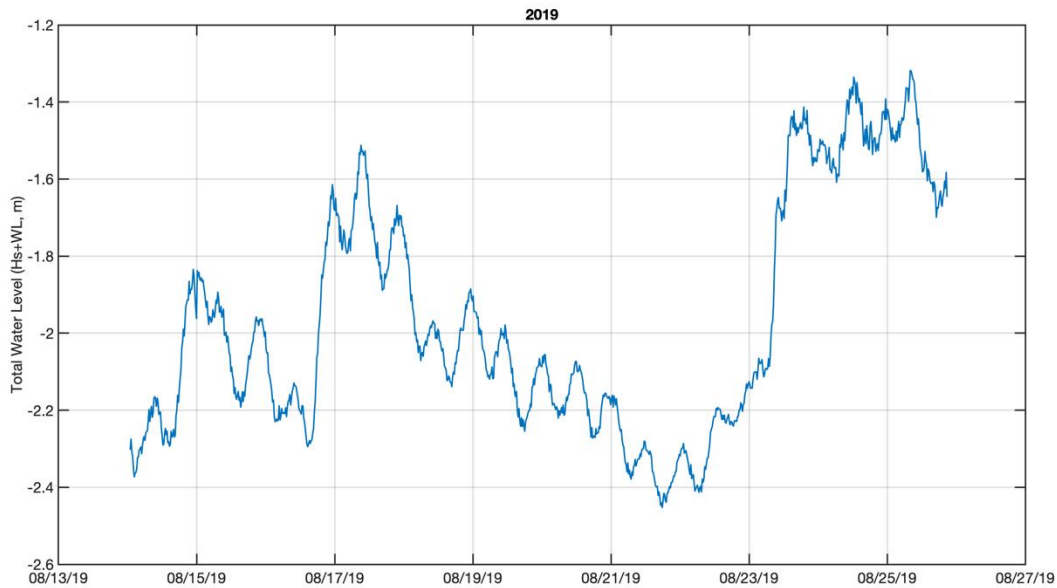


Figure 2.3-16. 2019 total water level referenced to WGS84 (m, water level plus significant wave height, Hs).

2.3.3. Analysis of Water Levels

The HOBO spit data, Section 2.3.1.2, was processed for quality control. Data were removed from the dataset and identified as Not-a-Number (NaN) if any of the following conditions were met:

- *all variables* – if less than -20°C air temperature, which is below the temperature range of instrument
- *Pabs, Twater, depth* – if less than 1 cm water, which is below the depth range of the instrument
- *Pabs, Twater, depth* –if less than or equal to 0°C water temperature, for the period during winter when the instrument was frozen into the ice

Linear interpolation was performed over missing data to remove NaNs from the dataset, except for data gaps of 3 hours or larger in length, which remain as NaNs. The sampling frequency changed when instruments were redeployed on August 3, 2018 from every 10 mins (1:13573) to every 30 mins (13574:end). The instrument on the bluff was also redeployed on December 2, 2018 between 2-4pm, but the sampling interval does not change.

Time series of the processed HOBO Spit are shown in Figure 2.3-17.

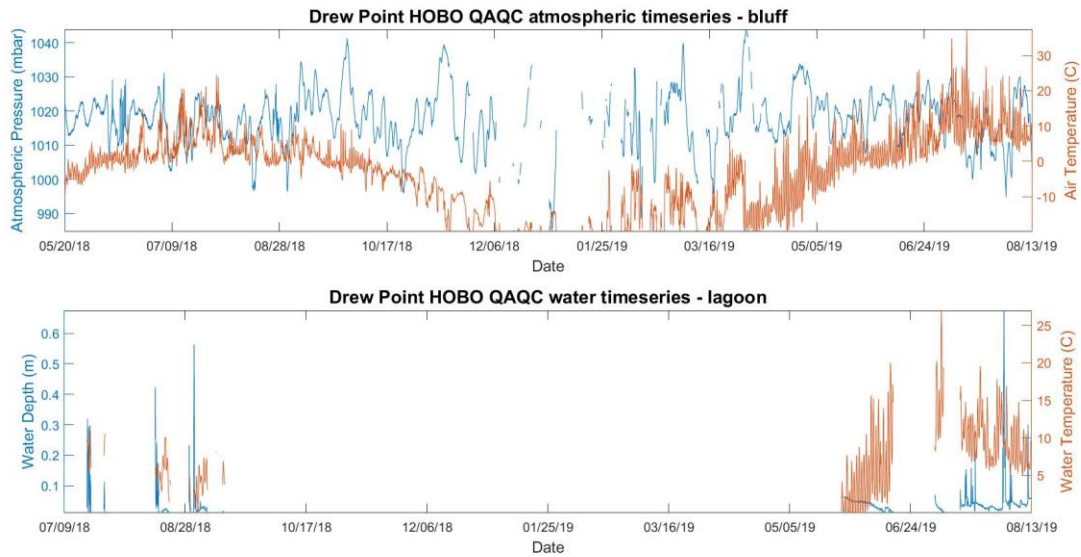


Figure 2.3-17. Timeseries of atmospheric pressure (mbar), air temperature (C°) (top panel); water depth (m) and water temperature (C°) (bottom panel) at Drew Point, Alaska from May 1, 2018 – August 15, 2019.

2.3.4. Analysis of Wind

The Beaufort Scale is included in Table 2.3-10. Beaufort Wind Scale for reference.

Table 2.3-10. Beaufort Wind Scale.

Beaufort scale	knots	m/s	Label
0	0-1	<0.5	calm
1	1-3	<1.5	light air
2	4-6	<3.1	light breeze
3	7-10	<5.1	gentle breeze
4	11-16	<8.2	moderate breeze
5	17-21	<10.8	fresh breeze
6	22-27	<13.9	strong breeze
7	28-33	<17.0	near gale
8	34-40	<20.6	gale
9	41-47	<24.2	severe gale
10	48-55	<28.3	strong storm
11	56-63	<32.4	violent storm
12	64-71	<36.5	hurricane

2.3.4.1. USGS Weather Station

Hourly average values for air temperature, wind speed and wind direction from 3m above the surface from August 1998 – February 2020 were obtained from the U.S. GEOLOGICAL SURVEY (USGS) Global Terrestrial Network for Permafrost Circumpolar Active Layer Monitoring Network Site (GTN-P/CALM code AK100 U20) at Drew Point Alaska, located at 70 51.872 N latitude and 153 54.405 W longitude (Urban, 2020).

A rose plot of the Drew Point winds is shown in Figure 2.3-18.

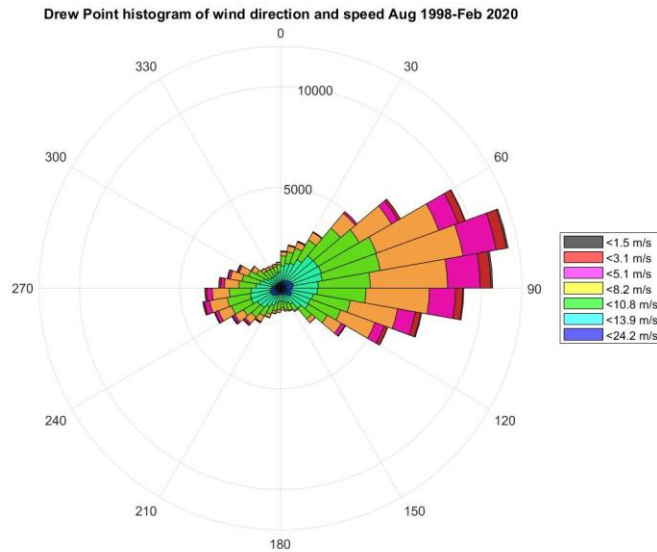


Figure 2.3-18. Histogram of wind speed and direction at Drew Point, Alaska from August 1998-February 2020, showing wind speeds (m/s) and direction (clockwise from 0° due north). Wind speeds range from 0-21.79 m/s and are binned according to the Beaufort wind scale shown below. Note, wind speeds within the Beaufort scales 0-1 and 7-9 were binned together, and no winds were recorded above severe gale speeds. Based on Drew Point wind data obtained from Frank Urban and described above (USGS met station at Drew Point).

2.3.4.2. ARM Mobile Facility Located at Oliktok Point

Measured values every minute of atmospheric pressure, wind speed, wind direction, eastward and northward components of wind from March 1 - October 31 in 2018 and 2019 were downloaded from the Department of Energy (DOE) website for the Atmospheric Radiation Measurement (ARM) facility at Oliktok Point (ARM 2015a, ARM 2015b).

ARM data were extracted from 487 Network Common Data Form (NetCDF) files of type oliinterpolatedsondeM1.c1.nc, each containing 1440 x 332 data arrays per variable. Data were measured at 332 heights in the atmosphere from 2 m to 40 km above mean sea level (MSL). Only the data at 2 m altitude data were extracted.

A rose plot of the Oliktok winds is shown in Figure 2.3-19. In general, the winds agree in scale and direction. Note that the USGS data set is a significantly longer record than the data set from Oliktok.

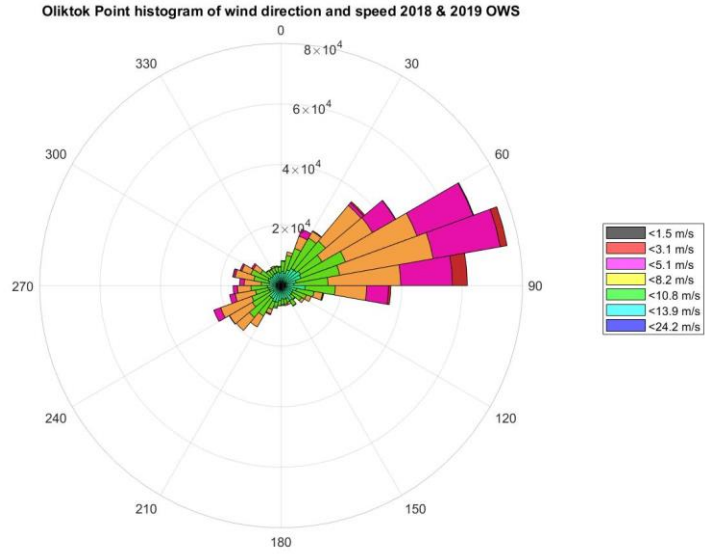


Figure 2.3-19. Histogram of wind speed and direction at Oliktok Point, Alaska during the open water season (OWS) from March 1 – October 31 in 2018 and 2019, showing wind speeds (m/s) and direction (clockwise from 0° due north). Wind speeds range from 0-12.9 m/s and are binned according to the Beaufort wind scale shown below. Note, wind speeds within the Beaufort scales 0-1 and 7-9 were binned together, and no winds were recorded above a strong breeze.

3. PERMAFROST MATERIAL ANALYSES

3.1. Coring Campaign

In total, 31 meters of permafrost cores from Drew Point were retrieved by a small team of University of Alaska, Fairbanks, researchers, led by Ben Jones during April 2018. Team members included: Chris Arp, Allen Bondurant, Go Iwahana, and Misha Kanevskiy.

“Cores were acquired at Drew Point during a snowmachine expedition between Utqiagvik and Teshekpuk Lake using two coring systems (Figure 3.1-1 and Figure 3.1-2). Near-surface cores (upper 4 to 6 m) were acquired using a SIPRE corer (7.5 cm diameter) and cores at depth were acquired using a JIPRO corer (7.5 cm diameter). As shown in Figure 3.1-3 we targeted each of the three dominant land surfaces present in the Drew Point region: a primary surface material that has not been reworked by thermokarst lake formation and drainage, an ancient drained thermokarst lake basin (DTLB) which would have drained ~5 kyr BP (Hinkel et al. 2003; Jones et al., 2012), and a young DTLB with most recent drainage occurred ~0.5 kyr BP (Jones et al., 2012). These three land surfaces capture variations in near-surface permafrost characteristics and the height of the bluffs abutting the eroding coastline.” (verbatim from Bristol et al. Submitted)



Figure 3.1-1. Collage of photos taken while SIPRE coring.

JiPRO Coring

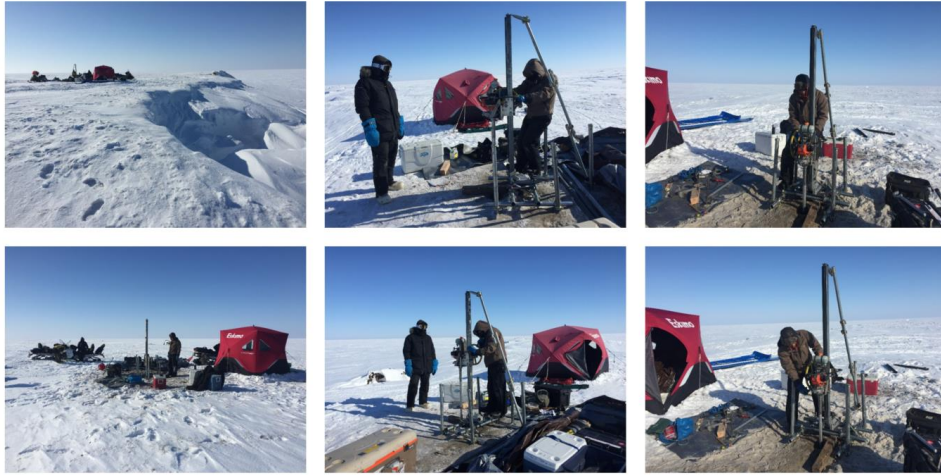


Figure 3.1-2. Collage of photos taken while JiPRO coring (taken by Misha).



Figure 3.1-3. From left to right, photographs of landscape classified as Primary Surface, Ancient DTLB (drained ~5 kyr BP), and Young DTLB (most recent drainage occurred ~0.5 kyr BP).

Details of all the cores at each land surface type are given in Table 3.1-1. Figure 3.1-4 shows the location of each core with the terrain classifications identified along the 9km study site that defines Drew Point. Detailed field notes can be found in Appendix B.

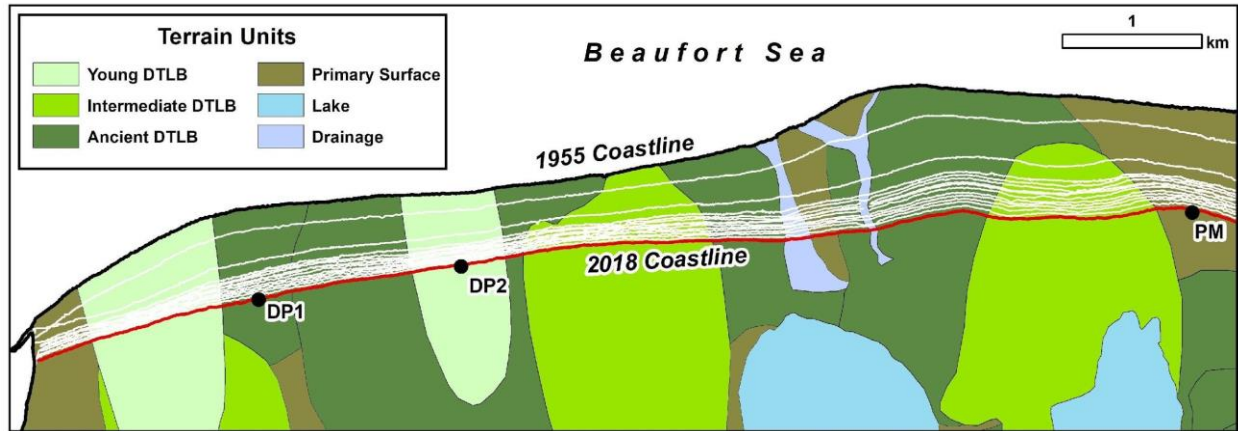


Figure 3.1-4. Map of our 9 km study coastline denoting coastline lost from 1955 (bold black line) and 2018 (bold red line), locations where permafrost was cored (DP1, DP2, PM), and terrain classifications. White lines show bluff line position for timesteps between 1955 and 2018.

There are five geologically distinct terrain units comprising the Drew Point coastline as shown in Figure 3.1-4 only 3% of the eroding coastline was classified as a lake or drainage. These units have distinct geomorphological, material, and geophysical properties. We have not fully characterized these properties for all of the terrain units, however, estimates of how the units differ from one another are available due to the subject matter expertise of Ben Jones who has worked at this site for over a decade. Brief descriptions of each terrain unit are given below.

Primary Surface: The primary surface is the geologically oldest and is characterized by predominately silty deposits (Kanevskiy et al. 2013). These units are the most ice rich both in terms of the amount of ice wedge volume (28% wedge ice) as well as the amount distributed in the permafrost and typically present as high centered polygons (Kanevskiy et al. 2013, Ben Jones personal communication). Multiple generations of ice wedges can be observed within the same polygonal system, however this aspect is not yet accounted for in the modeling (Kanevskiy et al. 2013). At Drew Point, these have the tallest bluffs (4.8 ± 0.1 m) and stores an estimated 106.3 kg m^{-2} TOC and 6.9 kg m^{-2} TN (Bristol et al. Submitted). These are also the most studied in terms of their geomechanical properties (Section 3.5). The primary surface comprises 14.9% of the coastline in 2018.

Young Drained-Lake Basin: Drained-lake basins of different ages are numerous in the Arctic Coastal Plain with the young having drained in the past 50-500yrs (Jones et al. 2012). Young drained-lake basins are the least ice rich; they may have ice wedges, but they are not predominate and likely exist below the surface (Ben Jones personal communication). Further, the permafrost itself is also the least ice rich of all of the terrain units; they are estimated to have only 3% wedge ice (Kanevskiy et al. 2013). Again, these are predominately silty in sediment constituency (Kanevskiy et al. 2013). Given the lack of ice wedges, polygons sizing is not applicable. Young DTLBs have an average bluff height of 4.1 ± 0.1 m and store 101.0 kg m^{-2} TOC and 6.9 kg m^{-2} TN (Bristol et al. Submitted). The young drained-lake basin comprises 14.5% of the coastline in 2018.

Intermediate Drained Lake Basin: Intermediate basins have drained in the past 500-2000yrs (Jones et al. 2012). These are, in a materials sense, intermediate in terms of their ice content. Ice wedge formations are present but are small; they are estimated to have 7% wedge ice (Kanevskiy et al. 2013). Polygons tend to be low-centered and large in extent while the permafrost itself is predominately silty with an intermediate ice content (Kanevskiy et al. 2013). Intermediate age

DTLBs have the lowest elevation bluffs (3.0 ± 0.1 m) and store an estimated 67.1 kg m⁻² TOC and 4.6 kg m⁻² TN (Bristol et al. Submitted). The intermediate drained-lake basin comprises 30.5% of the coastline in 2018.

Ancient Drained Lake Basin 1 & 2: Ancient basins have drained in the past 2000+ yrs (Jones et al. 2012). In terms of the drained-lake basins, the ancient have the highest ice content both in terms of the ice wedge sizes (11% wedge ice) as well as within the predominately silty permafrost (Kanevskiy et al. 2013). Polygons are high centered and the smallest along the coastline (Kanevskiy et al. 2013, Ben Jones personal communication). The decrease in sizes of polygons from young to old basins indicates that polygons are subdivided over time (Kanevskiy et al. 2013). Ancient DTLBs have a lower elevation of 3.7 m and store 81.1 m⁻² TOC and 5.6 kg m⁻² TN (Bristol et al. Submitted). The ancient drained-lake basin comprises 37% of the coastline in 2018.

For a 4-meter bluff (typical for our study coastline), the average 14C-TOC age of eroding organic matter is ~16 kyr BP when weighted by TOC stocks (Bristol et al. Submitted).

In the following analyses of the permafrost material properties, effective porosity is used. Effective porosity assumes a homogeneously distributed amount of void space that may be beyond the natural porosity due to cryogenic processes, such as ice lensing. Inherent in this use is that we are not explicitly treating the cryo-structure of excess ice in our analyses or our modeling.

Table 3.1-1. Detailed information on each core collected. Above Sea Level = ASL and Below Sea Level = BSL.

Core Identifier	Land Surface	Lat (N)	Lon (W)	Bluff Height (m)	Length (m)	Elevation (m)	Visual Cryopeg	Notes
DP1-1	Ancient DTLB	70.880547	153.890403	5.2	7.5	5.2m ASL to -2.3m BSL	0.2m ASL to >2.3m BSL	SIPRE coring from 0-5.1m; JIPRO coring from 5.1 -7.5m
DP1-2	Ancient DTLB	70.880525	153.890519		3.3	5.2m ASL to 1.9m ASL		
DP2-1	Young DTLB	70.882969	153.850392	3.9	4.6	3.9m ASL to -0.7m BSL	0.2m BSL to >0.7m BSL	SIPRE coring from 0-4.02m; JIPRO coring from 4.02-4.58m; confirming presence of cryopeg
DP2'-2	Young DTLB	70.878968	153.849627		3.0	3.9m ASL to 0.9m ASL		SIPRE coring only; encountered wedge ice from 0.88-2.42m
PM1-1	Primary Material	70.887056	153.706795	6.9	7.4	6.9m ASL to -0.5m BSL	0.4m ASL to >0.5m BSL	SIPRE coring from 0-6.33m; JIPRO coring from 6.33-7.38m
PM1-2	Primary Material	70.887044	153.706742		1.3	6.9m ASL to 5.6m ASL		SIPRE coring only; encountered wedge ice from 0.50-1.30m
PM1-3	Primary Material	70.887044	153.706259		4.0	6.9m ASL to 2.9m ASL		SIPRE coring only; collect additional material in upper 4m

“Cores were collected in air temperatures between -10°C and -20°C. They were photographed and described in the field and then packed into coolers for transport back to Utqiagvik and then flown frozen on Alaska Airlines back to the University of Alaska in Fairbanks where the cores were stored in a -20°C freezer room prior to shipping them frozen to Sandia National Laboratories in Albuquerque, NM for processing.” (verbatim from Bristol et al. Submitted)

Craig Connolly (UTA) and Tom Lorenson (USGS) traveled to Sandia National Laboratories in Albuquerque, NM during July 2018 to meet with Anastasia Ilgen (SNL), Charles Choens (SNL), Courtney Herrick (SNL), Dongmei Ye (SNL), Kylea J. Parchert (SNL), and Diana Bull (SNL) to divvy up the permafrost cores from Drew Point retrieved in April for material property and biogeochemical analyses. After visual inspection of each core (Figure 3.1-5), specific core sections were identified and reserved for geomechanical work. Core sections for geochemical analyses were then selected from the remaining material.



Figure 3.1-5. Sandia scientists examine core sections for geomechanical and geochemical analysis.

Following sectioning, core material for biogeochemical work was thawed in clean beakers and divvied up for specific analyses. First, small plugs of intact soil were extracted for biological work. Second, cores were mixed and pore water was extracted for strontium and oxygen isotope analysis, trace metals and major anion and cations, and dissolved organic carbon and total dissolved nitrogen analysis. Third, remaining core material was homogenized again and a small amount was collected for grain size analysis (~10–20 g wet weight). Fourth, core material was collected for bulk soil organic carbon and nitrogen content, and bulk soil stable carbon and radiocarbon analysis (~200+ g wet weight). When soil was at a surplus, additional material was allocated for organic chemistry (100–200 g wet weight) or refrozen and archived.

Samples for porewater strontium and oxygen isotope analyses were transported to the USGS Pacific Coastal and Marine Science Center in Santa Cruz by Tom Lorenson. Samples for porewater dissolved organic carbon and total dissolved nitrogen concentrations, bulk soil organic carbon and

nitrogen content, and bulk soil stable carbon and radiocarbon analyses were transported to the University of Texas Marine Science Institute by Craig Connolly.

After further sorting at the University of Texas Marine Science Institute, 45 bulk soil samples were transported by Craig Connolly to the National Ocean Sciences Accelerator Mass Spectrometer (NOSAMS) facility in Woods Hole for processing and analysis. This work occurred during September 2018. Percentages organic carbon and nitrogen in soils were measured on an Elementar el Vario Cube C/N analyzer, stable carbon isotope composition was measured on a VG Prism Stable Mass Spectrometer, and radiocarbon composition was measured on the Accelerator Mass Spectrometer system.

Beyond the geochemical processing (Section 3.2.1), samples were used for geomechanical studies (Section 3.5), for material characterization (effective porosity, sediment concentrations, density) (Section 3.3), for carbon decomposition experiments (Section 3.2.2), and also for exploratory genomic and bio-analyses (Appendix B). In total 33 samples were used in geomechanical studies, 45 samples in geochemical studies, 53 samples for material characterization, and 12 samples to analyze carbon decomposition.

The remaining permafrost core material is retained at SNL for prosperity and future experiments.

3.2. Permafrost Geochemical Analyses

Team Member Author: Emily Bristol (UTA)

Contributors: Craig Connolly (UTA), Jim McClelland (UTA), Benjamin Jones (UAF), Diana Bull (SNL), Robert Spencer (FSU) Anastasia G. Ilgen (SNL), R. Charles Choens (SNL), Thomas D. Lorenson (USGS), Bruce M. Richmond (USGS), Mikhail Kanevskiy (UAF), Go Iwahana (UAF)

3.2.1. *Synopsis: Geochemistry and Erosional Organic Carbon and Nitrogen Fluxes*

Accelerating erosion of the Alaska Beaufort Sea coast is increasing inputs of organic matter from land to the Arctic Ocean, and improved estimates of organic matter stocks in eroding permafrost are needed to assess their mobilization rates under contemporary conditions. We collected three permafrost cores (4.5-7.5 m long) along a geomorphic gradient near Drew Point, Alaska, where recent mean decadal-scale erosion rates average 17.2 m yr⁻¹.

The cores indicate that organic-rich soils (12-45% total organic carbon; TOC) in the active layer and upper permafrost accumulated during the Holocene (Figure 3.2-1). Below 3 m elevation, permafrost consists mainly of Late Pleistocene marine sediments with lower organic matter content (~1% TOC), lower C:N ratios, and higher $\delta^{13}\text{C}$ values. Radiocarbon-based estimates of organic carbon accumulation rates were 11.3 ± 3.6 g TOC yr⁻¹ during the Holocene and 0.5 ± 0.1 g TOC yr⁻¹ from 12 to 38 kyr BP. Porewater salinities increased with depth in the relict marine sediments, reaching values of ~20-37 near sea level and below. These elevated salinities inhibited freezing despite year-round temperatures below 0 °C.

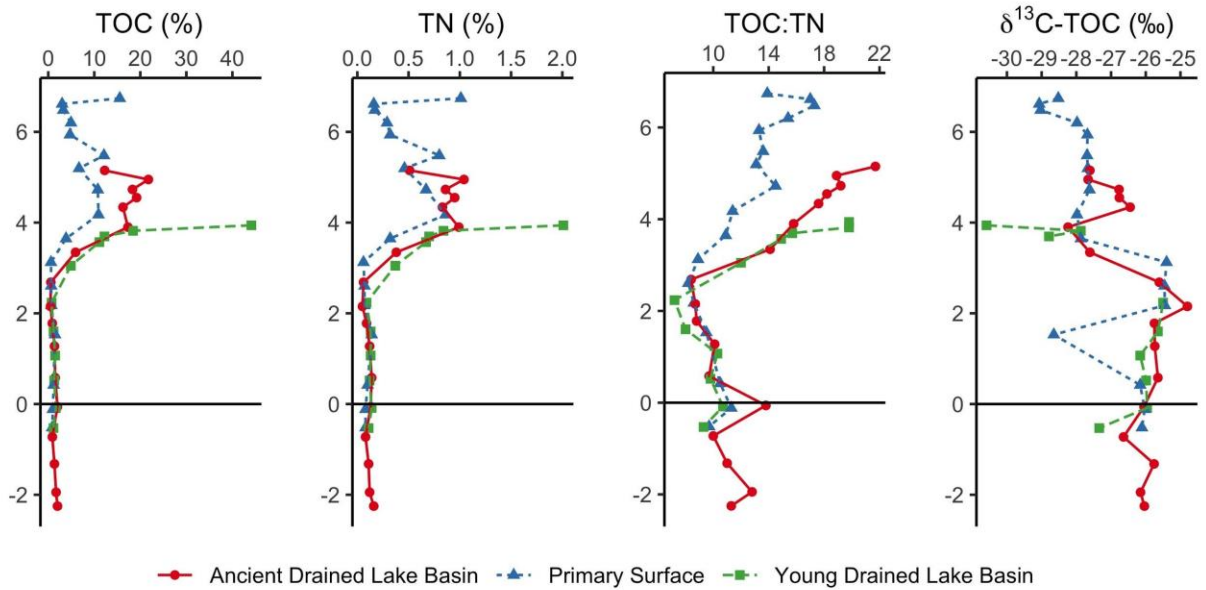


Figure 3.2-1. Soil total organic carbon (TOC; wt %), total nitrogen (TN; wt %), soil organic carbon to nitrogen molar ratio (C:N), and $\delta^{13}\text{C}$ -TOC (‰) profiles for three permafrost cores. Colors and symbols indicate the terrain classification each core was sampled from. The black horizontal lines indicate mean sea level.

We used organic matter stock estimates from the cores in combination with remote sensing time-series data to estimate carbon fluxes for a 9 km stretch of coastline near Drew Point. Erosional fluxes of TOC averaged 12,849 metric tons C yr^{-1} during the 21st century (2002-2018), nearly double the average for historical fluxes (1955-2002; Figure 3.2-2).

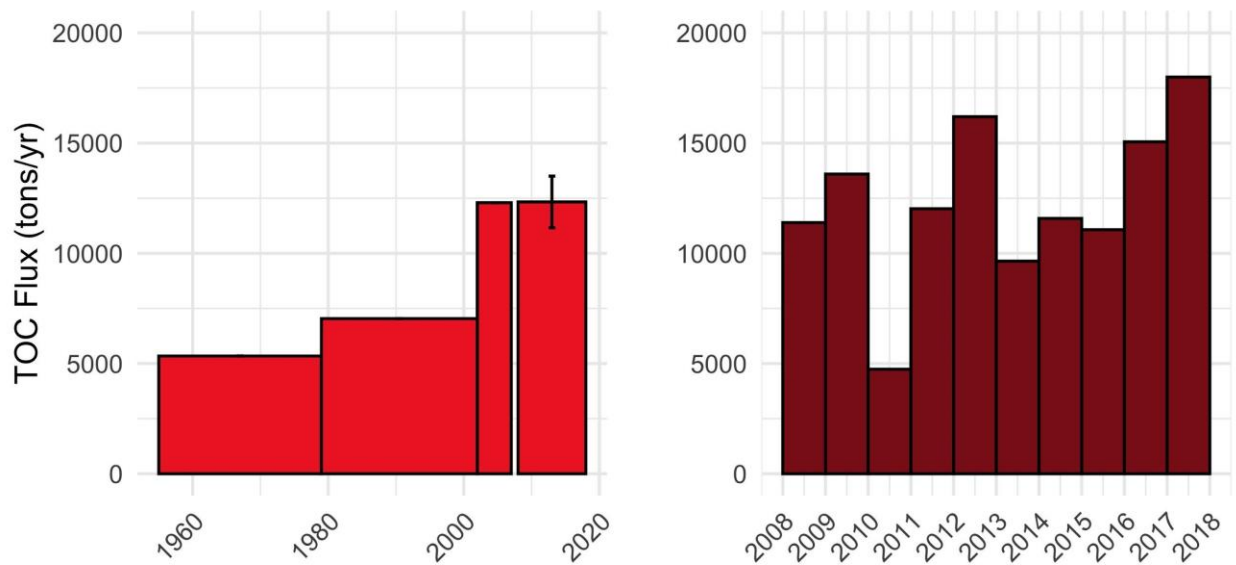


Figure 3.2-2. Estimation of total organic carbon fluxes to the ocean (metric tons TOC yr^{-1}) from the 9 km study section over four time steps from 1955 to 2018 and over annual time steps from 2008 to 2018. The error bar shows standard error.

Our estimate of the 21st century erosional TOC flux yr⁻¹ at Drew Point is similar to annual TOC fluxes from the Sagavanirktok and Kuparuk rivers, which rank as the second and third largest rivers draining the North Slope of Alaska. Nitrogen fluxes via coastal erosion at Drew Point were also quantified, and shown to be similar to riverine nitrogen fluxes. This study emphasizes coastal erosion as a pathway for carbon and nitrogen trapped in permafrost to enter modern biogeochemical cycles, where it may fuel food webs and greenhouse gas emissions in the marine environment.

3.2.2. Decomposition of Organic Carbon

Coastal erosion along the Beaufort Sea coast mobilizes large quantities of permafrost soil to the marine environment, where soil organic matter may be leached to dissolved organic matter (DOC) and rapidly decomposed. To assess the quantity and bioavailability of dissolved organic carbon (DOC) leached from active layer and permafrost soils in seawater, we designed a laboratory leaching and DOC incubation experiment. We examined three distinct soil horizons that are representative of eroding bluffs near Drew Point, Alaska: seasonally thawed active layer soils, organic-rich permafrost soils, and permafrost consisting of relict marine sediment that was deposited during a late-Pleistocene marine transgression. Soil/sediment samples were leached in seawater to compare DOC yields. Filtered leachate was then incubated for 26 and 90 days to measure bioavailable DOC (BDOC; i.e. DOC that is lost through incorporation in bacterial biomass or remineralized to inorganic forms).

Our results show that organic-rich permafrost samples leach the highest quantity of DOC, even when normalized by TOC. Active layer soils contain more DOC than relict marine sediments, but when normalized to TOC, active layer soils and relict marine sediments leached similar quantities of DOC. Despite leaching the most carbon, DOC from organic-rich permafrost was the least biodegradable, showing a loss of only $14\% \pm 3\%$ over 90 days (Figure 3.2-3). Relict marine sediment leachates had the highest losses of DOC, averaging $31 \pm 7\%$ loss over 90 days (Figure 3.2-3). Active layer leachates lost an average of $24 \pm 5\%$ DOC (Figure 3.2-3).

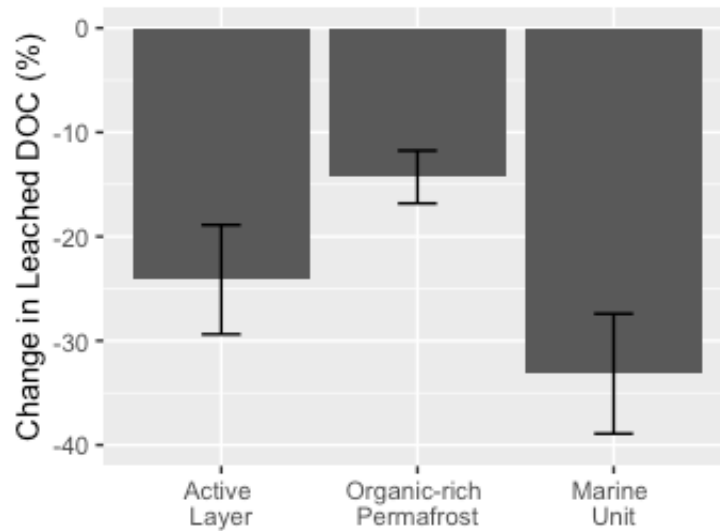


Figure 3.2-3. The figure shows the average percent loss of dissolved organic carbon (DOC) leached from active layer soils, organic-rich permafrost, and relict marine sediments over a 90-day incubation.

To scale the results of the experiment, we combined average leaching and BDOC values with our knowledge of soil organic carbon storage in eroding bluffs at Drew Point, Alaska. A typical 4 m bluff at Drew Pt stores 98.8 kg C m^{-2} . The active layer, assumed to reach a depth of 0.4 m in this region, stores 39.9 kg C m^{-2} . Organic rich permafrost between the relict marine unit and the active layer (spanning a depth of 0.6 m in a 4 m bluff) stores 25.1 kg C m^{-2} . From sea level to an elevation of 3 m, relict marine sediments store 33.8 kg C m^{-2} . Using our experimental leaching results, we expect a total of $340.6 \text{ g DOC m}^{-2}$ to leach from a 4 m eroding bluff. Of this, the active layer contributes an estimated $90.1 \text{ g DOC m}^{-2}$, organic rich permafrost contributes $157.9 \text{ g DOC m}^{-2}$, and relict marine sediments above sea level contribute $92.6 \text{ g DOC m}^{-2}$. When weighted by carbon storage in each of these soil/sediment horizons, an average 24.7% of leached DOC is expected to be bioavailable. Therefore, we estimate a total of 75 g BDOC m^{-2} is released from a 4 m bluff: $21.7 \text{ g BDOC m}^{-2}$ from active layer soils found to a depth of 0.4 m, $22.6 \text{ g BDOC m}^{-2}$ from a 0.6 m thick horizon of organic rich permafrost, and $30.7 \text{ g BDOC m}^{-2}$ from relict marine sediment found below an elevation of 3 m.

These results highlight differences in both the “leachability” and the lability of organic carbon found in three distinct soil horizons at Drew Point, Alaska, indicating how geomorphology and landscape history influence the characteristics of organic matter. This experiment also demonstrates that a notable fraction of DOC leached in seawater, approximately 25%, is bioavailable and may be decomposed on relatively short timescales in the marine environment. As erosion rates along the Beaufort Sea coast increase, decomposing soils are an increasingly important source of carbon emissions from the coastal environment.

3.3. Physical Composition

Team Member Author: Emily Bristol (UTA)

Contributors: Benjamin Jones (UAF), Charles Choens (SNL), Jennifer Frederick (SNL), Diana Bull (SNL), Jim McClelland (UTA), Siddharth Namachivayam (Pomona College)

We examined the physical composition (e.g. bulk density, gravimetric water content, effective porosity) of permafrost across a range of depths, and from various terrain classifications. A complete set of measurements including volume, wet weight, and dry weight were measured for 54 samples at the University of Texas Marine Science Institute. An additional 12 samples were measured for volume and wet weight at Sandia National Laboratories. Four samples were measured for wet weight and dry weight at University of Alaska Fairbanks, but did not have volume measurements. Of these 70 total samples, 59 were sent to Oregon State University to determine the fractions of sand, silt, and clay using the hydrometer method.

To determine the frozen bulk density and dry bulk density of a core section, we measured the volume of a frozen sample and the mass before and after drying at 50C for approximately one week. Volume of completely frozen (-20C) samples was determined using one of the two methods: using linear dimensions of near-cylindrical frozen core section to calculate volume, or by measuring the water volume displaced by a vacuum sealed frozen sample. The volume displaced by the plastic vacuum sealer bag was subtracted from the total volume. For a subset of samples, we measured volume using both methods, which yielded comparable results. In addition, we calculated gravimetric water content, which is defined as the mass ratio of water to dry soil/sediment. We also estimated the porosity of core samples. We assumed that soil/sediments are completely saturated with water, there is no air space, and soil/sediments are completely frozen. Therefore, we define porosity as the percent volume of ice (V_{ice}), where the density of ice (ρ_{ice}) assumed to be 0.917 g cm⁻³, m_{ice} is the mass of water loss during drying, and V_{total} and is the bulk sample volume:

$$porosity (\%) = \frac{V_{ice}}{V_{total}} \times 100 = \frac{m_{ice} \times \rho_{ice}}{V_{total}} \quad \text{Equation 3.3-1}$$

Our definition of porosity here is the effective porosity of the soil, i.e. the combination of natural porosity and excess ice.

In general, frozen and dry bulk density increase downcore while porosity and gravimetric water content decrease downcore (Figure 3.3-1. Down core profiles of frozen bulk density, dry bulk density, gravimetric water content, soil water content, and estimated porosity. Color and symbol indicate the terrain classification of the sample. One sample that was mostly ice is not shown in the gravimetric water content plot due to its high value (37,350 %).Figure 3.3-1). When plotted according to elevation, there are no clear differences in frozen or dry bulk density between terrain classifications. Porosity and gravimetric water content tend to be highly variable within the top meter of the tundra surface and become less variable with depth.

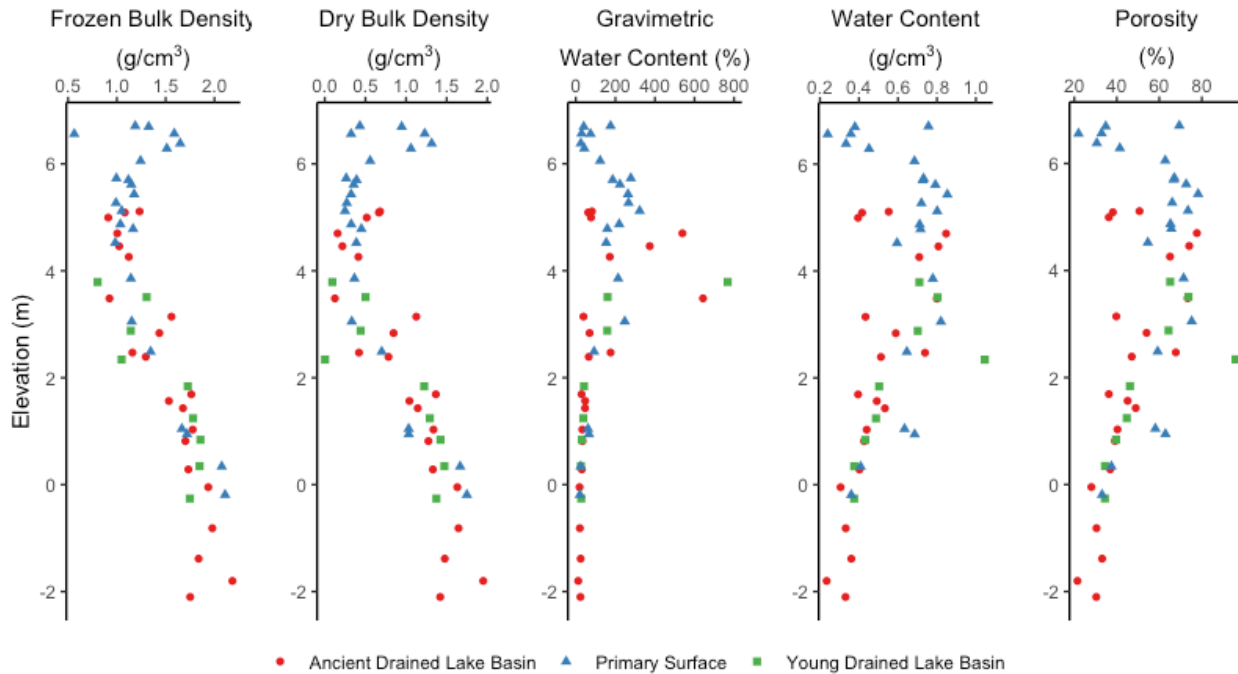


Figure 3.3-1. Down core profiles of frozen bulk density, dry bulk density, gravimetric water content, soil water content, and estimated porosity. Color and symbol indicate the terrain classification of the sample. One sample that was mostly ice is not shown in the gravimetric water content plot due to its high value (37,350 %).

For the four samples that had wet and dry weight measurements but no volume measurements to calculate frozen bulk density, we modeled frozen bulk density by assuming the particle bulk density of soil/sediment (ρ_{sed}) is 2.65 g cm^{-3} and the density of ice (ρ_{ice}) is 0.917 g cm^{-3} . Then, frozen bulk density (g cm^{-3}) was estimated from the dry sediment mass (m_{sed} ; g) and ice mass (m_{ice} ; g):

$$\text{Frozen bulk density} = \frac{m_{ice} + m_{sed}}{\frac{m_{ice}}{\rho_{ice}} + \frac{m_{sed}}{\rho_{sed}}} \quad \text{Equation 3.3-2}$$

For data where we had direct measurements of frozen bulk density, modeled frozen bulk density values generally showed close agreement (Figure 3.3-2).

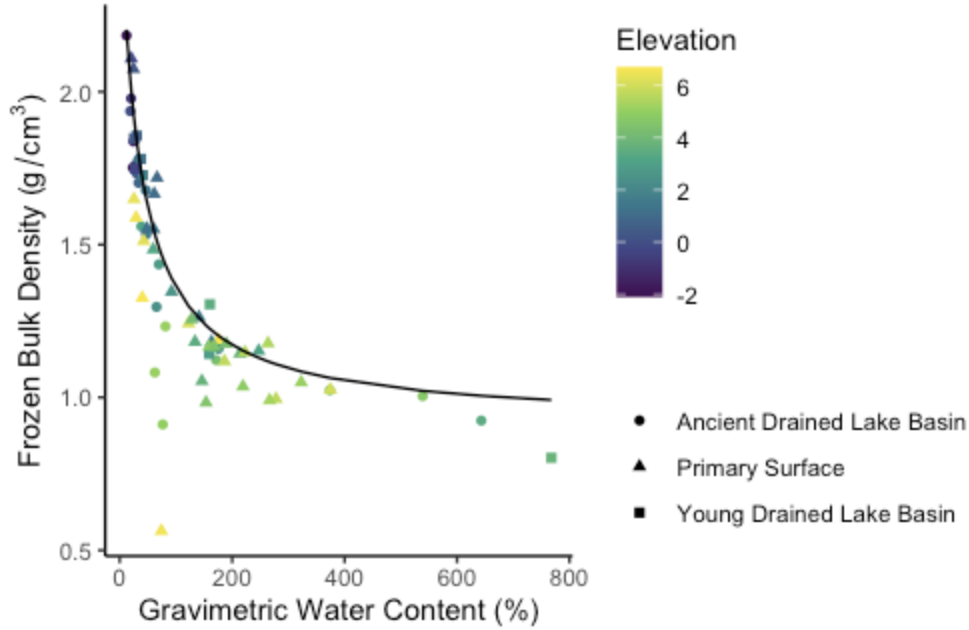


Figure 3.3-2. Comparison of modeled and measured frozen bulk density values. Data points represent core sections that had both water content and volume measurements. The color of the data points represents the elevation (m) of the sample, and the symbols represent the terrain unit. The black line is the modeled frozen bulk density as a function of gravimetric water content (i.e. wet mass and dry mass).

For a subset of 16 samples used for geomechanical testing (Section 3.5), we had wet and dry weight measurements to calculate gravimetric water content, but no volume measurement to calculate porosity. We developed two different methods to model porosity from gravimetric water content. Similar to the model for frozen bulk density, the first porosity model estimates the volume of the solid/dry fraction by assuming the particle bulk density of soil/sediment (ρ_{sed}) is 2.65 g cm^{-3} , so that

$$porosity (\%) = \frac{V_{ice}}{V_{total}} \times 100 = \frac{m_{ice} \times \rho_{ice}}{(m_{ice} \times \rho_{ice}) + (m_{sed} \times \rho_{sed})} \quad \text{Equation 3.3-3}$$

where m_{ice} is the mass of water loss during drying, m_{sed} is the mass of dry soil/sediment remaining after drying, and the density of ice (ρ_{ice}) assumed to be 0.917 g cm^{-3} . To check the accuracy of these assumptions, we compared modeled porosity with measured porosity for samples where we had known porosity measurements. This model overestimated porosity for our core samples, especially for samples with higher gravimetric water content (Figure 3.3-3). Porosity may have been overestimated because this first model did not account for peat, which has a much lower particle bulk density than we assumed for mineral sediments. We expect this first model to be most accurate in mineral sediments at depth, rather than organic-rich sediments or soils at the surface that may not be fully saturated. These results led us to develop a second porosity model where we modeled porosity as a function of gravimetric content using a power curve fit to our measured porosity data. The equation for this model is

$$porosity (\%) = -176.6 \text{ GWC}^{-0.2391} + 115.4 \quad \text{Equation 3.3-4}$$

where GWC is the gravimetric water content (%). This curve is a similar shape to our first model, but fits our data more closely (Figure 3.3-3).

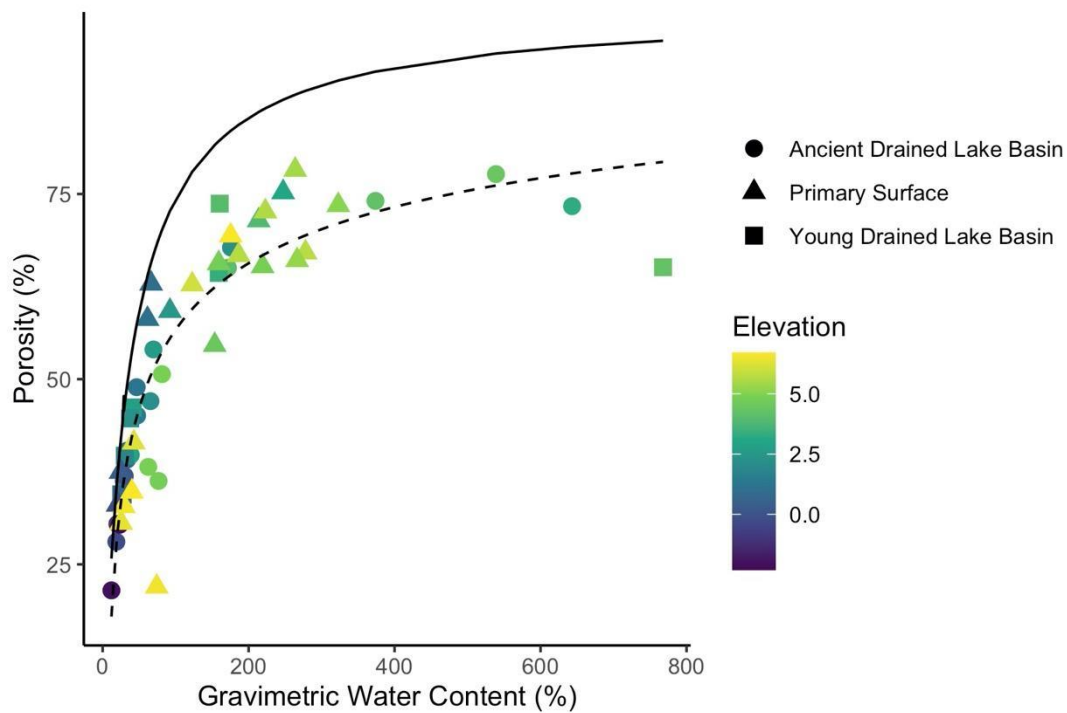


Figure 3.3-3. Porosity (%) as a function of gravimetric water content (%). Data points indicate the measured porosity for samples with a volume measurement. Data point shape indicates the terrain classification and the color scale indicates the elevation (m) of the sample. The first model method, which uses the particle bulk density of soil/sediment to estimate porosity, is shown as a solid line. The second model method, which fits a power curve to the data points, is shown as a dashed line.

Porosity was modeled as a function of elevation for each of the terrain classifications, where elevation has units of meters and porosity is unitless and expressed as a percent (Figure 3.3-4). Only data from samples above sea level were used in the following three models. Based on trends in the data, where porosity was lowest near sea level and at the surface, we chose to use a second-order or third-order regression model (Table 3.3-1). Reported R^2 values are adjusted for the number of predictors (Table 3.3-1).

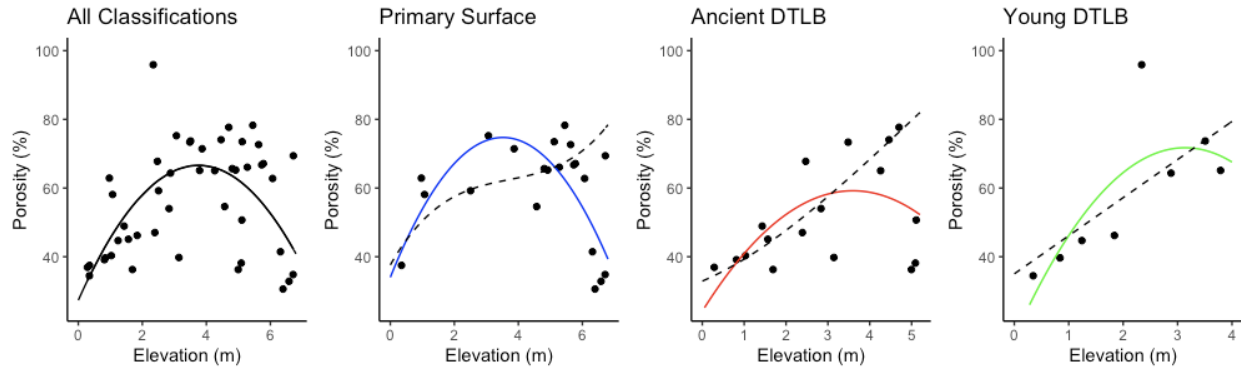


Figure 3.3-4. Porosity as a function of elevation for data above sea level. Solid lines show modeled porosity using a second order polynomial. The high porosity value in the Young DTLB figure was a sample that was nearly completely ice. Dashed lines show third order polynomial fits for the Primary Surface and Ancient DTLB, and a linear fit for DP2 that were used in initial model runs to assess model skill (Section 5.3.3).

Table 3.3-1. Model coefficients for models shown in Figure 3.3-4 (above). In form $y = a + bx + cx^2 + dx^3$, where x is elevation (m) and y is porosity (%).

Terrain Classification	Order	a	b	c	d	Adjusted R2
All	2	27.3318	20.9107	-2.7830	0	0.3325
Primary Surface	2	34.007	23.144	-3.289	0	0.4131
Ancient DTLB	2	24.150	19.494	2.710	0	0.2162
Young DTLB	2	16.598	16.598	-5.603	0	0.4375
Primary Surface	3	37.59971942	16.354346	-3.9010825	0.3498266	
Ancient DTLB	3	32.90534182	5.24687712	1.23323968	-0.08212388	
Young DTLB	1	35.02119934	11.09098594	0	0	

Since porosity tends to be more variable in the top ~0.5 m of soil, approximately the depth of the seasonally thawed active layer, we also modeled porosity using data above sea level but below a depth of 0.5. Linear fits were used to model data from all terrain classifications combined, as well as from the individual terrain classifications, see Figure 3.3-5 and Table 3.3-2. In the top 0.5 m of soil, porosity averages 45.0% with a standard error of 5.2% (n = 11).

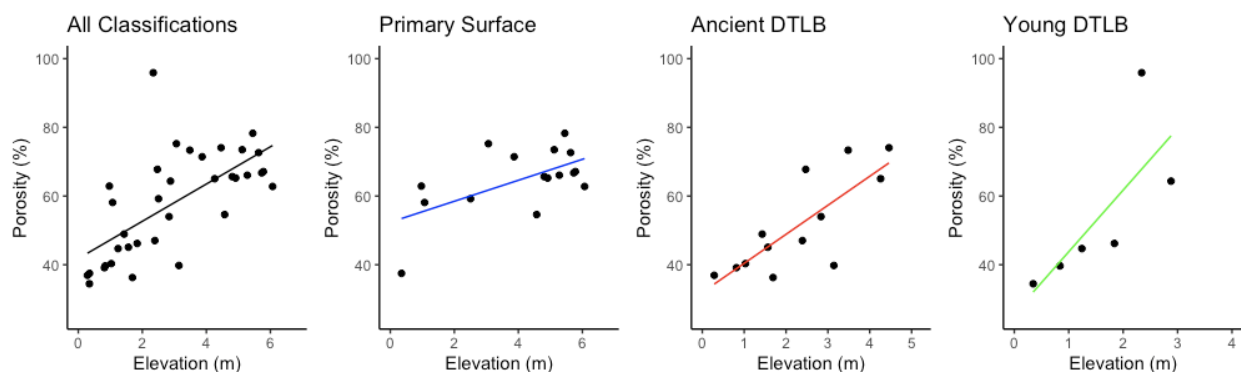


Figure 3.3-5. Porosity as a function of elevation, for permafrost above sea level and below a depth of 0.5 m. All models are linear fits. The high porosity value in the Young DTLB figure was a sample that was nearly completely ice.

Table 3.3-2. Model coefficients for models shown in Figure 3.3-5 (above). Equations are in the form $y = a + bx$ where x is elevation (m) and y is porosity (%).

Terrain Classification	Order	a	b	Adjusted R2
All	1	41.800	5.424	0.4215
Primary Surface	1	52.376	3.052	0.3094
Ancient DTLB	1	40.293	3.729	0.1154
Young DTLB	1	25.821	17.951	0.4509

Grain sizes were determined using a hydrometer method at Oregon State University. On average, soils/sediments were 23% sand, 45% silt, and 31% clay (Figure 3.3-6), with no notable trends in grain size downcore when data from all terrain classifications were grouped together. We fit linear models to sand, silt, and clay fractions as a function of elevation for data above sea level for each terrain classifications (Figure 3.3-7 and Table 3.3-3). When individual terrain classifications are considered, downcore trends vary slightly; e.g. the sand fraction decreases and clay fraction increases with depth in the ancient drained lake basin, but the opposite trend appears to occur in the young drained basin. Higher-order fits could also be used / necessary to obtain more realistic mixture models of frozen bulk density for instance (see Section 3.4).

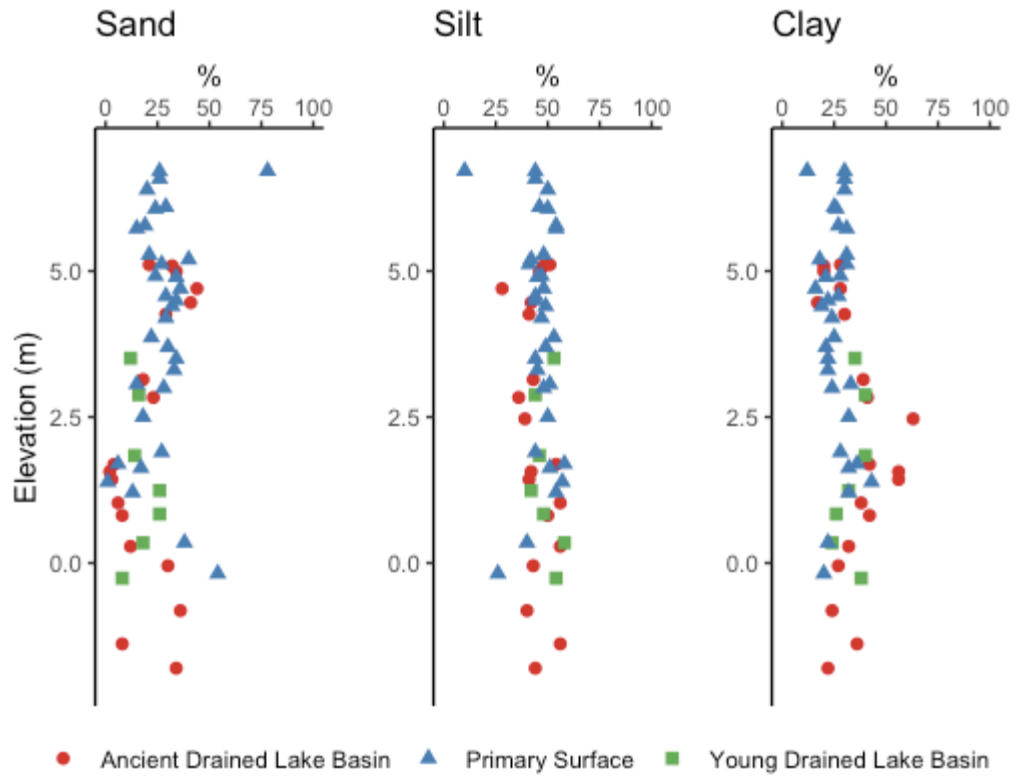


Figure 3.3-6. Downcore profiles of sand, silt, and clay fractions (%). Color and symbols indicate the terrain classification of the sample.

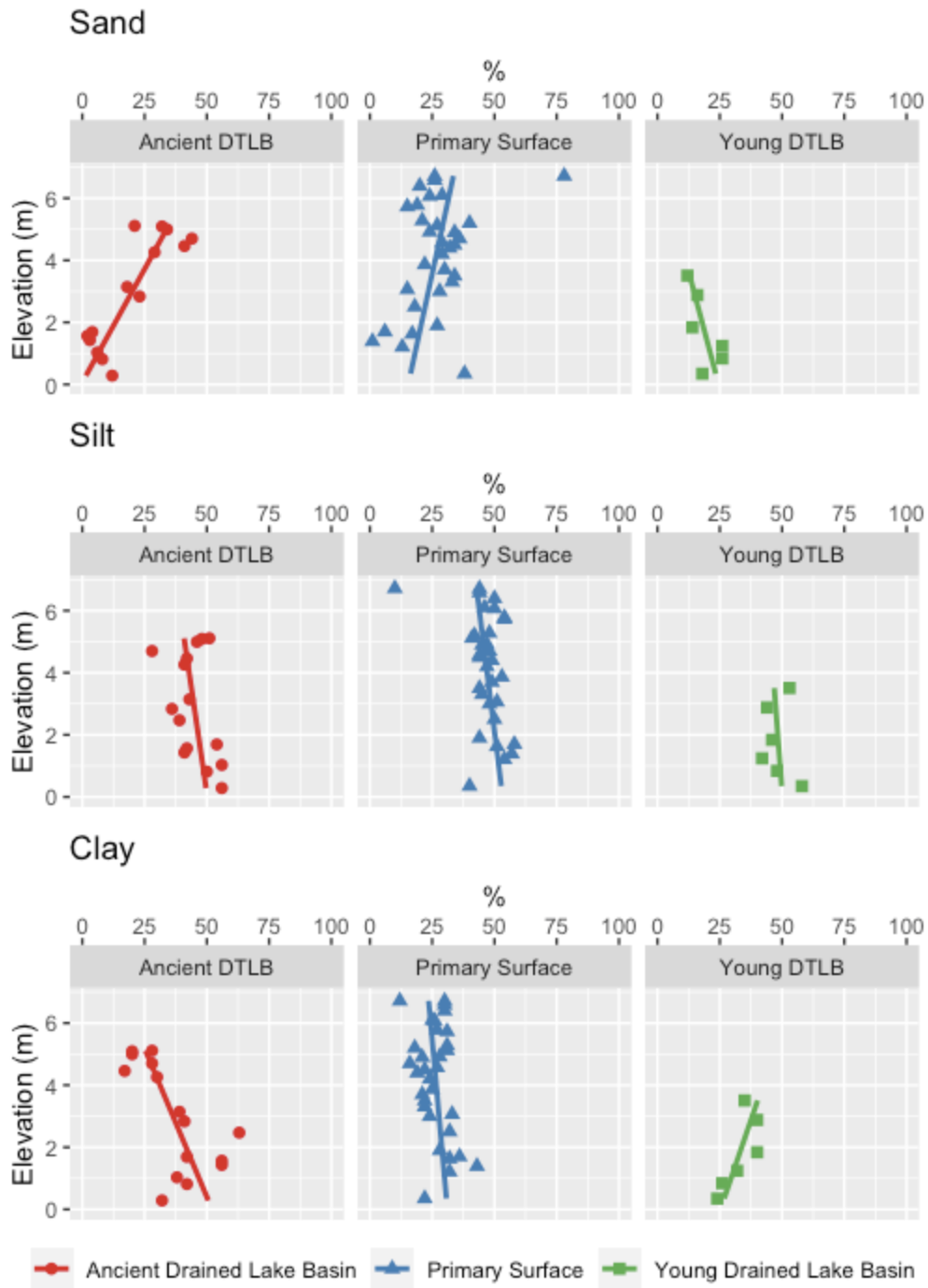


Figure 3.3-7. Linear models of grain fraction by elevation for data above sea level, in each of the terrain classifications.

Table 3.3-3. Coefficients for linear models of grain fraction. Equations are in the form $y = a + bx$ where x is elevation (m) and y is the grain fraction (%).

Terrain Classification	Sand		Clay		Silt	
	a	b	a	b	a	b
Ancient DTLB	-2.2178868	7.04844855	52.0885488	-5.2265565	50.2277657	-1.8327499
Young DTLB	24.5531799	-3.3146337	25.2783702	4.25412031	50.1684499	-0.9394866
Primary Surface	15.3798852	2.69940744	31.1098622	-1.1194243	53.3027167	-1.561118

The peat fraction was estimated by doubling the organic carbon content (Pribyl 2010). The estimated peat fraction data were fit with a family of generalized logistic curves, which give the peat fraction (in percent) with bluff depth (absolute elevation in this case).

$$P(z, z_c) = A + \frac{K - A}{(C + Qe^{B(z-z_c)})^{1/v}}$$

Equation 3.3-5

The values of the equation parameters control the general shape of the curve. The values chosen for the parameters are:

Parameter:	v	K	C	Q	B	Zc
Value:	4.0	2.3	1.0	1.0	9.0	3.5

The parameter that controls how far the curve gets stretched towards higher peat fractions at the surface is A. Based on the organic content analysis, the following parameters were chosen to represent A: 20 for Primary Surface, 38 for the ancient DTLB, and 93 for the young DTLB (see Figure 3.3-8). Furthermore, A can be varied in sensitivity studies to inform how the insulating properties of peat affect erosion rates.

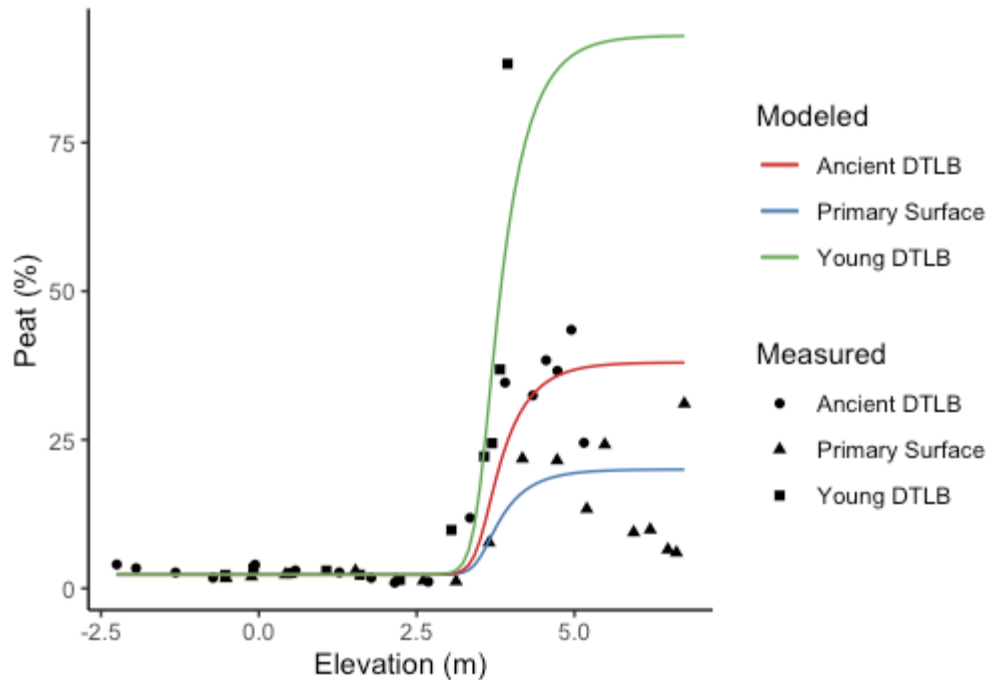


Figure 3.3-8. Peat fraction modeled as a function of elevation for each terrain classification. Points represent measured data, and lines represent the peat model. Peat (% by weight) was assumed to be twice the total organic carbon content (% by weight).

Porewater salinity (see Figure 3.3-9) was also modeled as a function of elevation using a logistic curve with the following equation:

$$y = \frac{36.840}{1 + e^{1+1.110(x-0.657)} + 0.058} \quad \text{Equation 3.3-6}$$

where y is the porewater salinity and x is the elevation (m).

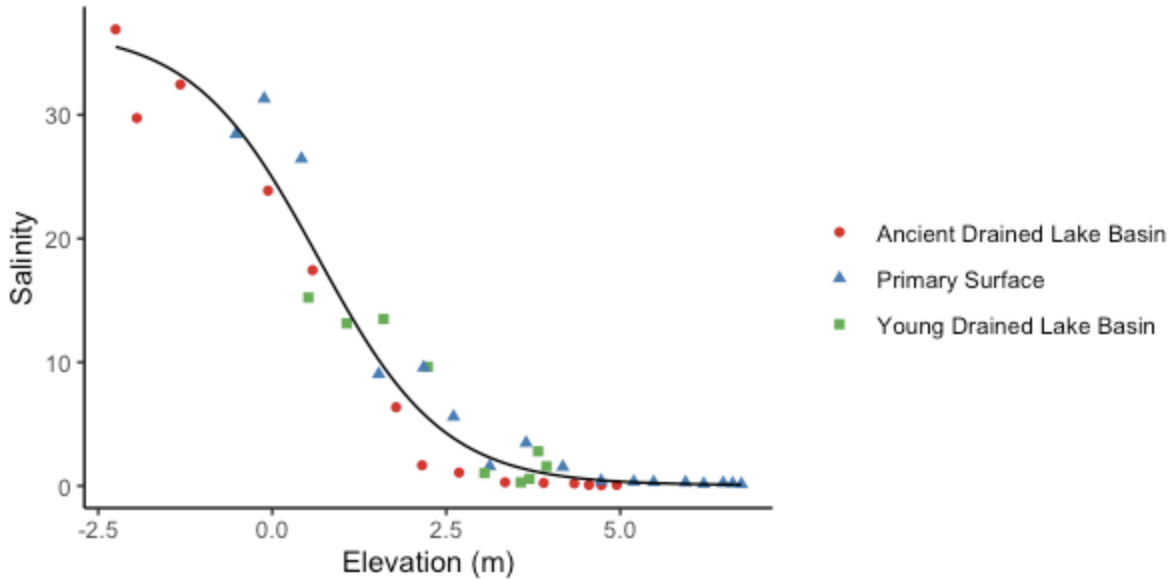


Figure 3.3-9. Salinity as a function of elevation. Measured porewater salinity is represented by data points, coded by color and shape to indicate terrain classification.

3.4. Thermal Properties

Team Member Author: Jennifer Frederick (SNL)

Contributors: Emily Bristol (UTA)

Using the experimentally determined material properties above for each terrain unit, high order fits were obtained with the express goal of matching the frozen bulk density using a mixture model of the underlying constituents (sediment, peat, and porosity) as accurately as possible. By achieving a good match between the mixture model constructed frozen bulk density and the experimentally measured bulk density, there is greater confidence that the other thermally derived properties (conductivity and specific heat) from the mixture models dependent upon the same constituents would also then be most accurate. Figure 3.4-1 through Figure 3.4-19 below detail best fits and resultant mixture models for each of the characterized cores.

Details of the thermal mixture model can be found in Section 4.3.3.2.

3.4.1. Ancient Drained Thermokarst Lake Basin

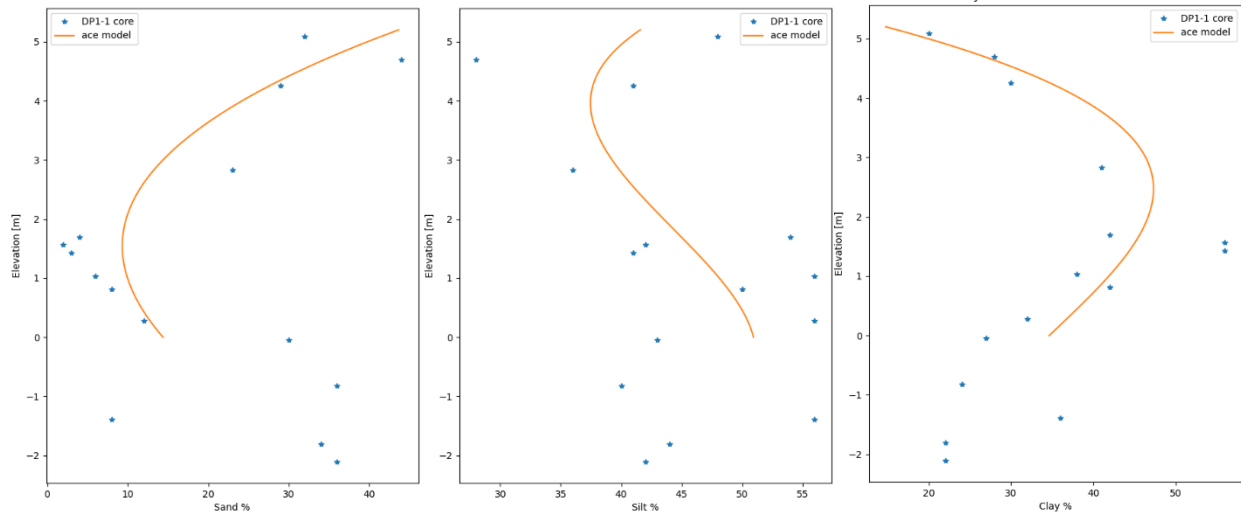


Figure 3.4-1. Measured sediment constituent fraction in the Ancient DTLB as a function of elevation with overlaying high-order fit for: a) sand, b) silt, and c) clay.

The equations for the fits used for sand, silt, and clay fractions for the ACE Ancient DTLB model are, as a function of bluff elevation, d ,

$$F_{sand} = 0.08407976d^3 + 1.86839231d^2 - 6.36727965d + 14.40651536 \quad \text{Equation 3.4-1}$$

$$F_{silt} = 0.35497644d^3 - 1.95635631d^2 - 1.22542844d + 50.94603553 \quad \text{Equation 3.4-2}$$

$$F_{clay} = -0.4390562d^3 + 0.087964d^2 + 7.59270809d + 34.64744911 \quad \text{Equation 3.4-3}$$

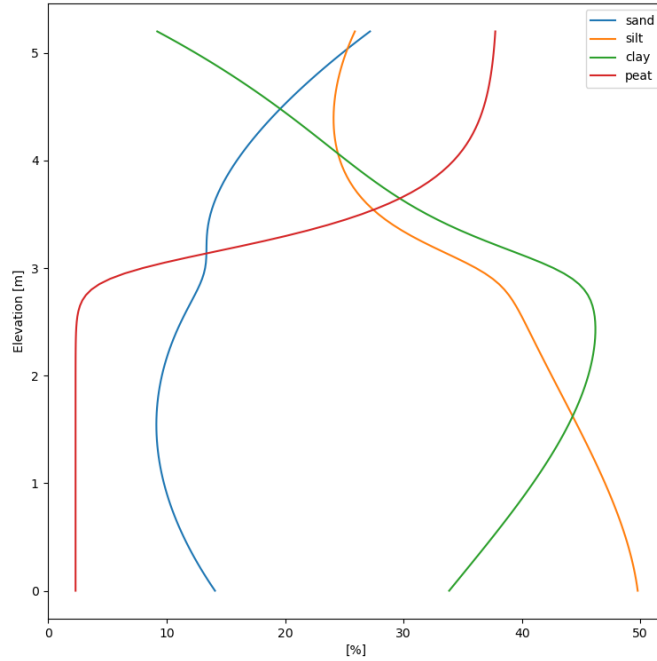


Figure 3.4-2. Model of soil constituents in the Ancient DTLB as a function of elevation, including peat.

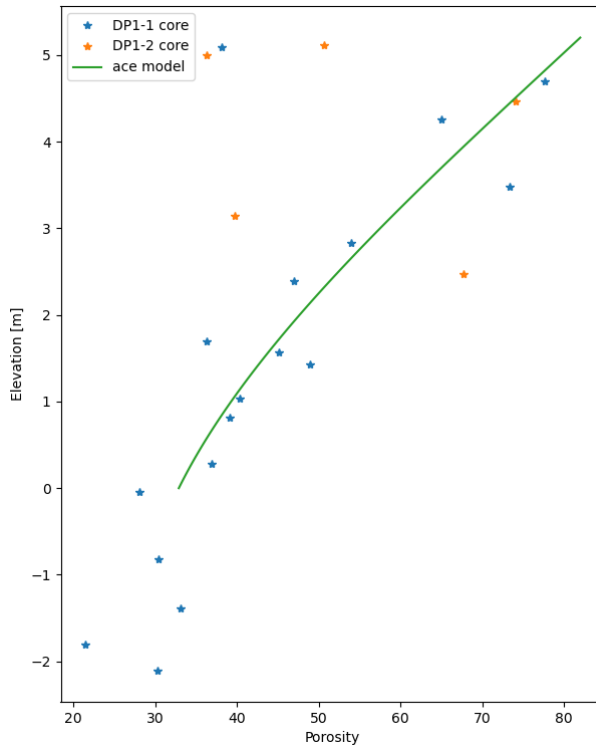


Figure 3.4-3. Measured porosity in the Ancient DTLB as a function of elevation with overlaying high-order fit. (fit details given in Table 3.3-1).

The equation for the fit used for porosity for the ACE Ancient DTLB model is, as a function of bluff elevation, d ,

$$\phi = -0.08212388d^3 + 1.23323968d^2 + 5.24687712d + 32.90534182 \quad \text{Equation 3.4-4}$$

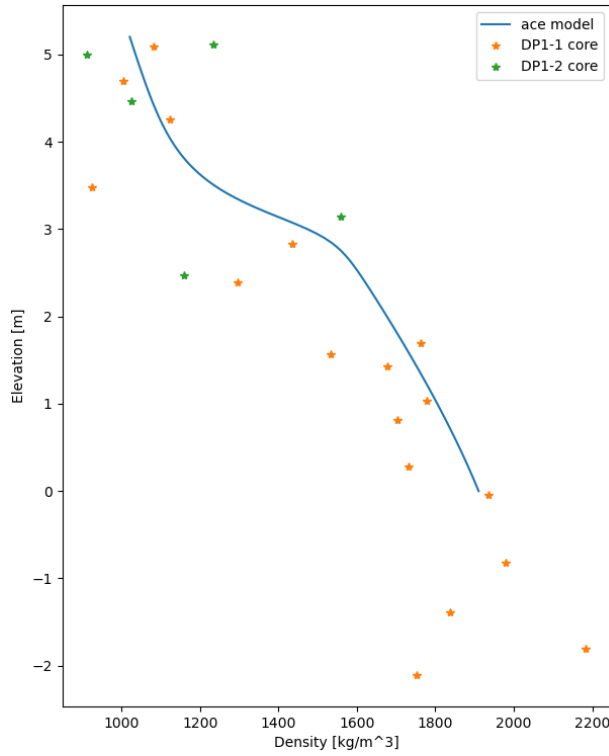


Figure 3.4-4. Model of frozen bulk density, at -20C, constructed from the model of soil constituents (Figure 3.4-2) and porosity (Figure 3.4-3.) overlaid on top of the experimentally obtained values. Visually, the models of underlying constituents are working very well as the solid line bisects the experimental data.

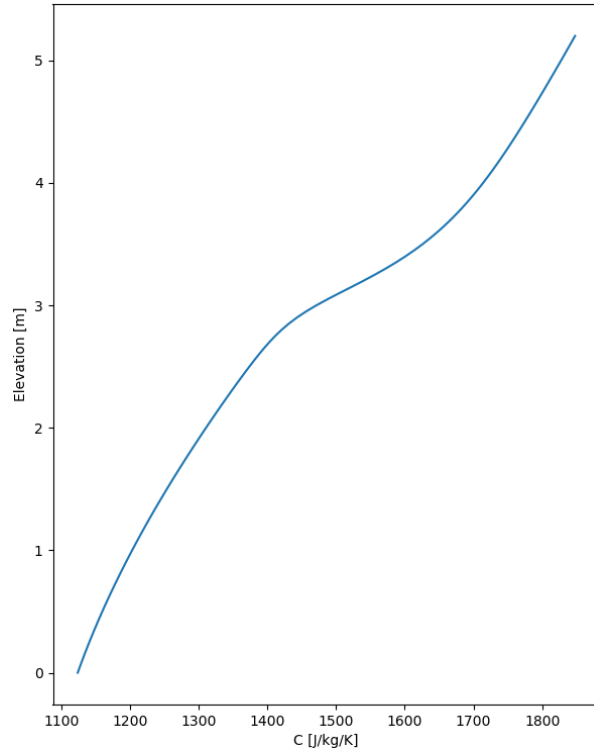


Figure 3.4-5. Model of fully frozen Ancient DTLB permafrost soil's specific heat capacity at -20C.

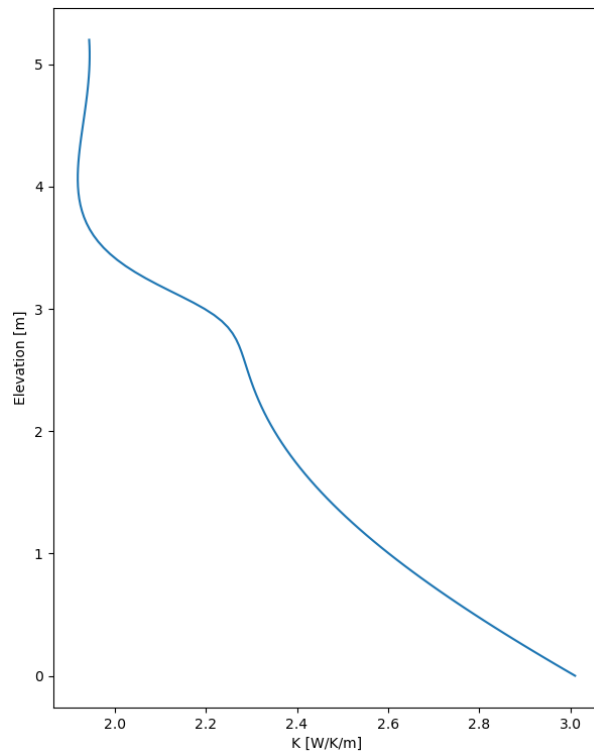


Figure 3.4-6. Model of fully frozen Ancient DTLB permafrost soil's thermal conductivity at -20C.

3.4.2. Young Drained Thermokarst Lake Basin

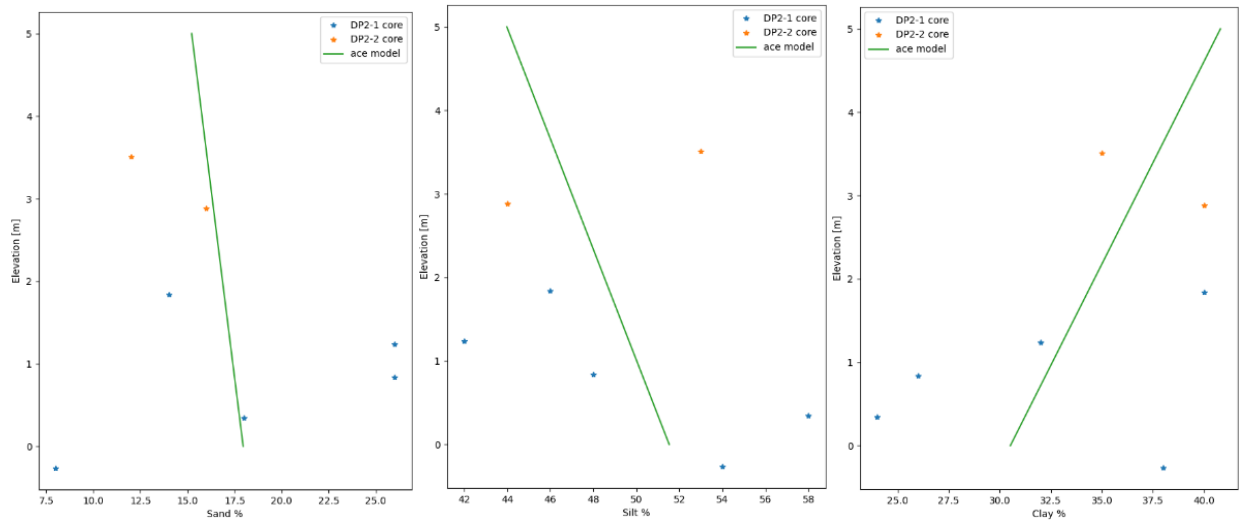


Figure 3.4-7 Figure 3.4-8 Measured sediment constituent fraction in the Young DTLB as a function of elevation with overlaying high-order fit for: a) sand, b) silt, and c) clay.

The equations for the fits used for sand, silt, and clay fractions for the ACE Young DTLB model are, as a function of bluff elevation, d ,

$$F_{sand} = -0.54670804d + 17.95475763 \quad \text{Equation 3.4-5}$$

$$F_{silt} = -1.50964697d + 51.52764787 \quad \text{Equation 3.4-6}$$

$$F_{clay} = 2.05635501d + 30.5175945 \quad \text{Equation 3.4-7}$$

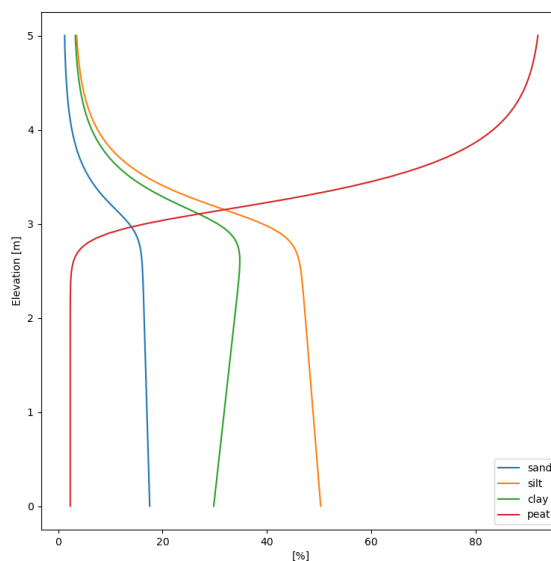


Figure 3.4-9. Model of soil constituents in the Young DTLB as a function of elevation, including peat.

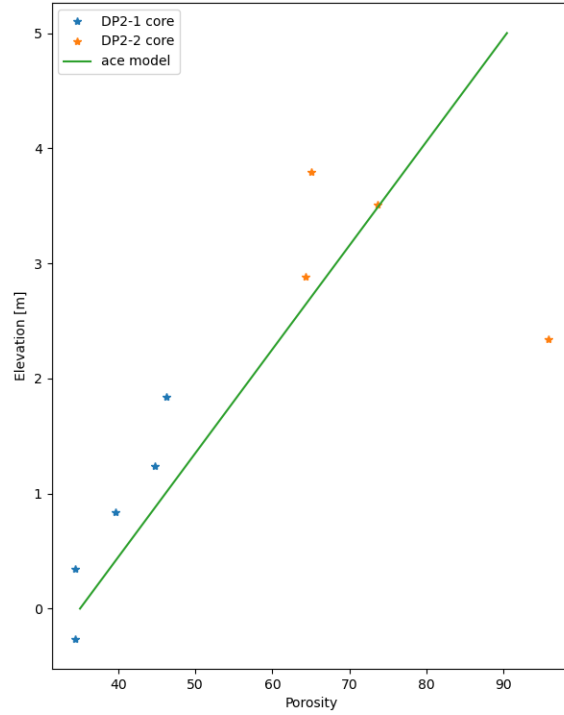


Figure 3.4-10. Measured porosity in the Young DTLB as a function of elevation with overlaying high-order fit. (fit details given in Table 3.3-1).

The equation for the fit used for porosity for the ACE Young DTLB model is, as a function of bluff elevation, d ,

$$\phi = 11.09098594d + 35.02119934 \quad \text{Equation 3.4-8}$$

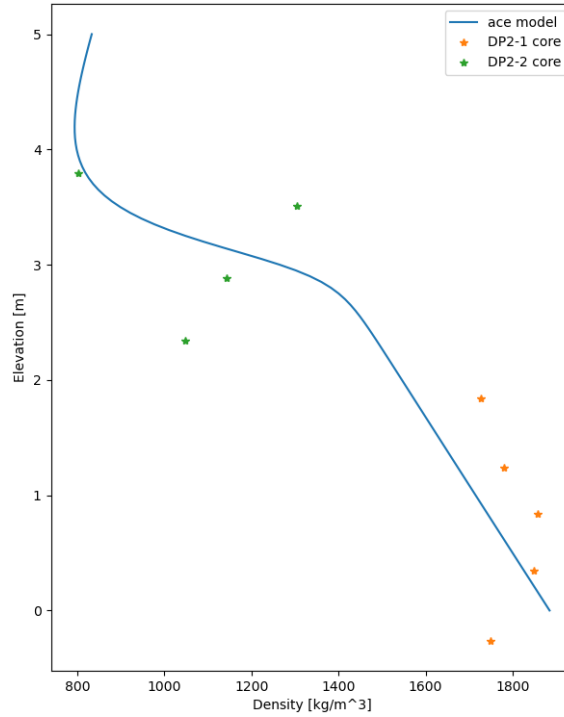


Figure 3.4-11. Model of frozen bulk density, at -20C, in the Young DTLB constructed from the model of soil constituents (Figure 3.4-2) and porosity (Figure 3.4-3.) overlaid on top of the experimentally obtained values. Visually, the models of underlying constituents are working very well as the solid line bisects the experimental data.

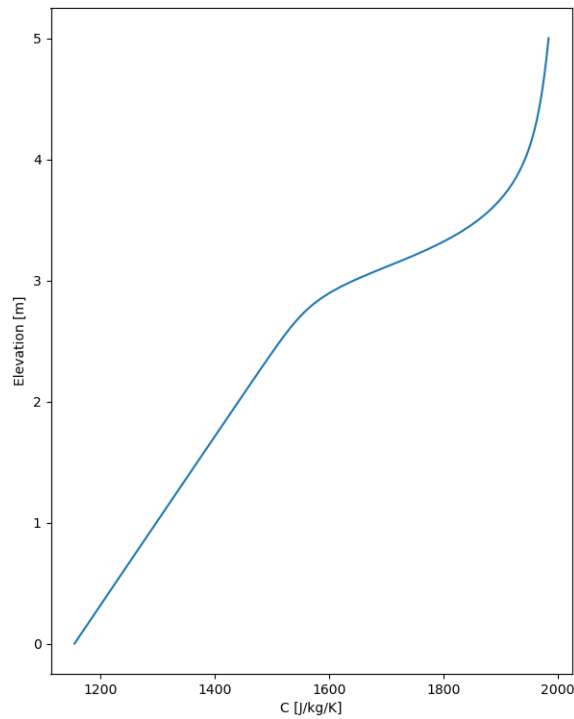


Figure 3.4-12. Model of fully frozen Young DTLB permafrost soil's specific heat capacity at -20C.

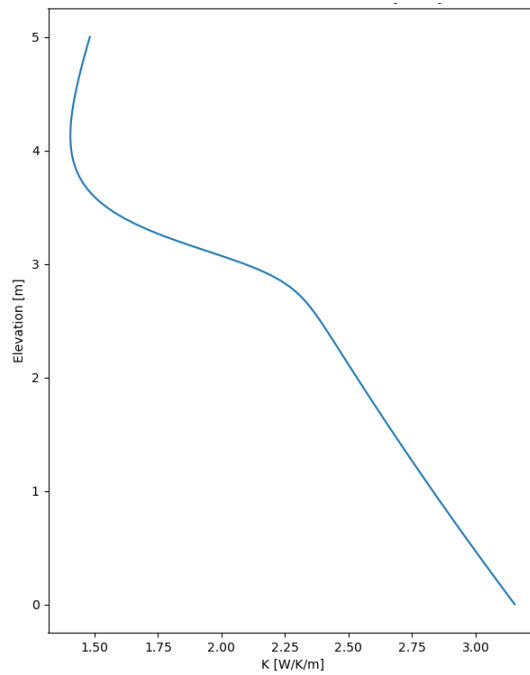


Figure 3.4-13. Model of fully frozen Young DTLB permafrost soil's thermal conductivity at -20C.

3.4.3. Primary Material

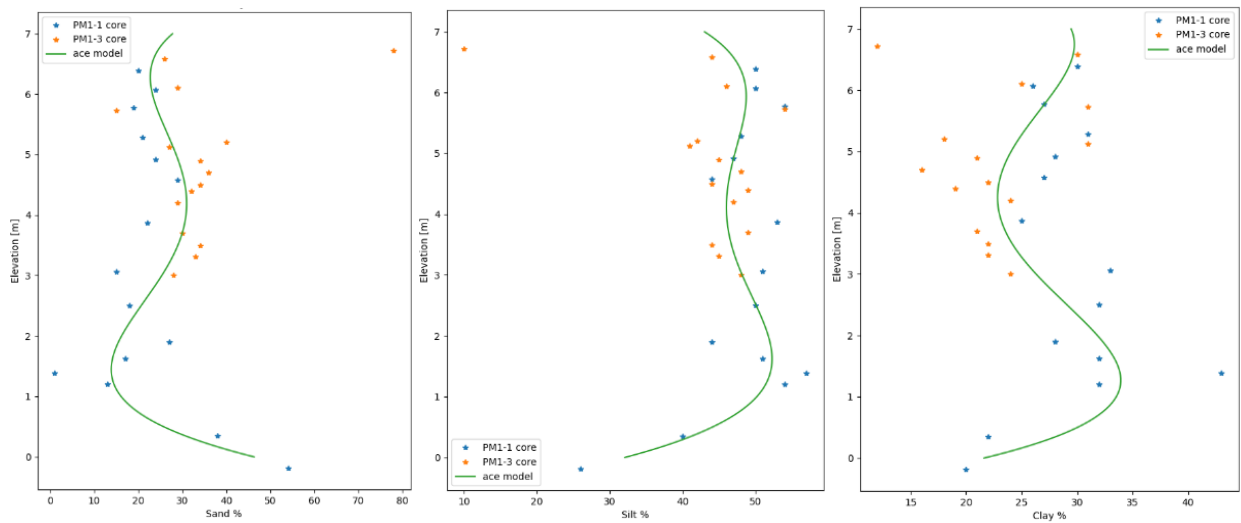


Figure 3.4-14. Measured sediment constituent fraction in the Primary Material as a function of elevation with overlaying high-order fit for: a) sand, b) silt, and c) clay.

The equations for the fits used for sand, silt, and clay fractions for the ACE Primary Material model are, as a function of bluff elevation, d ,

$$F_{sand} = 0.35887331d^4 - 5.7016609d^3 + 29.75138961d^2 - 54.6143397d + 46.30057453$$

Equation 3.4-9

$$F_{silt} = -0.1979451d^4 + 3.0801856d^3 - 16.115833d^2 + 31.3375013d + 32.077125$$

Equation 3.4-10

$$F_{clay} = -0.1574204d^4 + 2.575292d^3 - 13.4278558d^2 + 22.92203d + 21.615307$$

Equation 3.4-11

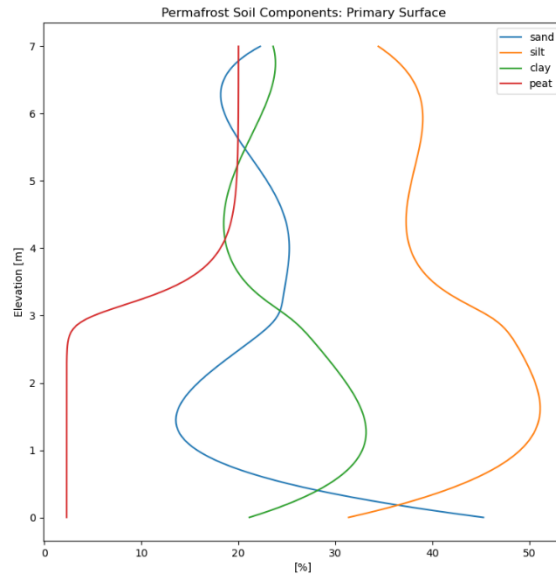


Figure 3.4-15. Model of soil constituents in the Primary Material as a function of elevation, including peat.

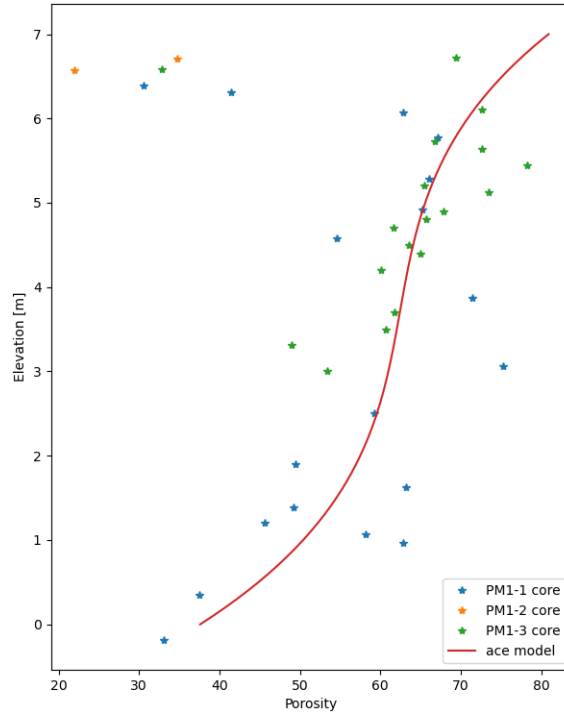


Figure 3.4-16. Measured porosity in the Primary Material as a function of elevation with overlaying high-order fit. (fit details given in Table 3.3-1).

The equation for the fit used for porosity for the ACE Primary Material model is, as a function of bluff elevation, d ,

$$\phi = 0.3498266d^3 - 3.9010825d^2 + 16.354346d + 37.59971942 \quad \text{Equation 3.4-12}$$

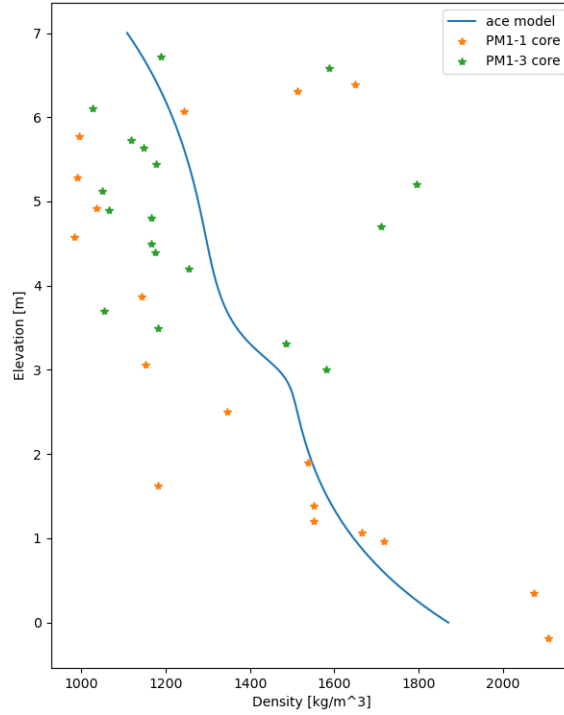


Figure 3.4-17. Model of frozen bulk density, at -20C, in the Primary Material constructed from the model of soil constituents (Figure 3.4-2) and porosity (Figure 3.4-3.) overlaid on top of the experimentally obtained values.

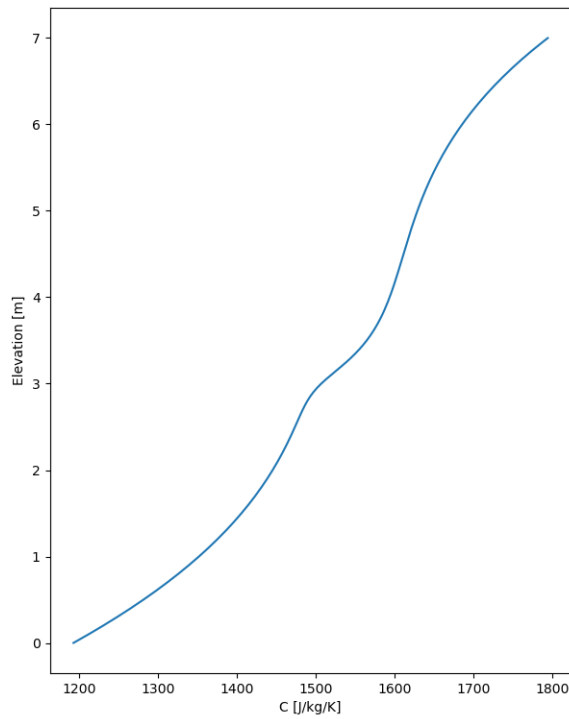


Figure 3.4-18. Model of fully frozen Primary Material permafrost soil's specific heat capacity at -20C.

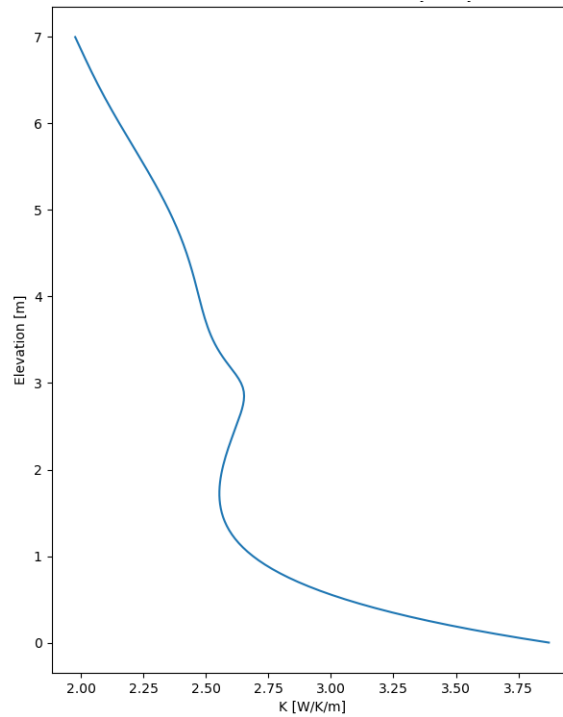


Figure 3.4-19. Model of fully frozen Primary Material permafrost soil’s thermal conductivity at -20C.

3.5. Physical Strength Properties

Team Member Author: Charles Choens (SNL)

Contributors: Emily Bristol (UTA), Jennifer Frederick (SNL), Alejandro Mota (SNL), Matt Thomas (USGS), Diana Bull (SNL)

3.5.1. Introduction

To predict the behavior of permafrost bluffs at the coast off Drew Point, Alaska, the integrated ACE model will incorporate material models of frozen soil with atmospheric conditions and oceanographic forcing to simulate coupled thermal-mechanical-erosive behavior. Integral to the material model in ACE are physical strength properties like failure strength and elastic moduli. Due to the observed failure and environmental conditions of cliff faces in the field, we are interested populating this model using tensile behavior for permafrost cores at near melting temperatures. Frozen soils are highly heterogeneous mixtures of soil and ice, and material models should be based on experimental observations. The majority of published studies focused on the behavior of ice or remolded frozen soils (Hanyes, 1973; Haynes and Karalius, 1977; Haynes et al., 1975; Hawkes 1969; Xu et al., 2017; Yamamoto and Springman, 2017; Yuanlin and Carbee, 1984; Yuanlin and Carbee, 1987; Zhou et al., 2015; Zhou et al., 2018) A previous study at SNL had investigated the behavior of intact frozen soil, however, these experiments were conducted on shallow cores at colder temperatures (Lee et al., 2002). To define the physical strength properties for material models in the terrestrial model, we conducted a series of geomechanics experiments on frozen soil samples

collected during field coring campaigns (Section 3.1) to determine failure properties, elastic moduli, and appropriate rheological models.

We conducted a series of different geomechanical experiments on cores from two different land surfaces on three different ice contents at three different temperatures near melting. We conducted unconfined compressive strength, UCS, experiments to measure behavior in compression; and we conducted direct tension, DT, and Brazilian tensile strength, BTS, experiments to measure the behavior in tension. In rocks, UCS tests are simple tests that produce high quality results. In frozen soils, preparation of experimental samples while controlling environmental conditions complicates any testing, but this style of testing produces the most consistent results. The tensile experiments are the bulk of testing as Drew Point cliff bluffs are failing in tension. DT tests can measure mechanical properties in tension, but this style of testing is very sensitive to grain structures and heterogeneities in geomaterials and can produce variable results. These tests also require the largest section of core and the most labor to produce an experimental sample, but they are the only type of testing that can measure elastic moduli in tension. BTS experiments are common experiments that can reliably measure tensile strength but not elastic moduli. The combination of the three different types of geomechanics tests provide insight to the mechanical properties that will be controlling bluff failure at Drew Point, Alaska. It is our hypothesis that ice will be a controlling factor in the strength of frozen soil. Since, soil is a cohesionless material; ice provides the cementation to withstand tensile stresses. We hypothesize that the total amount of ice present in a sample will control the strength, and temperature will act to modify ice content.

3.5.2. Methods

Experiments were conducted using cores of frozen soil from Drew Point, Alaska, that were collected during the FY18 core campaigns, see Section 3.1. The cores were initially stored at the University of Alaska Fairbanks before they were shipped to Sandia in FY18. Cores were inspected and visually classified as high, medium, and low ice content based on the presence of observable ice crystals. In general, cores with sections of large ice crystals or persistent ice veins/lensing were classified as high ice, and cores that appeared to be solidified soil with imperceptible crystals were classified as low ice. Samples that were in between were classified as medium ice content. Cores for geomechanical testing were stored in a residential chest freezer that maintained the temperature at approximately -18°C without freeze/thaw cycles. Three different sample geometries were used for the three different types of geomechanics tests. For UCS tests, samples were prepared into cylinders; for DT tests, cylinders with a necked midsection with a constant diameter (also known as a “dogbone” geometry); for BTS tests, short cylindrical discs (Figure 3.5-1a, c, e).

To machine cylindrical samples for UCS tests, sections of cores were cut into rectangular blanks slightly larger than the desired sample diameter using a bandsaw. Offcuts from the core were preserved for material property investigations, see Section 3.3. After the samples were prepared into rectangular blanks, they were turned into cylindrical samples on a metalworking lathe using a precision surface grinder with a steel bristle wire brush mounted onto the tool holder. Samples were held in place using plastic jigs with soft rubber faces and sanding sponges to form a deformable surface that could grip samples. During machining, the freezing temperatures in the samples were maintained with liquid nitrogen. A prepared sample is shown in Figure 3.5-1a. After the samples were machined to the desired diameter, they were dimensioned and weighed for density calculations and affixed to the endcaps using the pressure melting phenomena (Lee et al., 2002). Samples were placed on a jig made from a length of angle iron on a V block. Samples were placed in between the endcaps on the angle iron. One endcap was flush against a fixed stop, and the other endcap had a

~1" gap from another fixed stop. A stiff spring was placed in the gap to put the sample and endcaps under compression, causing pressure melting at the sample-end cap interfaces. This lightly adhered the samples to the endcaps and ensured the ends of the sample were parallel to one another and perpendicular to the cylindrical axis. Samples were loosely jacketed using a layer of thin latex.

The initial machining steps of dogbone samples for DT tests followed the methodology for UCS sample preparation. After the samples were machined into cylinders and measured for density, the necked diameter was created using an angle grinder with a steel bristle wire brush mounted onto the tool holder of the lathe. The angle grinder was advanced into the sample to the desired diameter, and then translated along the length of the sample to create a necked section with a constant diameter. A prepared sample is shown in Figure 3.5-1c. The ends of the samples were frozen into aluminum endcaps with additional water and instrumented with axial and radial lvdts.

For BTS samples, the ends of the cores were squared using the bandsaw. The cylindrical surface of the core was ground smooth using the precision surface grinder on the lathe, and the core was cut into ~25mm thick discs on the bandsaw. A prepared sample is shown in Figure 3.5-1e. Density was measured on the intact core prior to cutting discs.

Experiments were conducted in an environmental chamber on a servohydraulic load frame with a 22,000 lbf capability. The chamber was capable of temperatures from -60° to 150°C while maintaining temperatures within $\pm 0.25^\circ\text{C}$ for a period of time. The environmental chamber generated cryogenic temperatures using an attached dewar of liquid nitrogen and an internal circulation fan. Experiments were conducted at targeted temperatures of -6, -3, and -1°C, but setting the initial temperature was difficult due to the coarse analog controls. Temperatures also occasionally shifted by 0.5°C during extended use. Temperatures for the chamber and the data recording system were calibrated using a NIST traceable thermocouple meter. Reported sample temperatures are an average temperature in the chamber during equilibration and testing. Initial experiments in the chamber used buckets of ice and salt solutions mixed to freeze at desired temperatures to increase the thermal mass in the environmental chamber and stabilize the temperature. However, for experiments conducted in the summer months, the increased atmospheric humidity caused the environmental chamber to malfunction, and the additional thermal mass was replaced with an open beaker of Drierite to prevent condensation from frosting over the liquid nitrogen inlet. Samples were placed in a precooled chamber for 4-6 hours to allow the temperature in the sample to equilibrate to the desired test conditions. The bottom loading platen had significant thermal mass and the hydraulic ram conducted heat into the chamber, so samples would be stored off the platen in the chamber on insulation during thermal equilibration. The sample would be installed into the loading column right before testing to prevent the sample from melting.

UCS experiments were conducted at a constant axial displacement rate of 0.019 mm/sec. Axial displacement was measured using 2 axial lvdts with a maximum 6.35 mm stroke and a radial displacement with a lvdt with a maximum 2.54 mm stroke. Axial lvdts were attached to the samples using rings that were held to the endcaps with screws. Radial displacement was measured with a spring mounted circumferential chain gauge. A spherical seat was attached to the load column above the sample, helping prevent any off-axis loading effects that might have occurred due to the difficulty in preparing samples. For testing, the sample was placed on a ceramic spacer on the loading platen for testing. The top of the sample had an additional steel spacer between the endcap and the spherical seat (Figure 3.5-1b). These spacers help prevent diffusion of heat from the loading column into the sample.

DT experiments were conducted using a constant axial displacement of 0.19 mm/sec, applied in tension. Experiments were conducted at a faster rate than UCS tests to prevent the heat from the hydraulic ram from melting the sample-endcap bond. Samples used the same instrumentation as UCS samples. The axial lvdt rings had guide rods in low friction bushings that help align the rings. For UCS samples, the guide rods were removed before testing, but for DT samples, the guide rods were left in place to help align the sample during endcap assembly and to protect the sample during setup inside the chamber. For testing, the aluminum endcaps used for DT tests were machined with threaded holes that allowed the sample to be screwed into the loading column. The bottom endcap would thread onto the hydraulic ram in lieu of the bottom platen, and the top endcap had a threaded eyelet that was shackled to a cable pull assembly that was threaded into the load cell (Figure 3.5-1d).

BTS experiments were conducted at a constant axial displacement rate 0.19 mm/sec in compression. There was not a thermal buffer between the sample and the top piston, so the experiments were conducted at a faster axial strain rate than UCS experiments. Due to the experimental geometry, applying a compressive force across the diameter of a disc creates a tensile force in the center of the sample. At failure, a tensile crack will form in the center of the sample and propagate to the loading contacts. Samples were not instrumented with lvdts. For testing, the samples were placed on their circumference onto a ceramic spacer on a thin silicon rubber sheet on the bottom platen. The top platen was replaced with a skinner, longer piston to help align the sample in the loading column (Figure 3.5-1e). 2-4 tests were performed at each test to calculate an average tensile strength. BTS was calculated as

$$BTS = \frac{2P_B}{\pi tD} \quad \text{Equation 3.5-1}$$

Where P_B is the peak load, t is the thickness of the disc, and D is the diameter of the specimen.



Figure 3.5-1. Experimental setup for the different types of testing. a) Prepared UCS geometry on sample PM1-1 303-310. b) Deformed UCS experiment on sample PM 1-1 303-310. c) Prepared DT geometry on sample PM1-3 512-522. d) Deformed DT experiment on sample PM1-1 213-232.5. e) BTS experiment on DP 1-1 356-371.

In total, 5 UCS experiments were performed at targeted temperatures of -6 , -3 , and -1°C for visibly high ice contents and -6 and -3°C for visibly medium ice contents. 3 samples were lost during the first rounds of testing until the methodology was developed to protect the sample from heat conduction, allowing subsequent testing to be far more successful. 7 DT tests were successfully performed at targeted temperatures of -6 , -3 , and -1°C for visibly high and low ice contents out of a total of 13 samples. 12 BTS experiments were performed at targeted temperatures -6 , -3 , and -1°C for visibly high and low ice contents for DP1 and PM1 cores. Table 3.5-1 lists all sample prepped based on land surface and core depth, corresponding sample elevation, intended test type, targeted temperature, reported temperature, visible ice content, and result. All samples were preserved after testing for further material property analysis.

Elastic moduli for UCS and DT experiments were determined based on the slopes for stress, σ , versus strain, ϵ , curves during initial loading. Stress is calculated as the applied axial force divided by the cross sectional area of the sample, and strain is the change in length during deformation divided by the original length. Strain is calculated for axial deformation using the original sample length, and radial strain is calculated using the circumference of the sample. For DT samples, stress and strain are calculated based on the neck diameter, where stress will be highest. Young's modulus, E , reported here is defined as the tangent modulus, or the slope of axial stress versus axial strain. Poisson's ratio, ν , is defined as the ratio of radial strain to axial strain.

$$E = \frac{d\sigma}{d\epsilon_{axial}} \quad \text{Equation 3.5-2}$$

$$\nu = -\frac{\frac{d\sigma}{d\epsilon_{axial}}}{\frac{d\sigma}{d\epsilon_{radial}}} \quad \text{Equation 3.5-3}$$

The value of these slopes were picked in the linear portion of the loading curves, past the initial hysteresis from compressing sample-end cap-load column interfaces, to best represent the elastic behavior of the frozen soil. Unload-reload loops were performed on UCS experiments post yielding to determine elastic moduli after the samples had yielded, but only initial elastic moduli are of interest for the terrestrial material models.

Initial sample densities were measured during sample preparation, but densities were remeasured during material property investigations using sample offcuts and deformed samples. The remeasured values are used as the basis of material property determinations and reported here. Samples were vacuum sealed in plastic and immersed in water to accurately measure volume of odd shaped frozen soil chunks. Combined with mass from weighing samples, this method produced accurate density measurements. Samples were dried at low temperatures, and initial and final weights were used to calculate mass of water in the samples. The amount of water relative to the sample was used to calculate porosity, or the percentage of water content in the samples, frozen or liquid. See Section 3.3 for further details. Utilizing the sample temperature based on averaged chamber temperatures during equilibration and temperature, a freezing model was used to calculate the percentage of water present in frozen form, or ice saturation. See Section 4.3.3.2 for further details on freezing models. Ice saturation combined with porosity was used to calculate the fraction of ice in a frozen soil sample, or ice volume fraction. Experimental design was based on temperature and visible ice content as these were variables that could be controlled and determined prior to testing. The terrestrial material model will be based physical strength properties as a function of ice characteristics like ice saturation of ice volume fraction, which could not be determined until after testing.

Table 3.5-1. Frozen soil samples prepared for FY19 testing.

Sample	Elevation (m)	Test	Target Temp (°C)	Chamber Temp (°C)	Visual Ice Content	Result
PM 1-3 070-080	6.1	UCS			High	Failure
PM 1-3 80-112	6.0	DT			High	Failure
PM 1-3 113-120.5	5.7	BTS	-1	-0.8	High	Success
PM 1-3 131-138.5	5.5	BTS	-3	-2.9	High	Success

Sample	Elevation (m)	Test	Target Temp (°C)	Chamber Temp (°C)	Visual Ice Content	Result
PM 1-3 155-168.5	5.2	DT	-6		High	Failure
PM 1-3 168-181	5.1	DT	-3	-3.2	High	Success
PM 1-3 184.5-194.5	4.9	UCS	-1	-2.3	High	Success
PM 1-3 194.5-204.5	4.9	BTS	-6	-5.8	High	Success
PM 1-3 207-222	4.7	DT	-6		High	Failure
PM 1-3 227-233	4.5	UCS	-6	-6.4	High	Success
PM 1-3 238-247	4.4	UCS			High	Failure
PM 1-3 252-262	4.2	UCS			High	Failure
PM 1-3 303-310	3.7	UCS	-3	-2.3	High	Success
PM 1-3 326-338	3.5	DT	-6	-6.1	High	Success
PM 1-3 344-354A	3.4	UCS	-3	-3.4	Med	Success
PM 1-3 344-354B	3.3	UCS	-6	-6.2	Med	Success
PM 1-1 43-54	6.4	BTS	-1	-0.8	Low	Success
PM 1-1 101-113	5.8	DT	-1	-1.2	High	Success
PM 1-1 179-197	4.9	DT	-3		High	Failure
PM 1-1 213-232	4.6	DT	-3	-3.2	Low	Success
PM 1-1 481-505	1.9	DT	-6	-5.4	Low	Success
PM 1-1 500-512	1.7	DT	-1	-1.0	Low	Success
PM 1-1 512-522	1.8	DT	-1		Low	Failure
PM 1-1 532-550	1.4	DT	-6		Low	Failure
PM 1-1 550-568	1.2	DT	-6	-6.1	Low	Success
PM 1-1 568-578	1.1	BTS	-3	-2.9	Low	Success
PM 1-1 578-588	1.0	BTS	-6	-5.8	Low	Success
DP 1-1 232-241	2.8	BTS	-6	-6.5	High	Success
DP 1-1 346-356.5	1.7	BTS	-1	-1.1	Low	Success
DP 1-1 356-371	1.6	BTS	-3	-2.9	Low	Success
DP 1-1 371-383	1.4	BTS	-6	-6.5	Low	Success
DP 1-2 203-208.5	3.1	BTS	-1	-1.2	High	Success
DP 1-2 267-279	2.5	BTS	-3	-3.1	High	Success

3.5.3. Experimental Results

Density of measured samples varied from a low of 1.0 g/cc to a high of 1.8 g/cc (Figure 3.5-2a; Table 3.5-2). Density of permafrost decreases with increasing elevation, and it appears that cores taken from DP sites are denser than similar depth for PM cores. There is high variability in the

cores as ice content varied greatly sample to sample. Some samples also contained visible voids and fractures that appeared to be air filled. The density of ice is 0.92 g/cc, and the density of soils can range from 1.3 g/cc to over 2 g/cc with increasing consolidation. Presumably, the lower density samples from this study would correspond to higher ice contents, and higher density samples would correspond to lower ice contents. Decreasing density with increasing elevation would indicate that ice content increases and/or soil consolidation decreases.

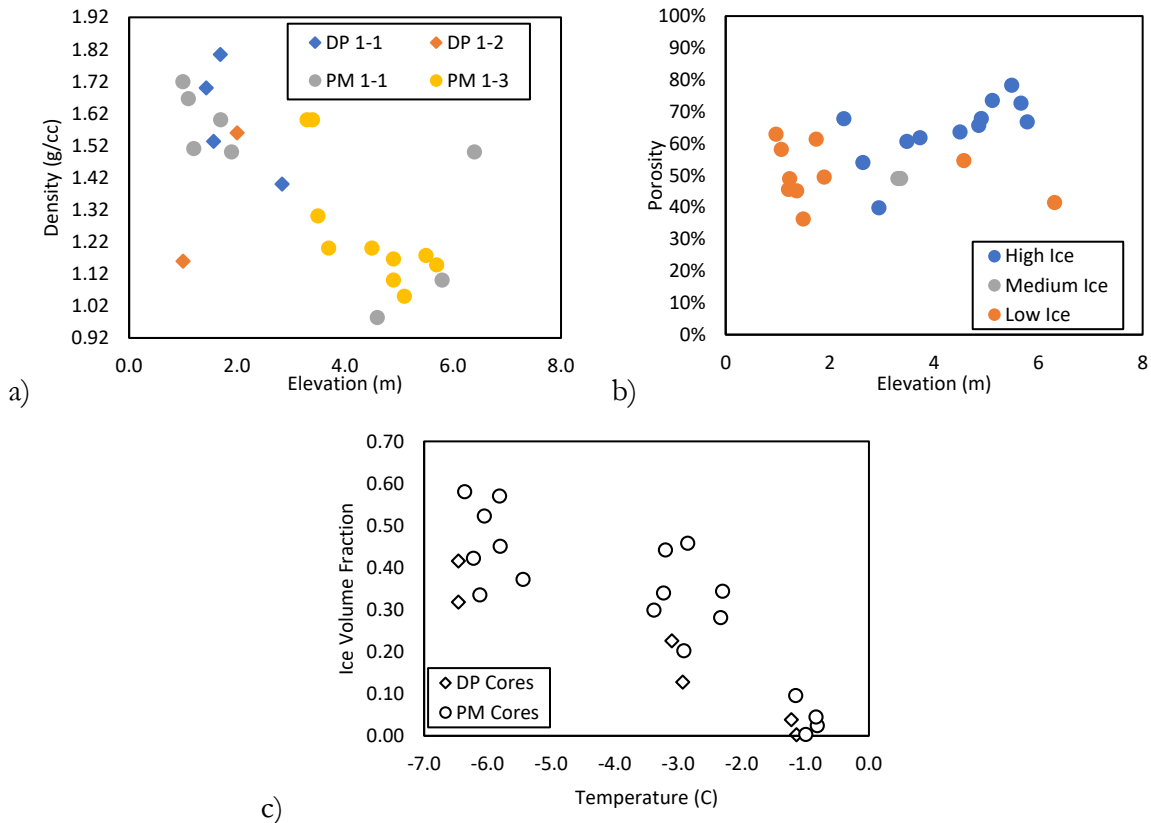


Figure 3.5-2. a) Measured density of frozen soil samples used for geomechanics testing. Lower bound for Density axis is set at the density of ice for comparison. b) Measured porosity of frozen soil samples used for geomechanics testing. c) Calculated volumetric fraction of ice at test temperatures.

Porosity of measured samples varied from a low of 36% to a high of 78% (Figure 3.5-2b; Table 3.5-2). Porosity of frozen soil samples increased with increasing elevation (Figure 3.3-5) corresponding to observed decreases in density, confirming that ice content increases with elevation. Visual estimates of ice content were generally accurate, but a lot of variability is present in the measurements. The average porosity of high ice samples was higher than low ice samples, but a lot of overlap was present (Figure 3.5-2b). Medium ice content was not an accurate assessment as porosity was in line with values for low ice content. For further details on density and porosity measurements, see Section 3.3. Table 3.5-2 also presents calculated melting temperatures, ice saturation values, and ice volume fractions. Melting temperatures are based on pore water salinity, grain size composition, and organic carbon content Section 4.3.3.2. Ice saturation is a function of the difference between the calculated melting temperature and sample temperature Section 4.3.3.2. Ice volume fraction is the fraction of frozen soil that is ice, calculated from the porosity and ice

saturation. Figure 3.5-2c shows the relationship between sample temperature and ice volumetric fraction. With decreasing temperature, ice volumetric fraction decreases in the samples, although there is a lot of variability due to the different ice structures in cores. DP cores generally have less ice than PM cores, but the sample size was smaller for DP cores. For details of these calculations, see Section 4.3.3.2.

Table 3.5-2. Material Properties of Frozen Soil Samples.

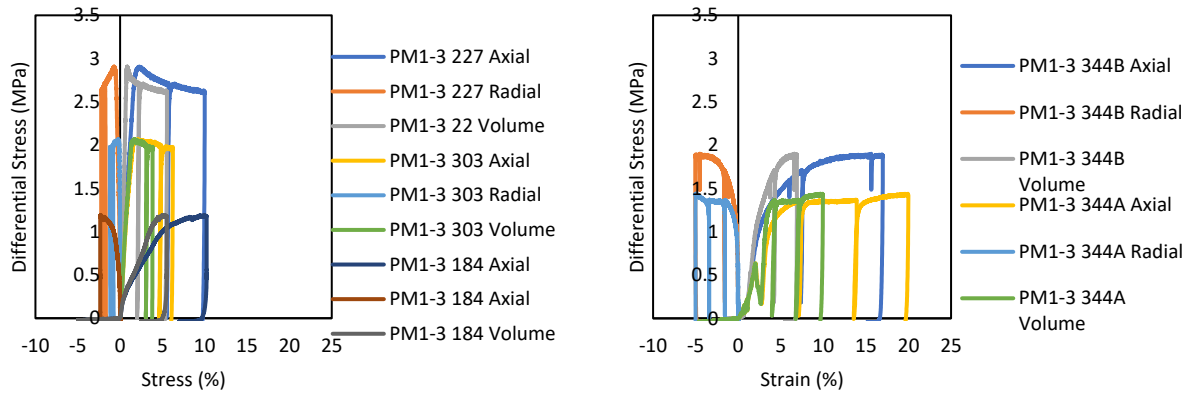
Sample	Elevation (m)	Density (g/cc)	Porosity (%)	Sample Temp (°C)	Melting Temp (°C)	Ice Saturation	Ice Volume Fraction
PM 1-3 113-120.5	5.7	1.1	73	-0.8	0.0	0.06	0.04
PM 1-3 131-138.5	5.5	1.2	78	-2.9	0.0	0.58	0.46
PM 1-3 168-181	5.1	1.0	73	-3.2	0.0	0.60	0.44
PM 1-3 184.5-194.5	4.9	1.1	68	-2.3	0.0	0.51	0.34
PM 1-3 194.5-204.5	4.9	1.2	66	-5.8	0.0	0.87	0.57
PM 1-3 227-233	4.5	1.2	64	-6.4	0.0	0.91	0.58
PM 1-3 303-310	3.7	1.2	62	-2.3	-0.1	0.45	0.28
PM 1-3 326-338	3.5	1.2	61	-6.1	-0.1	0.86	0.52
PM 1-3 344-354A	3.4	1.5	49	-3.4	-0.1	0.86	0.42
PM 1-3 344-354B	3.3	1.5	49	-6.2	-0.1	0.61	0.30
PM 1-1 43-54	6.4	1.5	41	-0.8	0.0	0.06	0.02
PM 1-1 101-113	5.8	1.1	67	-1.2	0.0	0.14	0.10
PM 1-1 213-232	4.6	1.0	55	-3.2	0.0	0.62	0.34
PM 1-1 481-505	1.9	1.5	49	-5.4	-0.4	0.75	0.37
PM 1-1 500-512	1.7	1.3	61	-1.0	-0.5	0.00	0.00
PM 1-1 550-568	1.2	1.6	46	-6.1	-0.7	0.73	0.33
PM 1-1 568-578	1.1	1.7	58	-2.9	-0.8	0.35	0.20
PM 1-1 578-588	1.0	1.7	63	-5.8	-0.8	0.72	0.45
DP 1-1 232-241	2.8	1.4	54	-6.5	-0.2	0.77	0.42
DP 1-1 346-356.5	1.7	1.8	36	-1.1	-0.6	0.01	0.00
DP 1-1 356-371	1.6	1.5	45	-2.9	-0.6	0.28	0.13
DP 1-1 371-383	1.4	1.7	49	-6.5	-0.7	0.65	0.32
DP 1-2 203-208.5	3.1	1.6	40	-1.2	-0.2	0.10	0.04
DP 1-2 267-279	2.5	1.2	68	-3.1	-0.3	0.33	0.23

3.5.3.1. Compressive Tests

UCS experiments on frozen soils underwent ductile deformation, undergoing large strains without fracturing (Figure 3.5-3). All volume strains for tests were compressive. Visibly high ice content samples show a transition in behavior with changing temperature (Figure 3.5-3a; Table 3.5-3). At -6.4°C, the samples undergo strain softening after yielding. The next experiment progressively weakens as target temperatures increase, despite the resulting average temperatures being equal. Porosity values are similar, so the dramatic change in strength is unclear. Visible inspection of the deformed PM1-3 184.5-194.5 did reveal high organic matter at one end that may be responsible for the reduced strength. For visibly medium ice content samples, the opposite trend is observed (Figure 3.5-3b; Table 3.5-3). At -3.4°C, the sample still behaves plastically, but at -6.2°C, the sample strain hardens after yielding. A temporary drop in strength is seen in the -3.4°C experiment that is not observed in any other tests. After the drop, the strength returned to behavior expected from the other experiments. This could represent melting of ice asperities at the sample-endcap interface, after which strengthening would occur as the sample made contact with the endcaps. The UCS tests show that mechanical properties depend on temperature (Figure 3.5-3, Figure 3.5-4; Table 3.5-3). Failure strength decreases almost linearly with increasing temperature (Figure 3.5-4a; Table 3.5-3). Young's modulus and Poisson's ratio are highly variable, but generally decrease with decreasing temperature (Figure 3.5-4b, c, Table 3.5-3). Failure strength, Young's modulus, and Poisson's ratio increase linearly with increasing ice content, although moduli are more variable (Figure 3.5-4d, e, f; Table 3.5-2). The relationship is much clearer between UCS and ice content than UCS and temperature.

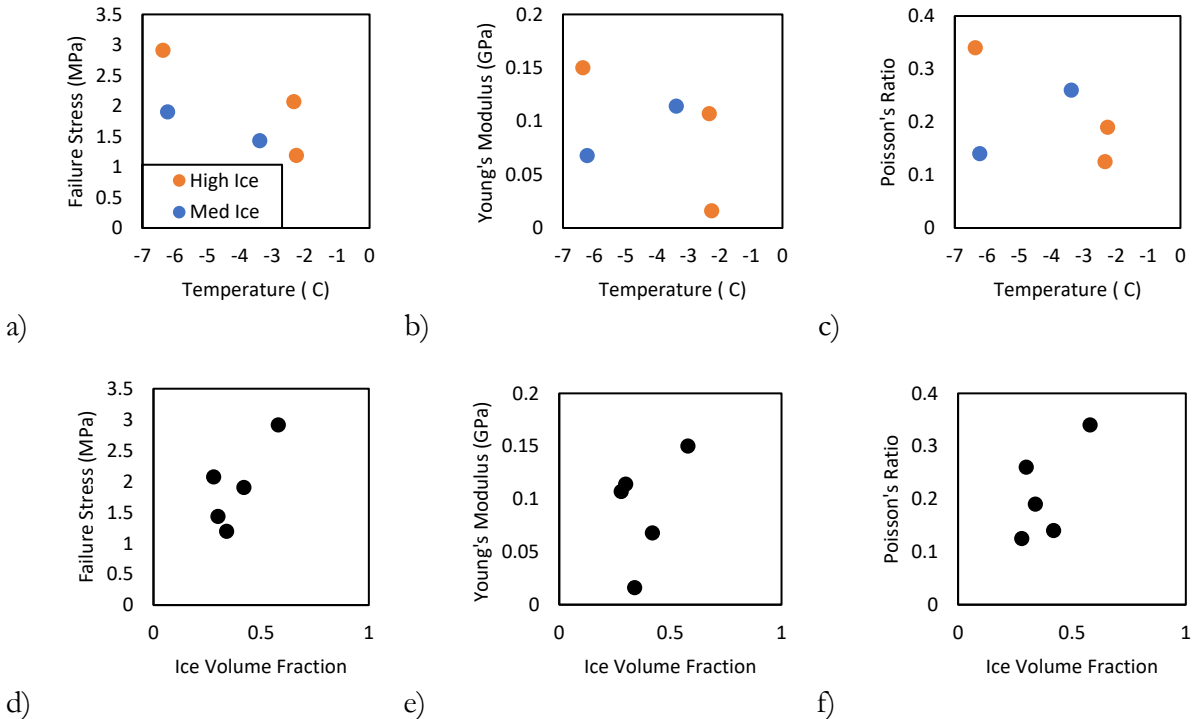
Table 3.5-3. Results for compressive tests on frozen soil.

Visibly High Ice					
Core	Temperature (°C)	Ice Volume Fraction	Failure stress (MPa)	Young's Modulus (GPa)	Poisson's Ratio
PM 1-3 227-233	-6.4	0.58	2.91	0.15	0.34
PM 1-3 303-310	-2.3	0.28	2.07	0.107	0.125
PM 1-3 184-194	-2.3	0.34	1.189	0.016	0.19
Visibly Medium Ice					
Core	Temperature (°C)	Ice Volume Fraction	Failure stress (MPa)	Young's Modulus (GPa)	Poisson's Ratio
PM 1-3 344-354B	-6.2	0.30	1.9	0.0677	0.14
PM 1-3 344-354A	-3.4	0.42	1.43	0.114	0.26



a) b)

Figure 3.5-3. a) Axial stress versus axial, lateral, and volume strain for visibly high ice content samples for temperatures of -6.4, -2.3, and -2.3°C. b) Axial stress versus axial, lateral, and volume strain for visibly medium ice content samples for temperatures of -6.2 and -2.33°C. Samples are listed by core and top depth of sample interval.



a) b) c) d) e) f)

Figure 3.5-4. Mechanical properties for visibly high ice content (orange circles) and visibly medium ice content (blue circles) samples. a) Failure strength versus temperature. b) Young's modulus versus temperature. c) Poisson's ratio versus temperature. d) Failure strength versus ice volume fraction for all UCS tests. e) Young's modulus versus ice volume fraction for all UCS tests. f) Poisson's ratio versus ice volume fraction for all UCS tests.

3.5.3.2. Extension (Tensile) Tests

Direct tensile tests behaved much differently than UCS test (Figure 3.5-5). Accumulated strain was very small, and all samples failed by the development of a through going fracture. Radial strains are small compared to axial strains. Compared to UCS tests, the results from DT tests are much more variable in relation to temperature (Figure 3.5-5, Figure 3.5-6; Table 3.5-4). For visibly high ice content samples, tensile strength increases from -6.1° C to -3.2°C, and then decreases at -1.2°C despite similar porosity and ice content values for PM1-3 326-338 and PM1-3 168-181. Strain before failure increased with decreasing tensile strength, but the large increase in strain for PM1-1 101-113 is unclear (Figure 3.5-5a; Table 3.5-4). For visibly low ice content samples, the two tests conducted at the coldest temperatures were both the strongest and weakest results. Otherwise, tensile strength decreased with higher temperatures (Figure 3.5-5b, Figure 3.5-6; Table 3.5-4). Elastic moduli are variable. There is no clear relationship between temperature and Young’s modulus and Poisson’s ratio (Figure 3.5-6b; Table 3.5-4). It is also unclear why the Young’s modulus was so much higher for PM 1-3 168-181 than all other tests. It appears that tensile strength increases with increasing ice content, but it is a steep relationship (Figure 3.5-6c; Table 3.5-2, Table 3.5-4). There is no clear relationship between ice content and Young’s modulus and Poisson’s ratio (Figure 3.5-6d; Table 3.5-2, Table 3.5-4).

Anywhere from 2 to 4 BTS experiments were conducted for each ice content and temperature. We report the mean values and standard deviations, which were surprisingly small (~1%) for such heterogeneous materials (Table 3.5-4). BTS experiments demonstrated much clearer behavior with temperature compared to DT experiments, but variability was still present (Figure 3.5-6a; Table 3.5-4). Tensile strength decreased with increasing temperature. In conducting experiments on BTS tests at target temperatures near -1°C, the resulting curves were semi-plastic and not brittle like the rest of the experiments. BTS tests are designed for brittle materials and this behavior may have resulted in overestimation of tensile strength at the warmest temperatures. Relationship between BTS failure strength and porosity is generally increasing strength with increasing ice content, but the results are sporadic. Despite the variation in measurements, the values of tensile strength are on the same order of magnitude for BTS and DT tests (Figure 3.5-6; Table 3.5-2, Table 3.5-4).

Table 3.5-4. Results for tensile testing on frozen soil.

Visibly High Ice Core	Temp (°C)	Ice Volume Fraction	Max Stress (MPa)	STD DEV (MPa)	Type	Young's Modulus (GPa)	Poisson's Ratio
PM1-3 326-338	-6.1	0.52	-0.52		DT	0.79	0.25
PM1-3 168-181	-3.2	0.44	-1.00		DT	6.90	0.03
PM1-1 101-113	-1.2	0.10	-0.45		DT	0.15	0.03
PM1-3 194.5-204.5	-5.8	0.57	-0.86	0.055	BTS		
PM1-3 131-138	-2.9	0.46	-0.81	0.006	BTS		
PM1-3 113-120.5	-0.8	0.04	-0.62	0.030	BTS		
DP1-1 232-241	-6.5	0.42	-0.82	0.084	BTS		
DP1-2 267-279	-3.1	0.23	-0.52	0.054	BTS		
DP1-2 203-208	-1.2	0.04	-0.63	0.049	BTS		

Visibly Low Ice

Core	Temp (°C)	Ice Volume Fraction	Max Stress (MPa)	STD DEV (MPa)	Type	Young's Modulus (GPa)	Poisson's Ratio
PM1-1 550-568	-6.1	0.33	-0.11		DT	0.21	0.14
PM1-1 481-505	-5.4	0.37	-0.87		DT	0.33	0.16
PM1-1 213-232	-3.2	0.34	-0.82		DT	1.81	0.23
PM1-1 500-512	-1.0	0.00	-0.43		DT	0.26	0.12
PM1-1 578-588	-5.8	0.45	-0.73	0.021	BTS		
PM1-1 568-578	-2.9	0.20	-0.40	0.029	BTS		
PM1-1 43-54	-0.8	0.02	-0.78	0.039	BTS		
DP1-1 371-383	-6	0.32	-0.94	0.060	BTS		
DP1-1 356-371	-3	0.13	-0.52	0.038	BTS		
DP1-1 346-356	-1	0.00	-0.31	0.035	BTS		

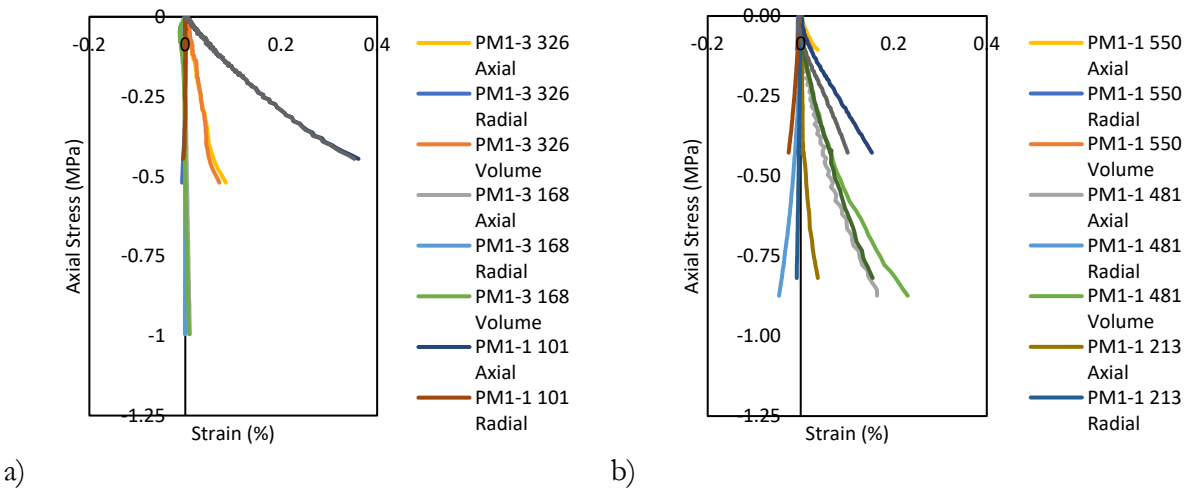


Figure 3.5-5. a) Axial stress versus axial, lateral, and volume strain for visibly high ice content samples for temperatures of -6.1, -3.2, and -1.2°C. b) Axial stress versus axial, lateral, and volume strain for low ice content samples for temperatures of -6.1, -5.4, -3.2, and -1.0°C. Samples are listed by core and top depth of sample interval.

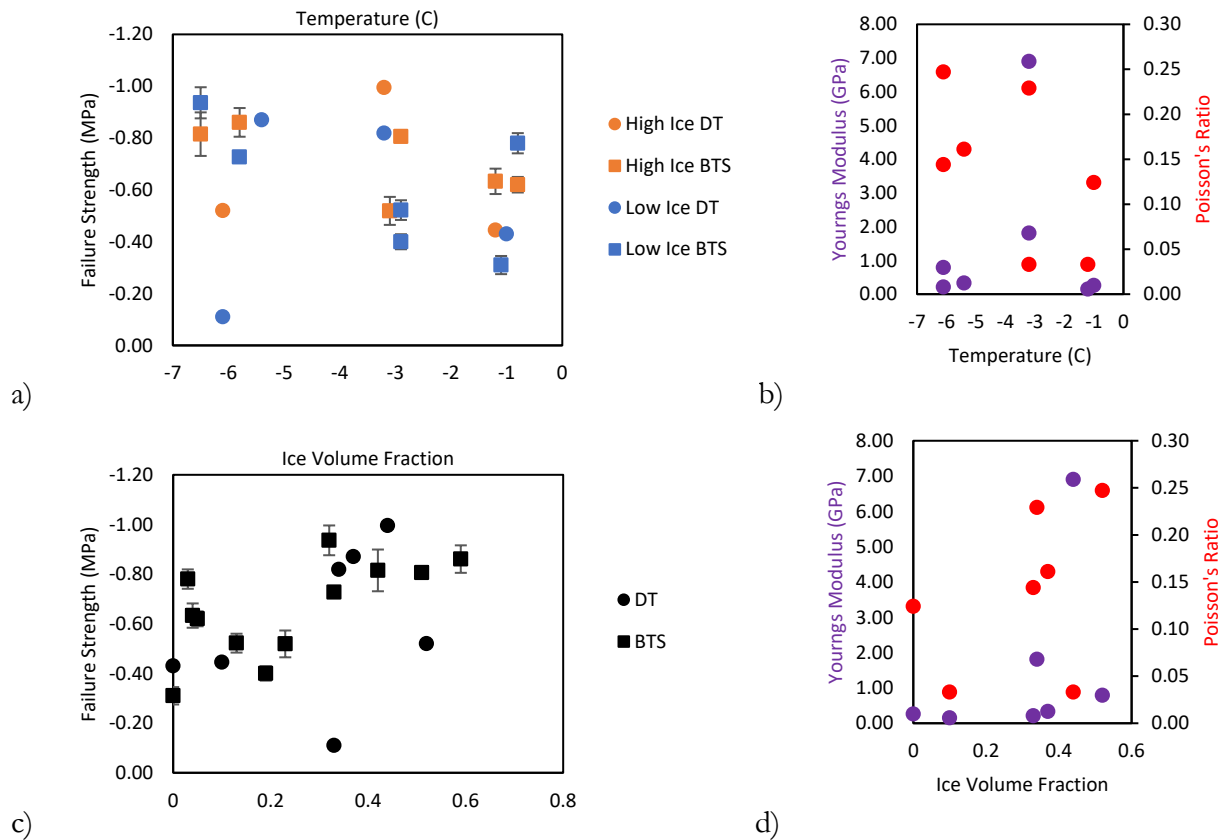


Figure 3.5-6. Mechanical properties for visibly high ice content (orange) and visibly low ice content (blue); results from DT tests (circles) and BTS (squares). a) Failure strength versus temperature. Error bars represent one standard deviation from the mean BTS value for a given condition. b) Young's modulus and Poisson's ratio versus temperature c) Failure strength versus ice volume fraction for all tensile samples. Error bars represent one standard deviation from the mean BTS value for a given condition. d) Young's modulus and Poisson's ratio versus ice volume fraction.

3.5.4. Discussion of Mechanical Results

Geomechanical testing on frozen soil cores proved challenging in the current study. Without dedicated cold workspaces and equipment, it was difficult to maintain precise sample alignment during fabrication, and sometimes sample integrity was jeopardized resulting in a lost sample. The inability to maintain a constant alignment during machining may be the principle reason behind the scatter of results observed in direct tensile tests. Temperature control during equilibration and testing of prepared samples was less than ideal and required constant monitoring to maintain proper temperatures. Temperatures could shift, or the liquid nitrogen cooling system could malfunction mid equilibration. The level gauges on liquid nitrogen dewars were rarely accurate, so it was not possible to estimate the amount of run time left for a given dewar. A full liquid nitrogen dewar was sourced for every experiment, but it was not possible to cool the environmental chamber overnight or to have long equilibration times for samples. For BTS tests, it could be difficult to re-chill the chamber and reestablish the target temperature after switching through a rapid succession of samples.

Sample cores were also extremely heterogeneous. This study investigated 2 different land surfaces from 4 different boreholes. The depth range of cores represent 40,000 years of deposition with multiple depositional environments. Salinity, organic content, grain size distribution, and ice content varied with depth. Some samples looked to be solidified mud with no perceptible ice, other samples were almost pure ice with blobs of soil inclusions. Ice distributions greatly varied, as sometimes ice was homogeneously distributed throughout a sample, and sometimes it was solid ice veins/lens cross cutting what would otherwise be low ice content soil. Most samples were mineralogic soils, but at least one samples had appreciable vegetal matter. It would be expected that consolidation of soils would also vary with depth, but addressing soil structure was beyond the scope of this study.

We designed our experimental matrix under the hypothesis that ice content would be a first order controlling factor on frozen soil strength, and temperature would act as a second order controlling factor by modifying the amount of ice in a sample and thereby altering strength. We intended to test frozen soil with different ice contents, but the heterogeneity of cores made it difficult to draw conclusions about ice content – temperature relationships. We estimated ice contents based on visual observations, which proved generally correct but lacked accuracy (Figure 3.5-2b; Table 3.5-2). Even though our estimates of ice content alone would ultimately not prove sufficient for model development, experiments on different ice contents did help address one aspect of frozen soil heterogeneity: textural variations. The different ice contents behaved similarly; temperature and frozen content had a much greater control on behavior. High ice is stronger than medium ice content, but both samples display similar elastic-plastic behavior. Only the sample with vegetation has a distinctly different stress strain reaction (Figure 3.5-3). Visibly high ice is stronger than medium ice when plotted against temperature, but ice volume fraction has a much clearer effect on failure strength (Figure 3.5-4d). For DT samples, resulting loading and failure behavior is similar for both ice contents (Figure 3.5-5). For DT and BTS failure strengths, visible ice contents do not appear to affect relationships with temperature (Figure 3.5-6a). This indicates that total ice content is more important for model development than ice texture or distribution. This supports the use of a continuum-based modelling approach for terrestrial behavior where soil properties are allowed to vary gradually, as opposed to a more discrete approach where individual soil horizons and larger ice lenses would be defined in the stratigraphy.

We conducted three different types of experiments, with each type resulting in different information and errors. Our initial tests were UCS tests, which are typically very reliable tests for geomaterials. This type of test produces compressive failure strength, Young's modulus, and Poisson's ratio. Sample processing is minimal, helping prevent some sample alignment issues seen in tensile tests. It was not possible to achieve the parallelism necessary for sample ends in typical geomechanics tests, but a spherical seat should have helped alleviate off axis loading. The primary concern with UCS testing is that the cliff faces are failing in tension, so tensile testing was prioritized.

Direct tensile tests are the only extension tests that produce elastic moduli measurements. These are not common tests because the geometries are extremely sensitive to alignment issues. For brittle and quasi brittle materials like most geomaterials, tensile failure occurs rapidly with little premonitory damage accumulation or significant yielding. Failure occurs when a microcrack oriented perpendicular to the applied stress starts to propagate from an existing imperfection. As the microcrack extends, it grows perpendicular to the applied stress, reducing the intact area of the sample. This increases the stress concentration and increases crack growth. This behavior can be seen in the sudden failure behavior of direct tensile tests (Figure 3.5-5). Natural geomaterials like rocks and soils are porous aggregates with ample sites for crack nucleation. Due to the random nature of these nucleation sites in natural materials, experiments investigating tensile strength can

yield results with high uncertainties. Frozen soil solidifies otherwise cohesionless soils, but plenty of crack nucleation sites exist: grain-grain boundaries, ice crystal-ice crystal boundaries, grain-ice crystal boundaries, open pores, and melt pockets. Testing was also exacerbated by experimental methodology. Lacking a dedicated cold prep facility, we were forced to periodically remove samples from lathes to refreeze sample during machining. Each time the sample was removed and replaced is a potential opportunity for misalignment. Because the neck diameter and sample diameter required different grinders, samples were moved in between steps, potentially affecting concentricity. Load column alignment is also vital for reliable results, which we tried to address using a cable pull. Issues with failure strength and moduli suggest that we were not entirely successful, and questionable results are attributable to misalignment.

BTS tests are the common approach to measure tensile strength in geomaterials. The sample prep is far simpler in these samples and avoids many of the issues inherent in DT tests. Our experiments produced consistent results with little statistical deviation for a given condition. Unfortunately, BTS cannot be used to measure elastic moduli. Also, BTS may not have been an appropriate choice for some of the experiments at temperatures near -1°C . BTS assumes brittle materials, and at the warmest temperatures samples squished plastically, violating the underlying assumptions.

Despite experimental difficulties, we did produce an internally consistent dataset. The different tests agree with each other. UCS failure strengths are higher than tensile strengths, which is to be expected for geomaterials (Figure 3.5-4, Figure 3.5-6; Table 3.5-3, Table 3.5-4). The different types of tensile testing agree with each other as well as tensile strengths are similar magnitudes (Figure 3.5-6; Table 3.5-4). Elastic moduli vary, but that is not uncommon in geomaterials, especially with highly heterogeneous samples. It is uncommon for Young's modulus in tension to be higher than in compression (Figure 3.5-4, Figure 3.5-6; Table 3.5-3, Table 3.5-4). It's unclear if the values for tension are affected by load column issues, or if the values in compression are superficially low due to end cap effects. Ice undergoes pressure melting, a phenomena we used to attach endcaps to the samples. It's possible that the same phenomena affect the samples during compression, reducing stiffness during loading. This may also explain the drop in stress during initial loading of PM1-3 344-354a at -3.4°C (Figure 3.5-3b).

For future studies, we recommend an extension of UCS testing. We presented a full investigation of target temperatures for different ice content samples from PM and DP land surfaces, but UCS testing lacked a full temperature investigation in PM land surfaces. We would suggest rerunning UCS tests to ensure a full range of temperature from -6°C to -1°C for different potential ice contents in PM and DP land surfaces. These tests would provide the best resources to parameterize the material model for the behavior at Drew Point, AK.

3.5.5. Development of a Strength Model

In the development of the material model to simulate the behavior in coupled multi-physics simulations, it was assumed that frozen soil is an elasto-perfectly-plastic material. This behavior would correspond to an initial linear elastic phase of loading during deformation, and upon reaching a yield stress, the behavior would transition to perfectly plastic behavior, as seen in UCS tests (Figure 3.5-3). The material model developed for the terrestrial model is based on volumetric content of ice in the form of a mixture model, which assumes that the material is a homogeneous mixture and takes on a volume averaged yield strength of the two constituents. The yield stress that would mark the transition between elastic and plastic was assumed to be a function of the combined properties of the soil component and ice component:

$$\sigma_{Total} = S_{Soil}\sigma_{Soil} + \theta f(T)\sigma_{Ice} \quad \text{Equation 3.5-4}$$

where σ_{Total} is the yield strength of the frozen soil, S_{Soil} is the volume fraction of soil, σ_{Soil} is the yield strength of soil, θ is the soil porosity, $f(T)$ is the percentage of H₂O in a frozen state within the pore space – ice saturation, and σ_{Ice} is the yield strength of ice. For further derivation of the material model, see Appendix A.

In order to parametrize the model, a decision was made to focus on the experimental results from UCS tests. In the field, the coastal bluffs are failing in tension as the blocks erode at the base and tip over into the sea. However, the tensile tests in this study have issues. The direct tensile experiments demonstrate the failure behavior and relative elastic moduli, but absolute values suffer from uncertainty. DT samples fail suddenly upon reaching the yield strength, demonstrating that k-power law shape for the J2-plasticity is an appropriate rheologic model. The spread in failure values and elastic moduli preclude the use of these values as the basis for the material model. BTS tests give a much more reliable estimate of tensile strength than DT tests, however, BTS tests still suffer from issues at warmer temperatures and do not provide elastic moduli measurements. BTS estimates are also lower than what would be expected. Tensile strength for pure ice is around 5 MPa, the pure ice prediction for BTS experiments would be 1.9 MPa. The UCS end member for pure ice predicts a value of 4.8 MPa, very close to the theoretical value. UCS tests are the most reliable type of testing employed in this study and do not suffer from many of the methodology issues that affected tensile testing. UCS tests produced a reasonable range of result for failure strength and moduli without any of the extreme outliers seen in DT tests.

Normally, geomaterials are asymmetric materials, meaning the behavior is different in tension and compression. Geomaterials are far stronger in compression, and the ratio of UCS values to BTS values is assumed 12:1 for common failure criteria. The behavior of frozen soil is not typical of geomaterials, and our material model is based on a mixture model for ice content. The behavior of ice is assumed to be symmetric in tension and compression as it does not suffer from the pore structures seen in rocks and soils. Albany also assumes symmetry for materials in compression and tension. Because this prioritizes failure relationships with ice content and ignores loading direction, we have chosen to prioritize UCS results for material model development. This should give the most reliable result for failure strength and elastic moduli to develop material models.

3.5.5.1. Failure Strength Using Volumetric Content of Ice in Frozen Soil Approach

The volumetric material model was developed from Equation 3.5-4 using results from UCS tests and core measurements made in Section 3.3. The volumetric content of ice was calculated from the total H₂O content (listed as porosity in Section 3.3) and ice saturation (calculated according to Section 4.3.3.2) - $S_{ice}(t)$. A best fit linear relationship was fit with failure strengths from UCS tests as the dependent variable against ice volume fraction as the independent variable, the blue curve in Figure 3.5-7. The fit is reasonable, but the coefficient of determination is less than ideal, 0.58. The relationship gives a slope of 4.20 MPa and an y-intercept of 0.23 MPa. The y-intercept value of 0.23 MPa represents the strength of ice-free soil in compression, which is an appropriate value for clay rich soils. The dashed curves in Figure 3.5-7 represent high and low bounds based on theoretical and observed strengths. The dashed red curves assumes a 5 MPa value for the strength of pure ice. Assuming the same value for soil strength, this increases the slope to 4.77 MPa. The dashed green curve assumes a strength of 1.94 for pure ice end member based on observations for BTS experiments. The green curve bounds all experimental results; the red curve bounds all but one experiment.

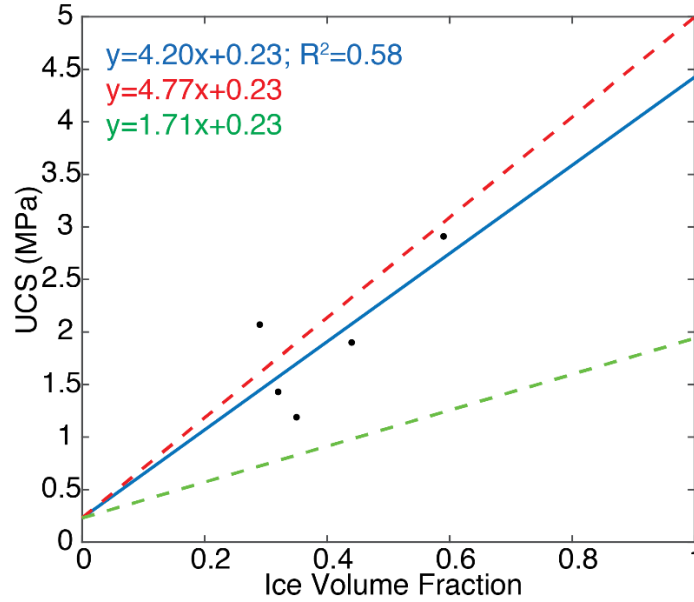


Figure 3.5-7. Failure strength versus ice volume fraction for UCS experiments. Blue line is linear best fit relationship to the experimental results. The dashed red line is a theoretical fit assuming 5 MPa for the strength of pure ice. The dashed green line shows the linear relationship based on the tensile strength observed in BTS samples.

3.5.5.2. Failure Strength Using an Ice Adhesion in Frozen Soil Approach

When frozen sediment fails, observational evidence indicates failure planes are typically along ice-sediment grain boundaries. Therefore, a volume averaged mixture model, as presented Section 3.5.5.1, may not be an appropriate model for the behavior of permafrost. What may control the strength of frozen soil then is the interfaces between ice crystals and sediments. Fully frozen, the ice-sediment interface would extend throughout the soil as a load bearing structure, but as soil warms, this interface shrinks, and soil strength is reduced. An alternative to a volume averaged mixture model is based on the strength of the ice-sediment interface σ_Y^{i-s} , and residual sediment strength when fully thawed σ_Y^s .

$$\sigma^* = \sigma_Y^s + f(T)\sigma_Y^{i-s} \quad \text{Equation 3.5-5}$$

The ice saturation, which ranges between 0 and 1, represents the relative amount of ice-sediment interface left intact. The values for the variables can be obtained from the relationship between the UCS experimental results and ice adhesion values. The best fit linear relationship is shown by the blue line, Figure 3.5-8. The values for σ_Y^s is 0.55 MPa and the value for σ_Y^{i-s} is 2.03 MPa. The coefficient of determination for this fit is low, 0.4. To capture all possible data values, an upper and lower bound was applied to the data. The dashed red curve represents the upper bound, and the dashed green curve represents the lower bound. Figure 3.5-8a calculates the bounding curves by assuming σ_Y^{i-s} is constant, and σ_Y^s can vary from 0.15 to 1.15 MPa. Figure 3.5-8b calculates the bounding curves by assuming σ_Y^s is constant, and σ_Y^{i-s} can vary from 1.15 to 3.45 MPa.

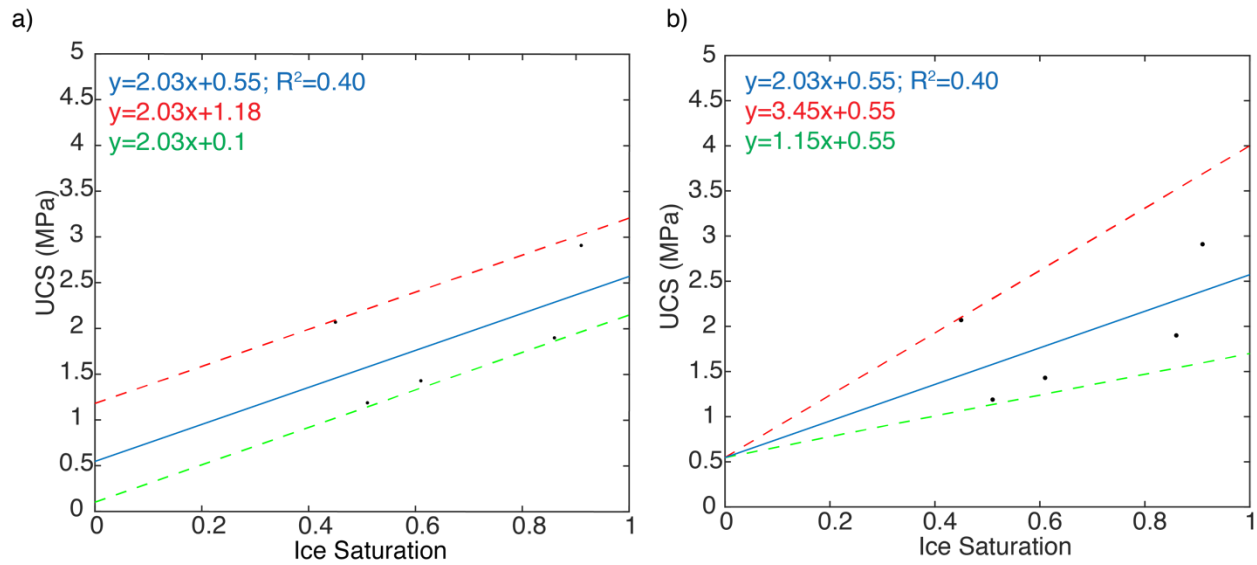


Figure 3.5-8. Failure strength versus ice saturation for UCS experiments. Blue line is linear best fit relationship to the experimental results. The dashed red line represents an upper bound to the data, and the dashed green line represents a lower bound to the data. a) Bounding curves assume different soil strength. b) Bounding curves assume different ice strength.

3.5.5.3. Elastic Moduli

Elastic moduli are populated using averaged values from UCS tests. Average Young's modulus is 0.09 ± 0.05 GPa. The maximum possible value is 0.15 GPa, and the minimum possible value is 0.02 GPa. Average Poisson's ratio is 0.21 ± 0.09 . The maximum possible value is 0.34, and the minimum possible value is 0.13. If an average strength was desired for the model, it would be 1.90 ± 0.67 MPa.

Elastic moduli can be fit against volumetric fraction of ice in samples (Figure 3.5-9). The coefficient of determination for Young's modulus is poor, demonstrating a poor dependence on ice content (Figure 3.5-9a). There is a greater dependence for Poisson's Ratio on ice content, but the coefficient of determination is still low (Figure 3.5-9b).

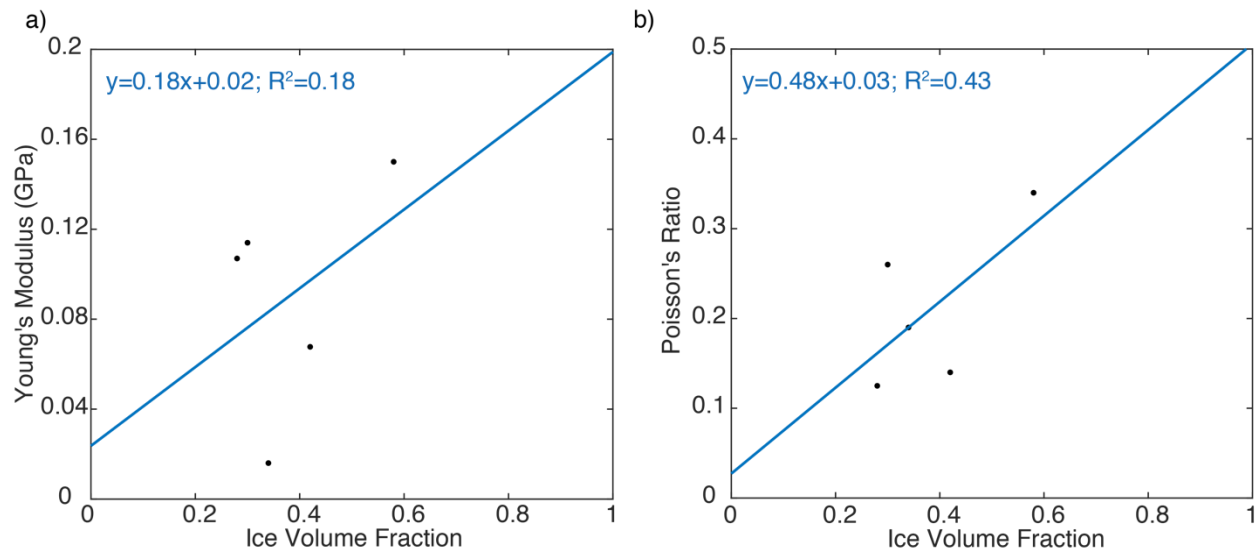


Figure 3.5-9. Elastic moduli versus ice volume fraction for UCS experiments. Blue line is linear best fit relationship to the experimental results. a) Young's modulus and b) Poisson's ratio.

3.5.6. Conclusions

A total of 24 successful geomechanics experiments were performed on frozen soil samples with 3 different ice contents from two different land surfaces at three different target temperatures of -6, -3, and -1°C. Selected cores had a porosity range from 36% to 78%, which corresponded to ice volume fractions in experiments from almost 0 to 0.58. It was expected that the strength of frozen soils would decrease as temperatures approached melting temperatures due to reduced ice content, and this relationship is demonstrated by UCS experiments. The relationship between failure strength and temperature was complicated by different ice contents, but the relationship between failure strength and ice volumetric fraction was much clearer. DT experiments and BTS experiments do not display a clear relationship with temperature, but the tensile strength does show a dependence on ice volumetric fraction. Results are scattered, but this could be due to the natural variability associated with tensile strengths in geomaterials, difficulty in preparing experimental geometries, and the highly heterogeneous nature of the frozen soil cores with depth. Strength variations could be best explained using measured ice contents as opposed to ice textures used as the basis of visible ice content determinations, supporting a continuum approach.

The material model is derived from UCS experiments due the higher reliability of this type of testing in natural geomaterials and assumed model symmetry. Materials models were based on UCS relationships between volumetric content of ice and ice saturation to estimate strength assuming failure is controlled by either total ice or remaining ice-sediment interface. UCS and DT tests demonstrate that an elastic-perfectly plastic rheology using k-power law for J2 plasticity.

4. MODEL DEVELOPMENT

4.1. Boundary Condition Sources

Team Member Author: Christopher Flanary (Integral Consulting)

Contributors: Craig Jones (Integral Consulting), Li Erikson (USGS)

Multiple atmospheric and oceanographic reanalysis datasets, as well as some measured data, were used for the Arctic Coastal Erosion (ACE) analysis and oceanographic modeling suite boundary conditions. Climate change atmospheric models were also sourced to provide boundary conditions for the oceanographic models. These reanalysis datasets and measured data are described in more detail in the following sections.

4.1.1. Atmospheric Boundary Conditions

Arctic System Reanalysis v2 (ASR), ERA5, and global climate model (GCM) projection atmospheric reanalysis datasets were used for building wind, sea ice, air temperature, and soil parameter boundary conditions for the terrestrial and oceanographic models. Three other atmospheric reanalysis datasets were evaluated for inclusion into this study (i.e., Chukchi-Beaufort Seas High-Resolution Atmospheric Reanalysis (CBHAR), North American Regional Reanalysis (NARR), and WRF-ERA), though after a performance assessment, only ASR and ERA5 were selected for moving forward. This performance assessment is described in more detail in Section 5.2.

Arctic System Reanalysis v2 (ASR) is a 15 km horizontal resolution polar central reanalysis dataset blended from modeling and observations (Bromwich et al 2018; Figure 4.1-1). Data is available from 2000-2016 in 3-hour increments. It is forced by the Polar Weather Forecast Model and the High Resolution Land Data Assimilation model.

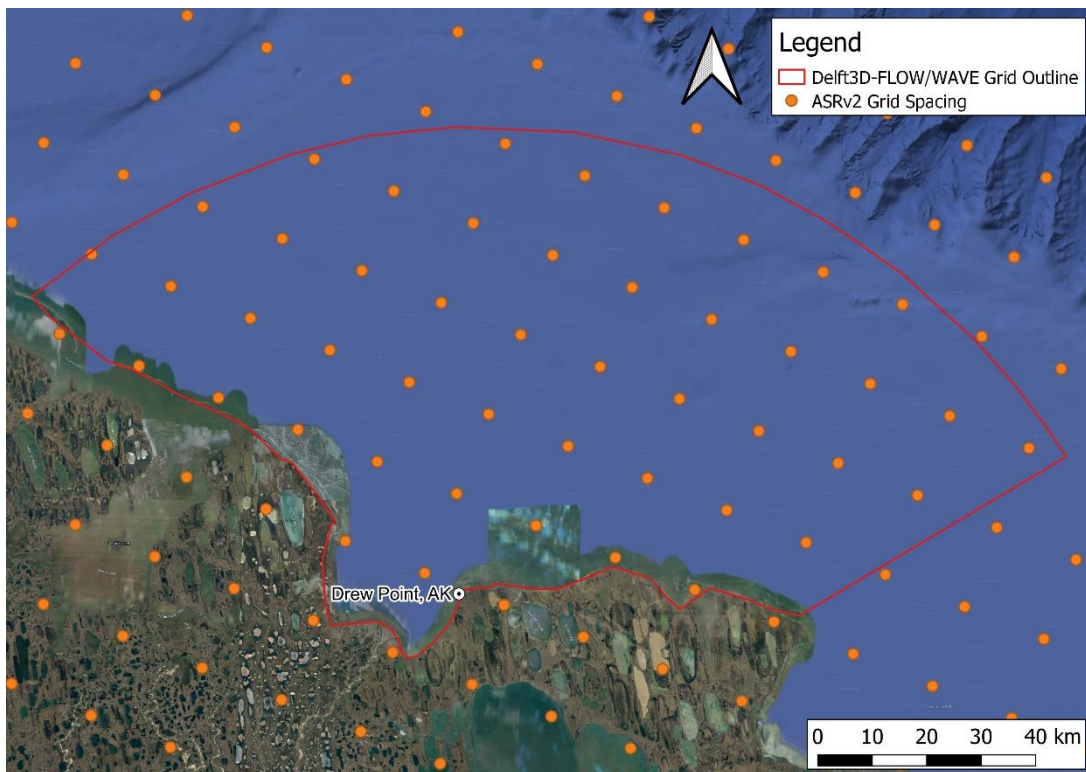


Figure 4.1-1. ASR Grid Spacing At Drew Point, AK Project Area.

ERA5 is a global climate reanalysis product from the European Centre for Medium-Range Weather Forecasts (C3S 2017; Figure 4.1-2). ERA5 has a 31 km horizontal resolution and is available from 1950 to present in 1-hour increments. For this study, ERA5 data were only used from 2017 – 2019.

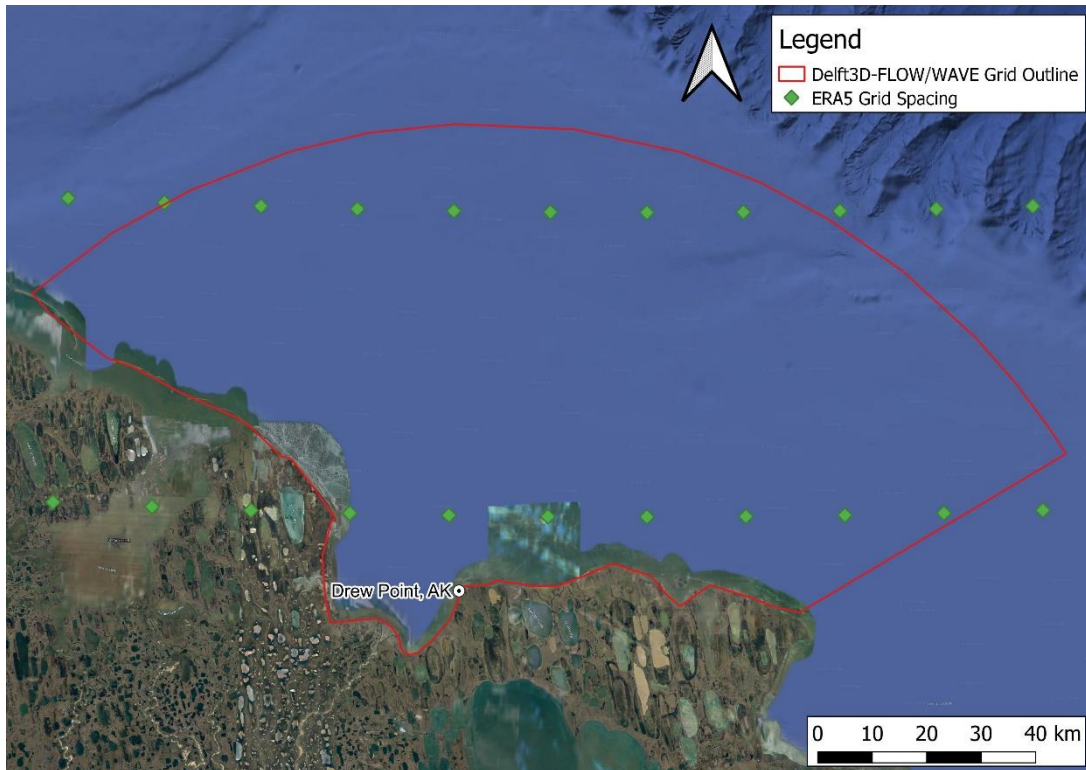


Figure 4.1-2. ERA5 Grid Spacing At Drew Point, AK Project Area.

GCMs provide predictions of atmospheric, terrestrial, and oceanographic values out to year 2100. For this study, projected simulations from NOAA’s Geophysical Fluid Dynamics Laboratory Coupled Physical Model (GFDL-CM3) were downscaled for the Alaska region (Griffies et al, 2011). GFDL-CM3 is one of the GCMs of the Coupled Model Inter-comparison Project 5 (CMIP5). This WRF downscaled product for the Alaska region has a 20 km horizontal resolution and hourly outputs; similar procedures were followed as in Bienick et al. (2016). These data were sourced to supply the wind forcing boundary conditions for the projected runs using the oceanographic modeling suite.

Variables from each reanalysis data source (ASR, ERA5 and GCMs) were used both by the terrestrial model directly and also by the oceanographic modeling suite (Table 4.1-1). For the terrestrial model, select variables from the reanalysis datasets were extracted at the location closest to 153.943°W 70.876°N (the white circle in Figure 4.1-1 and Figure 4.1-2). For the oceanographic modeling suite, the component wind speeds, sea ice fraction, and sea-level pressure from the reanalysis datasets were linearly interpolated onto the oceanographic model grids to provide boundary and initial conditions. Additional terrestrial variables (e.g., soil temperatures, skin

temperature, vegetation index, etc.) were downloaded from the reanalysis datasets and are currently used (or will be used in future iterations) as boundary conditions for the terrestrial model.

Table 4.1-1. Variables of Interest From Atmospheric Reanalysis and Projection Datasets.

ASR	ERA5	GCM
Component wind speeds	Component wind speeds	Component wind speeds
Temperature 2 m above ground	Temperature 2 m above ground	Temperature 2 m above ground
Sea surface temperature	Sea surface temperature	Surface pressure
Surface air pressure	Surface air pressure	Sea ice fraction
Sea ice fraction	Sea ice fraction	Snow Depth
Physical snow depth	Snow depth	Volumetric soil moisture content
Snow coverage fraction	Volumetric soil water	Vegetation fraction
Soil moisture	Leaf area index	Soil temperature
Soil temperature	Soil temperature	Surface skin temperature
Surface skin temperature	Skin temperature	
Dominant vegetation category	Type of vegetation	
Dominant soil category	Soil type	

4.1.2. Oceanographic Boundary Conditions

NOAA measured data, Global Ocean Forecasting System (GOFS) 3.1, and GCM climate projection oceanographic datasets were used for building water level, water temperature, and salinity boundary conditions for the oceanographic models.

The water level data for the oceanographic modeling suite were downloaded from NOAA’s Center for Operational Oceanographic Products and Services (CO-OPS) for the Prudhoe Bay, AK station (ID# 9497645). These data were available at 6-minute intervals and referenced to the oceanographic modeling suite vertical datum.

A comparison of the measured water level at Prudhoe Bay, AK and the GOFS 3.1 extracted water level predictions for two locations along the North Slope show good overall agreement in the water level trends (Figure 4.1-3). However, the higher frequency water level oscillations are not predicted by GOFS 3.1, likely due to the temporal output frequency. Providing high temporal resolution water level to the oceanographic models allows for the prediction of those higher frequency oscillations

that will be passed to the terrestrial model. Further evidence for the need for high temporal resolution water level data, water levels are expected to be wave and wind dominated and have relatively low ranges from low to high. This can change when significant storm events drive more water towards shore, causing the water to rise and hold until the storm conditions subside.

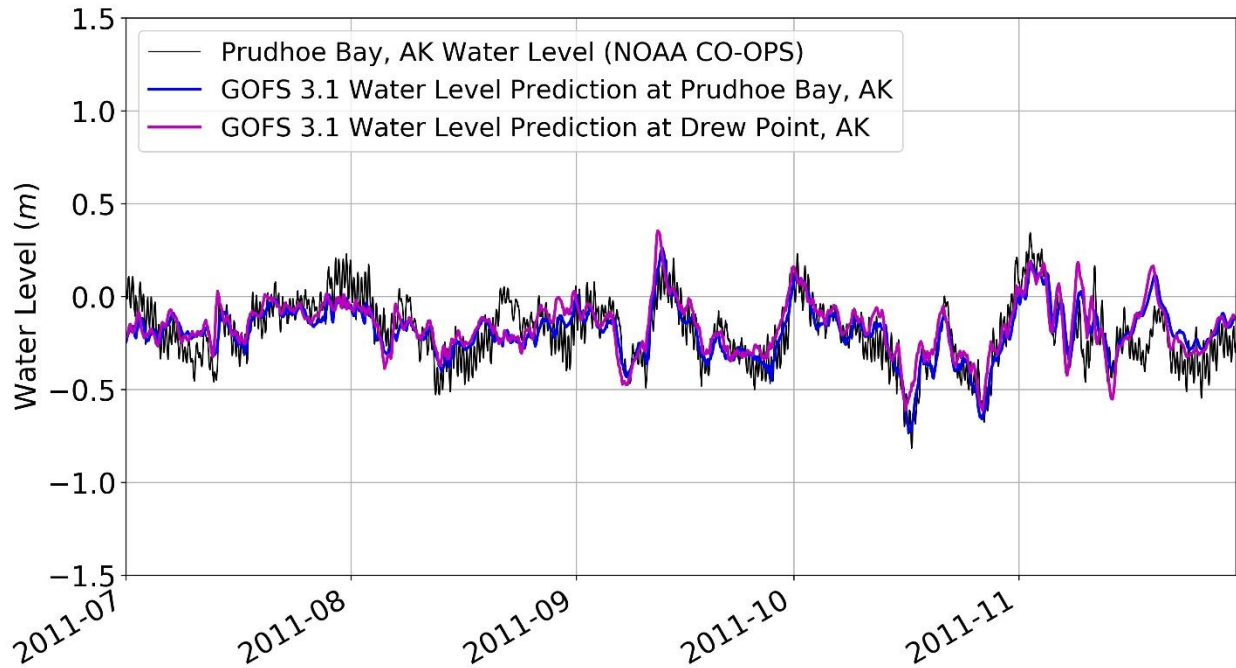


Figure 4.1-3. Time Series Comparison of Measured Water Level at Prudhoe Bay, AK To GOFS 3.1 Extracted Water Level Predictions at Prudhoe Bay and Drew Point, AK.

The GOFS 3.1 Global Reanalysis data set is a modeling system combining the Hybrid Coordinate Ocean Model (HYCOM) and the Navy Coupled Ocean Data Assimilation (NCODA) system (Cummings, 2005; Cummings and Smedstad, 2013). These data were provided by the HYCOM consortium, a multi-institute project sponsored by the National Ocean Partnership Program as part of the U.S. Global Ocean Data Assimilation Experiment. GOFS 3.1 data were used to build water temperature and salinity boundary conditions. Reanalysis data were available at 0.04° degree resolution in the project area and at 3 hour intervals from 1994 – 2015 (Figure 4.1-4). Analysis data were available at 0.04° degree resolution in the project area and at 3 hour intervals from 2016 – 2019. The reanalysis and analysis GOFS 3.1 model setup is identical. The atmospheric forcing for the analysis is derived from the Navy Global Environmental Model (NAVGEM), while the reanalysis is forced by NOAA’s National Center for Environmental Prediction (NCEP) Climate Forecast System Reanalysis (CFSR/CFSv2). Sea surface height data were available from this reanalysis dataset, though at 3-hour intervals, too coarse for the oceanographic model boundary conditions.

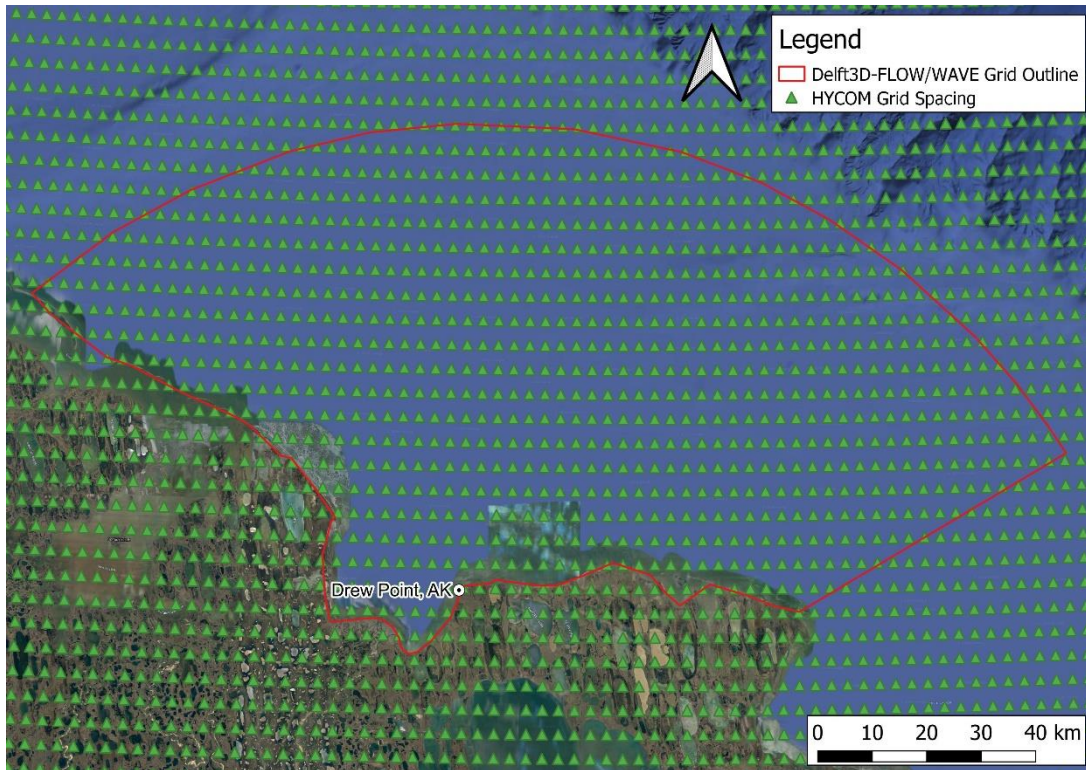


Figure 4.1-4. GOFS 3.1 HYCOM Grid Spacing At Drew Point, AK Project Area.

Since the necessary oceanographic variables (sea surface temperature, sea water salinity) were not available from the GFDL-CM3 GCM used for the atmospheric boundary conditions, these variables were sourced from the Canadian Centre for Climate Modeling and Analysis' second generation Canadian Earth System Model (CanESM2), another GCM from the CMIP5 (Figure 4.1-5). CanESM2 is a coupled physical atmospheric-ocean model with global coverage at 50 km horizontal resolution in the region of interest. The needed variables, sea surface temperature and sea water salinity, were available with monthly temporal resolution.

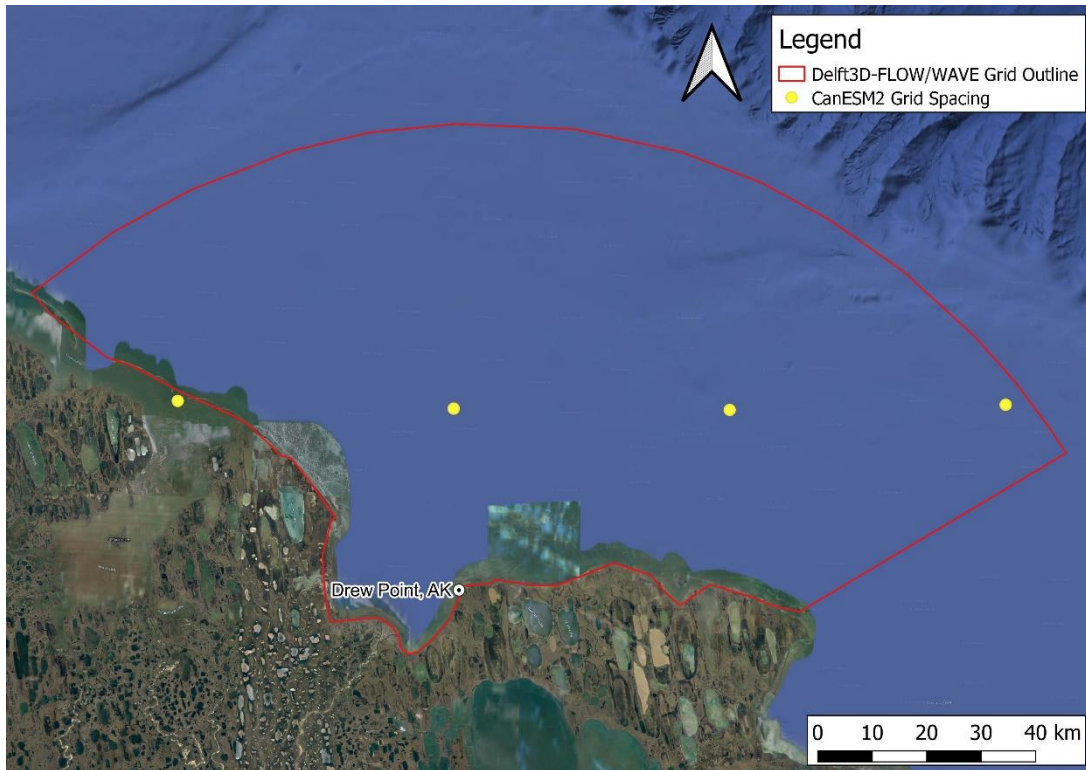


Figure 4.1-5. CanESM2 GCM Grid Spacing At Drew Point, AK Project Area.

4.2. Oceanographic Modeling Suite

Team Member Author: Christopher Flanary (Integral Consulting)

Contributors: Craig Jones (Integral Consulting), Erik Rogers (NRL)

Understanding how water levels vary at the coastal cliff faces along the Beaufort Sea will provide a better understanding of erosion and shoreline degradation along Drew Point and more generally along the Alaskan coast. While measurements can be made to quantify the coastal erosion process, not all conditions or variations thereof may be captured during a field campaign. The development and application of a hydrodynamic numerical model can be a valuable tool to understand how water levels, currents, and even water temperatures may change in the area of interest over a range of conditions.

The formulation of high temporal fidelity predictions of hydrodynamic and wave parameters along the Alaskan coast necessitates the application of site-specific numerical models. These models incorporate atmospheric and hydrodynamic factors such as sea ice coverages, winds, and regional water levels to determine relevant parameters such as water levels and wave heights in a region of interest. The following section outlines the use of a three-model oceanographic modeling suite to simulate conditions around Drew Point on the North Slope of Alaska. The first of the three-model system is the application of a spectral wave model, WAVEWATCH III® (WW3), to provide wave field information at an Arctic Ocean scale. The second and third models are a hydrodynamic and wave model used to simulate nearshore circulation and waves in the region of interest. The nearshore circulation model, or hydrodynamic and wave model, was developed using Delft3D-FLOW (Deltares 2018) and Delft3D-WAVE (Holthuijsen et al. 1993). Importantly, the Delft3D

models are open source and freely available for distribution to any interested parties in the future. In addition, Delft3D-WAVE uses SWAN (Simulating Waves Nearshore), a proven nearshore and shallow water spectral wave modeling system, as the wave model and is natively coupled to Delft3D-FLOW, providing an efficient computational environment.

The ability to couple WW3 and Delft3D-FLOW/WAVE provides an efficient method to resolve the dynamic interaction of swell, wind waves, and water levels. These predicted values and their coupled interaction will allow for the calculation of the time varying, high frequency water level inundating the bluff face, which will be passed to the terrestrial bluff face erosion model.

The following sections describe the setup of the three individual models of the oceanographic modeling suite.

4.2.1. WAVEWATCH III Wave Model Setup

The first model setup in the three-model system was the Arctic Ocean scale WW3 model. This WW3 model was necessary to provide spectral wave boundary conditions to the Delft3D-FLOW/WAVE near-shore model along the north coast of Alaska. The WW3 model received wind and sea ice inputs from various atmospheric reanalysis dataset and global scale bathymetric data.

WW3 is a modular spectral wave model written in Fortran90 that simulates wave propagation by solving an action balance equation in explicit form by marching in time. WW3 has multiple physics packages that can be easily enabled or disabled depending on the area of interest. WW3 can be easily compiled to work with single or nested grids, steady state or time varying input fields, and ice. The WW3 model consists of, in its simplest form, a grid preprocessor, an initial conditions processor, a model input preprocessor, the wave model, and output processors. WW3 uses a spatially varying wavenumber grid which reduces the loss of model resolution for simulated waves traveling from deep to shallow water and incorporates the effects of currents on wave propagation. This feature of WW3 makes it advantageous for use in shelf seas and regions with long swell over steady currents.

The WW3 model options and physics packages chosen for this Arctic Ocean domain include a higher order propagation scheme using a Tolman (2002) averaging technique, and a third order propagation scheme, flux computation was included in the source terms, linear input of source terms, boundary condition input and dissipation defined by Ardhuin et al. (2010), Discrete Interaction Approximation for nonlinear interactions, JONSWAP bottom friction formulation, frequency depended wave damping by sea ice, no scattering by sea ice, no wave reflection, Battjes-Janssen depth induced breaking, Lumped Triad Interaction method, no bottom scattering, and linear interpolation of boundary condition data. Additional details on these model options and physics packages can be found in WW3DG, 2019.

4.2.1.1. WW3 Model Grid and Bathymetry

A polar stereographic, curvilinear WW3 grid was provided by Erik Rogers that covered the Arctic Ocean (Figure 4.2-1; Rogers and Zieger 2014). The WW3 model wave grid is polar centric and extends south to 65°N. Its horizontal resolution is 18 km at 70°N. The area around the North Pole is masked due to the computation solution being complex. Bathymetric data for the model domain was obtained from the ETOPO1 1 arc-minute global relief model (Amante and Eakins 2009).

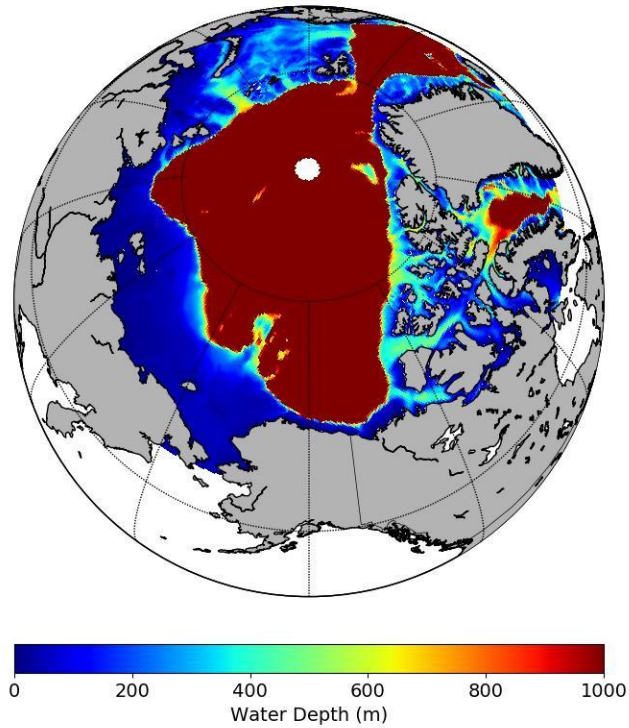


Figure 4.2-1. Arctic WW3 Model Grid Extents With ETOPO 1 Bathymetry.

4.2.1.2. WW3 Boundary Conditions

Wind forcing and sea ice boundary conditions for WW3 were derived from the ASR and ERA5 atmospheric reanalysis datasets as well as the GCM climate projection datasets described in the previous section. The wind component forcing and the sea ice fractions were linearly interpolated onto the WW3 grid to provide spatially and temporally varying forcing across the domain. The sea ice coverage fraction from the reanalysis datasets was a time varying boundary condition represented as a range from 0 to 1 to represent the density of sea ice (Figure 4.2-2). The sea ice coverage around the North Slope of Alaska, during 2011, does not begin to retreat offshore until July.

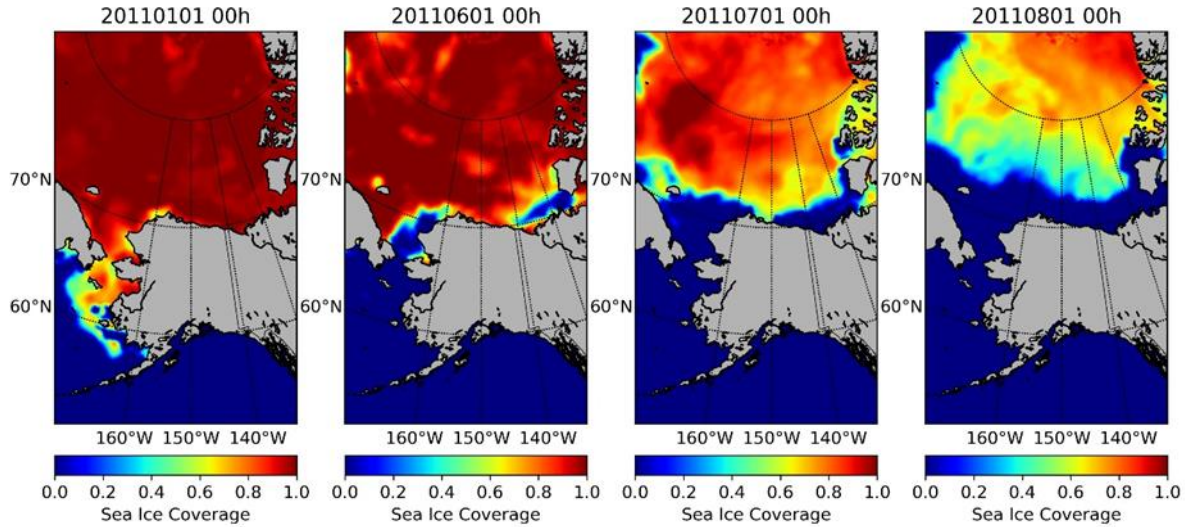


Figure 4.2-2. Sea Ice Coverage From ASRv2 Data Used in the Arctic WW3 Model.

Three other atmospheric reanalysis datasets were evaluated for inclusion into this study, CBHAR, NARR, and WRF-ERA, though after a performance assessment, only ASR and ERA5 were selected for moving forward. This performance assessment is described in more detail in Section 5.2.2.

The WW3 model was setup to run from July through November, based on sea ice extent, for years 2007 – 2019. This monthly delineation was used to allow for more manageable boundary condition and output data files sizes. ASR wind and sea ice data were used for years 2007 – 2016 and ERA5 wind and sea ice data were used for years 2017 – 2019.

For the climate projection simulations, WW3 was run for years 2020 – 2040 for months June through December. 606 output locations were defined, mostly in the nearshore region where water depths are ≤ 100 m and were output at 1-hour increments for the entire simulation period. These output locations were post-processed to produce mean wave parameters (Table 4.2-1), and can be further post-processed to produce 1-D wave spectra, for each of the output locations.

Table 4.2-1. WW3 Mean Wave Parameter Output Variables For All Output Stations.

WW3 Output Variable
Water depth
Current speed and direction
Wind speed and direction
Significant wave height
Mean wavelength
Mean wave period
Dominant wave direction
Dominant wave spreading
Dominant wave frequency
Mean wave direction
Mean wave spreading

4.2.2. Delft3D-FLOW/WAVE Model Setup

The Arctic WW3 model provides an excellent platform to relate regional wind conditions with large scale wave patterns within the Beaufort Sea. To provide higher resolution oceanographic predictions around Drew Point, Delft3D-FLOW and WAVE models were developed to provide nearshore circulation and wave predictions, respectively. To reiterate, Delft3D-WAVE uses SWAN, a proven nearshore and shallow water spectral wave modeling system, as the wave model and is natively coupled to Delft3D-FLOW, providing an efficient computational environment. This coupling of nearshore circulation and wave models, forced by a larger Arctic Ocean scale wave model, allows for the accurate simulation of water levels and wave induced setup along the northern Alaska coastline.

Delft3D-FLOW and WAVE are two separate models, though natively coupled. They have separate model grids, bottom elevations, and boundary conditions, but they do pass relevant information using 2-way coupling. The setup of each model is further described in the sections below.

4.2.2.1. Delft3D-FLOW

For this study, Delft3D-FLOW was chosen as the numerical modeling framework. This is the latest hydrodynamic solver from Deltares and was chosen due to its efficient solving methods, active user base, and most importantly the ability to couple with Delft3D-WAVE to account for the interaction of waves, currents, and water levels. The process for developing the model was similar to that of the WW3 model.

4.2.2.1.1. Delft3D-FLOW Grid and Bathymetry

Delft3D-FLOW utilizes a structured curvilinear mesh comprised of mostly square and rectangular grid cells. This allowed the space to be discretized down to a high resolution adequate for the project needs. The use of small-scale structured grids allows for the representation of complex shorelines and variations in resolution without sacrificing computational efficiency by including additional cells. The structured grid approach combines the advantages of the modelling flexibility of the single-domain unstructured approach with the efficiency and accuracy of the single-domain structured approach (Deltares 2018).

The Delft3D-FLOW structured curvilinear grid was constructed using Deltares' RGFRID and guided in the nearshore by the 2018 Drew Point shoreline polygon (Figure 4.2-3). The Delft3D-FLOW grid, consists of 31,072 elements and Delft3D-FLOW model encompasses an area of the Beaufort Sea adjacent to Drew point and extending northward by ~85 km and east and west along the coast (Figure 4.2-4). At the northernmost extents of the grid, the model has a 2 km resolution. The grid becomes more refined closer the coast and in the region surrounding Drew Point, where the resolution increases to 100 m.

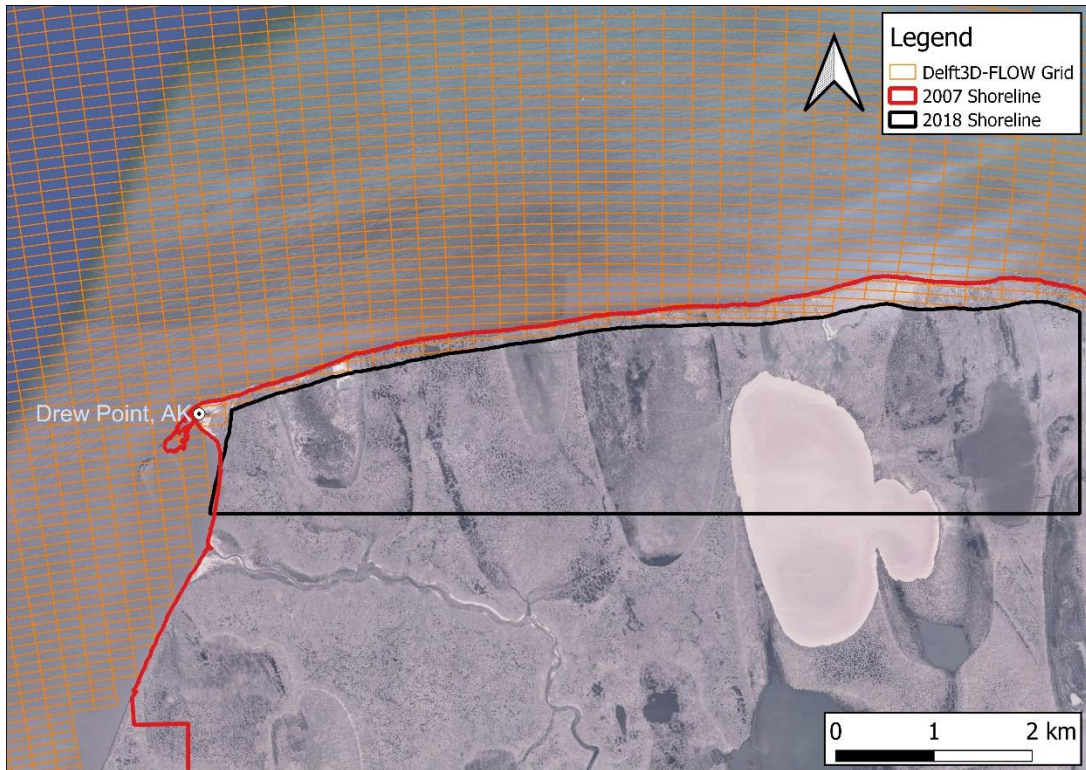


Figure 4.2-3. Delft3D-FLOW Grid in comparison to the Drew Point, AK 2007 and 2018 Shorelines.

The Delft3D-FLOW grid was setup with a single vertical layer. Barnhart et al. 2014a collected measured data during 2009 and 2010 ice free months and found that the nearshore waters offshore of Drew Point rarely have vertical temperature variations greater than 1°C. While there were indications of temperature differences, presumably due to the presence of ice, at the beginning of the ice-free conditions, the water column became well mixed after a single storm event. Water temperature is thought to be an important controlling factor in the rate of coastal erosion; however, the ice-free season nearshore water column was shown to be isothermal during the 2009 and 2010 deployment periods. While water column stratification is shown to exist prior to the ice-free season, during the period of interest (e.g., summer ice-free months), the water column is isothermal as a result of wind mixing. In addition, conductivity, temperature, and depth (CTD) casts around Drew Point were analyzed and found that minimal vertical stratification existed in the nearshore region around Drew Point (Section 2.3.1.8).

Bottom elevations for the Delft3D-FLOW grid were defined from the Alaska Regional Digital Elevation Model (ARDEM) version 2.0 (Figure 4.2-5) (Danielson et al. 2015; Danielson et al. 2008; Danielson et al. 2011). ARDEMv2 uses depths from the International Bathymetric Chart of the Arctic Ocean (IBCAO; Jakobsson et al. 2012) for the Arctic region and has horizontal resolution down to 500 m in the Beaufort Sea region. The ARDEM data were interpolated onto the grid so that each cell has a single depth value. Within the domain, bottom elevations ranged from 200 m near the continental shelf to the north to 0 m along the coastline.

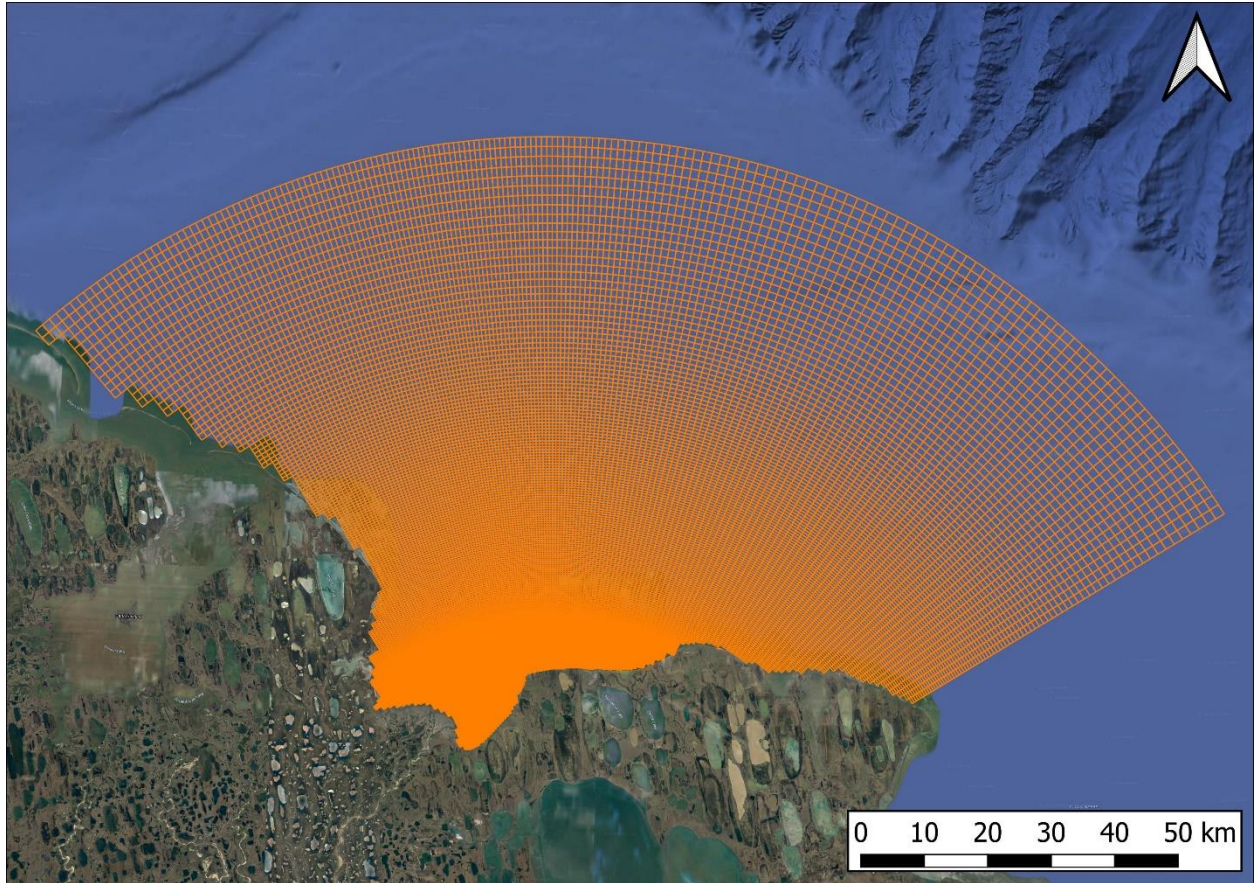


Figure 4.2-4. Delft3D-FLOW Nearshore Circulation Grid.

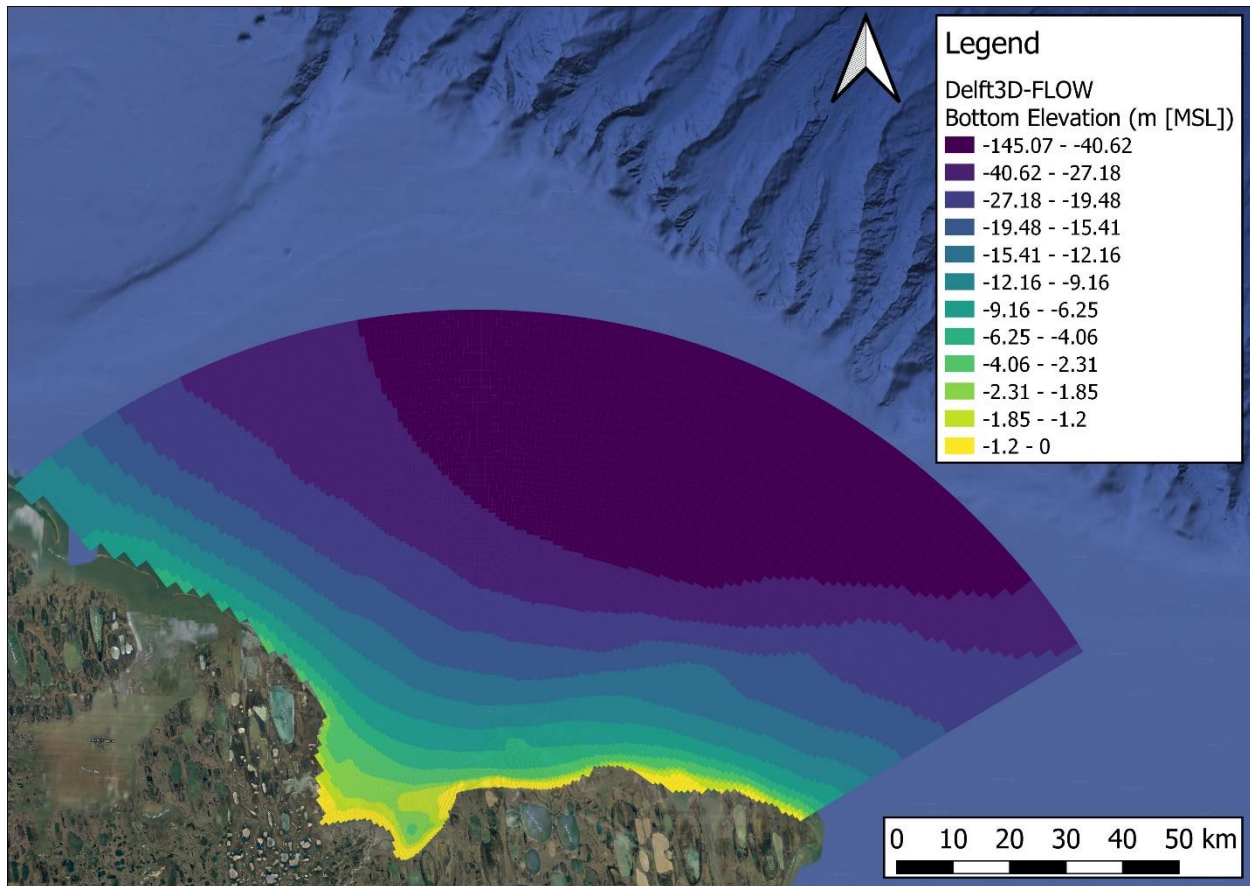


Figure 4.2-5. Delft3D-FLOW Bottom elevations Defined from ARDEMv2.

4.2.2.1.2. Delft3D-FLOW Boundary Conditions

Delft3D-FLOW can incorporate a number of hydrodynamic boundary conditions including water levels, currents, winds, and scalar quantities such as temperature and salinity. Limited measured data in the area of interest requires that some boundary condition data be source from global or basin scale models. In this case NOAA station data were used for water level and GOFS 3.1 data were used to provide water temperature and salinity boundary conditions to the outer extents of the Delft3D-FLOW model. ASR and ERA5 were used to provide wind forcing over the entire model domain for years 2007 – 2016 and 2017 – 2019, July through November, respectively.

The Delft3D-FLOW water level boundary condition were defined from the measured water level data from the NOAA NDBC Prudhoe Bay, AK station (ID #9497645) and were used and applied uniformly across the outer boundaries of the grid.

The GOFS 3.1 water temperature and salinity data were linearly interpolated to locations corresponding to the outer boundaries of the Delft3D-FLOW grid. Data were pulled from the surface layer of the GOFS 3.1 model, representing the top 2 m of the water column. Water temperatures of $\leq 0^{\circ}\text{C}$ were set to 0.001°C to avoid a limitation of the Delft3D modeling suite.

Wind boundary conditions for Delft3D-FLOW hindcasts (2007 – 2019) were derived from the ASR and ERA5 atmospheric reanalysis datasets. The wind component forcing were linearly interpolated

onto the Delft3D-FLOW grid to provide spatially and temporally varying forcing. Sea ice fraction data were not applied as a boundary condition to Delft3D-FLOW or WAVE.

For the climate projection nearshore simulations, the GFDL-CM3 GCM projections were used to provide wind forcing and the CanESM2 GCM were used for the water temperature and salinity boundary conditions. These simulations were set to run from 2020 – 2100, June through December.

4.2.2.1.3. Delft3D-FLOW Initial Conditions

Initial conditions provide the starting conditions within the domain. Data were provided for water level, currents, salinity, and water temperature for start of the simulation. Water level data, from the NOAA Prudhoe Bay, AK station, we applied uniformly across the model domain. Currents were set to 0 at initialization. Salinity and water temperature values were linearly interpolated from the GOFS 3.1 dataset onto the Delft3D-FLOW grid.

4.2.2.2. Delft3D-WAVE

Delft3D-WAVE was used, coupled with Delft3D-FLOW, to provide nearshore wave predictions. Delft3D-WAVE, uses SWAN, a third-generation wave propagation model that determines the sea state of random, short-crested waves. SWAN can calculate the wave field due to prescribed wave conditions at the boundaries or due to the application of wind conditions over the ocean surface. Additionally, the water level set-up due to waves in shallow waters as well as the net momentum flux (radiation shear stress) can be resolved and incorporated directly into Delft3D-FLOW simulations through the two-way coupling of Delft3D-FLOW and WAVE.

The model options and physics packages chosen for the Delft3D-WAVE domain include: 3rd generation physics, Battjes-Janssen depth induced breaking, Lumped Triad Interaction method, JONSWAP bottom friction, quadruplets, Komen et al. white capping, and refraction. Additional details on these model options and physics packages can be found in Deltares 2018.

4.2.2.2.1. Delft3D-WAVE Grid and Bathymetry

To facilitate the coupling with Delft3D-FLOW for the Drew Point study area, a separate curvilinear structured mesh comprised of mostly square and rectangular grid cells was constructed. This allowed the space to be discretized down to a high resolution adequate for the project needs. The use of small-scale structured grids allows for the representation of complex shorelines and variations in resolution without sacrificing computational efficiency by including additional cells.

The Delft3D-WAVE model encompasses an area of the Beaufort Sea adjacent to Drew point and extending outwards to the east and west along the coast (Figure 4.2-6). At the northernmost extents of the grid, the model has a 3 km resolution. The grid becomes more refined closer the coast and in the region surrounding Drew Point, where the resolution increases to 400 m.

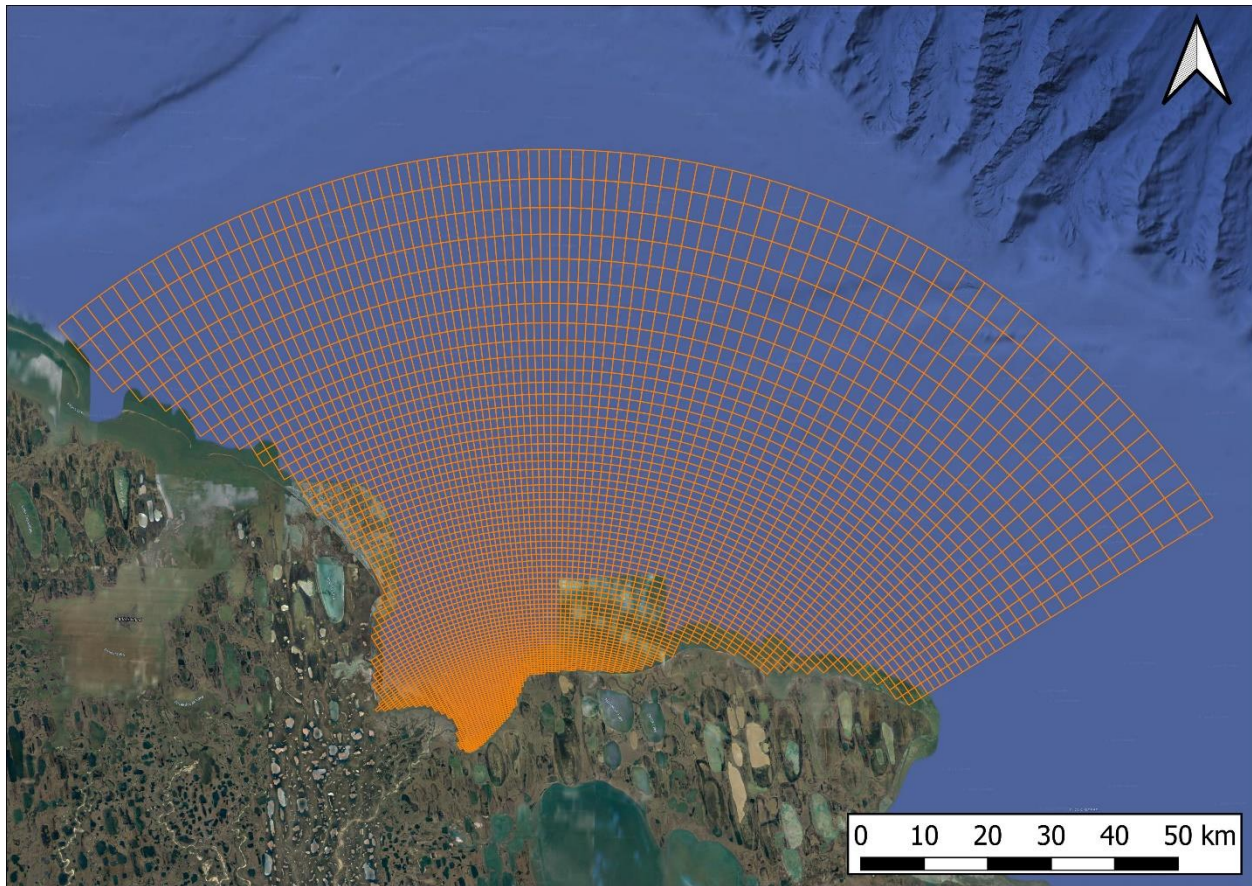


Figure 4.2-6. Delft3D-WAVE Nearshore Spectral Wave Grid.

Bottom elevations for the Delft3D-WAVE grid were defined from the ARDEM, using the same method as for the Delft3D-FLOW grid. The ARDEM data were interpolated onto the grid so that each cell has a single depth value. Within the domain, bottom elevations ranged from 200 m near the continental shelf to the north to 0 m along the coastline.

4.2.2.2.2. *Delft3D-WAVE Boundary Conditions*

Delft3D-WAVE can have boundary conditions of wave information, water level, and currents. When coupled with Delft3D-FLOW, wind, water level, and currents information are passed from the FLOW side. For this application, only wave information is provided as a wave boundary condition, with other parameters passed to Delft3D-WAVE with the native coupling.

Along the outer boundary of the Delft3D-WAVE grid, mean wave parameters (i.e., significant wave height, peak wave period, peak wave direction, directional spreading), were applied from WW3. The WW3 model provided wave boundary conditions at 1-hour intervals at each grid cell along the outer model boundary. Delft3D-WAVE ingested these mean wave parameters at the boundary and assumed a JONSWAP spectral shape with a peak enhancement factor of 3.3 for propagating the wave energy into the nearshore domain. A JONSWAP spectral shape and peak enhancement factor of 3.3 is typical for this environment.

Initial conditions are not defined for the Delft3D-WAVE domain. The initial conditions set for the Delft3D-FLOW model are passed to the wave model and the wave conditions are assumed to be calm.

4.2.3. Delft3D-FLOW/WAVE Model Simulations

The coupled Delft3D-FLOW/WAVE nearshore circulation and wave model was setup to run yearly from 2007 – 2019, only during the same month range of the WW3 simulations, July through November. ASR wind data were used for years 2007 – 2016 and ERA5 wind data were used for years 2017 – 2019. GOFS 3.1 reanalysis data were used for 2007 – 2015 and GOFS 3.1 analysis data were used for 2016 – 2019. For the climate projection simulations, the coupled Delft3D-FLOW/WAVE model was setup to run from 2020 – 2040, June through December.

Delft3D-WAVE was setup to resolve 24 frequency bins ranging from 0.05 – 1 Hz and was run in stationary computational mode which allows for the coupling of the Delft3D-FLOW results. A total of 58 output locations were defined, mainly focusing on the nearshore region and specific data locations (Figure 4.2-7). In the Drew Point nearshore region, within 300 m of the shoreline, model output points were defined along shore and cross shore to allow for comparisons of predicted values in the along shore and cross shore directions (Figure 4.2-8). Variables from Delft3D-FLOW (i.e., water level, currents, salinity, water temperature) were output at 15-minute intervals and variables from Delft3D-WAVE (i.e., mean wave parameters, 1D wave spectra) were output at 1-hour increments for the entire simulation period.

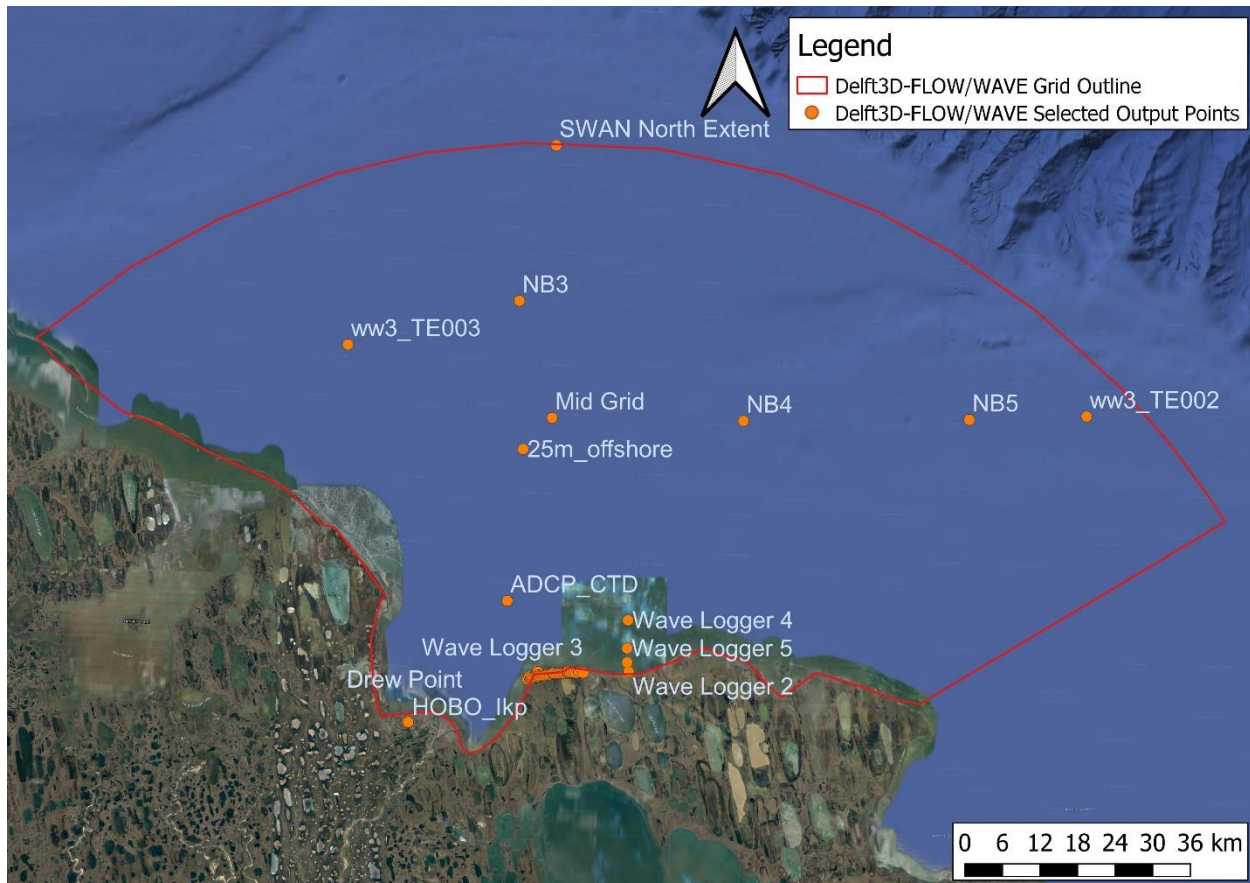


Figure 4.2-7. Final Output Locations For Delft3D-FLOW/WAVE Simulations and Delft3D-FLOW/WAVE Grid Outline.

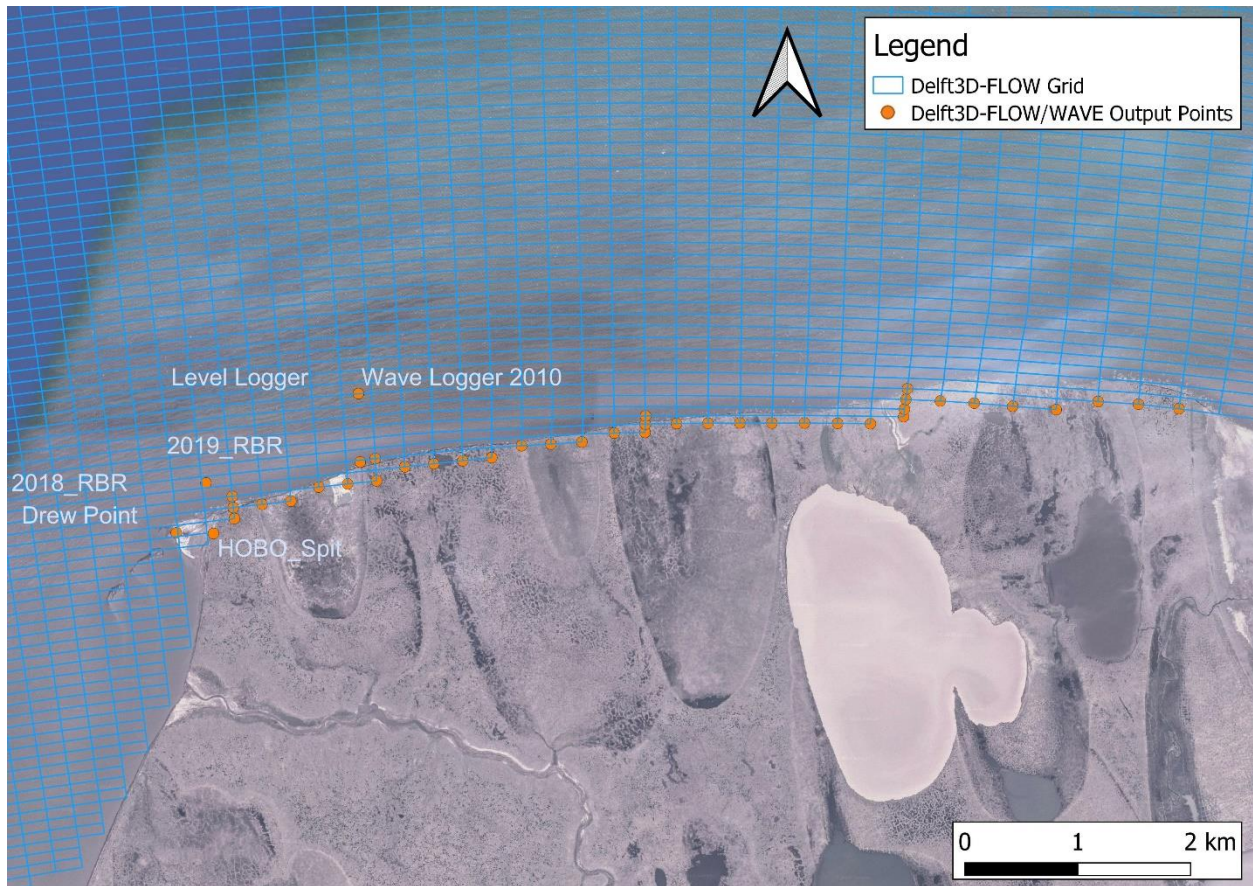


Figure 4.2-8. Final Output Locations For Delft3D-FLOW/WAVE Simulations and Delft3D-FLOW Grid in the Drew Point, AK Nearshore Region.

The final Delft3D-FLOW/WAVE product delivered to the terrestrial model was a 2 Hz water surface elevation (η), salinity, and water temperature time series. The water surface elevation, or η , was computed from the 1D variance density, output hourly from the WAVE side and the 15-minute water level output from the FLOW side. η was computed on a 2 Hz time step for each hour output over the simulation period. Then the 15 min water level signal from the FLOW side of the model was linearly interpolated onto a 2 Hz time step and added to the η signal. In addition, the 15 min salinity and water temperature from the FLOW side of the model were linearly interpolated onto a 2 Hz time step. This final time series product provided a 2 Hz signal of salinity, water temperature, and water surface elevation with tidal, wind wave, and swell components. The equations used for the calculation of the 2 Hz η signal are shown below:

$$\eta(t) = \sum_S a_S \cos(2\pi f_S t + \theta_S) \quad \text{Equation 4.2-1}$$

$$a_S = \sqrt{2 S_f \Delta f} \quad \text{Equation 4.2-2}$$

$$\theta_S = \text{random}(0, 2\pi) \quad \text{Equation 4.2-3}$$

where $\eta(t)$ is the time varying eta, as is the amplitude of the surface displacement calculated using S_f , the variance density at each frequency, Δf is the difference in each frequency, f_s is the frequency, t is the time, Θ_s is the wave phase represented by a random number between 0 and 2π , computed at each frequency S .

4.2.4. WW3 and Delft3D-FLOW/WAVE Simulations

Once the WW3 and Delft3D-FLOW/WAVE boundary and initial conditions were all defined (Table 4.2-2), the workflow for running the models from 2007 – 2019, and climate projection simulations were setup and initialized (Figure 4.2-9). Upon running the models for the 2007 – 2019 time periods, the model predictions were compared to the available measured data in the Beaufort Sea and along the North Slope of Alaska to evaluate the model performance, Section 5.2. Once the model performance was evaluated and the model prediction were shown to accurately reproduce the measured data, the data were processed and provided to the terrestrial model.

The comparisons of the WW3 and Delft3D-FLOW/WAVE model to measured data and internal comparisons is discussed in detail in Section 5.2.

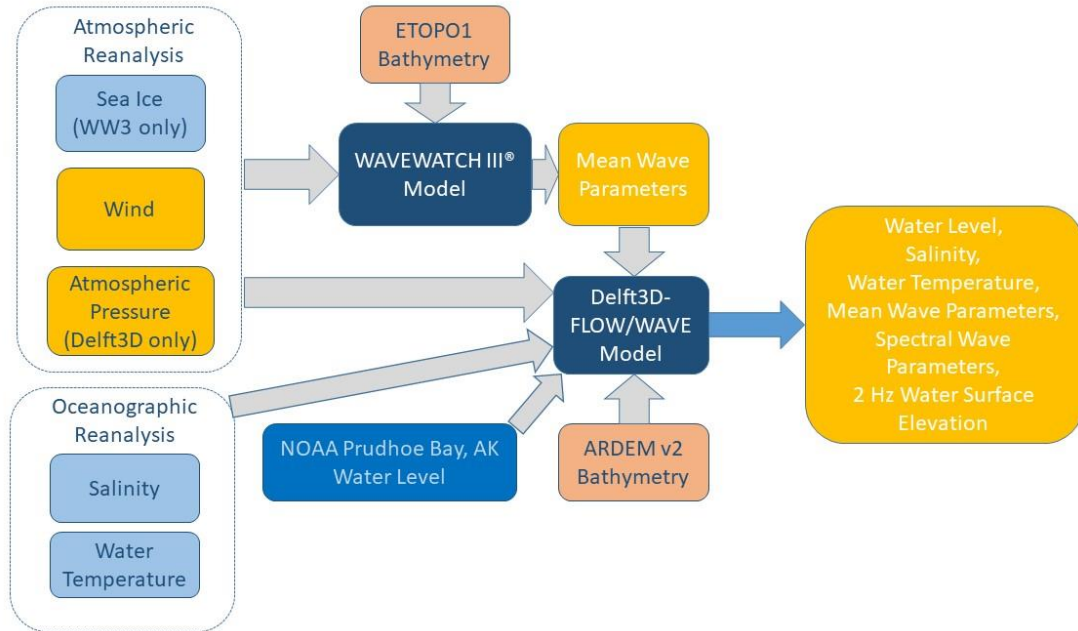


Figure 4.2-9. Arctic coastal Erosion Oceanographic Modeling Suite Workflow.

Table 4.2-2. Descriptive Information about WW3 and Delft3D-FLOW/WAVE Models in the Oceanographic Modeling Suite.

	Bathymetry Source	Wind / Sea Ice BC Source	Salinity / Temperature BC Source	Water Level BC Source	Waves BC Source	Smallest resolution
WW3	ETOPO-1 (1 arc-minute resolution)	ASR/ERA5 (15 & 18km) 3-hourly				18km
Delft3D-FLOW	ARDEM v2.0 (500m resolution interpolated)	ASR/ERA5 (15 & 18km) 3-hourly	HYCOM 3-hourly	NOAA Prudhoe Bay Tide Gauge Hourly		0.1km
Delft3D-WAVE	ARDEM v2.0 (500m resolution interpolated)	ASR/ERA5 (15 & 18km) 3-hourly			WW3	0.2km

4.3. Terrestrial Model – Albany

4.3.1. Thermal Model

Team Member Author: Jennifer Frederick (SNL)

Contributors: Alejandro Mota (SNL), Irina Tezaur (SNL)

4.3.1.1. Strong Form

The governing equation for heat transfer by conduction in a saturated porous media including water-ice phase change is described by

$$\overline{\rho c} \frac{\partial T}{\partial t} = \nabla \cdot (K \cdot \nabla T) + \vartheta \quad \text{Equation 4.3-1}$$

where ρ is the bulk density, c is the bulk specific heat, T is the temperature, K is the bulk thermal diffusivity tensor, and ϑ is the heat source term due to phase change (latent heat). The bar over the term $\overline{\rho c}$ indicates a volume-averaged mixture model (e.g. bulk) for the density and specific heat of each material component. The possible material components include water and ice in the pore space, ϕ , and rock mineral grains (e.g., sand, silt, clay) in the solid, $1 - \phi$, where porosity is defined as

$$\phi = V_{void} / V_{total} \quad \text{Equation 4.3-2}$$

the ratio of the void volume V_{void} to the total volume V_{total} .

4.3.1.2. Thermal Model Variational Form

The standard variational form of $(\overline{\rho c} - \rho_{ice} L_f \frac{\partial i}{\partial T}) \frac{\partial T}{\partial t} = \nabla \cdot (K \cdot \nabla T)$ equation 4.3-43 is formulated by first defining the residual form as

$$R := (\overline{\rho c}') \frac{\partial T}{\partial t} - \nabla \cdot (K \cdot \nabla T) \quad \text{Equation 4.3-3}$$

where R is the residual which we want to minimize. Let $\xi \in \mathcal{V}$ be test functions, such that they are square-integrable and have a square-integrable first derivative. The weak form is

$$R := \int_{\Omega} (\overline{\rho c}') \frac{\partial T}{\partial t} \xi \, dV - \int_{\Omega} \nabla \cdot (K \cdot \nabla T) \xi \, dV \quad \text{Equation 4.3-4}$$

Where Ω represents the domain. By identity,

$$\nabla \cdot (K \cdot \nabla T) \xi = \nabla \cdot [\xi (K \cdot \nabla T)] - (\nabla \xi) \cdot (K \cdot \nabla T) \quad \text{Equation 4.3-5}$$

Inserting this identity to replace the second term on the right-hand side in

$R := \int_{\Omega} (\overline{\rho c}') \frac{\partial T}{\partial t} \xi \, dV - \int_{\Omega} \nabla \cdot (K \cdot \nabla T) \xi \, dV$ equation 4.3-4, the weak form becomes

$$R := \int_{\Omega} (\overline{\rho c}') \frac{\partial T}{\partial t} \xi \, dV - \int_{\Omega} \nabla \cdot [\xi (K \cdot \nabla T)] \, dV + \int_{\Omega} (\nabla \xi) \cdot (K \cdot \nabla T) \, dV \quad \text{Equation 4.3-6}$$

Next, the divergence theorem is applied to the second term on the right-hand side in

$R := \int_{\Omega} (\overline{\rho c}') \frac{\partial T}{\partial t} \xi \, dV - \int_{\Omega} \nabla \cdot [\xi (K \cdot \nabla T)] \, dV + \int_{\Omega} (\nabla \xi) \cdot (K \cdot \nabla T) \, dV$ equation 4.3-6 and the weak form becomes

$$R := \int_{\Omega} (\overline{\rho c}') \frac{\partial T}{\partial t} \xi \, dV - \int_{\Gamma} [\xi (K \cdot \nabla T)] \cdot \mathbf{n} \, dA + \int_{\Omega} (\nabla \xi) \cdot (K \cdot \nabla T) \, dV \quad \text{Equation 4.3-7}$$

where \mathbf{n} is the outward unit normal on the boundary surface Γ . The term on the boundary surface is equivalent to a heat flux boundary condition where,

$$-(K \cdot \nabla T) \cdot \mathbf{n} = \bar{q} \quad \text{on } \Gamma \quad \text{Equation 4.3-8}$$

Finally, the standard variational form of the thermal problem expressed as a residual is

$$R := \int_{\Omega} (\overline{\rho c}') \frac{\partial T}{\partial t} \xi \, dV + \int_{\Gamma} \xi \bar{q} \, dA + \int_{\Omega} (\nabla \xi) \cdot (K \cdot \nabla T) \, dV \quad \text{Equation 4.3-9}$$

4.3.1.3. Salinity Enhanced Melting

The transport of salt is not explicitly modeled in ACE as an additional governing equation, however, the effect of salt from the ocean water in contact with the bluff face is treated as an enhanced diffusion process on the faces of the bluff grid cells exposed to ocean water. This parameterization represents the mechanical force of the seawater entering the permafrost soil and reducing its melting temperature, as the process of molecular diffusion of salt at the boundary is orders of magnitude slower and likely plays no significant role in the erosion of the bluff face.

An enhanced diffusion model is applied only to the grid cell faces that are exposed to the water. Salt transport by diffusion is described by

$$\frac{\partial \mathbf{c}}{\partial t} = \nabla \cdot (\mathbf{D}_e \cdot \nabla \mathbf{c}) \quad \text{Equation 4.3-10}$$

where \mathbf{c} is the salt concentration and \mathbf{D}_e is an enhanced salt diffusion coefficient. Assuming the grid cell represents a control volume,

$$\int_V \frac{\partial \mathbf{c}}{\partial t} dV = \int_V \nabla \cdot (\mathbf{D}_e \cdot \nabla \mathbf{c}) dV = \int_S \mathbf{D}_e \cdot \nabla \mathbf{c} \cdot \mathbf{n} dS \quad \text{Equation 4.3-11}$$

Furthermore, assuming that the flux of salt over the surface integral only occurs across the face of the grid cell exposed to the water, then the change in the salt concentration over time inside this grid cell can be approximated as,

$$\mathbf{c}^{t+1} = \mathbf{c}^t + \mathbf{D}_e \frac{dc}{dx} A \frac{\Delta t}{V} \quad \text{Equation 4.3-12}$$

where $\frac{dc}{dx}$ is the gradient in salt concentration between the ocean water and the grid cell, A is the cross-sectional area of the face of the grid cell exposed to ocean water, Δt is the time step size, and V is the grid cell volume.

4.3.2. Mechanical Model

Team Member Author: Alejandro Mota (SNL)

Contributors: Jennifer Frederick (SNL), Irina Tezaur (SNL), Chris Flanary (Integral)

4.3.2.1. Mechanical Model Variational Form

We start by defining the standard finite deformation variational formulation. Let $I := \{t \in [t_0, t_N]\}$ be a closed time interval with $t_0 < t_N$, and $t_0, t_N \in \{R\}$. Then consider a body as the regular open set $\Omega \subset \{R\}^3$ undergoing a motion described by the mapping $\mathbf{x} = \boldsymbol{\varphi}(\mathbf{X}, t): \Omega \times I \rightarrow \{R\}^3$, where $\mathbf{X} \in \Omega$ and $t \in I$. Assume that the boundary of the body is $\partial\Omega = \partial_\varphi\Omega \cup \partial_T\Omega$ with unit normal \mathbf{N} , where $\partial_\varphi\Omega$ is a prescribed position boundary, $\partial_T\Omega$ is a prescribed traction boundary, and $\partial_\varphi\Omega \cup \partial_T\Omega = \partial\Omega$. The prescribed boundary positions or Dirichlet boundary conditions are $\boldsymbol{\chi}: \partial_\varphi\Omega \times I \rightarrow \{R\}^3$. The prescribed boundary tractions or Neumann boundary conditions are $\mathbf{T}: \partial_T\Omega \times I \rightarrow \{R\}^3$. Let $\mathbf{F} := \nabla\boldsymbol{\varphi}$ be the deformation gradient. Let the initial position and velocity at time t_0 be $\mathbf{x}_0 \equiv \mathbf{X}: \Omega \rightarrow \{R\}^3$, and $\mathbf{v}_0: \Omega \rightarrow \{R\}^3$, correspondingly. Let also $\rho_0\mathbf{B}: \Omega \rightarrow \{R\}^3$ be the body force, with ρ_0 the mass density in the reference configuration. Furthermore, introduce the kinetic energy of the body as

$$T(\boldsymbol{\varphi}) := \frac{1}{2} \int_\Omega \rho_0 \dot{\boldsymbol{\varphi}} \cdot \dot{\boldsymbol{\varphi}} dV \quad \text{Equation 4.3-13}$$

and its potential energy as

$$V(\boldsymbol{\varphi}) := \int_\Omega A(\mathbf{F}, \mathbf{Z}) dV - \int_\Omega \rho_0 \mathbf{B} \cdot \boldsymbol{\varphi} dV - \int_{\partial_T\Omega} \mathbf{T} \cdot \boldsymbol{\varphi} dS \quad \text{Equation 4.3-14}$$

in which $A(\mathbf{F}, \mathbf{Z})$ is the Helmholtz free-energy density and \mathbf{Z} is a collection of internal variables. The Lagrangian function of the body is then

$$L(\boldsymbol{\varphi}, \dot{\boldsymbol{\varphi}}) := T(\dot{\boldsymbol{\varphi}}) - V(\boldsymbol{\varphi}) \quad \text{Equation 4.3-15}$$

which gives rise to the action functional

$$\mathbf{S}[\boldsymbol{\varphi}] := \int_I \mathbf{L}(\boldsymbol{\varphi}, \dot{\boldsymbol{\varphi}}) dt \quad \text{Equation 4.3-16}$$

According to the Variational Principle of Hamilton, the equation of motion is obtained by finding the critical point of the action functional $\mathbf{S}[\boldsymbol{\varphi}]$ over the Sobolev space $W_2^1(\Omega \times I)$ that is comprised of all functions that are square-integrable and have square-integrable first derivatives Marsden & Ratiu (1999) define

$$\mathcal{S} := \{\boldsymbol{\varphi} \in W_2^1(\Omega \times I): \boldsymbol{\varphi} = \boldsymbol{\chi} \text{ on } \partial_\varphi \Omega \times I; \boldsymbol{\varphi} = \boldsymbol{x}_0 \text{ on } \Omega \times t_0\} \quad \text{Equation 4.3-17}$$

and

$$\mathcal{V} := \{\boldsymbol{\xi}_i \in W_2^1(\Omega \times I): \boldsymbol{\xi}_i = \mathbf{0} \text{ on } \partial_\varphi \Omega \times I \cup \Omega \times t_0\} \quad \text{Equation 4.3-18}$$

where $\boldsymbol{\xi}_i$ is a test function. This leads to

$$\begin{aligned} \delta S &:= DS[\boldsymbol{\varphi}](\boldsymbol{\xi}) = \int_I \left(\frac{\partial L}{\partial \boldsymbol{\varphi}} \cdot \boldsymbol{\xi} + \frac{\partial L}{\partial \dot{\boldsymbol{\varphi}}} \cdot \dot{\boldsymbol{\xi}} \right) dt = \int_I \left(\frac{\partial L}{\partial \boldsymbol{\varphi}} - \frac{d}{dt} \frac{\partial L}{\partial \dot{\boldsymbol{\varphi}}} \right) \cdot \boldsymbol{\xi} dt \\ &= \int_I \left[\int_\Omega (\rho_0 \mathbf{B} \cdot \boldsymbol{\xi} - \mathbf{P} : \nabla \boldsymbol{\xi}) dV + \int_\Omega \rho_0 \dot{\boldsymbol{\varphi}} \cdot \dot{\boldsymbol{\xi}} dV + \int_{\partial_T \Omega} \mathbf{T} \cdot \boldsymbol{\xi} dS \right] dt = 0 \\ &= \int_I \left[\int_\Omega (\nabla \cdot \mathbf{P} + \rho_0 \mathbf{B} - \rho_0 \dot{\boldsymbol{\varphi}}) \cdot \boldsymbol{\xi} dV + \int_{\partial_T \Omega} \mathbf{T} \cdot \boldsymbol{\xi} dS \right] dt = 0 \quad \text{Equation 4.3-19} \end{aligned}$$

where $\mathbf{P} = \partial A / \partial \mathbf{F}$ denotes the first Piola-Kirchhoff stress. The Euler-Lagrange equation corresponding to $\mathbf{S}[\boldsymbol{\varphi}] := \int_I \mathbf{L}(\boldsymbol{\varphi}, \dot{\boldsymbol{\varphi}}) dt$ Equation 4.3-16 is then

$$\nabla \cdot \mathbf{P} + \rho_0 \mathbf{B} = \rho_0 \dot{\boldsymbol{\varphi}} \text{ in } \Omega \times I \quad \text{Equation 4.3-20}$$

with the initial conditions

$$\boldsymbol{\varphi}(X, t_0) = \boldsymbol{x}_0 \text{ in } \Omega \quad \text{Equation 4.3-21}$$

$$\dot{\boldsymbol{\varphi}}(X, t_0) = \dot{\boldsymbol{x}}_0 \text{ in } \Omega \quad \text{Equation 4.3-22}$$

and the boundary conditions

$$\boldsymbol{\varphi}(X, t) = \boldsymbol{\chi} \text{ on } \partial_\varphi \Omega \times I \quad \text{Equation 4.3-23}$$

$$\mathbf{P}\mathbf{N} = \mathbf{T} \text{ on } \partial_T \Omega \times I \quad \text{Equation 4.3-24}$$

4.3.2.2. Dynamic Wave Pressure

Predictions from the oceanographic coupled model were used to compute pressure due to surge water levels and wave action on vertical coastal structures, representative of the bluff face along the coastline of Drew Point, Alaska. The peak pressure exerted on the bluff face, at some height above the mean water level, depending on the wave height is only for a very short duration, usually 0.01 to 0.03 seconds, and can exceed several hundred kN/m² (Partensky 1989). Pressure over a range of heights along the bluff face were calculated according to the following methodology.

Following the methodology published in Partensky 1989, the peak pressure, p_c , pressure at mean water level, p_o , and pressure at the bottom of the bluff face, the cliff toe, p_s , were computed using the following equations:

$$p_c = \frac{\rho H_b}{2t_1} (gh_s)^{1/2} \quad \text{Equation 4.3-25}$$

$$p_o = \frac{\pi \rho H_b^2}{t_1 L} (gh_s)^{1/2} \quad \text{Equation 4.3-26}$$

$$p_s = \frac{\pi \rho H_b^2}{t_1 L \cosh kh_s} (gh_s)^{1/2} \quad \text{Equation 4.3-27}$$

Where ρ is the density of seawater, set to 1025 kg/m³, H_b is set as the breaking wave height, t_1 is the duration of the impact, set as 0.04 seconds, g is the gravitational constant, h_s is the dynamically changing water contact history on the bluff face, L is the wavelength, computed using the predicted water level and wave period, and k is the wave number, computed using the predicted wave period.

The wave pressure Neumann BC to be implemented at the bluff face is as follows:

$$p(z) = \begin{cases} p_0 + m_1 z, & -h_s \leq z \leq 0 \\ p_0 + m_2 z, & 0 \leq z \leq h_c \\ m_3(z - h_c - 0.5H_b), & h_c \leq z \leq h_c + 0.5H_b \end{cases} \quad \text{Equation 4.3-28}$$

where

$$m_1 = \frac{p_0 - p_s}{h_s} \quad \text{Equation 4.3-29}$$

$$m_2 = \frac{p_c - p_0}{h_c} \quad \text{Equation 4.3-30}$$

$$m_3 = -\frac{2p_c}{H_b} \quad \text{Equation 4.3-31}$$

An overview of all of the wave pressure variables is given in Table 4.3-1.

Table 4.3-1. Overview of dynamic wave pressure variables.

Parameter	Interpretation	Value
t_1	impact duration	0.04 s
H_b	breaking wave height	1.5 m
g	gravity	9.806 m/s ²
ρ	density of water	1025 kg/m ³
L	wave length	$L_0 \tanh(kb)$ (or $8H_b$ for now)
h_s	water height	given from data (function of time)
h_c	height above water of the maximum pressure	$0.7H_b$
k	wave number	$2\pi/L_0$
L_0	wave length of deep water wave	$gT_p^2/2\pi$
T_p	peak wave period	from oceanographic model

The oceanographic and terrestrial models will be corrected to a vertical datum in which 0 represents the base of the bluff face, or the cliff toe. This assumption means that the h_s value from above, representative of the hydrostatic pressure exerted on the bluff face due to water contact, is 0 unless there is a storm surge, or during higher tides. It was also assumed that given the low slope of the bottom topography in the Drew Point nearshore region, the direction of wave propagation was

perpendicular to the shoreline and bluff face. A diagram from Partensky 1989 shows the relationship of the various calculated and predicted parameters along a vertical coastal structure (Figure 4.3-1).

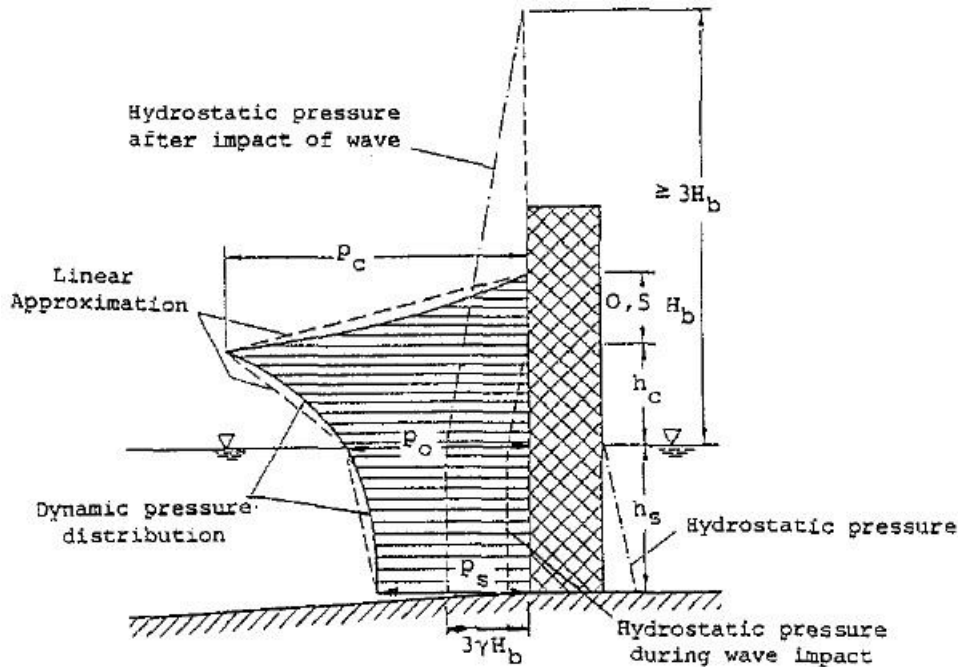


Figure 4.3-1. Diagram of dynamic pressure distribution along a vertical coastal structure as a result of surge and wave action (Partensky 1989).

4.3.3. Material Model

Team Member Author: Alejandro Mota (SNL), Jennifer Frederick (SNL)

Contributors: Jennifer Frederick (SNL), Irina Tezaur (SNL)

4.3.3.1. Mechanical Material Model

The full technical description of the mechanical material model can be found in Appendix A. It describes the mechanical constitutive model used for ice and permafrost soil materials, which are modeled using the standard J_2 plasticity model extended to the large-deformation regime.

Novel to the ACE model, the yield strength of permafrost is a function of the ice volume fraction, or the ice saturation. In this way, deformation and failure are coupled to the thermal state of the material, as temperature and salinity determine the ice saturation in the permafrost soil.

4.3.3.2. Thermal Mixture Models

The water saturation, w , or ice saturation, i , is defined as the fraction of water or ice occupying the pore space and can vary from 0 to 1. The volume fraction of each material component occupying the pore space is $S_{ice} = \phi i$ for ice, and $S_{water} = \phi w$ for water. The volume fraction of each material component forms the basis of the mixing model formulations.

The mixture model for the bulk density, ρ_{bulk} , and bulk specific heat, c_{bulk} , is then defined as

$$\rho_{bulk} = \phi(i\rho_{ice} + w\rho_{water}) + (1 - \phi)\rho_{soil} \quad \text{Equation 4.3-32}$$

$$c_{bulk} = \phi(ic_{ice} + wc_{water}) + (1 - \phi)c_{soil} \quad \text{Equation 4.3-33}$$

where ρ_{ice} is the density of ice, ρ_{water} is the density of water, ρ_{soil} is the density of the rock mineral grains (soil), c_{ice} is the specific heat of ice, c_{water} is the specific of heat water, and c_{soil} is the specific heat of the rock mineral grains (soil). The values for the soil density, ρ_{soil} , and the soil specific heat, c_{soil} , can be obtained with knowledge of the soil composition:

$$\rho_{soil} = f_{peat}\rho_{peat} + f_{sand}\rho_{sand} + f_{silt}\rho_{silt} + f_{clay}\rho_{clay} \quad \text{Equation 4.3-34}$$

$$c_{soil} = f_{peat}c_{peat} + f_{sand}c_{sand} + f_{silt}c_{silt} + f_{clay}c_{clay} \quad \text{Equation 4.3-35}$$

where f_{peat} , f_{sand} , f_{silt} , and f_{clay} are the soil composition fractions of peat, sand, silt, and clay, respectively. The soil compositions range from 0 to 1. Table 4.3-2 and Table 4.3-3 provide the values used for the density and specific heat of each permafrost component.

Table 4.3-2. Density values for each permafrost constituent.

Constituent	Density [kg/m ³]
peat	250
sand	2650
silt	2650
clay	2650
ice	920
water	1000

Table 4.3-3. Specific heat values for each permafrost constituent (Robertson 1988).

Constituent	Heat Capacity [J/kg/K]
peat	1.9e3
sand	0.7e3
silt	0.7e3
clay	0.6e3
ice	2.09e3
water	4.18e3

The bulk thermal diffusivity tensor K can account for anisotropic materials and is also defined by a mixture model based on the thermal diffusivity of each material component. However, the mixture model for K is not a simple volume-average of the thermal diffusivity of each material component since the connected structure of the solid phase components (soil) can conduct heat more favorably than the materials in the pore space. It is defined as

$$K_{bulk} = K_{ice}^{i\phi} K_{water}^{w\phi} K_{soil}^{1-\phi} \quad \text{Equation 4.3-36}$$

where K_{ice} is the thermal conductivity of ice, K_{water} is the thermal conductivity of water, and K_{soil} is the thermal conductivity of the rock mineral grains (soil). Similar to the soil density and soil specific heat, the soil thermal conductivity is obtained by

$$K_{soil} = f_{peat}K_{peat} + f_{sand}K_{sand} + f_{silt}K_{silt} + f_{clay}K_{clay} \quad \text{Equation 4.3-37}$$

Table 4.3-4 provides the values used for the thermal conductivity of each permafrost component.

Table 4.3-4. Thermal conductivity values for each permafrost constituent (Robertson 1988; O'Connor et al. 2020).

Constituent	Thermal Conductivity [W/K/m]
peat	0.08
sand	8.0
silt	4.9
clay	0.4
ice	1.6
water	0.58

The source term ϑ is defined according to

$$\vartheta = \rho_{ice}L_f \frac{\partial i}{\partial t} = \rho_{ice}L_f \frac{\partial i}{\partial T} \frac{\partial T}{\partial t} \quad \text{Equation 4.3-38}$$

where ρ_{ice} is ice density, L_f is the latent heat of formation (water-ice phase change), and i is ice saturation (which varies from 0 to 1). The function $\frac{\partial i}{\partial T}$ describes how ice saturation changes with temperature. This function is non-zero only during phase change and must be smooth and continuous.

The freezing of saturated soils is a very complex process and depends on a number of factors, including but not limited to pore fluid salinity, sediment type, and pore size. In general, pore water freezing is mainly determined by the solution properties for pores larger than 0.2 μm , but for pores smaller than 0.2 μm , the effect of pore size on water freezing becomes important (Wan & Yang 2020). Experimental studies by Darrow et al. (2009), Darrow (2011), and Kruse & Darrow (2017) are used as the basis for soil freezing curves for clay and silt. Furthermore, we assume a narrow, approximately 4C width freezing curve for sand and peat material. We treat sand and peat similarly because of the large pore size in both materials.

A generalized logistic curve is used to describe the soil freezing curve, which gives the ice saturation as a function of current temperature (T) and freezing temperature (T_f).

$$i(T, T_f) = A + \frac{K-A}{(C+Qe^{-B(T-T_f)})^{1/v}} \quad \text{Equation 4.3-39}$$

The values of the equation parameters control the general shape of the curve. The values chosen for the parameters are:

Parameter:	A	K	C	Q	B
Value:	0.0	1.0	1.0	0.001	10.0

The only parameter that is sediment type dependent is v , which controls the tail drop off. Based on the shapes in *Darrow (2011)*, the following parameters were chosen to represent clay and silt. Furthermore, for sand and peat, the value of v was chosen to give an approximate 4C width to the curve.

Sediment Type:	clay	silt	sand/peat
v :	70.0	25.0	5.0

Within the ACE source code, the soil freezing curve equation is calculated after determining the bulk value of v , which is computed as

$$v_{bulk} = f_{clay}v_{clay} + f_{silt}v_{silt} + f_{sand}v_{sand} + f_{peat}v_{peat} \quad \text{Equation 4.3-40}$$

where f represents the sediment fraction in the bulk soil mixture (given as model input).

Figure 4.3-2, Figure 4.3-3, Figure 4.3-4, and Figure 4.3-5 show the soil freezing curves for pure clay, pure silt, pure sand/peat, along with several hypothetical soil mixtures. It is assumed the freezing temperature is 0C for all plots.

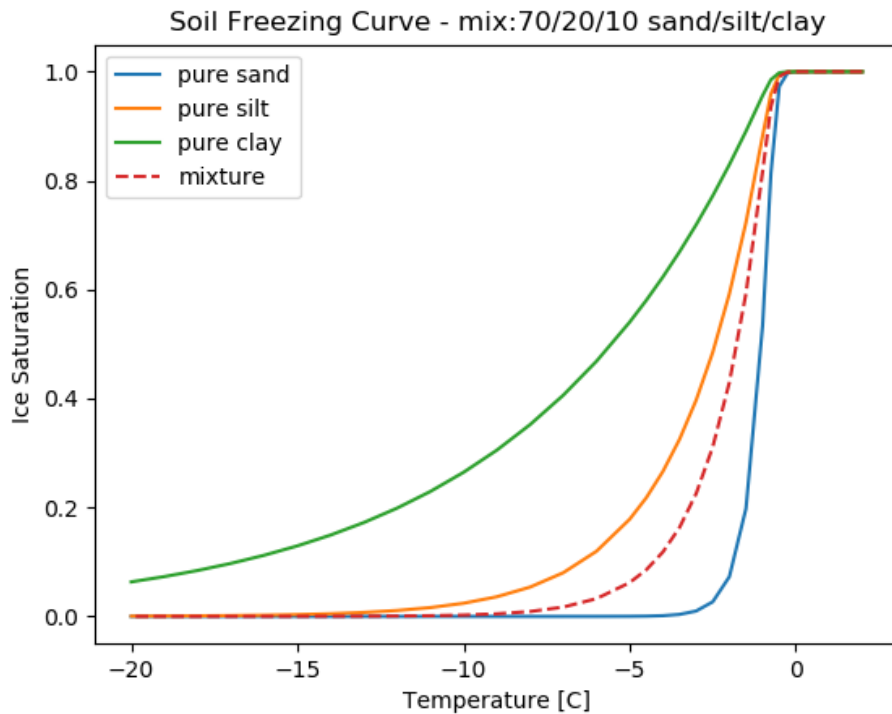


Figure 4.3-2. Soil freezing curve for a 70/20/10 sand/silt/clay mix.

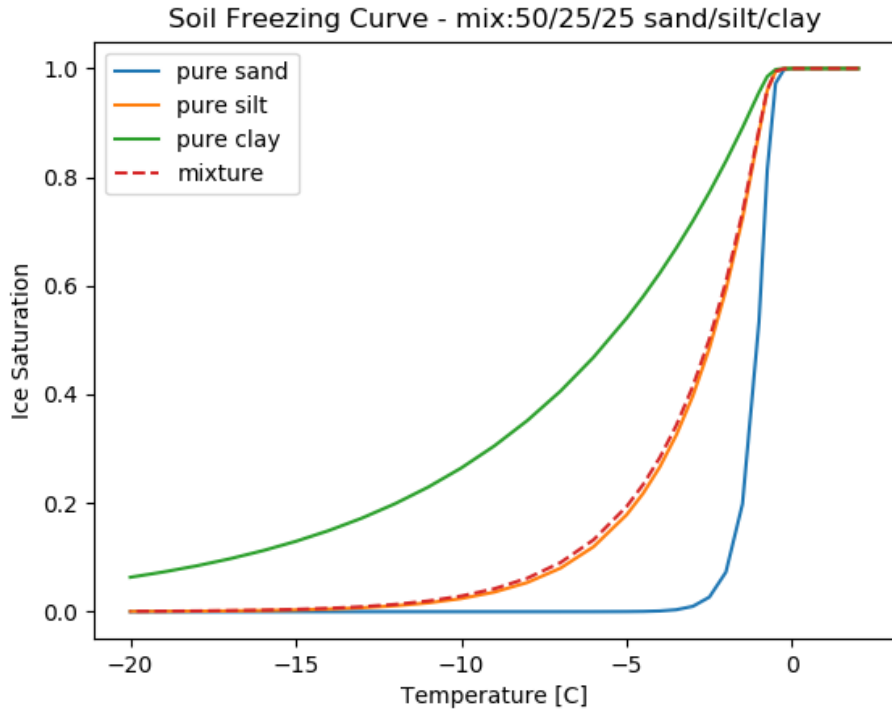


Figure 4.3-3. Soil freezing curve for a 50/25/25 sand/silt/clay mix.

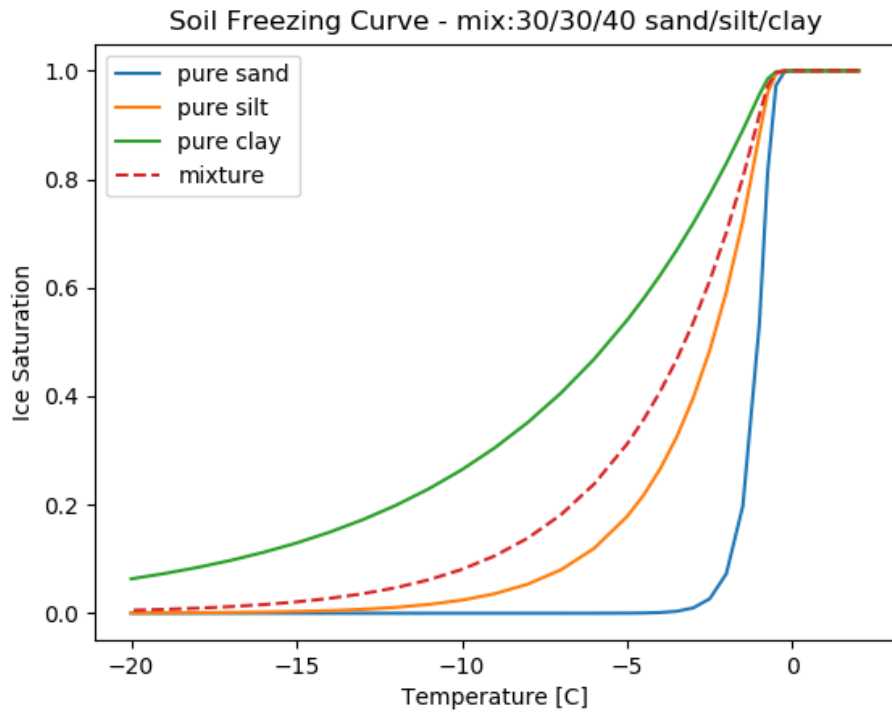


Figure 4.3-4. Soil freezing curve for a 30/30/40 sand/silt/clay mix.

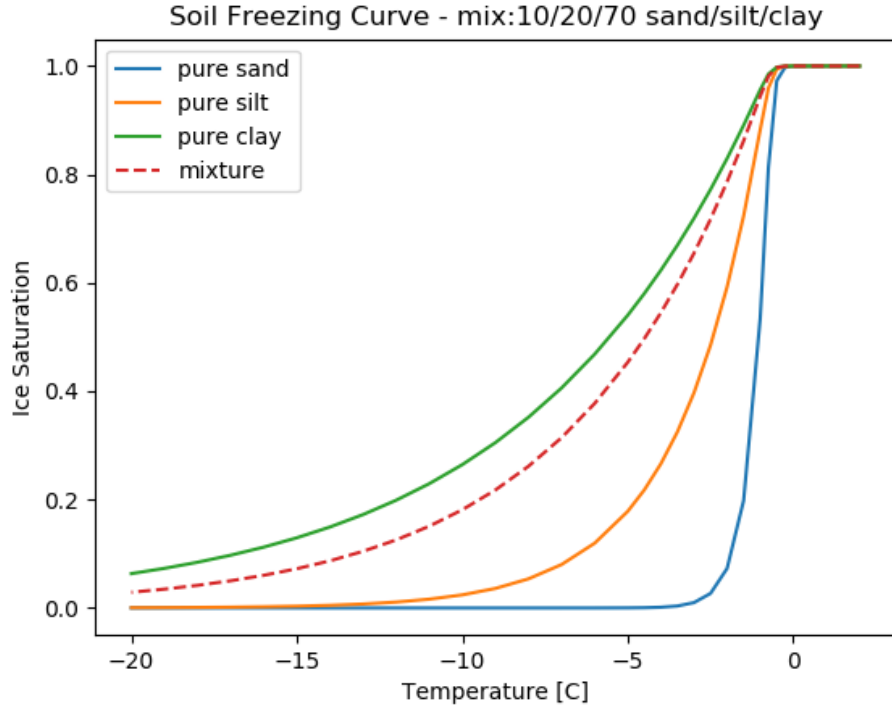


Figure 4.3-5. Soil freezing curve for a 10/20/70 sand/silt/clay mix.

The freezing/melting temperature is a function of pressure and salinity of the pore water. The volume change that occurs during ice-water phase change is ignored. The freezing/melting temperature is calculated according to

$$T_f = -0.0575S + 0.00170523S^{1.5} - 0.0002154996S^2 - \left(\frac{0.000753}{10000P}\right) \quad \text{Equation 4.3-41}$$

where S is the pore water salinity in units of ppt, and P is the local pressure in units of Pascals.

The governing equation can now be reformulated as

$$\bar{\rho c} \frac{\partial T}{\partial t} = \nabla \cdot (K \cdot \nabla T) + \rho_{ice} L_f \frac{\partial i}{\partial T} \frac{\partial T}{\partial t} \quad \text{Equation 4.3-42}$$

$$\left(\bar{\rho c} - \rho_{ice} L_f \frac{\partial i}{\partial T}\right) \frac{\partial T}{\partial t} = \nabla \cdot (K \cdot \nabla T) \quad \text{Equation 4.3-43}$$

where the term in parenthesis multiplying the change in temperature with time, $\left(\bar{\rho c} - \rho_{ice} L_f \frac{\partial i}{\partial T}\right)$, is coined “thermal inertia” and labeled as $\bar{\rho c}'$.

4.3.4. Thermo-mechanical Coupling and Implementation

Team Member Author: Irina Tezaur (SNL)

Contributors: Alejandro Mota (SNL), Jennifer Frederick (SNL)

4.3.4.1. Sequential Thermo-Mechanical Coupling Algorithm

Having described the individual components comprising the ACE model, namely the thermal and mechanical problems, let us now turn our attention to the coupling of these two physics sets. In our formulation, the thermal and mechanical equations are coupled using a sequential iterative approach depicted in Figure 4.3-6 and Algorithm 1. Both problems are advanced forward dynamically using a time-integration scheme. In our coupling methodology, there is no direct dependence between mechanical and thermal PDEs; the dependence is achieved through the material model defining the mechanical problem, as will be made clear shortly. Also worth noting is that in our coupling methodology, it is the mechanics problem that performs the erosion; once an eroded geometry is produced by the mechanics problem, the subsequent thermal solve is performed on the new eroded geometry to ensure compatibility between the thermal and mechanical problems.

We start by defining several parameters, namely the minimum time-step $\Delta t_{min} > 0$, the maximum time-step $\Delta t_{max} > \Delta t_{min}$, the initial time step $\Delta t_0 \in [\Delta t_{min}, \Delta t_{max}]$, the initial time $t_0 \geq 0$, and the final time $T_{max} > t_0$. We also define two parameters that control the time-step: the “amplification factor” $A_f \geq 1$ and the “reduction factor” $R_f \in [0, 1]$. Lastly, we generate an initial geometry $\Omega_0 \in \mathbb{R}^3$ on which we wish to solve the problem.

The coupling algorithm proceeds as follows. We begin by advancing the thermal problem in time by one time-step and extracting from it the ice saturation f . We then proceed to do a mechanical solve corresponding to the same time-step, with is used to define the material model for the mechanics problem. The mechanics problem applies the erosion criteria described in Appendix A and produced a (possibly new eroded) geometry $\tilde{\Omega}$, provided the time-advancement succeeded. In this case of a successful thermal and mechanical solve, we increment the time-step and repeat the process, this time solving the thermal problem on the new geometry $\tilde{\Omega}$, produced by the mechanical problem. The time-step is incremented based on the initial time-step Δt_0 multiplied by the amplification factor A_f . In the case the time-advancement is not successful, we reduce the time-step by the reduction factor R_f and repeat the process without updating the geometry. The algorithm is summarized in Algorithm 1 and depicted in Figure 4.3-6. Note that our coupling algorithm does not specify which time-integration scheme must be used to advance the thermal and mechanical problems, and the schemes need not be the same, i.e., it is possible to advance one of the problems explicitly and the other implicitly. It turns out that this feature is critical to good computational performance of the coupled model.

Algorithm 1 Sequential thermo-mechanical coupling algorithm. Here Ω_0 is the initial domain on which the problem is solved; Δt_0 , T_{max} , t_0 , Δt_{min} , Δt_{max} are non-negative real numbers denoting the initial time step, the maximum time, the initial time, the minimum time-step and the maximum time-step respectively; $R_f \in [0, 1]$ is the “reduction factor”

for the time-step adaptation; $A_f \geq 1$ is the “amplification factor” for the time-step adaptation. Note that the following relations must hold: $\Delta t_{min} \leq \Delta t_0 \leq \Delta t_{max}$, and $t_0 \leq$

T_{max} .

```

Given:  $\Delta t_0, T_{max}, t_0, \Delta t_{min}, \Delta t_{max}, R_f, A_f, \Omega_0$ ;
Set  $k = 0$ ;
while  $t_k < T_{max}$  do
  Set  $t_{k+1} = t_k + \Delta t_k$ ;
  Advance thermal problem in  $\Omega_k$  from time  $t_k$  to  $t_{k+1}$  and extract from
  it the ice saturation  $f_k$ ;
  Advance mechanical problem in  $\Omega_k$  from time  $t_k$  to  $t_{k+1}$  with input ice
  saturation  $f_k$ , which will produce (possibly new eroded) geometry  $\tilde{\Omega}$ ;
  if time advancements are successful then
    Set  $\Delta t_{k+1} = \min(A_f \Delta t_k, \Delta t_{max})$ ;
    Set  $k = k + 1$ ;
    Set  $\Omega_k = \tilde{\Omega}$ ;
  else
    Set  $\Delta t_k = \max(R_f \Delta t_k, \Delta t_{min})$ ;
  end
end

```

We select a sequential coupling algorithm for our thermo-mechanical over a monolithic approach for several reasons. First, due to differences in units, the thermal and mechanical variables have drastically different orders of magnitude. This would make a monolithically coupled thermo-mechanical problem highly ill-conditioned and very difficult/computationally expensive to solve. Additionally, with monolithic coupling, it is not possible to advance the thermal problem forward in time explicitly while time-integrating the mechanical problem implicitly – both problems must be advanced forward in time in the same way: explicitly or implicitly. Both of these approaches have undesirable outcomes: solving the mechanical problem explicitly is not feasible, as tiny time-steps will be required by the CFL condition; solving the thermal problem implicitly is slow and the physics present challenges for the Newton nonlinear solver. As discussed below in Section 4.3.4.2, it is actually straightforward to modify Algorithm 1 such that it emulates monolithic coupling.

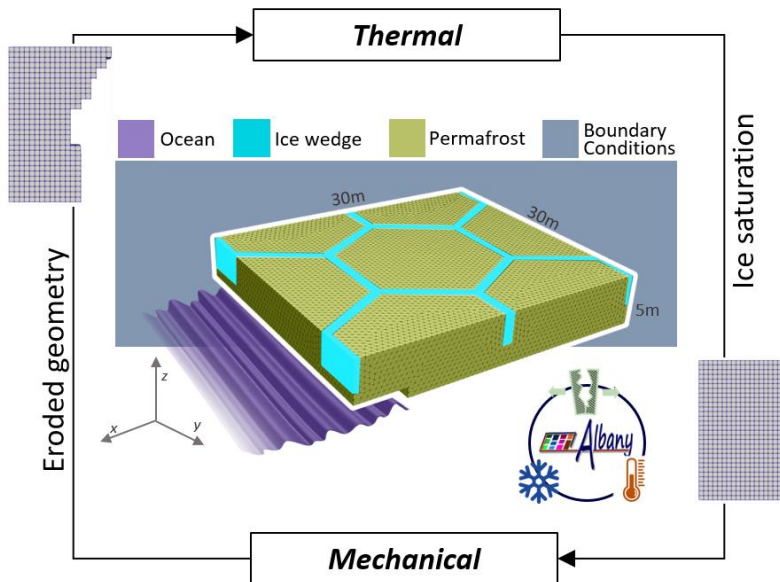


Figure 4.3-6. Schematic depicting sequential thermo-mechanical coupling.

4.3.4.2. Implementation in Albany LCM Code

The terrestrial permafrost model described herein is implemented within a software framework known as ALBANY LCM². ALBANY LCM is a spin-off from ALBANY³, an open-source C++ object-oriented, parallel, unstructured-grid, implicit finite element code for solving general partial differential equations. ALBANY was developed using the “Agile Components” code development strategy in which mature modular libraries from the TRILINOS⁴ (Heroux et al., 2003) project are glued together using template-based generic programming and abstract interfaces, giving users access to dozens of capabilities at runtime simply by changing an option in the input file. Over the years, ALBANY has hosted a number of science and engineering applications, including the AERAS global atmosphere code (Spotz et al., 2015), the Albany Land-ICE (ALI) (Tezaur et al., 2015) ice sheet model solver, the Quantum Computer Aided Design (QCAD) (Gao et al., 2013) simulator, and the Laboratory for Computational Mechanics (LCM) (Sun et al., 2013) research code. This last project comprises ALBANY LCM and is specifically targeted at solid mechanics applications. It contains our implementation of the coupled thermo-mechanical permafrost model of Arctic coastal erosion described herein. A more detailed description of ALBANY, including a detailed description of its underlying design and the physics implemented therein, can be found in Salinger et al. (2016).

ALBANY LCM was modified for the targeted application in a number of important ways. The PDEs and relevant oceanic and atmospheric boundary conditions defining the thermal problem (Section 4.3.1) were added to the code. The mechanical model used in ACE existed already within ALBANY LCM, but had to be modified to work with the appropriate material models for ice and permafrost developed for this application (Appendix A), which were added also to the code. These material models are based on a traditional finite deformation J_2 material model, available within ALBANY LCM.

In addition to adding the relevant thermal and mechanistic physics and material models to ALBANY LCM, it was necessary also to make a number of infrastructure changes to this code base. Chief among these was the addition of the capability to dynamically erode the underlying mesh geometry (described in Appendix A). Another important modification was the introduction of the sequential thermomechanical coupling algorithm described in Section 4.3.4.1 (Figure 4.3-6 and **Error! Reference source not found.**). Our sequential thermo-mechanical solver was modeled after an existing implementation of the alternating Schwarz method for concurrent multi-scale coupling in solid mechanics (Mota et al., 2017; Mota et al., 2020). This coupling was achieved through EXODUS output files, which pass relevant information between the thermal and mechanical problems. Specifically, when the thermal problem (lines 5-6 of Algorithm 1) does a time-advancement for time-step $n \in \mathbb{N}$, it writes an EXODUS file with the name `thermal.e-s.n`, which contains the solution for the temperature field as well as the ice saturation f_k . Now, when the mechanical problem (lines 7-8 of Algorithm 1) commences its time-integration, it “restarts” from the output file produced by the thermal problem, `thermal.e-s.n`. It is through this EXODUS file that the ice saturation field f_k is passed into the mechanics material model, where it is used to define the mechanics problem. Similarly, once the mechanics problem completes a solve, it writes an exodus file, `mechanics.e-s.n`, which is used as a “restart” file for the next thermal solve. Since the mechanics problem is the one that performs the mesh erosion (Appendix A), the procedure

² ALBANY LCM is available on GitHub: <https://github.com/SNLComputation/LCM>.

³ ALBANY is available on GitHub: <https://github.com/SNLComputation/Albany>.

⁴ TRILINOS is available on GitHub: <https://github.com/trilinos/trilinos>.

ensures that the thermal problem always gets the most recent eroded geometry produced by the mechanical solve⁵. Both the thermal and mechanical models are advanced forward in time dynamically using an appropriate time-integration scheme. For time-integration of the thermal and mechanical problems, we rely on the TEMPUS (Ober et al., 2018) and PIRO packages from TRILINOS, respectively. In the numerical results presented herein (Section 5.3, the thermal problem is advanced forward in time using an explicit Forward Euler time-stepper from TEMPUS, whereas the mechanical problem is advanced forward in time using an implicit trapezoidal rule stepper (i.e., a Newmark Beta scheme with $\gamma = 1/2$ and $\beta = 1/4$). Mass lumping is employed in the explicit thermal solve. Note that the mass matrix for the thermal problem changes in time, and therefore needs to be recomputed in each time-step, prior to being lumped.

While the current implementation performs sequential coupling, with a single thermal and mechanical solve occurring within each time-step, it is important to emphasize that the coupling framework can achieve a tighter coupling by increasing the number of thermal and mechanical solves within each time-step, following the alternating Schwarz coupling method (Mota et al., 2017; Mota et al., 2020). Specifically, one can add an additional iteration loop within the `while` loop in **Error! Reference source not found.** around the thermal and mechanical advancement steps. Iterating between these problems within a given time-step has the effect of emulating strong (monolithic) coupling, as discussed in (Mota et al., 2017; Mota et al., 2020).

4.4. Vertical Datum

Team Member Author: Christopher Flanary (Integral Consulting)

Contributors: Ben Jones (UAF), Diana Bull (SNL)

A vertical datum is a zero-elevation surface that heights of measured data points are referenced to. Vertical datums are grouped into two main categories, orthometric and tidal. Orthometric vertical datums are established from Earth's gravity field to set a fixed height that can be referenced to. Tidal datums are developed from water surface elevation records from a local station, usually referenced to surfaces of high or low water. Orthometric datums are constants across Earth's surface while tidal datums are local and vary from site to site. The establishing of a project vertical datum, consistent for all the data products, ensures that all the data is properly vertically referenced.

The terrestrial data products were all referenced to WGS84 Ellipsoid, an orthometric vertical datum. The oceanographic models produced water levels referenced to Mean Sea Level (MSL). A correction factor between these datums was found based on elevation surveys conducted around Drew Point in which the bluff toe and water level were measured from the AUV survey data, see Figure 4.4-1. Nine distinct survey days were then canvassed, in a similar method to that shown in Figure 4.4-1, to determine the water level and bluff toe location in WGS84 ellipsoid heights. Table 4.4-1 below is a summary of this data. On each day, 8 distinct measurements were taken for each water level and bluff toe height measurements; the values displayed in Table 4.4-1 are the average values from those 8 measurements. Over the two years the values stay relatively consistent with the water level showing the most variability (as would be expected). An average water level of 2.23m below the WGS84 ellipsoid and bluff toe of 1.99m below the WGS84 ellipsoid were obtained. These

⁵ Note that in our present implementation we always restart the thermal problem from the output mesh produced by the mechanical problem, even if no erosion occurred, when, in fact, this is only necessary when erosion has occurred. The main reason for this is that performing the restarts in each step simplifies greatly the implementation of our coupling method, at a slight computational expense.

measurements allowed for the conversion from the oceanographic model tidal datum to the project orthometric vertical datum (Figure 4.4-2). From this analysis, an average correction factor of 0.24m, is applied to the oceanographic model tidal datum to set all data in the proper vertical reference frame. This correction would ideally be used as a model sensitivity parameter when the predicted water levels are passed to the terrestrial model.

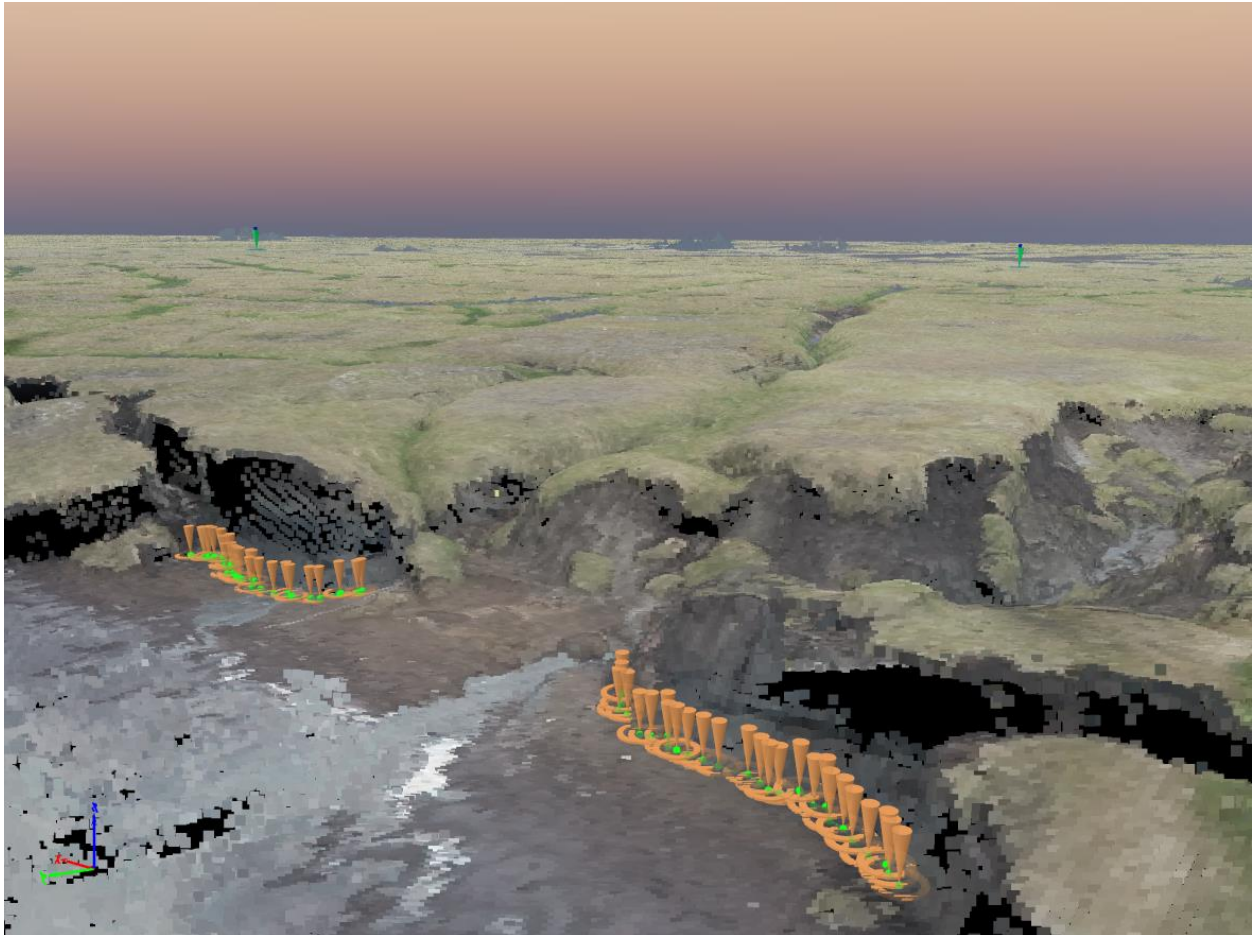


Figure 4.4-1. Example analysis within AUV survey data to obtain bluff toe elevation in WGS84 Ellipsoid.

Table 4.4-1. Experimental data used to establish vertical datum conversion between terrestrial and oceanographic products.

	Water Level (m)	Bluff Toe (m)	Difference (m)
24-Jul-18	-2.356	-2.001	-0.355
29-Jul-18	-2.439	-2.018	-0.421
3-Aug-18	-2.325	-2.034	-0.291
30-Sep-18	-2.250	-2.010	-0.240
2-Aug-19	-1.996	-1.956	-0.040

5. MODEL EXECUTION

5.1. Boundary Condition Implementation

Team Member Author: Diana Bull (SNL)

Contributors: Jennifer Frederick (SNL), Christopher Flanary (Integral Consulting)

The Arctic Coastal Erosion Model requires knowledge of atmospheric, oceanographic, and subterranean heat flux conditions. Currently the ACE model employs atmospheric and ocean temperatures as Dirichlet boundary conditions and subterranean heat flux as a Neumann boundary condition. The temperatures vary from time step to time step whilst the subterranean heat flux is treated as a constant. Ocean salinity and water contact are used to calculate enhanced melting on the bluff face as described in Section 4.3.1.3. Ocean water contact is used to compute the dynamic forces due to waves on the vertical bluff face as described in Section 4.3.2.2.

5.1.1. Atmospheric Inputs

The terrestrial surface skin temperature provided through both reanalysis data sets and through the downscaled climate projections every 3-hours, as detailed in Section 4.1.1, was used as the Dirichlet temperature boundary condition for the thermal portion of the terrestrial model. Skin temperature represents the temperature of the ground surface, as measured by its long wave radiation wavelength. The skin temperature data was interpolated using a piecewise cubic to match the time step of the oceanographic data; Figure 5.1-1 shows the 2007 ASR skin temperature with interpolation to 60sec. The output point closest to Drew Point from each source, shown in Figure 5.1-2 (ASR, ERA5, and projection), provided this data.

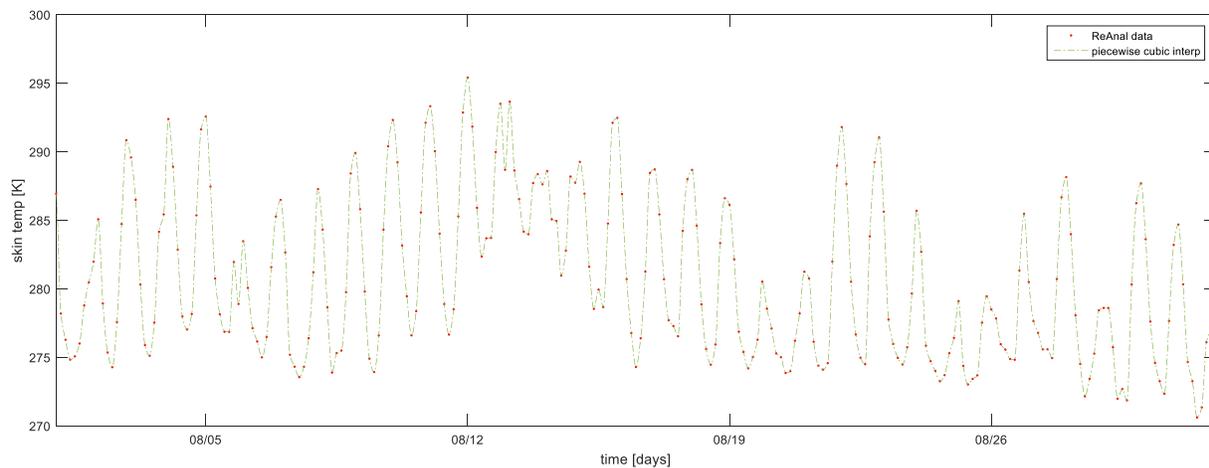


Figure 5.1-1. 2007 skin temperature for the month of August from ASR (red dot) with piecewise cubic interpolation to 60sec (dashed green line).



Figure 5.1-2. Map indicating the output locations for skin temperature.

5.1.2. Oceanographic Inputs

Ocean temperature, salinity, and wave spectral moments were exported from the nearshore models hourly whilst water level was exported every 15min at one of the 58 output locations (see Figure 4.2-7). The wave spectrum evolved according to the nearshore physics from a prescribed JONSWAP spectrum at the WW3 boundary. Spectral moments at a given output point were derived using standard techniques from the naturally evolved spectral shape (Ochi, 2005). The water surface elevation, or eta, was computed from the 1D variance density, output hourly from the Delft3D-FLOW/WAVE model. Eta was stochastically computed, according to the equation below, on a 2 Hz time step for each hour output over the simulation period. Then the 15 min water level signal from the FLOW side of the model was linearly interpolated onto a 2 Hz time step and added to the eta signal. In addition, the 15 min salinity and water temperature from the FLOW side of the model were linearly interpolated onto a 2 Hz time step. This final time series product provided a 2 Hz signal of salinity, water temperature, and water surface elevation with tidal, wind wave, and swell components. The equations used for the calculation of the 2 Hz eta signal are shown below:

$$\eta(t) = \sum_S a_S \cos(2\pi f_S t + \theta_S) \quad \text{Equation 5.1-1}$$

$$a_S = \sqrt{2 S_f \Delta f} \quad \text{Equation 5.1-2}$$

$$\theta_S = \text{random}(0, 2\pi) \quad \text{Equation 5.1-3}$$

where $\eta(t)$ is the time varying eta, as is the amplitude of the surface displacement calculated using S_f , the variance density at each frequency, Δf is the difference in each frequency, f_s is the frequency, t is the time, Θ_s is the wave phase represented by a random number between 0 and 2π , computed at each frequency S . A final record of water contact with the bluff face is then produced by correcting for the vertical datums (see Section 4.4). An example output from this process is shown in Figure 5.1-3 below.

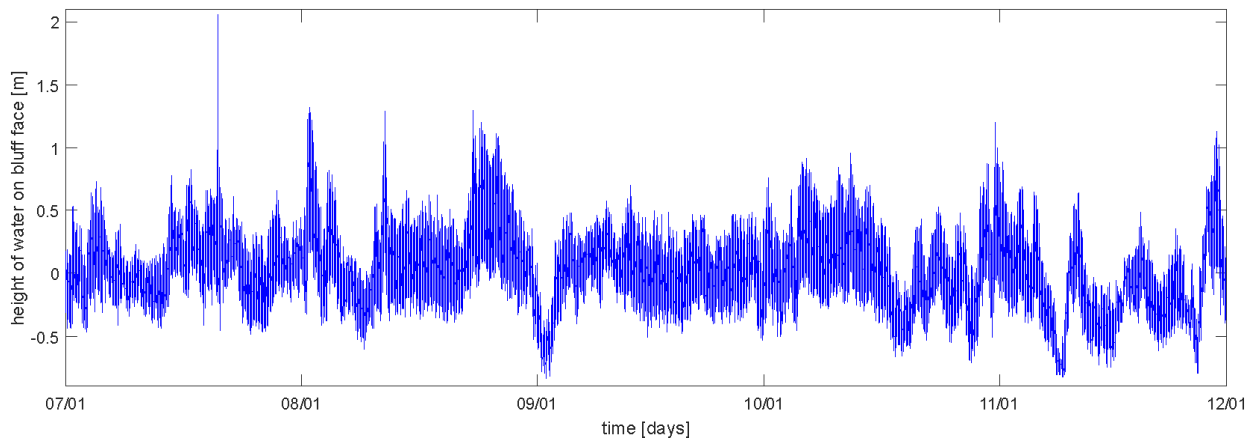


Figure 5.1-3. Example 2019 oceanographic model output that forms the basis of the terrestrial model inputs. The water contact record is established by combining water level and spectral properties.

The final water contact record in combination with the ocean temperature was used to establish the Dirichlet temperature boundary condition for the thermal portion of the terrestrial model.

Additionally, the final water contact record in combination with the ocean salinity was used as input for the salinity enhanced melting calculation described in Section 4.3.1.3. Lastly, the final water contact record established the dynamic forces on the vertical bluff faces as described in Section 4.3.2.2.

5.1.3. Exposure Time / Grid Spacing

The thermal evolution of the permafrost bluff is driven by both the magnitude and duration of external temperatures. The thermal exposure, comprised of magnitude and duration, should account for the total delivery of thermal energy into the terrestrial system. Correct accounting of ocean water contact with the bluff requires a specific approach. Further, since the temperature is a Dirichlet boundary condition it must be provided with a vertical resolution that matches the resolution of the terrestrial grid.

The spectral shape in the nearshore environment evolves according to the nearshore physics, hence there is not a standard shape (i.e., Bretschneider, JONSWAP, etc.) to describe the wave spectrum. Without a standard shape, the derivation of the distribution of wave heights in an hourly record is

most easily obtained from the time history of the random sea. The approach taken to establish ocean wave exposure requires binning the wave heights according to the vertical grid resolution defined by the terrestrial model; see Figure 5.1-4 for an illustration of the effect of distinct vertical resolutions. A central binning technique is pursued, not a heavy-sided (e.g. the 0.0m bin encompasses plus or minus $\frac{1}{2}$ the bin width, not plus the bin width). The total frequency of water contact is multiplied by the resolution of the wave history (0.5sec) to establish the total duration of water contact with each vertical slice.

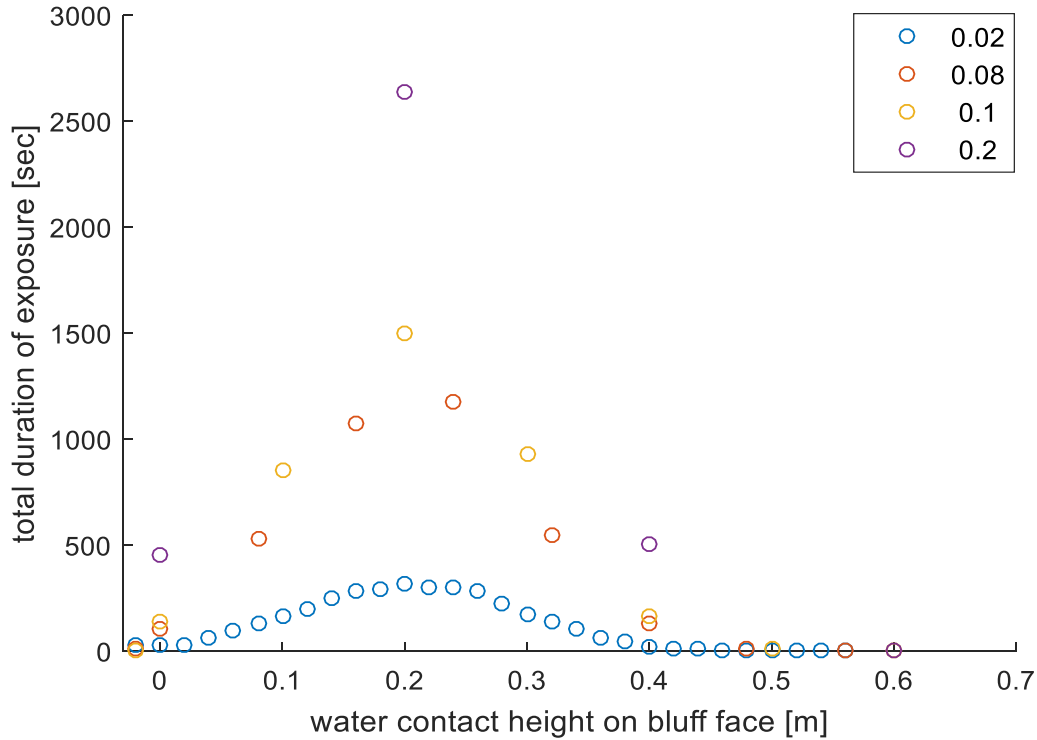


Figure 5.1-4. Illustration of the effect of the vertical resolution of the terrestrial grid (0.02m, 0.08m, 0.1m, and 0.2m) on the total duration of water contact with each slice for a 0.5Hz time history. A randomly selected hour, 93, in 2019 is used to show the effect on the binning of the water contact history with distinct vertical resolutions. As the vertical resolution increases from 0.2m, the peak duration of exposure decreases as previously excluded water contact levels become populated.

Thermal conduction is a slow process (10's of minutes) in comparison to the variation of water contact with the permafrost bluff (seconds). Hence, the minimum time step by which the terrestrial simulation progresses is expected to be much slower than the variation of water contact with the bluff. Further manipulation of the binned water contact data to match a minimum time step proceeds by summing durations that are shorter than the minimum time step with durations at the next vertical level, either up or down depending upon the slope, until the duration in a vertical bin is equivalent to or greater than the minimum time step for the terrestrial simulation. Figure 5.1-5 illustrates the effect of increasing the simulation time step from 0.5sec to 1hour for a given vertical resolution of 0.1m. This exposure processed water contact history ensures the total thermal energy delivery is included as completely as possible regardless of the simulation time step. A new waveform is then constructed by randomly distributing the total exposure in each vertical resolution in increments of the simulation time step.

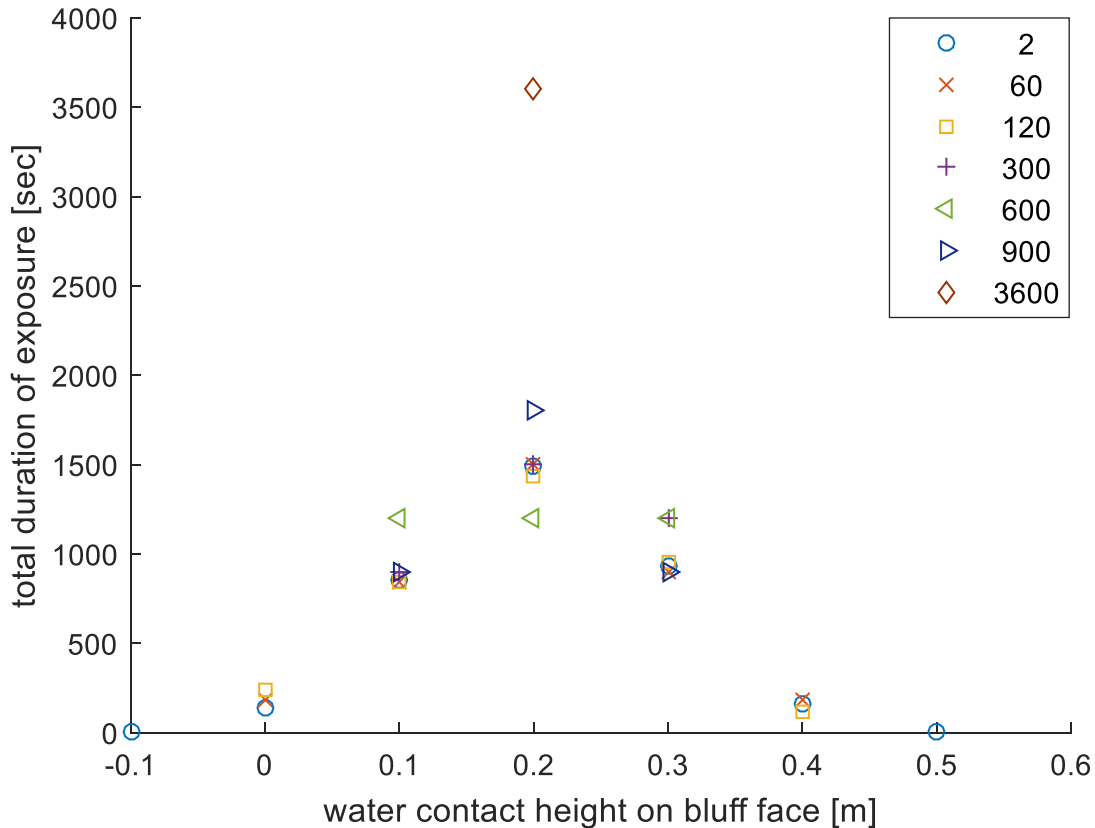


Figure 5.1-5. Illustration of the effect of the minimum simulation time step on a 0.1m vertical resolution grid. A randomly selected hour, 93, in 2019 is used to show the effect of the minimum simulation time step on the simulated exposure used by the terrestrial model. As the simulation time step increases the exposure magnitude (water contact height on bluff face) and duration become coarser.

With a newly constructed water contact history that is binned both by the vertical resolution of the terrestrial grid and the simulation time step, the ocean temperature can then be supplied to each valid vertical layer as prescribed by the water contact history. As the processes described above are followed, both the temperature and salinity data undergo the same process and individual values are averaged to produce a single temperature and salinity that is most representative of the simulation time step at the given vertical resolution.

In the end, each vertical grid layer is supplied a boundary condition file at a selected simulation time step in which the ocean temperatures are substituted for the skin temperature if water is in contact with the bluff face. Figure 5.1-6 through Figure 5.1-9 show a subset of these Dirichlet boundary conditions for a 10min simulation time step over the 2019 summer in which the ocean water temperatures are shown as blue dots when the water is in contact with the identified vertical layer. When the ocean water is not in contact with the vertical layer, the terrestrial skin temperature is used as the boundary condition.

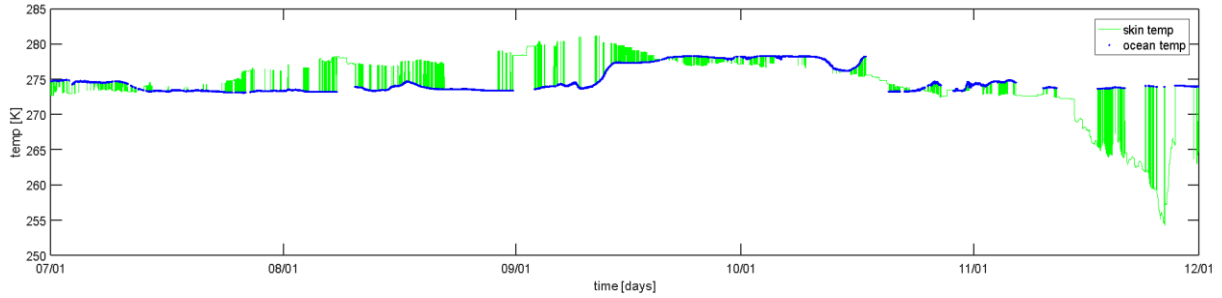


Figure 5.1-6. Temperature boundary condition at 0.0m for a vertical resolution of 0.1m and a simulation time step of 10min over the 2019 summer in which the ocean water temperatures are shown as blue dots when the water is in contact with the identified vertical layer.

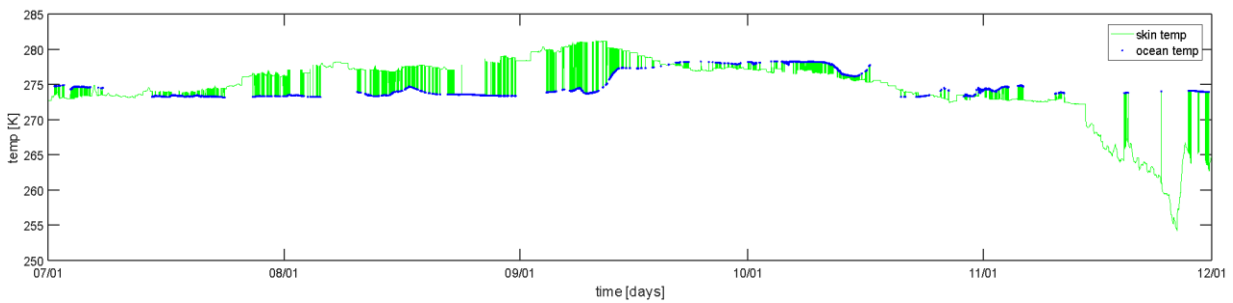


Figure 5.1-7. Temperature boundary condition at 0.2m for a vertical resolution of 0.1m and a simulation time step of 10min over the 2019 summer in which the ocean water temperatures are shown as blue dots when the water is in contact with the identified vertical layer.

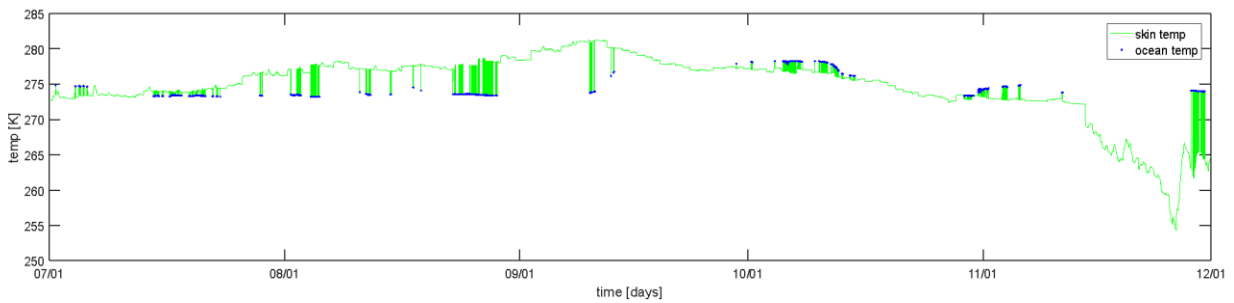


Figure 5.1-8. Temperature boundary condition at 0.4m for a vertical resolution of 0.1m and a simulation time step of 10min over the 2019 summer in which the ocean water temperatures are shown as blue dots when the water is in contact with the identified vertical layer.

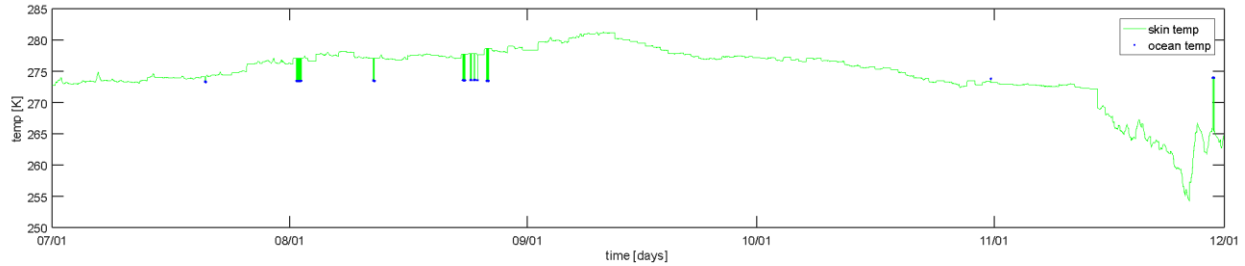


Figure 5.1-9. Temperature boundary condition at 0.8m for a vertical resolution of 0.1m and a simulation time step of 10min over the 2019 summer in which the ocean water temperatures are shown as blue dots when the water is in contact with the identified vertical layer.

This exposure processing method enables the calculation of duration of water contact at each vertical level over any desired time period (the entire summer, each month, etc.) which allows for highly informed correlation between the oceanographic environment and erosion. For instance, this allows for a tight coupling between the Structure for Motion (SfM) analyses presented in Section 2.2.2 and the oceanographic conditions. As an example, for a water contact history that has been established using a simulation time step of 2sec and a vertical resolution of 0.02m, Figure 1-10 shows the percentage of time between successive AUV surveys that water is in contact with a particular height up the permafrost cliff face. It is clear that between the first surveys the largest wave environment existed, followed by a very calm period, followed by two periods of activity the second of which had a longer sustained interaction at a lower height. These results compared with the storm analysis presented in Figure 5.1-10 match closely.

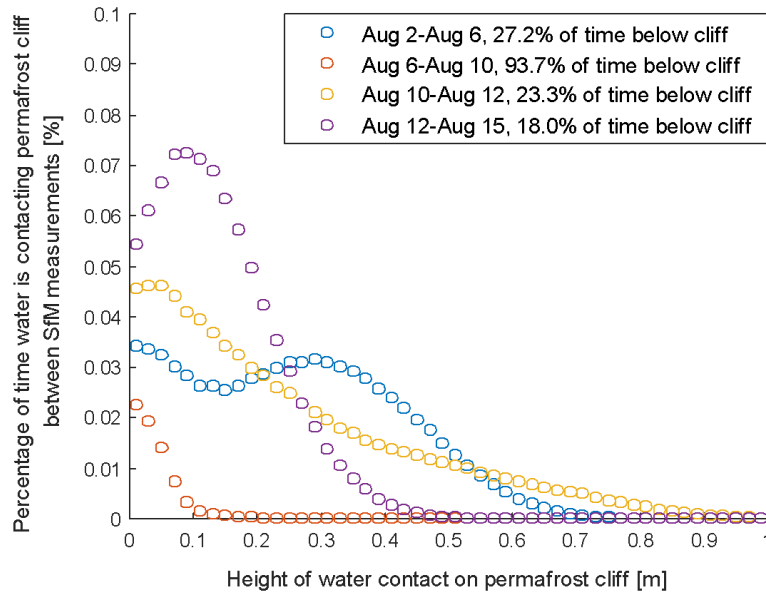


Figure 5.1-10. Percentage of time between successive AUV surveys that water is in contact with a particular height up the permafrost cliff face; the time spent below the cliff face is given in the legend.

Given that the ACE model does not solve the governing equations for transport, the ocean salinity at the cliff face is not treated as a true boundary condition in the model. Instead, it is provided as input to the simulation for use by the salinity enhanced melting routine at a high spatial resolution. The same process described above was used to establish the same time step with a vertical resolution of 0.02m; see the 2019 record in Figure 5.1-11. Nodes on the current boundary that are in contact with the ocean interpolate for the correct value from the time history provided.

Similarly, the dynamic pressure from the ocean environment uses the time history and water contact history as a Neumann Boundary Condition. Hence, the same process described above was used to establish the same time step with a vertical resolution of 0.02m.

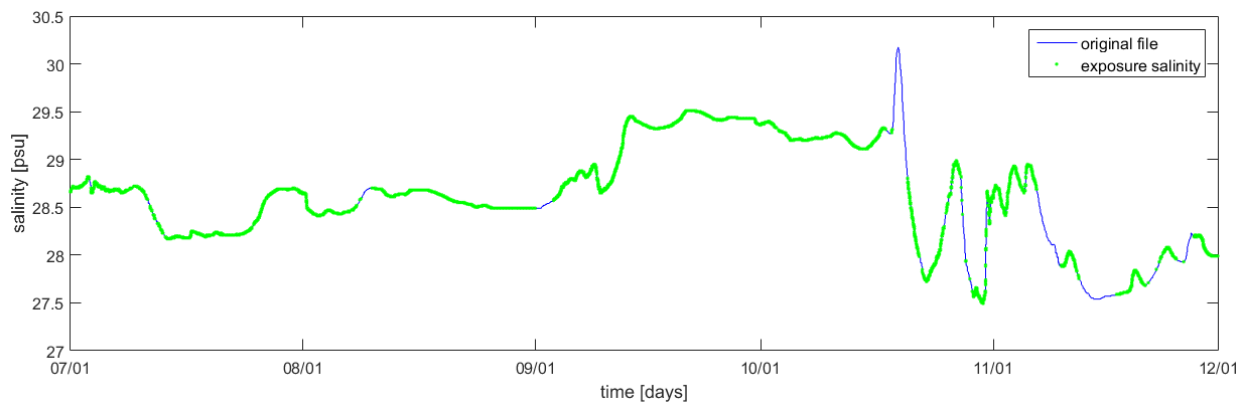


Figure 5.1-11. Salinity history over the 2019 summer. Original in blue and exposure calculated using a simulation time step of 60sec and a vertical resolution of 0.02m shown as green dots. Only time periods in which water is in contact with any portion of the permafrost bluff face is shown in green.

5.1.4. Storm Identification

To further assist coupling between the modeled oceanographic data and the field observations, automatic storm identification has been developed by determining the number of consecutive hours with water levels above a particular vertical level. Cut-off values for the number of consecutive hours and the vertical level can then be imposed to identify the presence of a storm.

There is no consensus within the oceanographic community on the constitution of a storm, especially in the Arctic in which there are few experimental records of wave energy. However, storms will typically last for six hours or more since the wind conditions needed to generate storm waves must be sustained.

For illustration purposes, Figure 5.1-12 identifies storms in 2019 between July 30th and August 16th for which a vertical level of 0.4m is in contact with ocean water for at least 6 consecutive hours. The water contact history has been established using a simulation time step of 2sec and a vertical resolution of 0.02m. Storms are identified in Figure 5.1-12 with vertical red lines and the duration, in hours, of each storm is given between the cut-off lines.

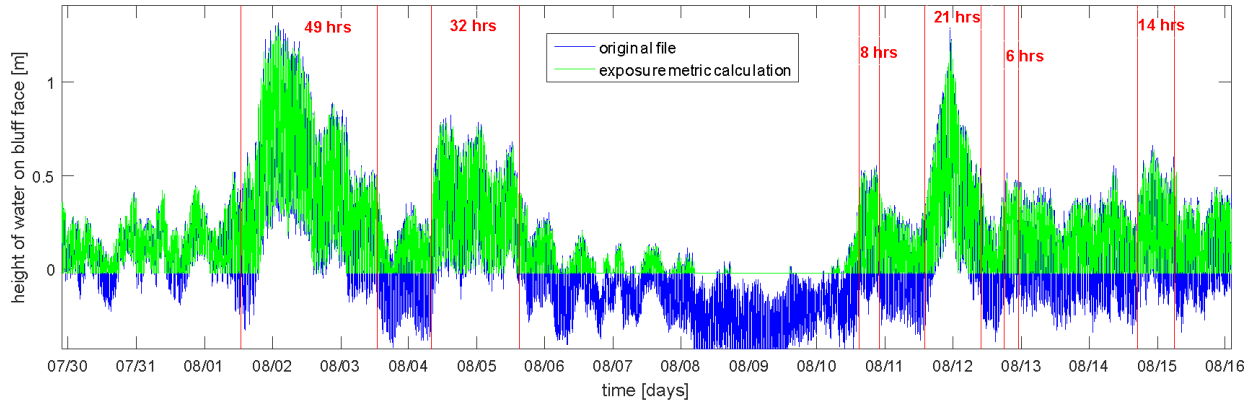


Figure 5.1-12. Identification of time periods for which a vertical level of 0.4m is in contact with ocean water for at least 6 consecutive hours in 2019; establishing these time periods as illustrative storms. Water contact history has been established using a simulation time step of 2sec and a vertical resolution of 0.02m.

5.1.5. Geothermal Heat Flux Input

At the bottom of the domain, a geothermal heat flux (Neumann) boundary condition is applied. The value of the geothermal heat flux was determined using temperature measurements in a deep borehole at Drew Point obtained from the DOI/GTN-P Deep Borehole Array project (Clow 2014). The project was designed to monitor the thermal state of permafrost on the Arctic Slope of Alaska and is the US Department of the Interior contribution to the Global Terrestrial Network for Permafrost (GTN-P). Because the boreholes are very deep (500m at the Drew Point test well), they provide a good estimate of the geothermal heat flux in the region. Figure 5.1-13 shows the temperature record at the Drew Point test well from September 1978 until August 2007. The value of the temperature gradient between 100-200m was used to establish the geothermal heat flux value. Geothermal heat flux, q , is determined by

$$q = -K \frac{dT}{dz} \quad \text{Equation 5.1-4}$$

where K is the thermal conductivity of the ground, and $\frac{dT}{dz}$ is the temperature gradient with depth. An average temperature gradient of 30 K/m was observed between 100-200m. A typical thermal conductivity value of 2.67 W/K/m was chosen, which gives a heat flux value of $\sim 0.08 \text{ W/m}^2$.

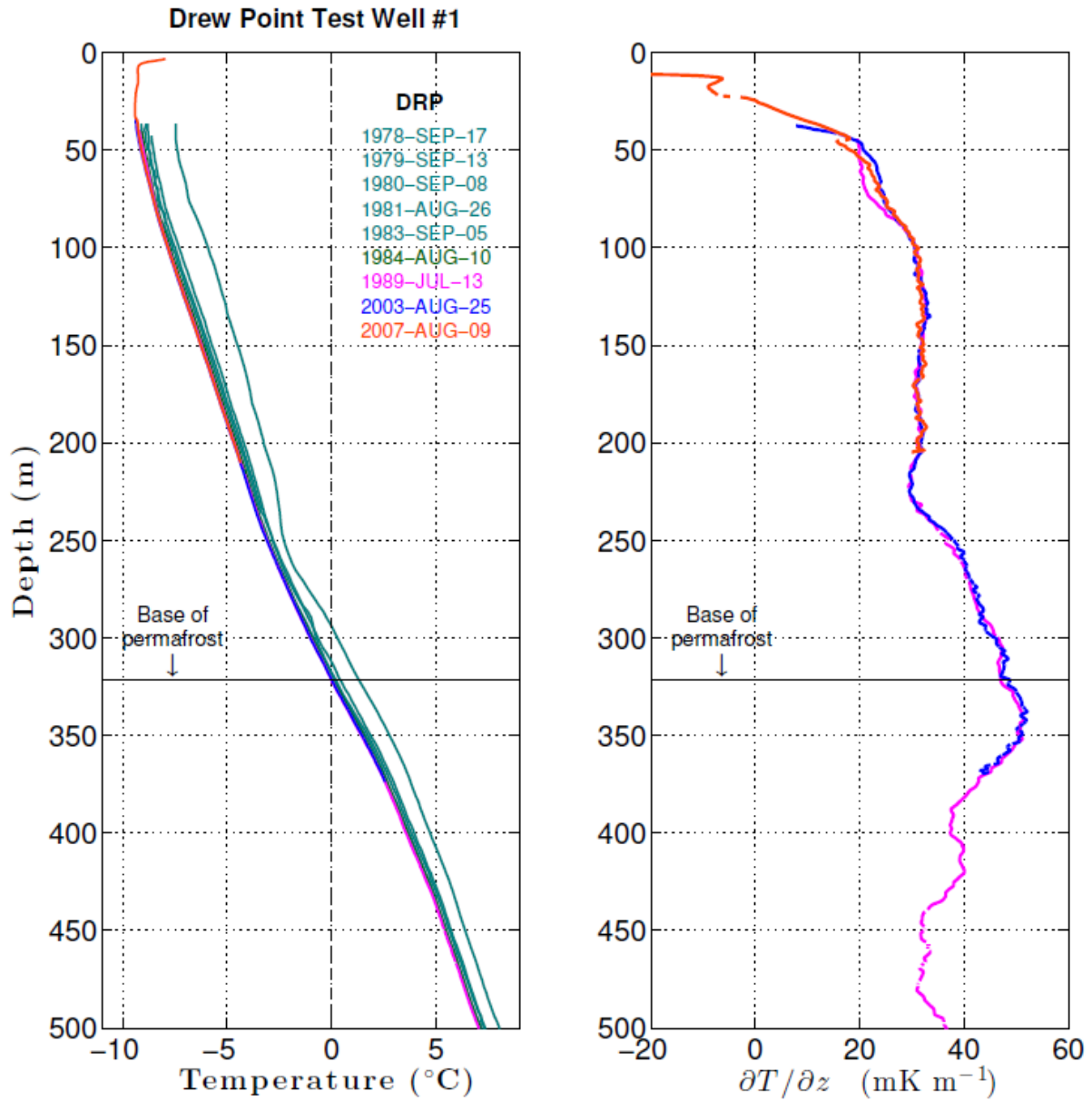


Figure 5.1-13. Temperature records at the Drew Point deep borehole, used to determine the value of the geothermal heat flux boundary condition. Adapted from Clow (2014).

5.2. Oceanographic Validation

Team Member Author: Christopher Flanary (Integral Consulting)

Contributors: Craig Jones (Integral Consulting), Eloise Brown (UAF), Jeremy Kasper (UAF), Li Erikson (USGS), Jim Thomson (UW), Katherine Barnhart (USGS), Mike Angelopolous (AWI), Guido Grosse (AWI)

Once the WW3 and Delft3D-FLOW/WAVE models were setup, the bottom elevations were compared to nearshore bathymetry data around Drew Point to confirm the bottom elevations in the model were similar to the elevations in the project area.

Upon running the models for the 2007 – 2019 time periods, the model predictions were compared to the available measured data in the Beaufort Sea and along the North Slope of Alaska. These data included offshore wave buoys, nearshore bottom moorings, and water-level sensors. Comparing the model predictions from the three-model system to multiple points of measured data ensured that the models were accurately predicting the hydrodynamics in the project area before passing results to the terrestrial model.

Evaluation of the model, or model validation, was performed to qualitatively and quantitatively assess how well the model predicted observed conditions. Quantitative metrics were selected and used to evaluate the model performance, or the ability of the model to accurately reproduce the observed conditions at all selected measurement locations. These metrics, combined with the qualitative evaluation (e.g., visual inspection of model results), provide an assessment of how well the model predicts the measured values at the study site. The metrics used to evaluate model performance include the model skill score (Wilmott 1981), root mean square error (RMSE), and the Pearson correlation coefficient. The model skill score served as the primary basis for evaluating model ability across a range of parameters and was computed as follows:

$$\text{Skill} = 1 - \frac{\sum(x_{\text{model}} - x_{\text{meas}})^2}{\sum(|x_{\text{model}} - \bar{x}_{\text{meas}}| + |x_{\text{meas}} - \bar{x}_{\text{model}}|)^2} \quad \text{Equation 5.2-1}$$

Where x_{meas} is the measured value, x_{model} is the model-predicted value, and \bar{x}_{meas} is the average measured value. The skill score varies from 0 to 1, with 1 representing perfect agreement between measured and modeled data. The classification of model skill values, as well as Pearson correlation coefficient, described below, are characterized in Table 5.2-1, based on values presented in Allen et al. (2007).

Table 5.2-1. Model Skill Performance Metrics.

Skill Score	Performance
0–0.2	Poor
0.2–0.5	Good
0.5–0.65	Very Good
0.65–1	Excellent

The RMSE is a measure of the average difference between model-predicted and measured values and was computed as follows:

$$RMSE = \sqrt{(x_{model} - x_{meas})^2} \quad \text{Equation 5.2-2}$$

The computed RMSE was compared with measured values such that an acceptable RMSE value is ± 30 percent of the average measured values (USEPA 1990).

Finally, the Pearson correlation coefficient was used to ensure the model is qualitatively reproducing the temporal variability in measured values by computing the linear association of modeled and measured values. The Pearson correlation coefficient (r) was computed as follows:

$$r = \frac{n \sum(x_{meas}x_{model}) - \sum(x_{meas}) \sum(x_{model})}{\sqrt{[n \sum(x_{meas}^2) - (\sum x_{meas})^2][n \sum(x_{model}^2) - (\sum x_{model})^2]}} \quad \text{Equation 5.2-3}$$

Where n is the number of data points in the time series. Evaluation of the correlation coefficient depends on the number of samples compared; the values vary from 0 (no correlation) to 1 (perfect correlation). The r value can be classified with the same performance values as used for the model skill score (Table 5.2-1).

Together, these metrics provide a robust evaluation of the model’s ability to reproduce measured data.

These data comparisons are discussed in the sections below.

5.2.1. Bathymetry Comparison

As discussed in Section 4.2, the bathymetric data used to set the bottom elevations for the Delft3D-FLOW and WAVE grids were defined from the Alaska Regional Digital Elevation Model (ARDEM) version 2.0 (Danielson et al. 2015, Danielson et al. 2008, Danielson et al. 2011). ARDEMv2 uses depths from the International Bathymetric Chart of the Arctic Ocean (IBCAO; Jakobsson et al. 2012) for the Arctic region and has horizontal resolution down to 500 m in the Beaufort Sea region.

The ARDEM/IBCAO data are a data set comprised of multiple surveys using multiple methods (e.g., single beam, multi-beam). As a result, the ARDEM/IBCAO bottom elevations were compared to nearshore single beam and multibeam elevation data collected around Drew Point as detailed in Section 2.3.1 (Figure 5.2-1). The nearshore single beam data were collected within 1 km of the Drew Point shoreline, while the multibeam data extended more than 20 km offshore. The nearshore single beam data does not match well to the ARDEM/IBCAO data (Figure 5.2-2). The ARDEM/IBCAO data is an Arctic Ocean/Beaufort Sea scale dataset, and thus the nearshore data have less correlation with the larger scale dataset. The multibeam data has an excellent correlation with the ARDEM/IBCAO data (Figure 5.2-3). These multibeam data cover a much larger area offshore of Drew Point and extend into deeper water, though they do extend to within 100 m of the shoreline and overlap with the nearshore single beam data. Given the excellent correlation of the ARDEM/IBCAO data to the multibeam as compared to the nearshore single beam data, the ARDEM/IBCAO data was concluded to be acceptable to use for the Delft3D-FLOW and WAVE domains.

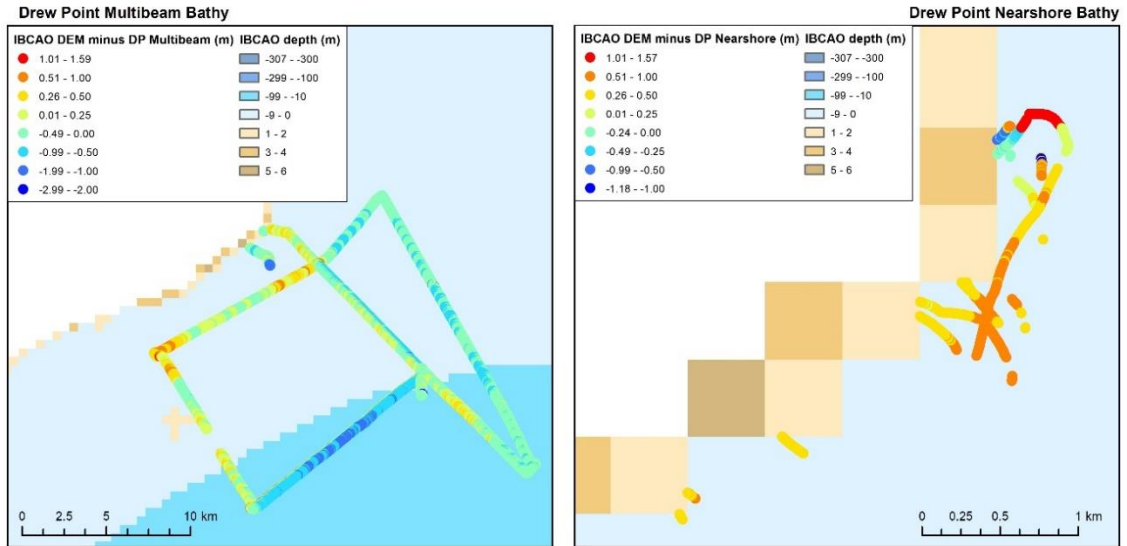


Figure 5.2-1. Spatial Comparison of ARDEM/IBCAO depths to the Drew Point Nearshore Single Beam and Multibeam Depths.

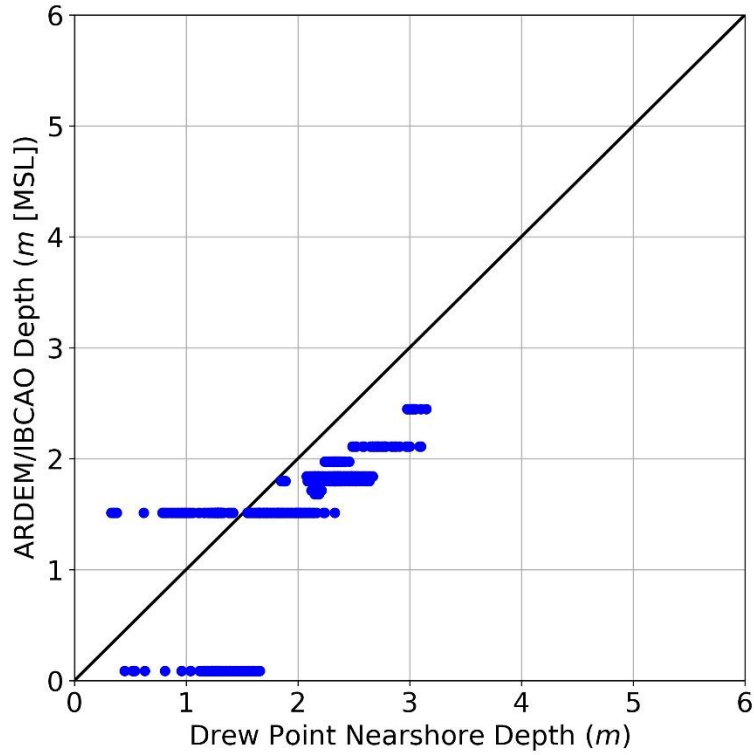


Figure 5.2-2. Scatter Plot Comparison of ARDEM/IBCAO depths to the Drew Point Nearshore Single Beam Survey Depths.

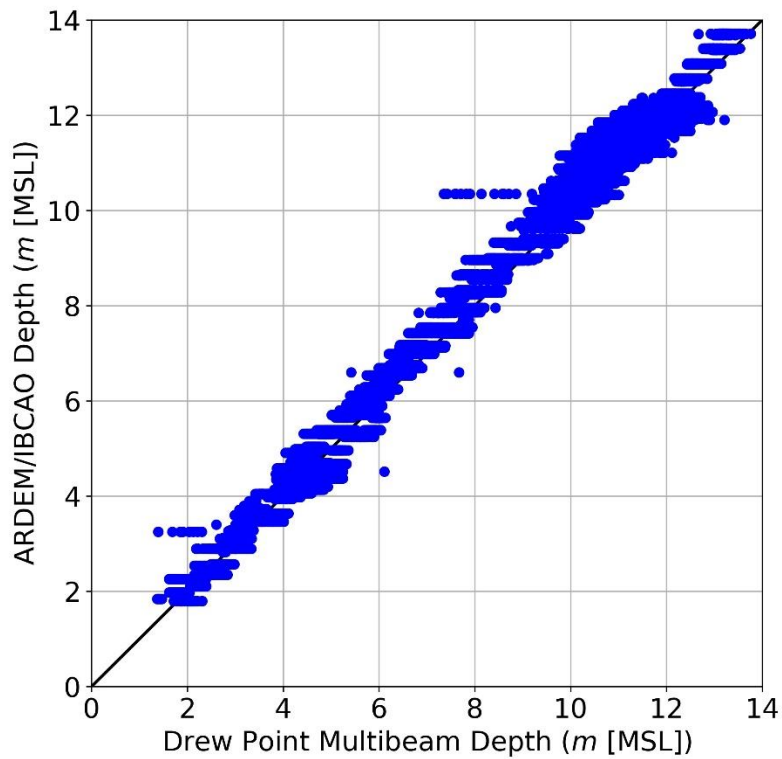


Figure 5.2-3. Scatter Plot Comparison of ARDEM/IBCAO depths to the Drew Point Multibeam Survey Depths.

5.2.2. WW3 – BOEM Buoy Comparison

This section details the comparison of WAVEWATCH III (WW3) simulated wave height and peak wave period to industry wave data near Drew Point, Alaska, from 2011 through 2019. Four different Arctic atmospheric reanalysis data sets were used to develop WW3 model wind and sea ice forcing files. The four Arctic atmospheric reanalysis data sets are ERAI-WRF, ASR, NARR, and CBHAR. The purpose of these model-measured data comparisons is to select the best performing atmospheric reanalysis data set to apply to the nearshore wave and circulation models being developed.

5.2.2.1. Arctic Atmospheric Reanalysis Data

Four Arctic atmospheric reanalysis data sets were initially evaluated to supply the wind forcing and sea ice fraction for the WW3 model. These reanalysis data sets were ERA-Interim (ERAI-WRF), the Arctic System Reanalysis v2 (ASR), the North American Regional Reanalysis (NARR), and the Chukchi-Beaufort Sea High-Resolution Atmospheric Reanalysis (CBHAR) (Table 5.2-2). The best performing atmospheric reanalysis data set, as compared to measured wave data, would be selected to use with the Delft3D-FLOW/WAVE model (wind only).

These reanalysis data sets and the Arctic Ocean WW3 model performance using these data sets is discussed below.

Table 5.2-2. Arctic Atmospheric Reanalysis Data Sets used for WW3 Forcing.

Model	Wind Resolution	Wind Time Step	Temporal Coverage
ERAI-WRF	20 km	1 hour	1979–2017
ASR	15 km	3 hour	2000–2017
NARR	32 km	3 hour	1979–2019
CBHAR	20 km	1 hour	1979–2009

ERAI-WRF is a 20 km resolution, dynamically downscale product developed as part of a Bureau of Ocean Energy Management project (C3S 2017). It is an ERA-Interim product forced by Weather Research and Forecasting (WRF) model. The extents of the ERAI-WRF domain did not cover the entire WW3 model domain, so its parent model, ERAI, was used to fill in the data gaps. ERAI-WRF wind speed and direction and sea ice coverage were used to develop the model forcing files.

ASR is a 15 km resolution, polar central reanalysis data set blended from modeling and observations (Bromwich et al. 2018). It is forced by the Polar Weather Forecast Model and the High Resolution Land Data Assimilation model. ASR wind speed and direction and sea ice coverage were used to develop the model forcing files.

NARR is a 32 km resolution reanalysis data set forced by the Global Reanalysis 2 (Mesinger et al. 2006)⁶. NARR wind speed and direction were used to develop the model forcing files. The extents of the NARR domain did not cover the entire WW3 model domain. As a result, ASR wind data was blended with the NARR data where necessary to provide a complete atmospheric data set.

⁶ NCEP reanalysis data provided by NOAA/OAR/ESRL PSD, Boulder, Colorado, available at <https://www.esrl.noaa.gov/psd/>.

CBHAR is a 20 km resolution Arctic model forced with ERAI, NARR, and other atmospheric modeling systems (Liu et al. 2014). CBHAR has a shorter time range as compared to the other reanalysis data sets. CBHAR wind speed and direction and sea ice coverage were used to develop the model forcing files.

Sea ice coverage was an additional time varying input condition included in the WW3 models. Sea ice coverage is included in the ERAI-WRF, ASR, and CBHAR reanalysis data but not included in the NARR data. As a result, the ASR sea ice coverage data were used with the NARR wind forced simulations.

5.2.2.2. Output Stations

In total, 606 output stations were available in the Arctic to compare with the WW3 model. Forty-eight of these locations collected data from 1982 through 2015 and could be used to evaluate the model predictions. For this atmospheric reanalysis comparison, 6 of the 48 locations closest to Drew Point, Alaska, were selected (Figure 5.2-4).

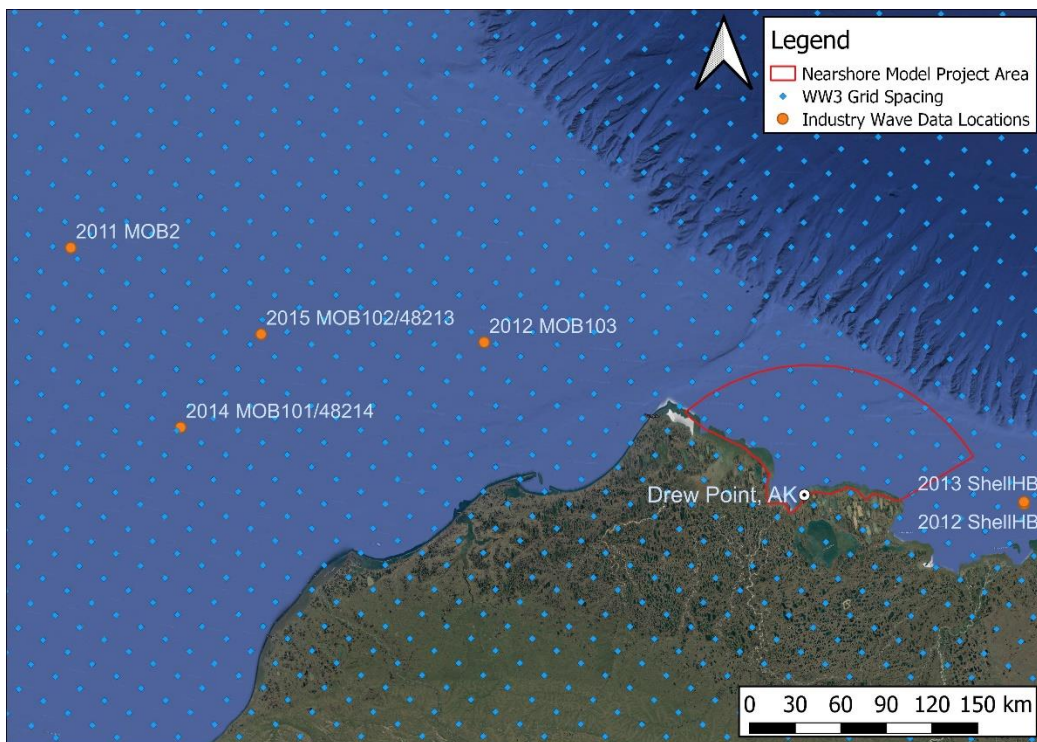


Figure 5.2-4. WW3 model grid centers and selected industry wave measurement stations around Drew Point, Alaska. Industry wave measurement stations made available through the BOEM project Jeremy Kasper is PI on.

Table 5.2-3 presents the stations, available wave parameters, and their temporal coverage used for the WW3 model comparisons. The years in bold are the 6 stations compared in the following section. Significant wave height and peak wave period were the wave parameters compared for this evaluation.

Table 5.2-3. Selected Industry Wave Measurement Station Summary.

Industry Wave Station	Temporal Coverage	Wave Parameters Available
MOB2	2011 , 2015	Hs, Tp, Dp, Hmax
MOB103	2012	Hs, Tp, Dp, Hmax
ShellHB	2012, 2013 , 2014	Hs, Tp, Hmax
MOB101/NDBC 48214	2012, 2013, 2014 , 2015	Hs, Tp, Dp
MOB102/NDBC 48213	2012, 2013, 2015	Hs, Tp, Dp

Notes:

Temporal coverage is only for select summer months during years shown in table.

Bold years are the selected years for the comparison presented herein.

Hs = significant wave height

Tp = peak wave period

Dp = peak wave direction

Hmax = maximum wave height

5.2.2.3. Results

The figures and tables below present comparisons and quantitative performance metrics for the Arctic Ocean WW3 model forced with ERAI-WRF, ASR, and NARR for the selected industry wave data locations. CBHAR model results were not included in this analysis given that the data are available only through 2009. The focus for this memorandum is on deep water (>20 m) wave measurements because large scale models like the Arctic WW3 model do not capture nearshore wave dynamics with good accuracy. Figure 5.2-5 through Figure 5.2-9 show a direct comparison of simulated and measured data (gray markers) and the colored markers show the quantiles of the simulated and measured data for each model forcing. The closer the data points fall on the 1:1 solid black line, the better the model-measured agreement and similarity of the underlying probability distribution.

Table 5.2-4 through Table 5.2-9 show quantitative performance metrics for the comparison of simulated and measured significant wave height and peak wave period.

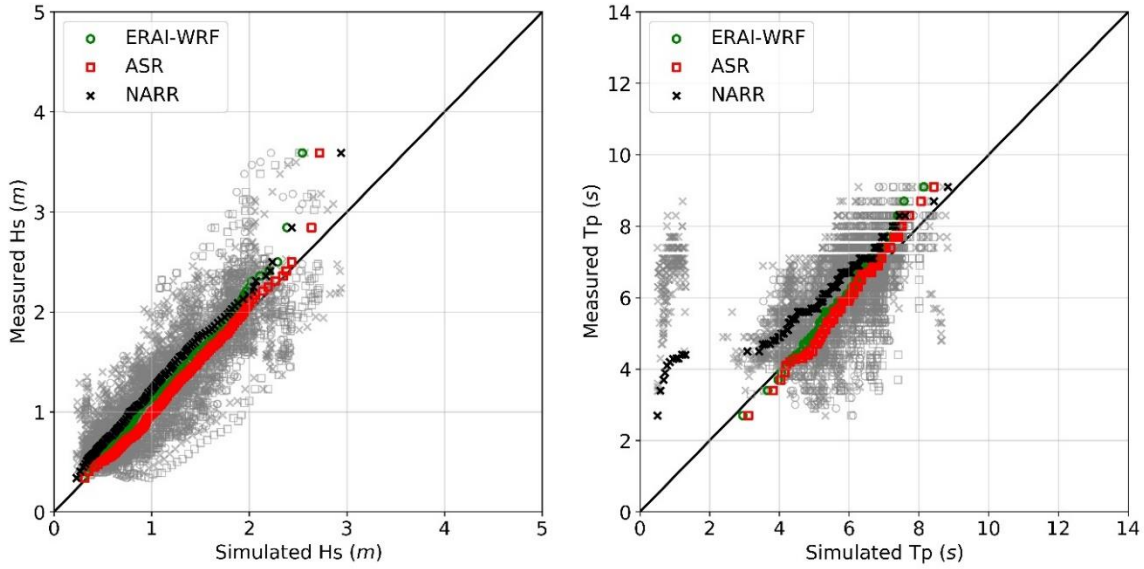


Figure 5.2-5. 2011 MOB2 comparison of simulated and measured significant wave height (left) and peak wave period (right) for the Arctic WW3 model forced by ERAI-WRF, ASR, and NARR. The gray symbols are a direct comparison of simulated and measured data. The colored symbols are quantile-quantile values.

Table 5.2-4. WW3 Significant Wave Height / Peak Wave Period Performance Metrics at 2011 MOB2 Site for the Arctic Reanalysis Data Sets.

Reanalysis Forcing	Correlation Coefficient	RMSE (m / s)	Skill
ERAI-WRF	0.87 / 0.68	0.32 / 0.9	0.92 / 0.79
ASR	0.85 / 0.68	0.31 / 0.9	0.92 / 0.81
NARR	0.84 / 0.24	0.39 / 2.1	0.89 / 0.55

Notes:

RMSE = root mean square error
Skill from Wilmott (1981)

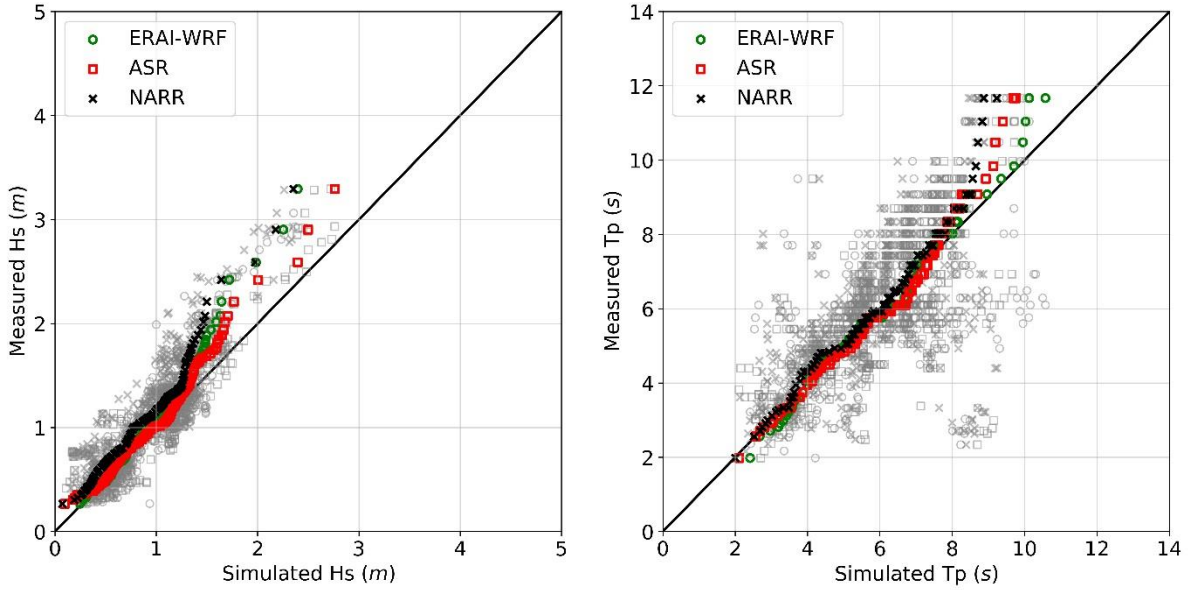


Figure 5.2-6. 2012 ShellHB comparison of simulated and measured significant wave height (left) and peak wave period (right) for the Arctic WW3 model forced by ERAI-WRF, ASR, and NARR. The gray symbols are a direct comparison of simulated and measured data. The colored symbols are quantile-quantile values.

Table 5.2-5. WW3 Significant Wave Height / Peak Wave Period Performance Metrics at 2012 ShellHB Site for the Arctic Reanalysis Data Sets.

Reanalysis Forcing	Correlation Coefficient	RMSE (m / s)	Skill
ERAI-WRF	0.91 / 0.64	0.27 / 1.6	0.92 / 0.80
ASR	0.94 / 0.72	0.22 / 1.4	0.96 / 0.85
NARR	0.90 / 0.61	0.34 / 1.7	0.88 / 0.77

Notes:

RMSE = root mean square error
Skill from Wilmott (1981)

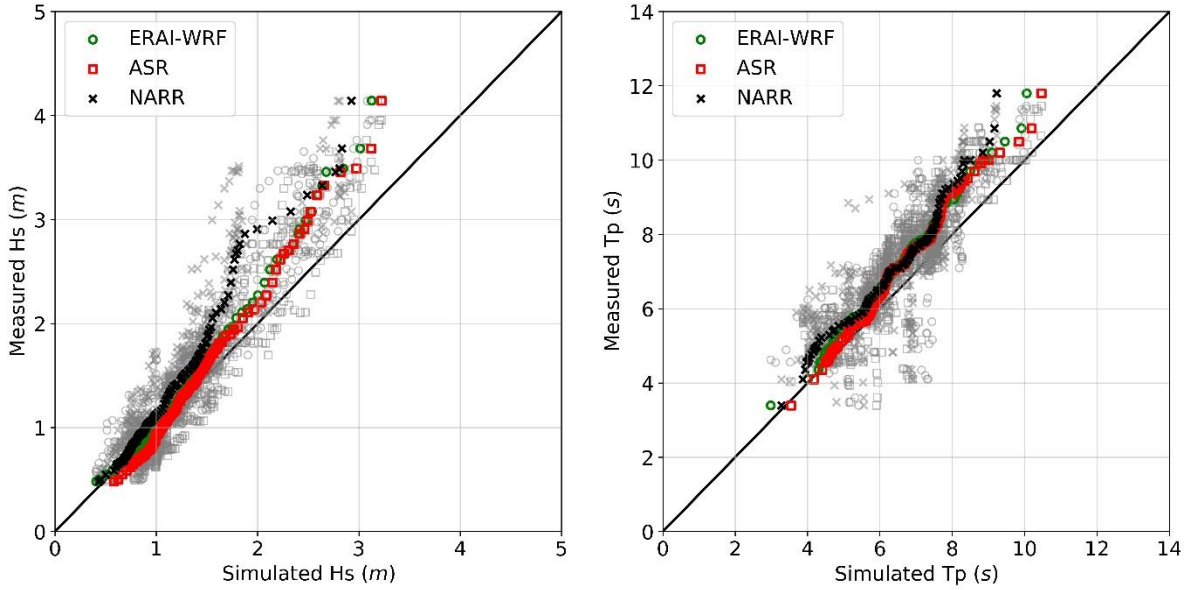


Figure 5.2-7. 2012 MOB103 comparison of simulated and measured significant wave height (left) and peak wave period (right) for the Arctic WW3 model forced by ERAI-WRF, ASR, and NARR. The gray symbols are a direct comparison of simulated and measured data. The colored symbols are quantile-quantile values.

Table 5.2-6. WW3 Significant Wave Height / Peak Wave Period Performance Metrics at 2012 MOB103 Site for the Arctic Reanalysis Data Sets.

Reanalysis Forcing	Correlation Coefficient	RMSE (m / s)	Skill
ERAI-WRF	0.95 / 0.85	0.33 / 1.1	0.94 / 0.87
ASR	0.95 / 0.89	0.31 / 0.9	0.95 / 0.90
NARR	0.92 / 0.85	0.45 / 1.1	0.88 / 0.85

Notes:

RMSE = root mean square error
Skill from Wilmott (1981)

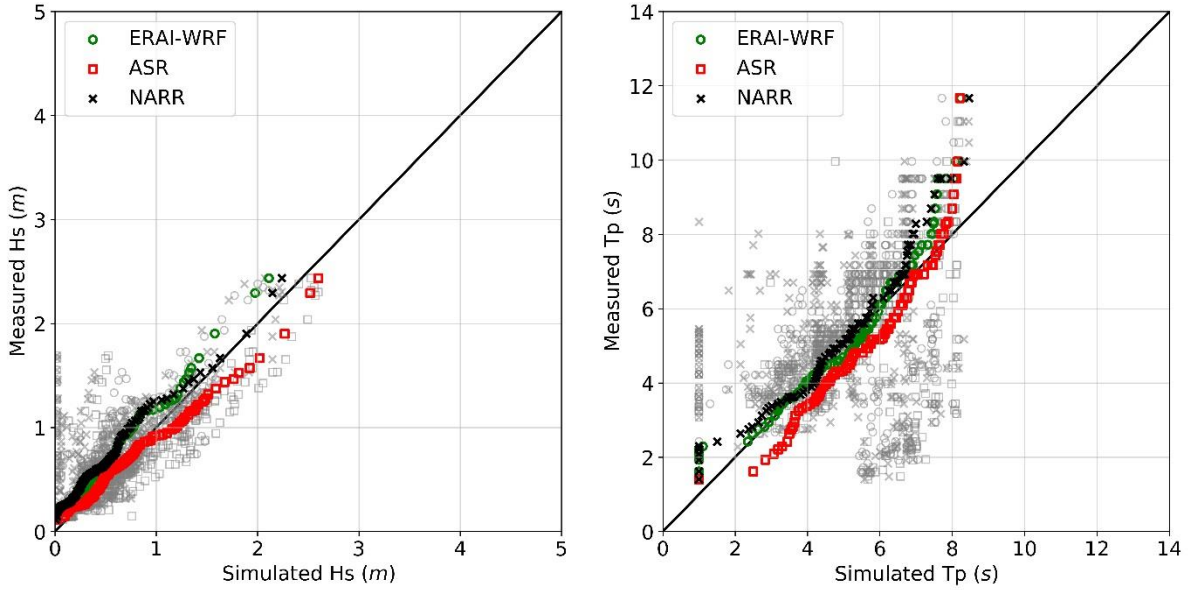


Figure 5.2-8. 2013 ShellHB comparison of simulated and measured significant wave height (left) and peak wave period (right) for the Arctic WW3 model forced by ERAI-WRF, ASR, and NARR. The gray symbols are a direct comparison of simulated and measured data. The colored symbols are quantile-quantile values.

Table 5.2-7. WW3 Significant Wave Height / Peak Wave Period Performance Metrics at 2013 ShellHB Site for the Arctic Reanalysis Data Sets.

Reanalysis Forcing	Correlation Coefficient	RMSE (m / s)	Skill
ERAI-WRF	0.78 / 0.45	0.33 / 2.0	0.85 / 0.66
ASR	0.85 / 0.49	0.29 / 1.8	0.91 / 0.71
NARR	0.73 / 0.27	0.37 / 2.3	0.83 / 0.56

Notes:

RMSE = root mean square error
Skill from Wilmott (1981)

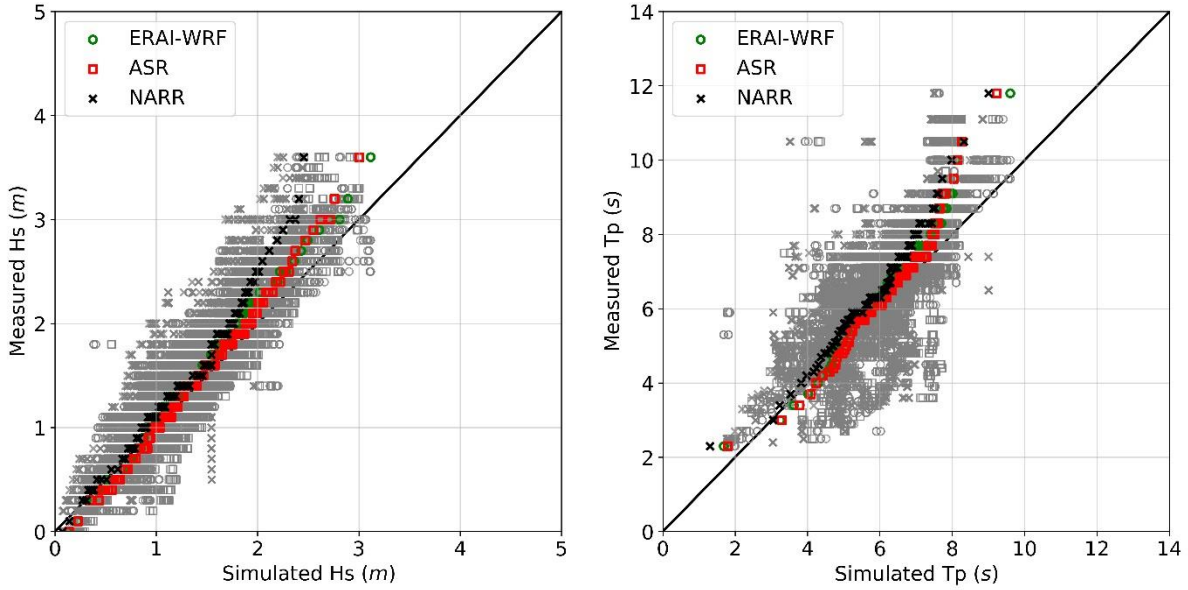


Figure 5.2-9. 2014 MOB101 comparison of simulated and measured significant wave height (left) and peak wave period (right) for the Arctic WW3 model forced by ERAI-WRF, ASR, and NARR. The gray symbols are a direct comparison of simulated and measured data. The colored symbols are quantile-quantile values.

Table 5.2-8. WW3 Significant Wave Height / Peak Wave Period Performance Metrics at 2014 MOB101 Site for the Arctic Reanalysis Data Sets.

Reanalysis Forcing	Correlation Coefficient	RMSE (m / s)	Skill
ERAI-WRF	0.93 / 0.76	0.29 / 1.0	0.95 / 0.83
ASR	0.94 / 0.75	0.25 / 1.0	0.96 / 0.84
NARR	0.87 / 0.75	0.40 / 1.1	0.89 / 0.80

Notes:

RMSE = root mean square error
Skill from Wilmott (1981)

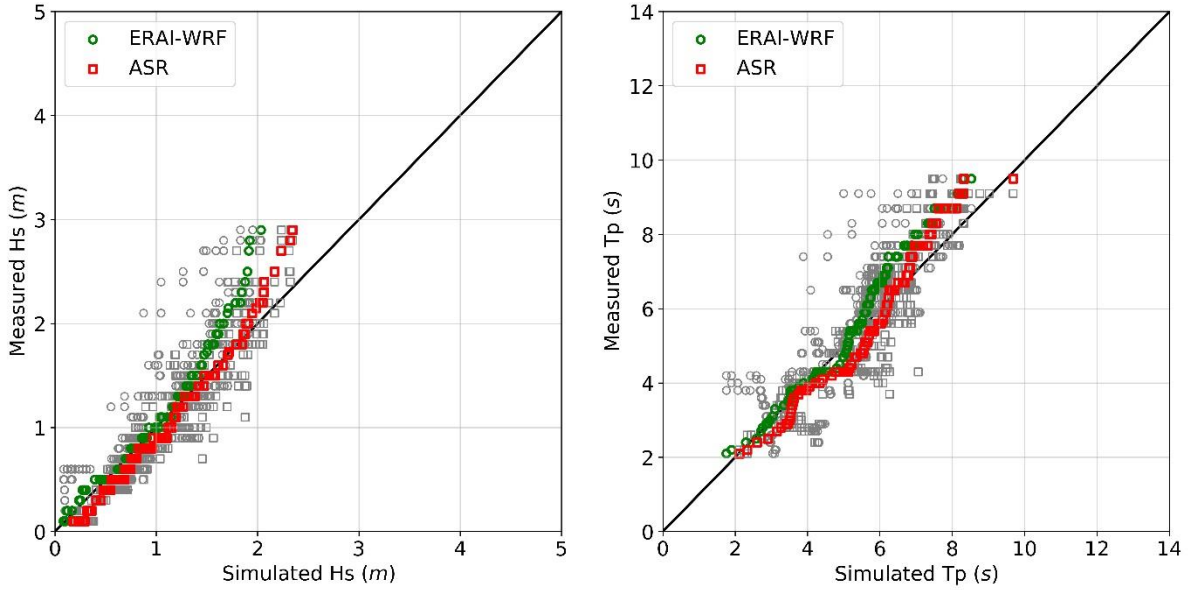


Figure 5.2-10. 2015 MOB102 comparison of simulated and measured significant wave height (left) and peak wave period (right) for the Arctic WW3 model forced by ERAI-WRF and ASR. The gray symbols are a direct comparison of simulated and measured data. The colored symbols are quantile-quantile values.

Table 5.2-9. WW3 Significant Wave Height / Peak Wave Period Performance Metrics at 2015 MOB102 Site for the Arctic Reanalysis Data Sets.

Reanalysis Forcing	Correlation Coefficient	RMSE (m / s)	Skill
ERAI-WRF	0.89 / 0.88	0.33 / 1.0	0.92 / 0.91
ASR	0.94 / 0.91	0.24 / 0.8	0.96 / 0.94
NARR			

Notes:

RMSE = root mean square error
Skill from Wilmott (1981)

Table 5.2-10 presents the average quantitative model performance metrics for ERAI-WRF, ASR, and NARR for significant wave height and peak wave period at the six selected industry wave data stations.

Table 5.2-10. Average WW3 Significant Wave Height / Peak Wave Period Performance Metrics for the Six Selected Stations for the Arctic Reanalysis Data Sets.

Reanalysis Forcing	Correlation Coefficient	RMSE (m / s)	Skill
ERA1-WRF	0.89 / 0.71	0.31 / 1.3	0.92 / 0.81
ASR	0.91 / 0.74	0.27 / 1.1	0.94 / 0.84
NARR	0.85 / 0.54	0.39 / 1.7	0.87 / 0.71

Notes:

RMSE = root mean square error
Skill from Wilmott (1981)

Overall, the ERA1-WRF and ASR atmospheric reanalysis data sets accurately simulate significant wave height and peak wave period at the selected industry buoy locations. The model does underpredict the measured wave heights above 2 m for most of the time periods and stations selected, though skill scores are still high. ASR outperforms ERA1-WRF with average skill of 0.94 as compared to the ERA1-WRF average skill of 0.92 for significant wave height. The average skill values for peak wave period for ASR and ERA1-WRF are 0.84 and 0.81, respectively.

Moving forward, ASR was selected to be used with the Delft3D-FLOW/WAVE nearshore models.

5.2.3. WW3 – UW CODA Buoy Comparison

Jim Thomson, Ph.D. at the University of Washington (UW) deployed 6 bottom moorings offshore of the North Slope of Alaska in 2019 (www.apl.uw.edu/coda). These moorings contained RBR pressure loggers which were used to compute significant wave height, peak wave period, and peak wave direction. Two of the 6 locations were selected to compare to WW3 predictions (Figure 5.2-11). Location S2-P1 was deployed 5.6 km offshore in a water depth of 14 m and location S3-P1 was deployed 5.6 km offshore in a water depth of 21 m.

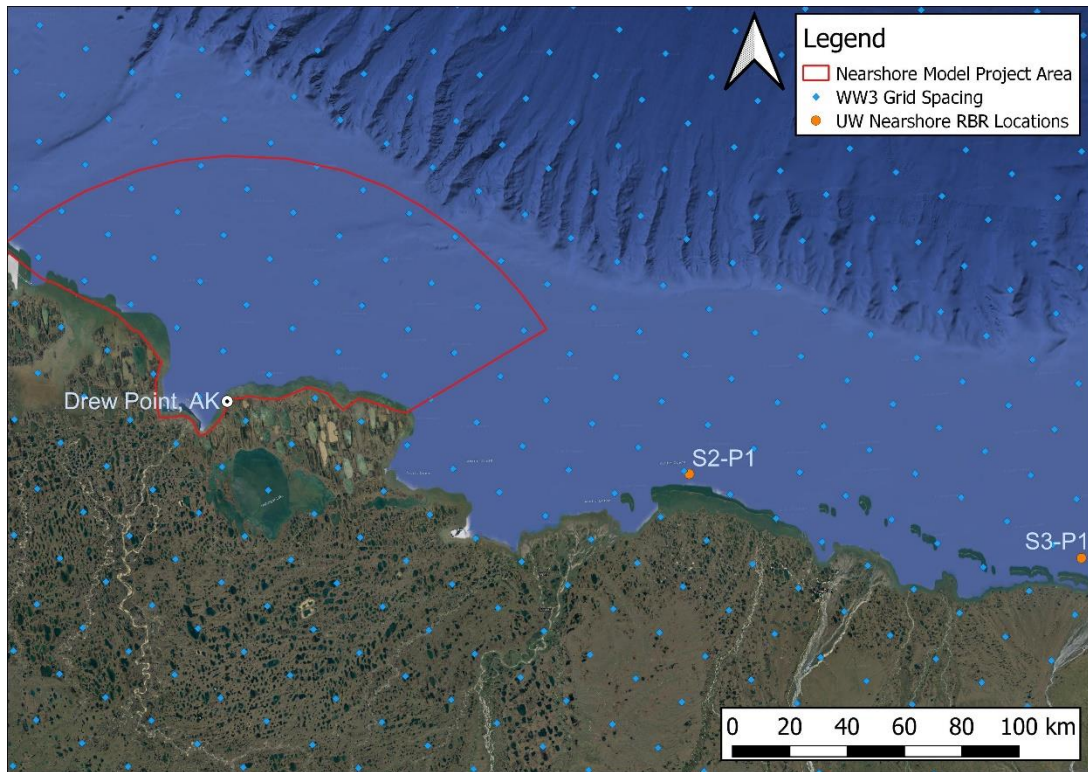


Figure 5.2-11. University of Washington RBR Measurement Locations along the North Slope of Alaska.

Figure 5.1-12 and Figure 5.2-13 compare the Arctic Ocean WW3 wave height and period predictions to the S2-P1 and S3-P1 measurement stations, respectively. Predictions from the WW3 grid cell closest to each measurement station were extracted for the comparisons below. Outside of the two higher wave events on 09/01/2019 and 10/19/2019, WW3 accurately predicted the measured wave heights. The peak wave periods were accurately predicted during the whole measurement period. The underprediction of the wave heights during the two events was caused by the atmospheric reanalysis forcing dataset, ERA5 in this case, underpredicting the peak wind speeds during these events (Figure 5.2-14). Aside from the under prediction of the larger wind events, the quantitative performance metrics for significant wave height at the S2-P1 and S3-P1 locations indicate an excellent model to measured data comparison (Table 5.2-11 and Table 5.2-12). The peak wave period predictions range from good to excellent at both locations. The lower performance metrics for the peak wave period as compared to the significant wave height predictions was a result of the short duration over and under predictions during the data record at both locations. Overall, the model accurately predicted the significant wave height and peak wave period for both locations, providing confidence in the WW3 model predictions.

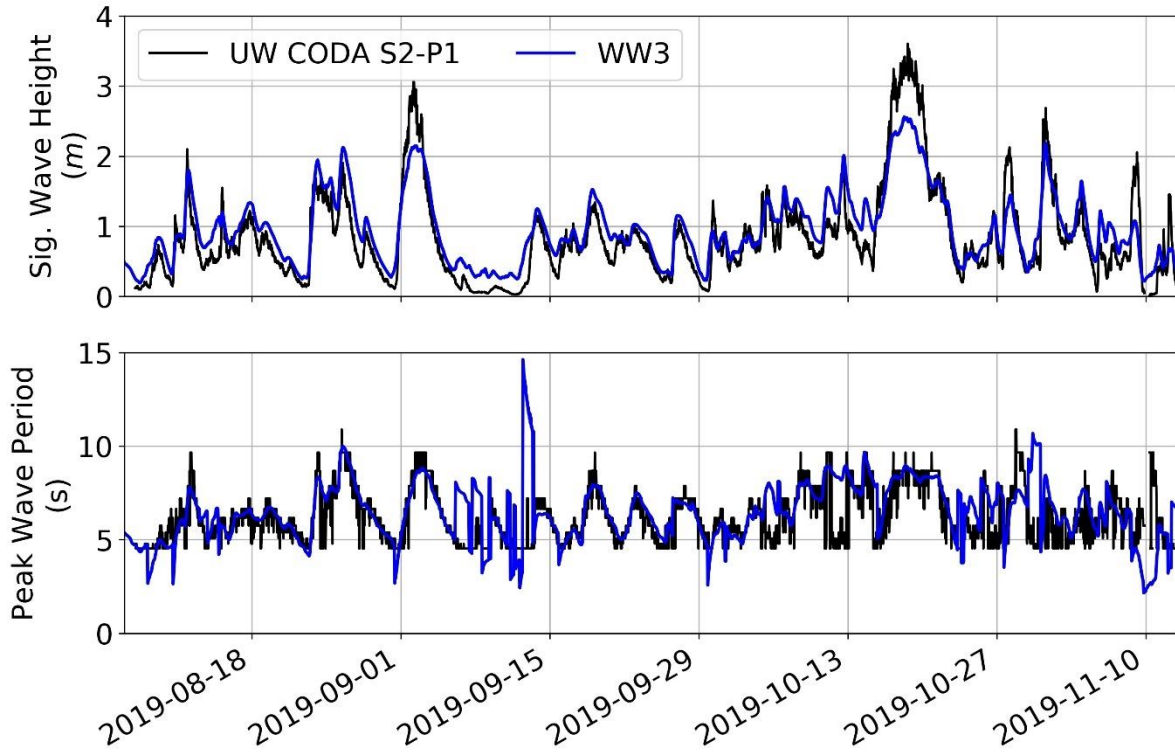


Figure 5.2-12. Comparison of the Arctic Ocean WW3 Predicted Significant Wave Height and Peak Wave Period to the UW Measured Data at Location S2-P1.

Table 5.2-11. WW3 Significant Wave Height / Peak Wave Period Performance Metrics at UW CODA S2-P1 Site.

Reanalysis Forcing	Correlation Coefficient	RMSE (m / s)	Skill
ERA5	0.92 / 0.48	0.30 / 1.55	0.93 / 0.72

Notes:

RMSE = root mean square error
Skill from Wilmott (1981)

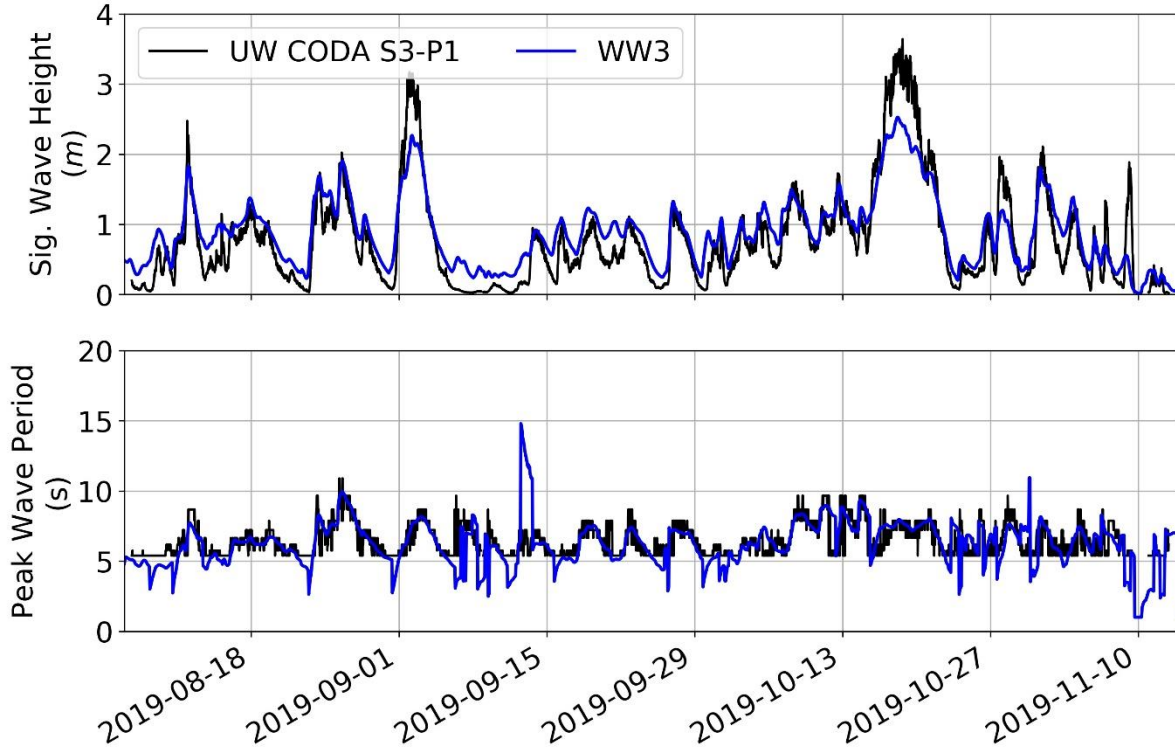


Figure 5.2-13. Comparison of the Arctic Ocean WW3 Predicted Significant Wave Height and Peak Wave Period to the UW Measured Data at Location S3-P1.

Table 5.2-12. WW3 Significant Wave Height / Peak Wave Period Performance Metrics at UW CODA S3-P1 Site.

Reanalysis Forcing	Correlation Coefficient	RMSE (m / s)	Skill
ERA5	0.93 / 0.59	0.33 / 1.27	0.93 / 0.74

Notes:
 RMSE = root mean square error
 Skill from Wilmott (1981)

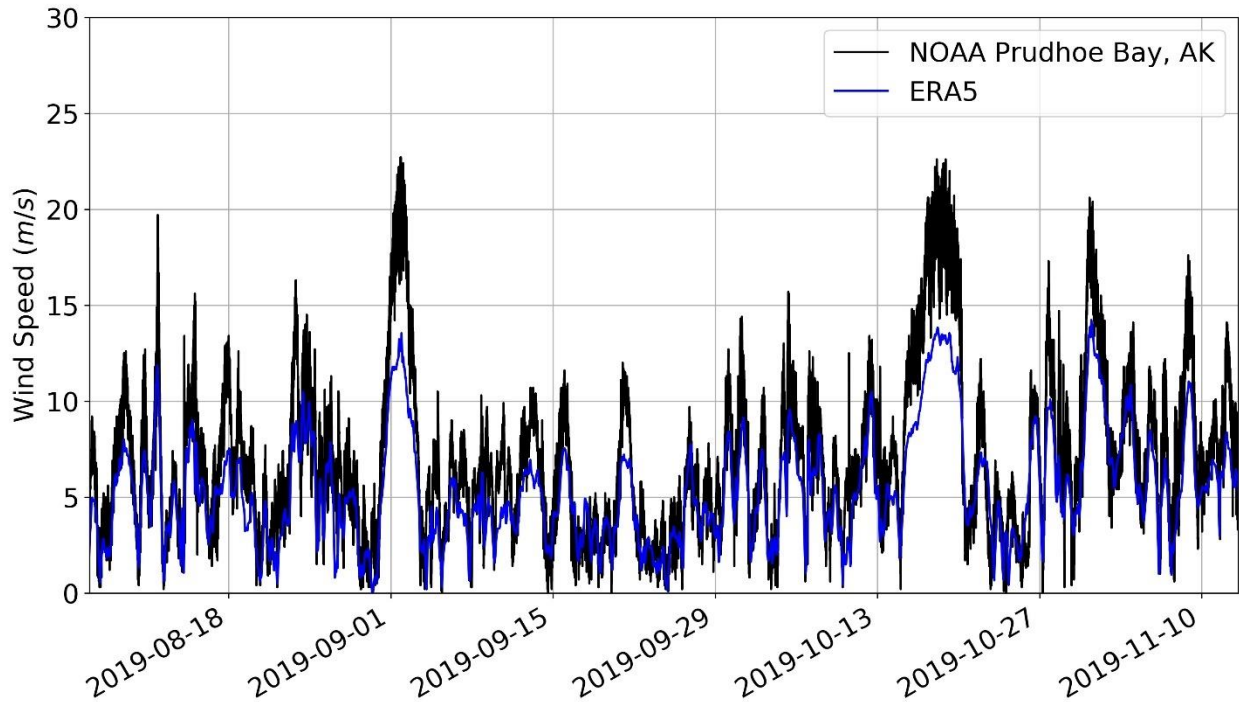


Figure 5.2-14. Comparison of NOAA Prudhoe Bay, AK Station Wind Speeds with ERA5 Predicted Wind Speeds.

5.2.4. SWAN – Barnhart Nearshore Comparison

Barnhart et al. (2014b) presents modeling of permafrost bluff erosion along the Alaskan Beaufort Sea coastline. In addition to the modeling, water temperature sensors, water level, and wave loggers were deployed offshore of Drew Point in the summers of 2009 and 2010. For this study, the Wave Logger 2 station, deployed 100 m offshore of Drew Point in 2009 in a water depth of 1.9 m was used for the comparison to the Delft3D-FLOW/WAVE predictions (Figure 5.2-15). The other stations and the 2010 data from Barnhart et al. 2014 were not available for this analysis.

The Delft3D-FLOW/WAVE predicted significant wave height and peak wave period are in good agreement with the measured data (Figure 5.2-16). The Delft3D-FLOW/WAVE model did over predict the significant wave height outside of higher wind or swell events. This is likely a result of a difference in how the nearshore wave energy dissipates in the model compared to the conditions during the deployment periods. The quantitative performance metrics for significant wave height at the Wave Logger 2 location indicate an excellent model to measured data comparison (Table 5.2-13). The peak wave period predictions range from very good to excellent. Overall, the model accurately predicted the measured data for this station, providing confidence in the Delft3D-FLOW/WAVE model predictions.

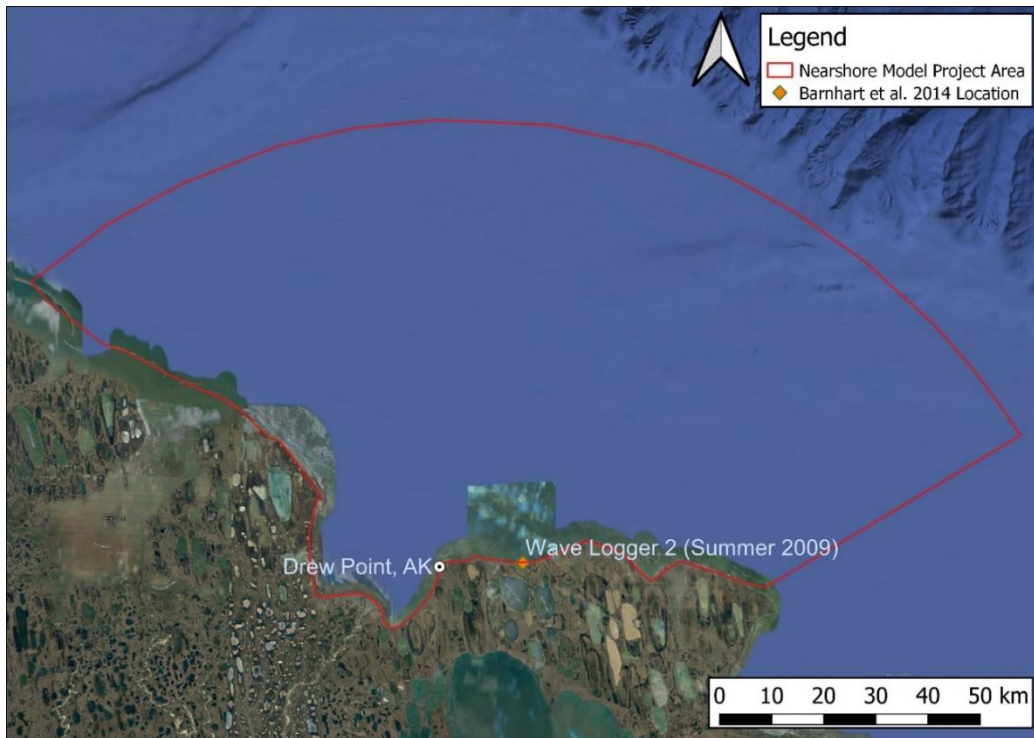


Figure 5.2-15. Location of Wave Logger 2 Measurement Station from Barnhart et al. 2014b.

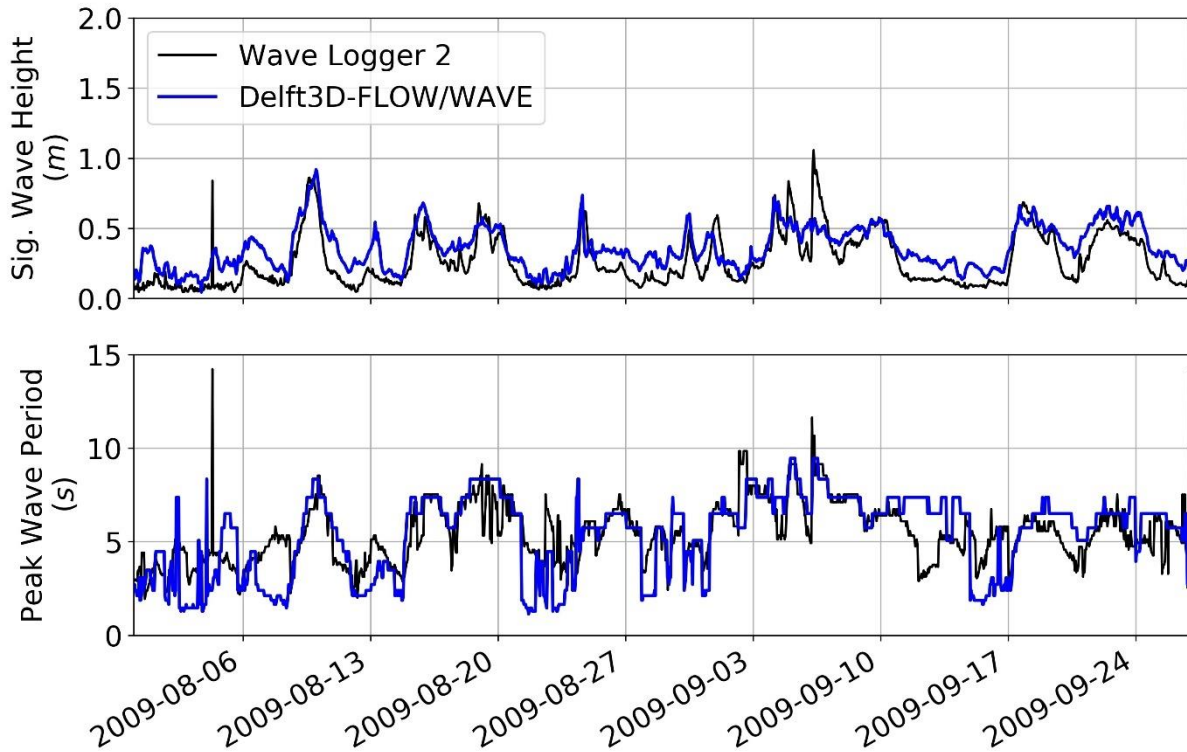


Figure 5.2-16. Comparison of the Delft3D-FLOW/WAVE Predicted Significant Wave Height and Peak Wave Period to the Barnhart et al. 2014b Wave Logger 2 Measurement Station.

Table 5.2-13. Delft3D-FLOW/WAVE Significant Wave Height / Peak Wave Period Performance Metrics at Barnhart et al. 2014b Wave Logger 2 (2009) Site.

Reanalysis Forcing	Correlation Coefficient	RMSE (m / s)	Skill
ASR	0.82 / 0.63	0.14 / 1.66	0.83 / 0.77

Notes:

RMSE = root mean square error

Skill from Wilmott (1981)

5.2.5. SWAN – 2018 2019 Field Data Comparison

Nondirectional wave spectra (wave height and period), water level fluctuations and water temperature data were collected by an RBR TDWave sensor in 2018 and 2019 in the nearshore environment of Drew Point, see Section 2.3.1.3. The Delft3D-FLOW/WAVE nearshore model predictions were compared to the 2018 and 2019 Drew Point RBR data. The predicted water levels and peak wave period are in good agreement with the 2018 and 2019 RBR data (Figure 5.2-18 and Figure 5.2-19). The Delft3D-FLOW/WAVE model over predicts the significant wave height outside of higher wind or swell events. This is likely a result of a difference in how the nearshore wave energy dissipates in the model compared to the conditions during the deployment periods. The measured peak wave period for the 2018 and 2019 RBR locations is sparse likely due to a lower

threshold of measured wave height due to the instrument configuration. The quantitative performance metrics for water level at the 2018 and 2019 RBR locations indicate an excellent model to measured data comparison (Table 5.2-14 and Table 5.2-15). While there was a significant wave height overprediction, the quantitative metrics indicate very good to excellent model performance. The peak wave period comparisons provided a challenge for the quantitative metrics; the measured peak wave period data is sparse and noisy, where the model predicted a smoother signal. However, the skill values for peak wave period indicate very good to excellent model performance, which matches with the qualitative assessment of the model predictions. Overall, the model accurately predicted the measured data for the 2018 and 2019 RBR stations, providing confidence in the Delft3D-FLOW/WAVE model predictions.



Figure 5.2-17. Location of 2018 and 2019 Drew Point RBRs.

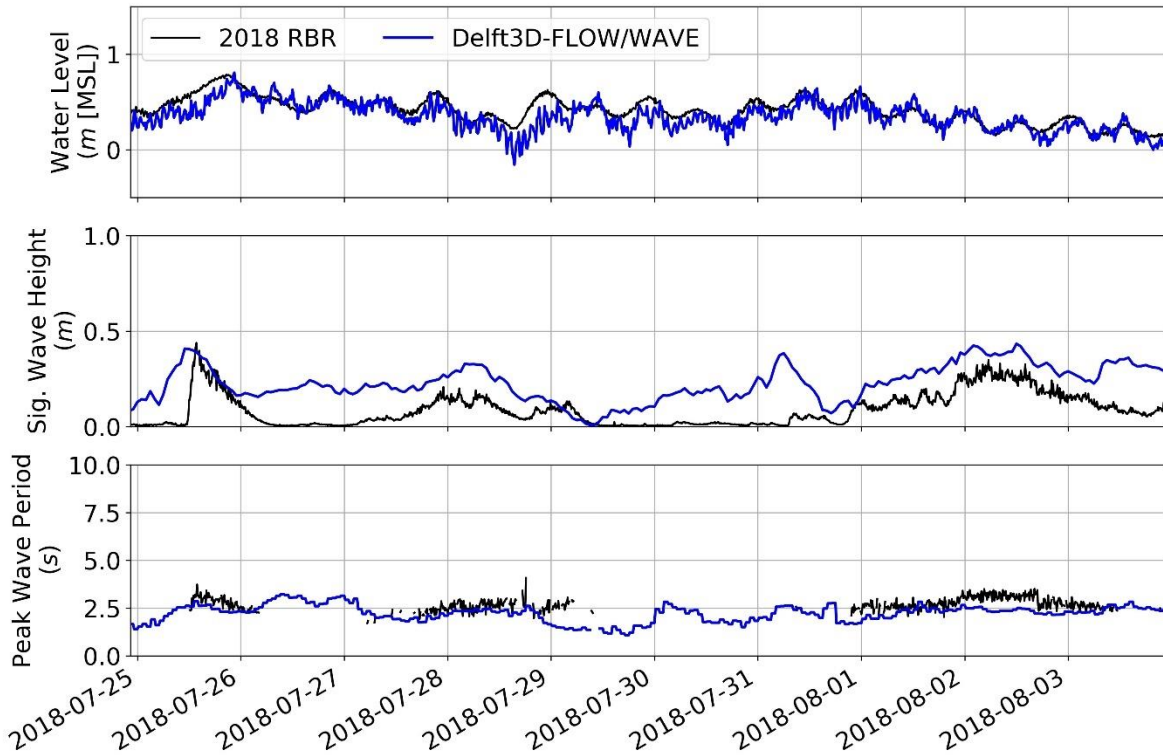


Figure 5.2-18. Comparison of the Delft3D-FLOW/WAVE Predicted Water Level, Significant Wave Height, and Peak Wave Period to the Drew Point 2018 RBR Measurement Station.

Table 5.2-14. Delft3D-FLOW/WAVE Water Level / Significant Wave Height / Peak Wave Period Performance Metrics at 2018 RBR Site.

Reanalysis Forcing	Correlation Coefficient	RMSE (m / s)	Skill
ERA5	0.78 / 0.62 / 0.30	0.11 / 0.16 / 0.58	0.84 / 0.72 / 0.64

Notes:

RMSE = root mean square error
Skill from Wilmott (1981)

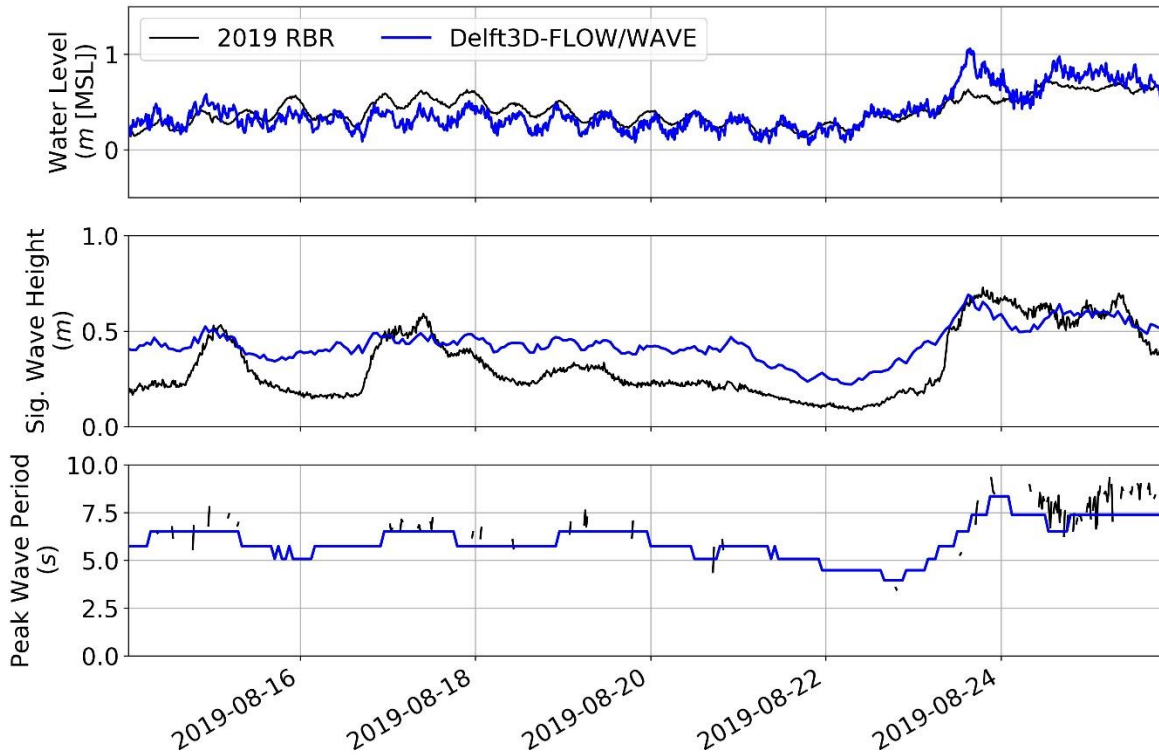


Figure 5.2-19. Comparison of the Delft3D-FLOW/WAVE Predicted Water Level, Significant Wave Height, and Peak Wave Period to the Drew Point 2019 RBR Measurement Station.

Table 5.2-15. Delft3D-FLOW/WAVE Water Level / Significant Wave Height / Peak Wave Period Performance Metrics at 2019 RBR Site.

Reanalysis Forcing	Correlation Coefficient	RMSE (m / s)	Skill
ERA5	0.79 / 0.87 / 0.73	0.13 / 0.15 / 3.47	0.86 / 0.78 / 0.73

Notes:

RMSE = root mean square error

Skill from Wilmott (1981)

5.2.6. Nearshore Water Level Comparison

As a final model to data comparison, the Delft3D-FLOW/WAVE predicted water levels were compared to two water level sensors deployed around Drew Point (Section 2.3.1.1 and Section 2.3.1.2). The two measurement stations selected for comparison to the model predictions were the Drew Point Spit station and the Ikpikpuk Delta station (Figure 5.2-20).

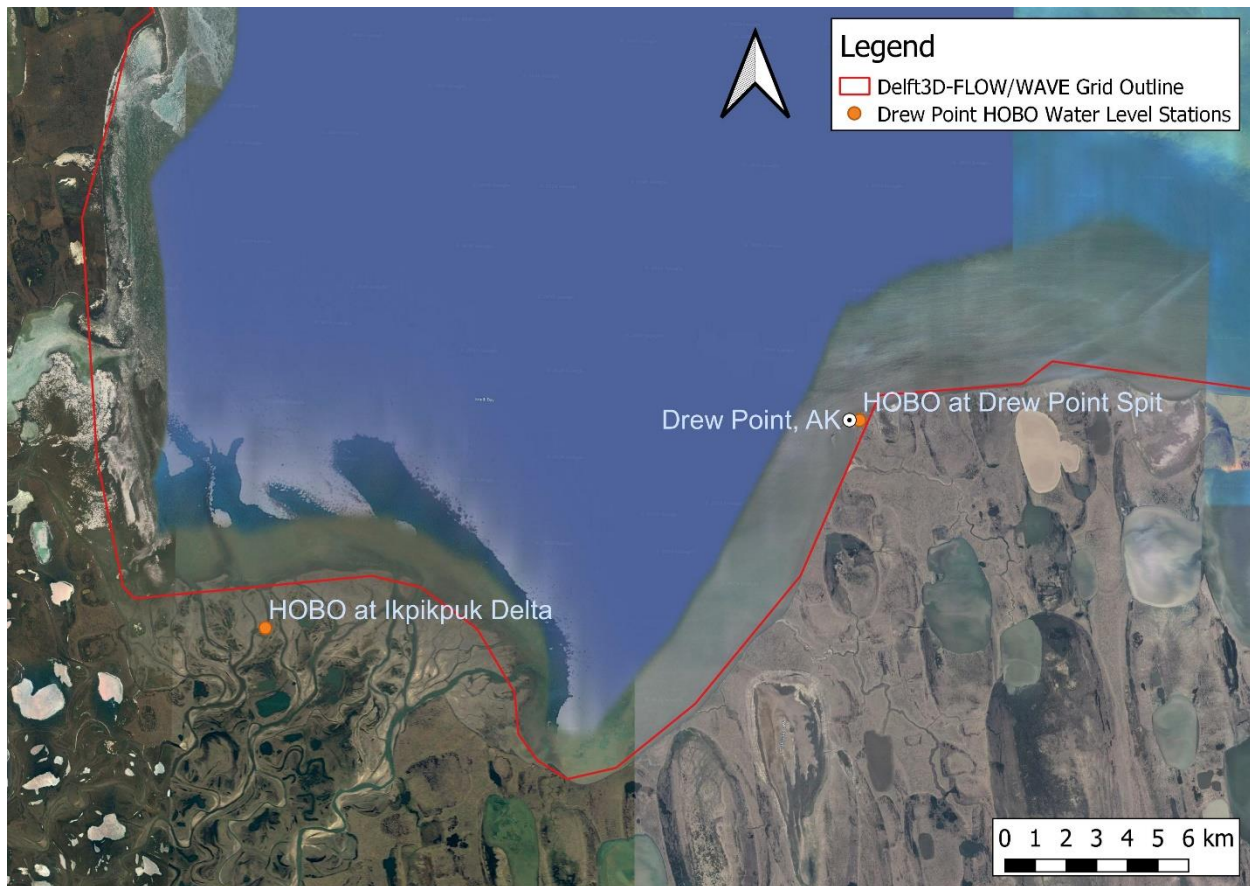


Figure 5.2-20. Delft3D-FLOW/WAVE Output Locations for Comparison to Nearshore Water Level Sensors.

The Delft3D-FLOW/WAVE 2 Hz water surface elevations, which incorporate water level, waves, wind setup, were compared to the 2011, 2012, and 2018 measurements at the Ikpikpuk Delta water inundation sensor (Figure 5.2-21, Figure 5.2-22, and Figure 5.2-23). The elevation of this sensor was surveyed after the 2011 data were collected. These comparisons were meant as a general comparison for the timing of when the water surface elevation was predicted to be above the cliff toe height. A perfect match isn't expected due to a number of factors (e.g., geometry of the coast, river dynamics influencing the sensor), and importantly, the Delft3D-FLOW/WAVE grid doesn't extend inshore of the coastline where the sensor was deployed. Given the uncertainty in the elevation of the sensor, and the spatial difference between the grid extent and the sensor location, the predicted water surface elevation has a good temporal match to the measured data, when the predicted water level is above the cliff toe height, there is a corresponding measurement from the sensor.

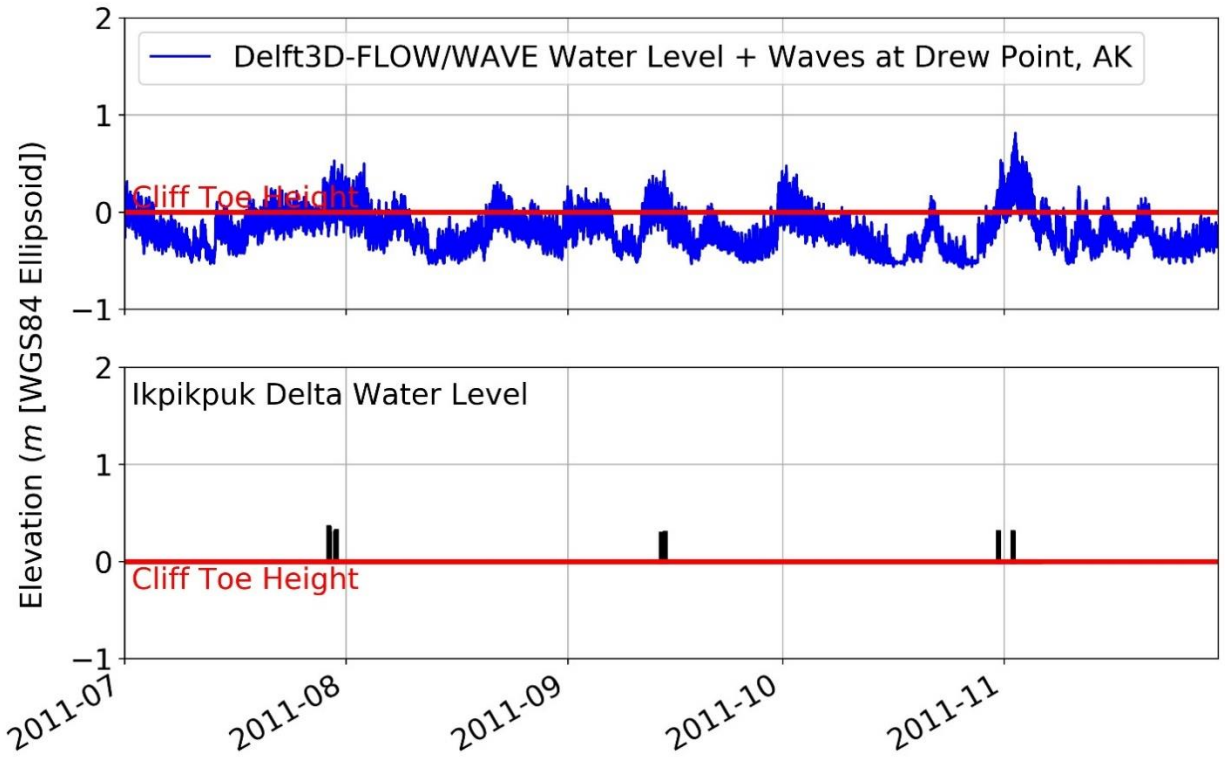


Figure 5.2-21. Comparison of the Delft3D-FLOW/WAVE Predicted Water Level to the 2011 Data from the Ikpikpuk Delta Water Inundation Station. The Established Cliff Toe Height is shown as the Red Line.

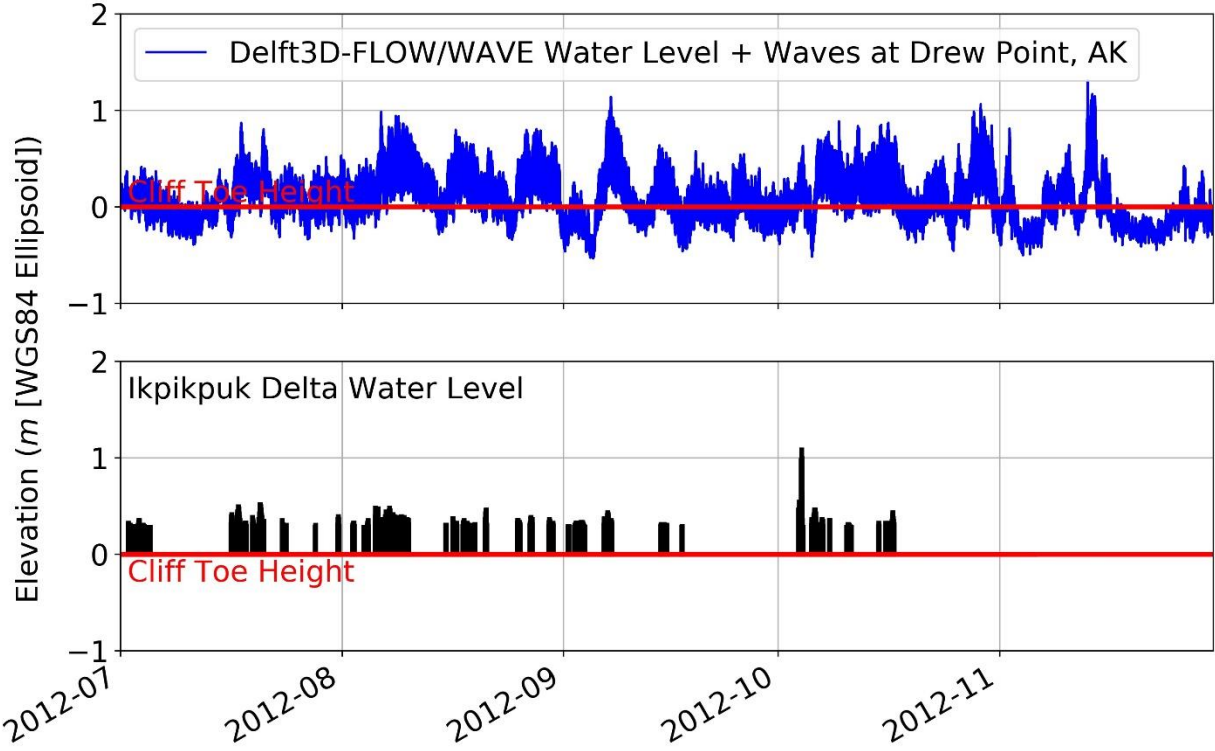


Figure 5.2-22. Comparison of the Delft3D-FLOW/WAVE Predicted Water Level to the 2012 Data from the Ikpikpuk Delta Water Inundation Station. The Established Cliff Toe Height is shown as the Red Line.

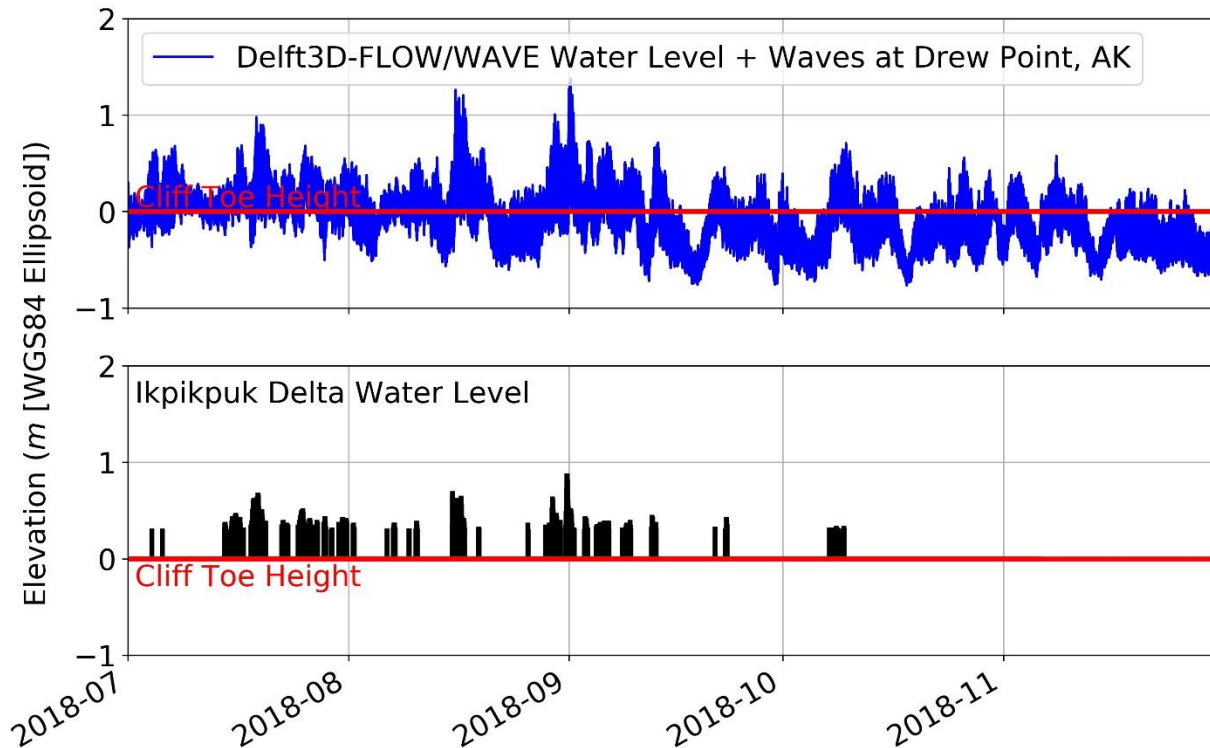


Figure 5.2-23. Comparison of the Delft3D-FLOW/WAVE Predicted Water Level to the 2018 Data from the Ikpikpuk Delta Water Inundation Station. The Established Cliff Toe Height is shown as the Red Line.

Lastly, the Delft3D-FLOW/WAVE water levels were compared to the measured water levels at the Drew Point Spit for 2018 and 2019 (Figure 5.2-24 and Figure 5.2-25). This water-level sensor was not surveyed for vertical elevation and was deployed inshore as an inundation tracker, thus it was meant as a general comparison for the timing of the higher water level events. The larger predicted water level events do coincide with measured peaks from the Drew Point Spit sensor. This provides further confidence in the timing of the predicted higher water level events that will be passed to the terrestrial model.

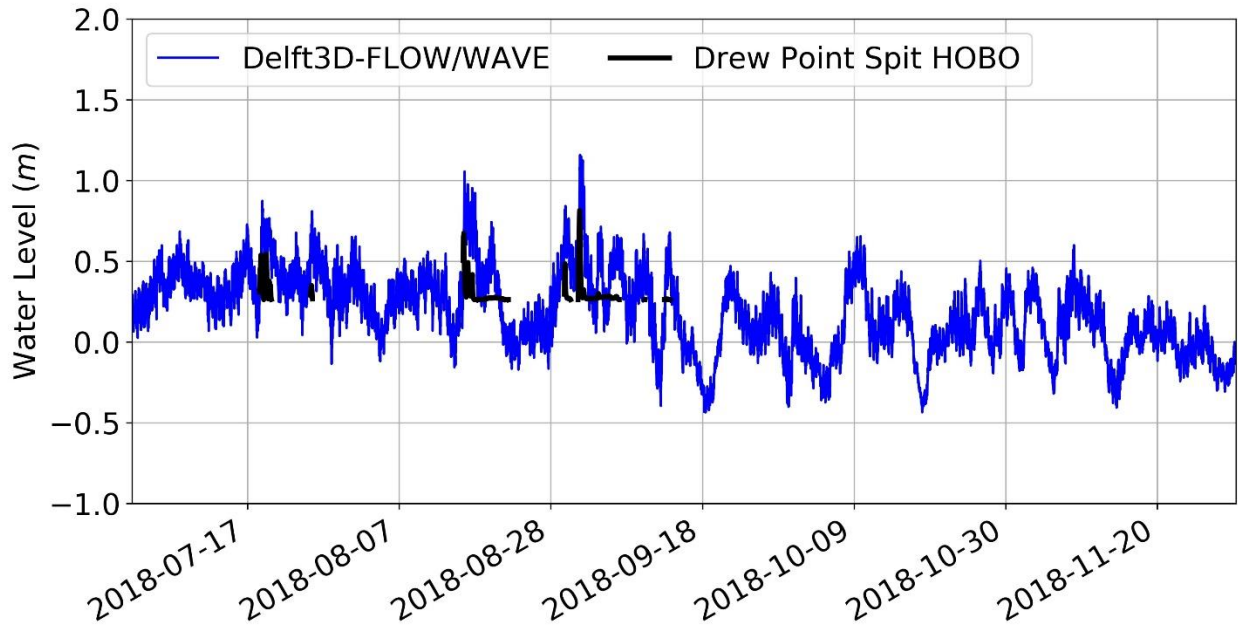


Figure 5.2-24. Comparison of the Delft3D-FLOW/WAVE Predicted Water Level to the 2018 Data from the Drew Point, AK Spit Water Level Station.

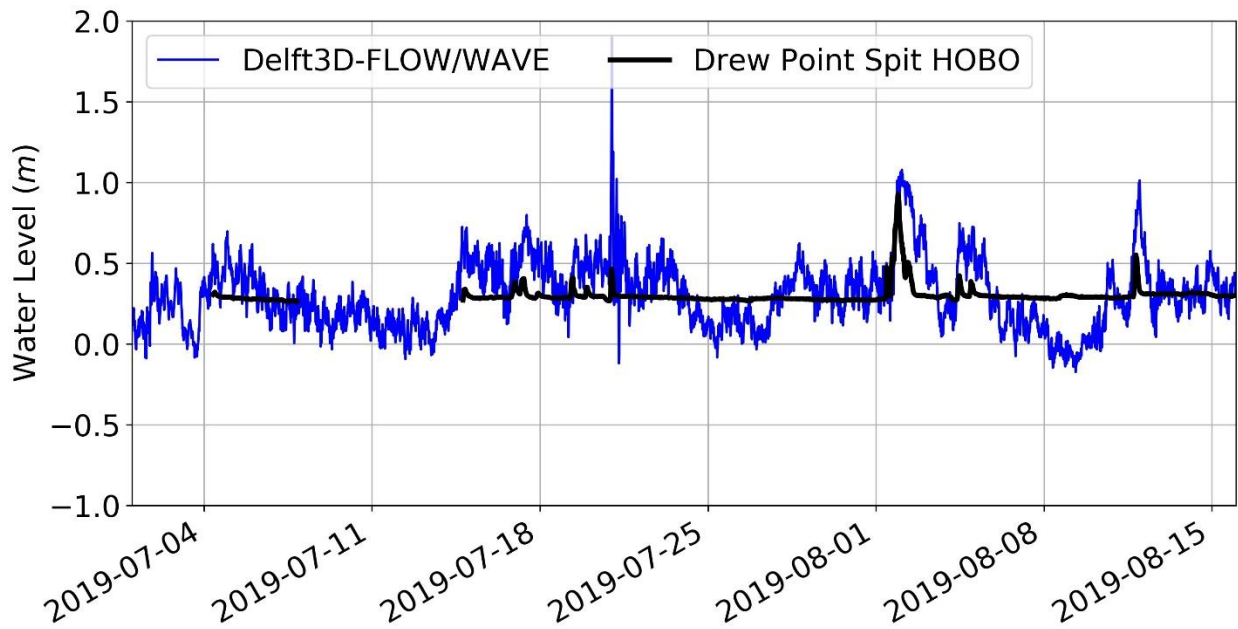


Figure 5.2-25. Comparison of the Delft3D-FLOW/WAVE Predicted Water Level to the 2019 Data from the Drew Point, AK Spit Water Level Station.

5.2.7. Future Steps

Should funding for this project continue, a full calibration and validation with the WW3 and Delft3D-FLOW/WAVE models would be performed to improve model performance at all the available data stations.

Model calibration and validation, as used in U.S. Environmental Protection Agency guidance (USEPA 2009) are defined as follows:

- **Model calibration**—Using site-specific information from a historical period to adjust model parameters to more accurately reflect measured site-specific conditions
- **Model validation**—Demonstrating that the calibrated model accurately reproduces known conditions over a period different from that used for calibration.

Along with a model calibration and validation, a model sensitivity would be performed after the validation to assess the sensitivity of the WW3 and Delft3D-FLOW/WAVE models to various wave physics packages and calibration parameters (e.g., bottom roughness, wind friction coefficients, JONSWAP values).

In addition to the full model calibration, validation, and sensitivity testing to improve the model performance, further funding would allow for a more detailed spatial comparison of model output along shore and cross shore. These analyses would improve the understanding of how the hydrodynamics and waves change along the North Slope and with changing bottom elevations. Furthermore, this information would improve the understanding of the ocean side forces contributing to the varying erosions rates along the North Slope coastline.

5.2.8. Oceanographic Modeling Conclusions

During the validation of WW3 and Delft3D-FLOW/WAVE, the model predictions were compared to an array of offshore, nearshore, and inshore measurement stations. These data included, water level, inundation, significant wave height, and peak wave period. The WW3 model predictions in offshore regions matched well to measured data, providing confidence in the boundary conditions supplied to the Delft3D-FLOW/WAVE model. In general, the Delft3D-FLOW/WAVE model predictions matched well to the various measured data locations. The water level predictions were inconsistent at times with the measured data, likely a result of forcing from Prudhoe Bay, ~200 km away from Drew Point, though the timing of the higher water level and inundation events did match the measured data. The significant wave height predictions did miss some of the higher wave events in the measured data, and over predicted the wave heights during lower wind speeds. However, with the inclusion of a model calibration and validation, described in the previous section, would improve these predictions. The model predicted peak wave periods did match well to the measured data.

Overall, the WW3 and Delft3D-FLOW/WAVE models accurately predicted the measured water levels, wave heights, and wave periods at inshore and offshore locations. While both models did over and under predict the measured data during some time periods, the quantitative metrics support a very good to excellent model validation. Specific to the scope of this project, the inshore locations are where the model predictions were extracted and will be passed to the terrestrial model and the Delft3D-FLOW/WAVE nearshore model accurately predicts the overall site conditions around Drew Point, providing confidence in the wave histories being passed to the terrestrial model.

5.3. Erosion Model Demonstration

Team Member Author: Jennifer Frederick (SNL)

Contributors: Alejandro Mota (SNL), Irina Tezaur (SNL), Diana Bull (SNL), Benjamin Jones (UAF)

A unique dataset was collected in 2018 in which a vertical thermistor string captured the temperature evolution of a bluff in the Ancient DTLB surface landscape from April through a block breakage

event. The development of a niche approximately 2.5m deep and 2.5m tall was recorded with the temperature probe. A time-lapse camera was able to capture the block breaking. This location was also part of the AUV surveys and the SfM analysis.

This section details the field data, oceanographic environment, and the ACE model performance. The terrestrial and oceanographic output locations are summarized in Table 5.3-1.

Table 5.3-1. Summary of locations and distance between them.

Terrestrial Location		Oceanographic Location		Distance between (km)
Latitude (N)	Longitude (W)	Latitude (N)	Longitude (W)	
70° 52' 50.02"	153° 53' 25.45"	70° 52' 54.66"	153° 53' 55.36"	0.3348

5.3.1. Field Data

The vertical thermistor string with 10 temperature sensors was placed in the DP1-1 core hole in March 2018. Starting on July 21, 2018 temperature values were reported hourly. Details of the vertical thermistor string can be found in Section 2.2.1.4.

The AUV survey on the 3rd of August was able to initialize geomorphological characteristics of the model including the size of the polygon block and the distance from the bluff edge to the vertical thermistor string. Figure 5.3-1 overlays these initialization dimensions with an image of the location on August 3rd, 2018. As noted in Section 3.1 the bluff height at this location is 5.2m.

The temperature profile, shown in Figure 5.3-2, shows an initial niche formation between the 15th and 20th of August. Secondary niche formation leading to failure commenced on the 29th of August. As confirmed by the time-lapse camera, the block failed on September 1, 2018 at 6am UTC.



Figure 5.3-1. Image of vertical thermistor location with dimensions overlaid of the polygon size and ice wedge width on August 3rd 2018. The following dimensions correspond with the lines identified in the plot: 1. 2.62m, 2. 6.5m, 3. 10.8m, 4. 5.65m, and 5. 3.0m.

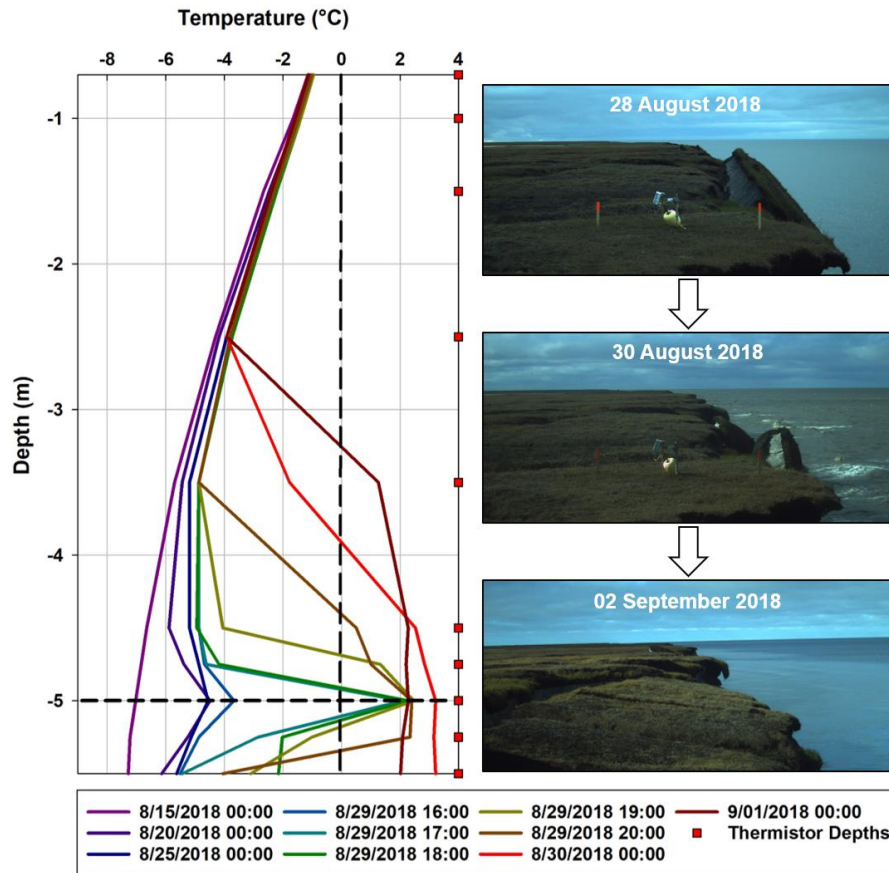


Figure 5.3-2. Permafrost borehole temperature profile showing niche development and block collapse paired with time lapse camera images. The bluff toe is at -5.2 m depth. Initial niche development occurred between 15 Aug and 20 Aug. Secondary niche development that led to block failure commenced on 29 Aug. Niche height grew to ~1.8 m between 29 August and 01 September prior to block failure. (times given in UTC).

5.3.2. Oceanographic Conditions

Figure 5.3-3 shows the water contact history from August 15th – September 3rd 2018 in UTC; this is the time period in which the niche developed and the block broke. The vertical thermistor begins to show significant niche development around the 17th of August, which motivated the time range shown in Figure 5.3-3. The time range commenced and ended with significant storms.

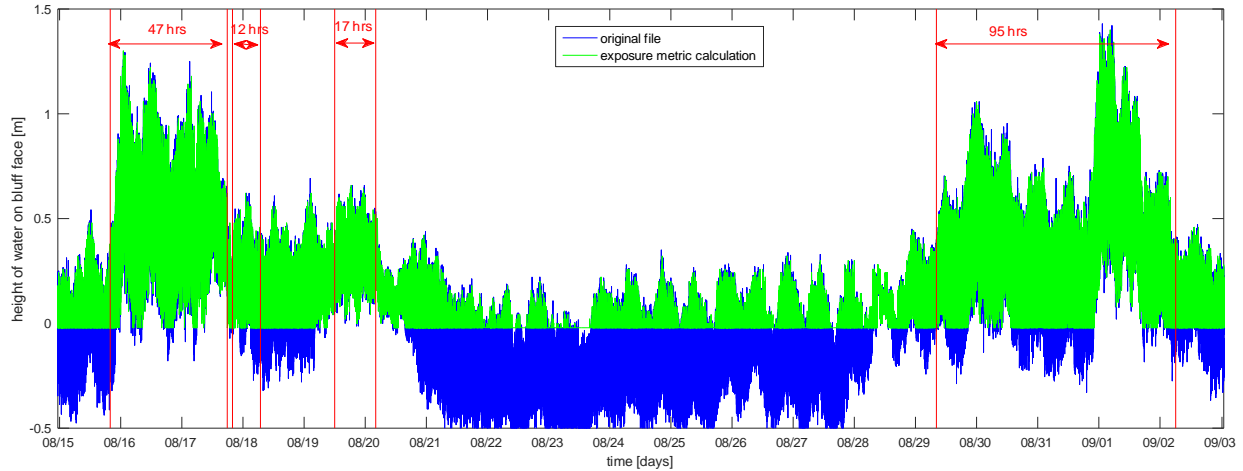


Figure 5.3-3. Water contact history from closest oceanographic grid cell with permafrost bluff over the time period in which the niche developed and the block broke (August 15th – September 3rd 2018). Raw file processed with a simulation time step of 2sec and a vertical resolution of 0.02m. Area between red lines indicate a water contact level of 0.4m up the bluff face has occurred for at least 12 consecutive hours; the number of consecutive hours is given above the arrows.

The distribution of water contact with the bluff between the two bounding AUV surveys (August 3rd and September 30th) is shown with circles in Figure 5.3-4. This time period is further segmented to show August 3rd – 15th in red dots, August 15th – September 3rd in yellow dots, and September 3rd – 30th in purple dots. The middle time period between August 15th – September 3rd in yellow dots corresponds to the time history shown in Figure 5.3-3. It is clear that the high contact levels are achieved during this time period when the niche developed and the block broke.

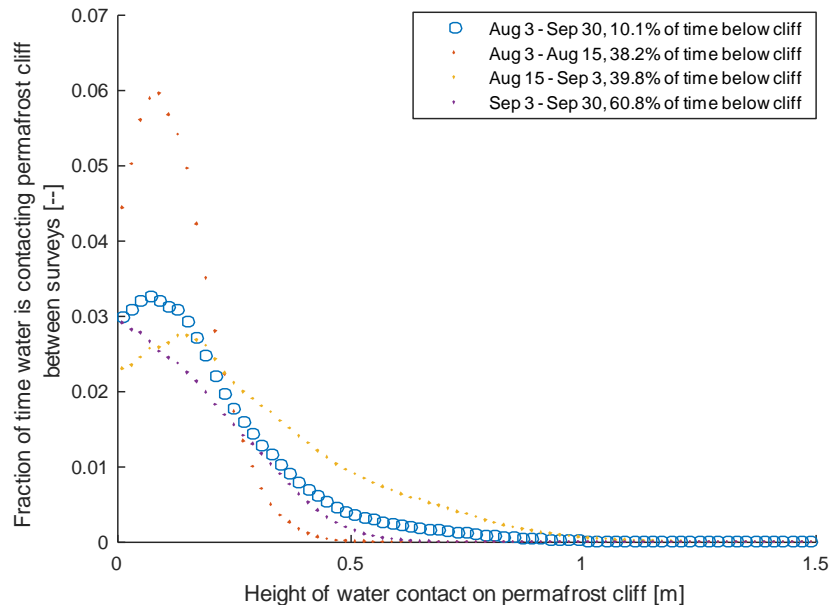


Figure 5.3-4. Distribution of the water contact history with the bluff face from closest oceanographic grid cell with the location of the vertical thermistor in 2018. Duration of exposure has been normalized by the total time between surveys. The percentage of time where the ocean did not contact the bluff is given in the legend.

5.3.3. Erosion Model Performance

5.3.3.1. Model Set-up

Initial model performance is established using a quasi-two-dimensional grid in which the bluff edge is only two model grid cells thick, yet the x-dimension running into land is representative of the inland direction at the vertical thermistor location (see Figure 5.3-5). As directed by Figure 5.3-1, the length of the polygon is 6.5m followed by an ice wedge that is 3m thick extending down the entire bluff. On August 3rd, the thermistor string was 2.62m from the bluff edge.

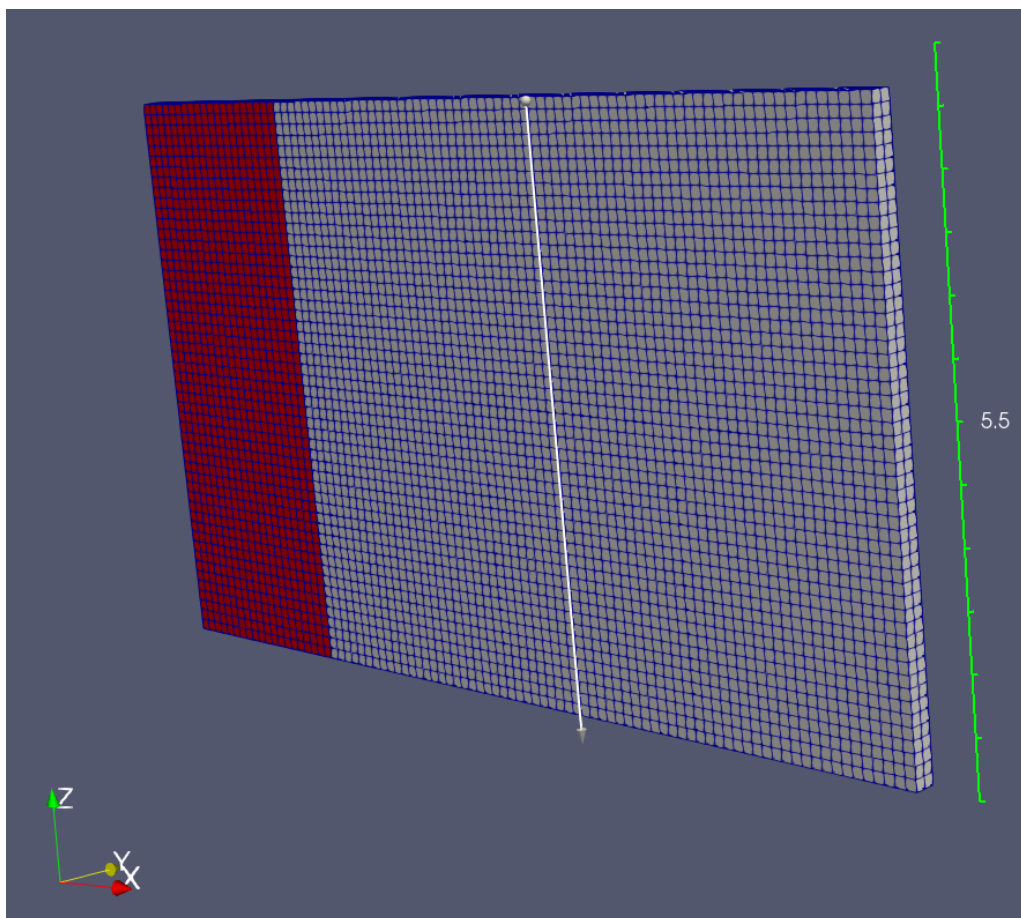
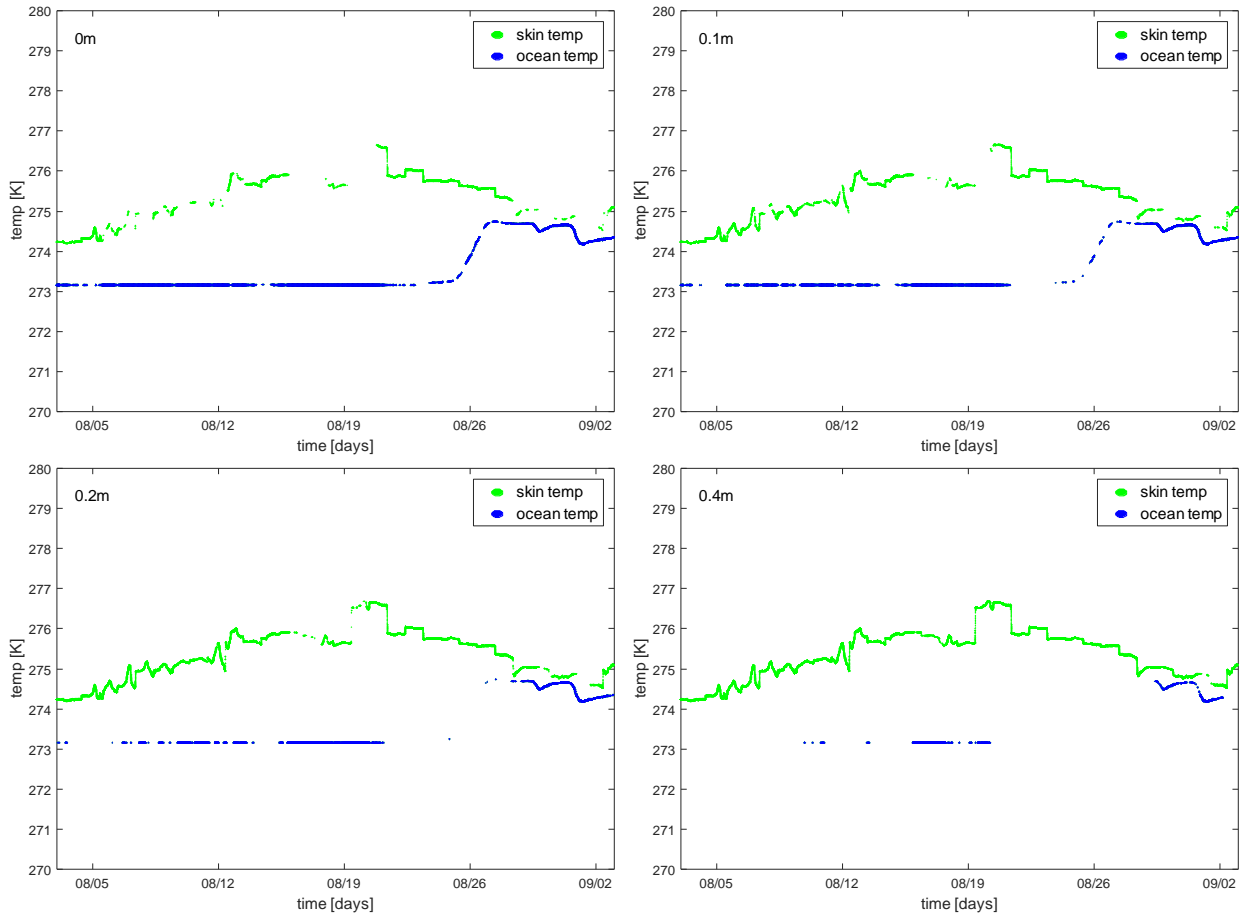


Figure 5.3-5. Quasi-2D finite element grid used to compare with the vertical thermistor field data. The location of the vertical thermistor is shown with the silver arrow. Red grid cells represent ice wedge material while gray cells represent permafrost material.

With this quasi-2D set-up, the temperature profile in the bluff, rates of thermal denudation, and the niche development can be compared with field data. Since block breakage is inherently a three-dimensional phenomenon, this aspect of the field data will not be verified with this model set-up. However, Thomas et al. (2020) has shown, as part of this project, that the niche geometry has the greatest influence on stress concentration in a 3D permafrost bluff. Hence, a strong comparison between the quasi-2D results and the field data inspires confidence that the 3D results will also be strongly correlated.

Temperature boundary conditions were developed in UTC from the 3rd of August until the 3rd of September 2018 using a vertical resolution of 0.05m and a simulation time step of 2min. Figure 5.3-6 shows the temperature boundary conditions for a subset of the vertical resolutions. The ocean provides most of the temperature boundary condition at 0.0m but decreases in importance moving up the bluff face until 1.2m after which the temperature boundary condition is given exclusively by the skin temperature. This pattern is in complete agreement with the ocean water contact history shown in Figure 5.3-7.

Water contact history (Figure 5.3-7) and ocean salinity (Figure 5.3-8) were both generated for the terrestrial model using a vertical resolution of 0.02m and a simulation time step of 2min.



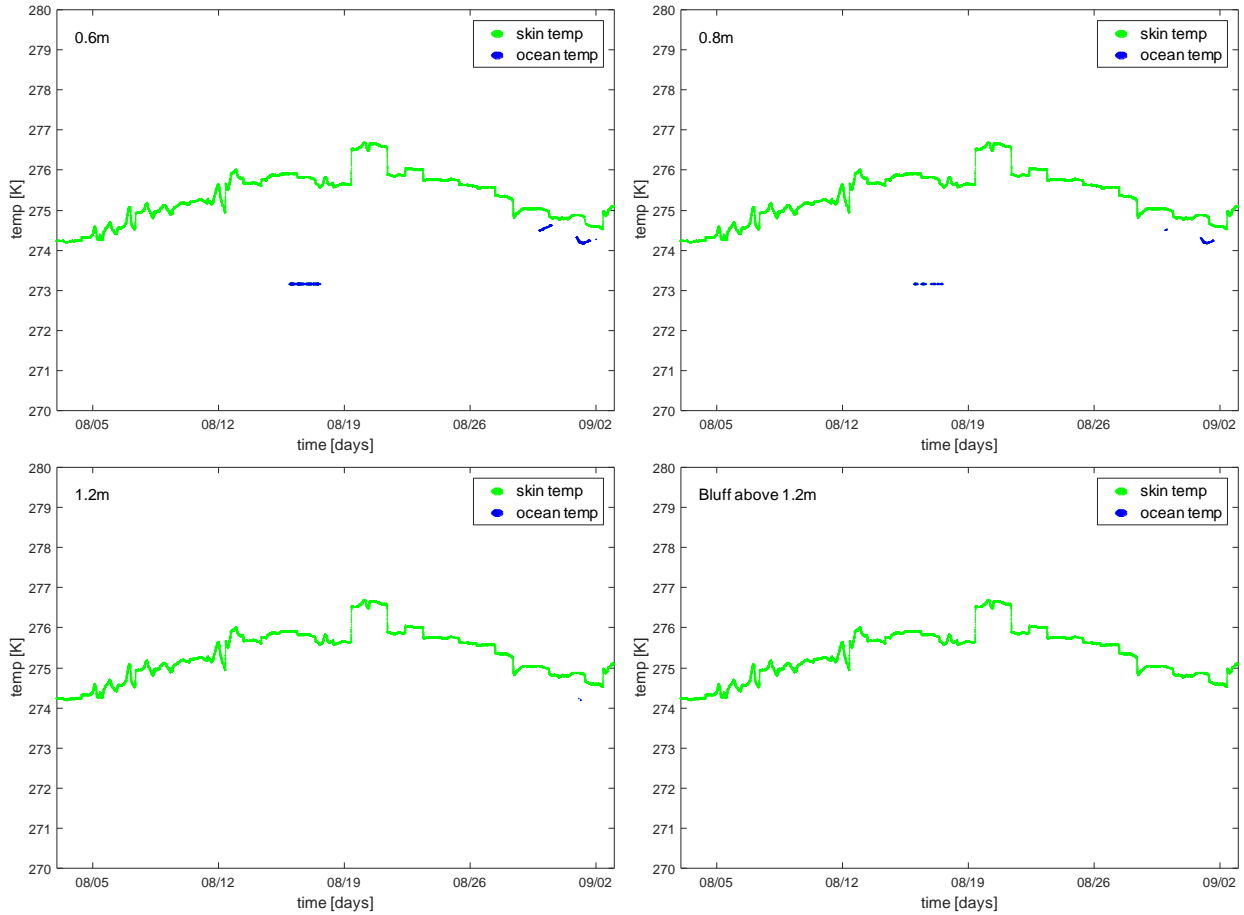


Figure 5.3-6. Subset of temperature boundary conditions applied in the terrestrial model for comparison with the vertical thermistor data; applicable vertical level identified in top left-hand corner of each temperature B.C. time history.

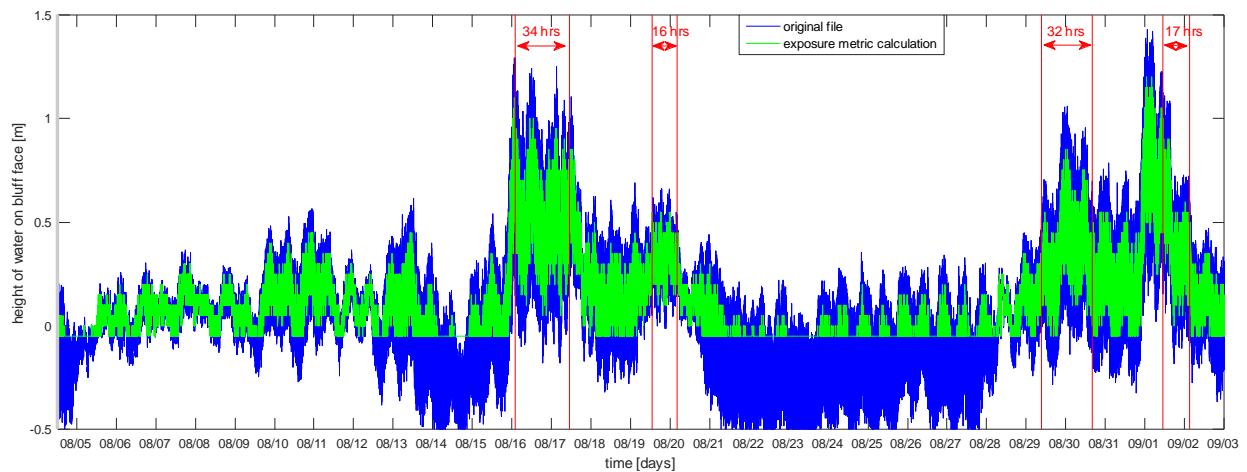


Figure 5.3-7. Ocean water contact time history processed with a simulation time step of 2min and a vertical resolution of 0.02m. This time history is used in the terrestrial model to determine both the height of salinity enhanced melting and dynamic pressure from the ocean on the bluff face.

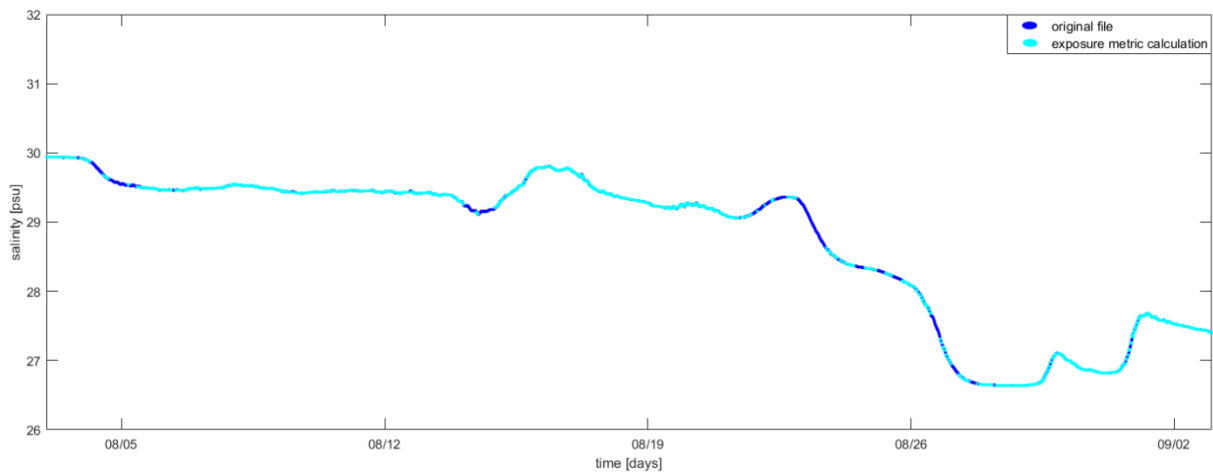


Figure 5.3-8. Ocean salinity time history processed with a simulation time step of 2min and a vertical resolution of 0.02m. Cyan values indicate some level of the bluff is in contact with the ocean water, water contact history given in Figure 5.3-7, and that salinity enhanced melting is thus occurring in the model calculation.

The initial temperature field (Figure 5.3-9) was set to the corresponding temperature profile recorded with the vertical thermistor. The initial ice saturation (Figure 5.3-10) was calculated according to the temperature field and the freezing curve determined by the material model (which was set to the Ancient Drained Lake Basin model, previously described in Section 3.4.1). The material model also determines the soil composition fractions of sand, silt, clay, and peat, as well as the porosity, which are all used to determine the bulk thermal properties of the material, such as the density, specific heat capacity, and thermal conductivity. The mechanical parameters, as well as the grid resolution and time step resolution, are shown in Table 5.3-2.

The chosen yield strengths in this niche formation demonstration simulation for the ice-sediment bond strength and the soil yield strength are much lower than the experimentally derived values, by roughly an order of magnitude. The low values were required in order to get realistic niche progression in terms of niche shape. The model run here does not yet have the dynamic ocean water pressure boundary conditions fully implemented, and therefore, no external stresses are applied to the bluff from the ocean. The only affect that the ocean has on the bluff is its water temperature and salinity. However, the air temperature during this time of year (August) is much warmer than the water temperature. Therefore the air temperature, which is above zero at all times during the simulation period, has already thawed the bluff face. When the ocean water comes into contact with the bluff face, it actually cools it down, at the same time increasing its salinity. The salinity increase, due to the enhanced salt diffusion process model, works against the cooling temperature effect, and the bluff exposed to the water stays mostly thawed out. The experimentally derived values for the ice-sediment bond strength and the soil yield strength were too high for niche formation without including the additional stress from the dynamic ocean water pressure boundary condition. In other words, when the experimentally derived values for ice-sediment bond strength and the soil yield strength were applied, the model never formed a niche, even during a storm period. Under self-weight only, the bluff yield strength was too high to meet any of the failure criteria in which the stress in the bluff exceeded the yield strength. Reducing the values for the yield strengths successfully led to niche formation, although the niche erosion is likely not driven by the ocean

boundary conditions without the implementation of the dynamic ocean water pressure boundary condition. Once the dynamic ocean water pressure boundary condition can be properly applied, the grid cells exposed to the ocean will experience stress that is very near or exceeds the local yield strength, on the order of the experimentally derived values for yield strength.

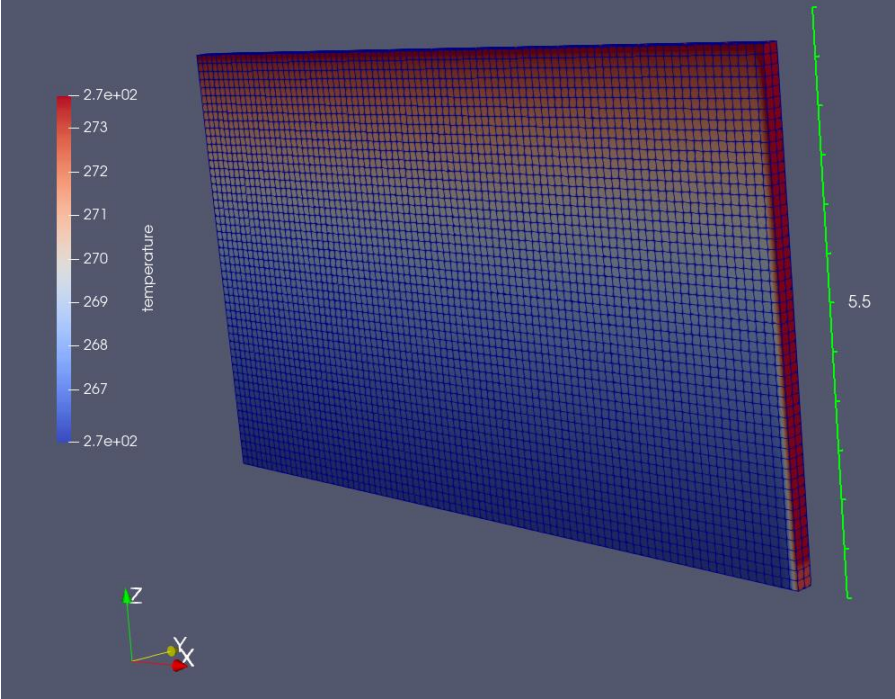


Figure 5.3-9 Initial temperature field [K] in the computational domain. The top of the bluff is warmer than the bottom due to surface warming and a geothermal gradient. The bluff face is also above freezing due to contact with the air or ocean.

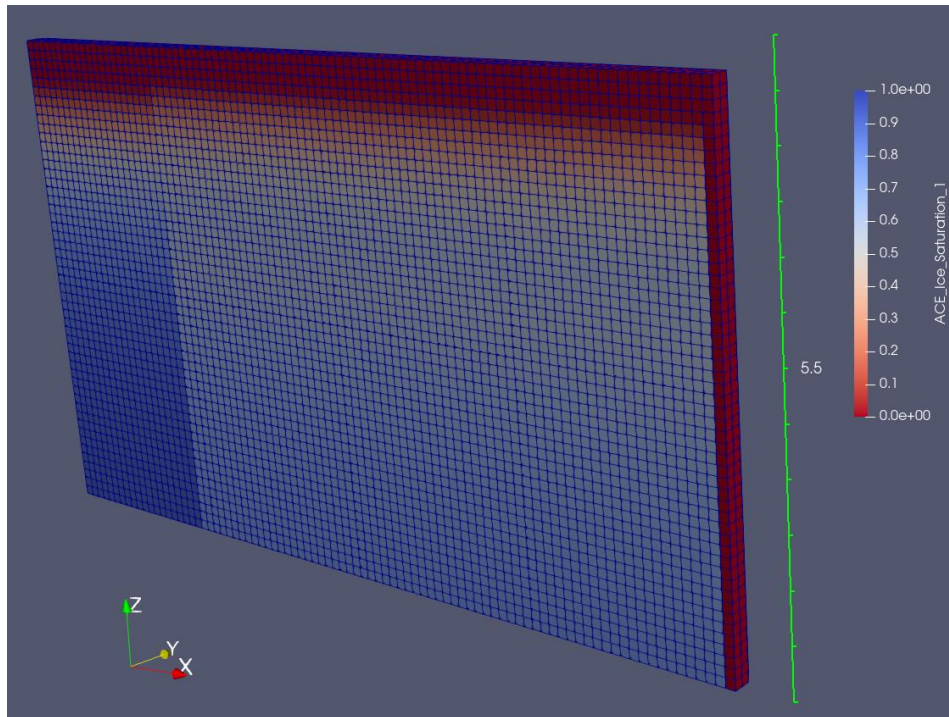


Figure 5.3-10 Initial ice saturation field in the computational domain. The ice wedge and permafrost material can be distinguished visually by the difference in ice content. The top surface of the bluff is completely thawed, as well as the face of the bluff.

Table 5.3-2. Model parameters used for the niche formation demonstration simulation.

Model Parameter	Value	Units
Elastic Modulus	0.1e+09	
Poissons Ratio	0.2	
Yield Strength I-S ⁷⁸	1.5e+05	Pa
Soil Yield Strength ⁹	0.705e+05	Pa
Material model used	Ancient Drained Lake Basin	N/A
Time Step Size	3600	sec
Grid Resolution	0.10	m
Simulation Start Time	2084820.0 ¹⁰	sec

⁷ I-S ice-sediment bond.

⁸ experimentally derived value is 1.96e+06 Pa.

⁹ experimentally derived value is 0.55e+06 Pa.

¹⁰ Simulation start time represents the date/time 07/25/2018 at 3:07:00UTC.

5.3.3.2. Model Demonstration

The model was run starting at the date and time of 07/25/2018, 3:07:00 UTC, and continued until the first block collapse event. Because the full implementation of the dynamic ocean water pressure boundary condition is not complete, the niche formation progressed due to self-weight only, which is not entirely the correct mechanism and resulted in accelerated niche progression because of the weaker yield strength values that were required. However, it is sufficient to demonstrate the functionality of the coupled thermo-mechanical model and adaptive mesh erosion processes.

A time series of model snapshots are shown in Figure 5.3-11, with time marching forward from top to bottom. On the left-hand side column of figures, the ice saturation is shown, and on the right-hand side column of figures, the grid cell failure state is shown for the same snapshot in time. The failure state of the grid cells ranges from 0 to 8 and is a sum of the number of integration points in each element (i.e. grid cell) that have met or exceeded one of the two failure criteria. As described in Appendix A, the first failure criteria is stress calculated at the integration point exceeding the local yield strength, while the second failure criteria is an element rotating beyond a critical angle. In this simulation, at least half of the integration points (i.e., 4 integration points) within the element failed, then the element would be removed.

Niche progression can be seen beginning at the bluff toe, and ultimately progressing inland ~ 3 m deep before the block collapse event was predicted. As the niche advances inland, the grid cells experiencing failure are located at the back wall of the niche, driving it to advance deeper. Exposure to the air or the ocean causes the newly exposed permafrost at the boundaries of the niche to thaw. Once the niche advances ~ 2 m, the tensile stress near the surface of the permafrost block begins to exceed the yield strength of the unfrozen soil in the active layer.

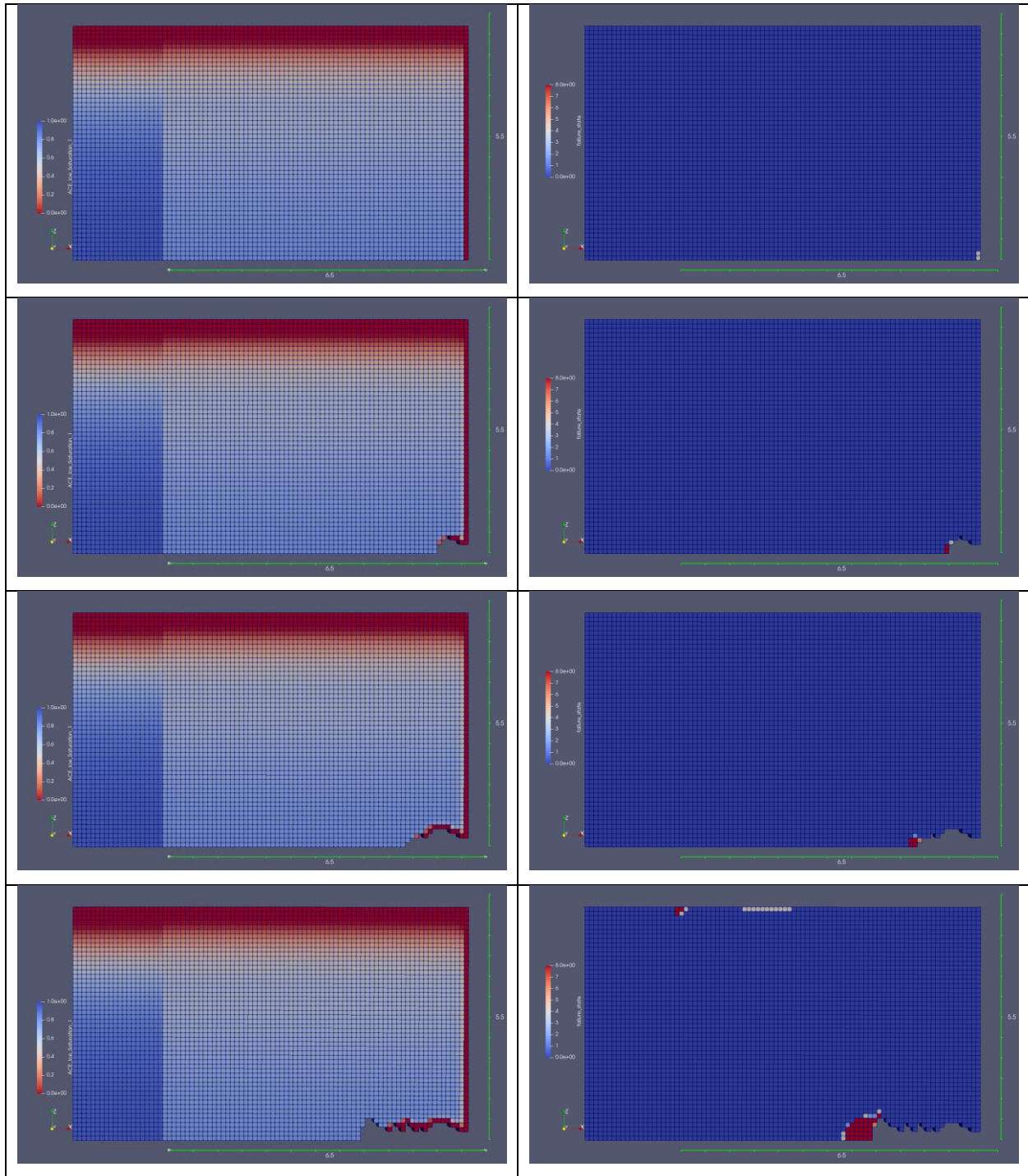


Figure 5.3-11 Niche formation progression on the quasi-2D grid. Niche formation progresses from the top to the bottom in the column of figures. Left-hand column shows the ice saturation field (blue represents 100% ice and red represents 0% ice), and the right-hand column shows the failure state of each grid cell (blue represents 0 failed integration points, white represents 4 failed integration points (indicating the element will be removed), and red indicates 8 failed integration).

In Figure 5.3-12 and Figure 5.3-13, the final model output is shown for the time step immediately preceding the block collapse event. Two potential regions for tension fracture formation can be seen at the surface, $\sim 2/3$ ds of the distance inland from the bluff face and at the ice wedge-permafrost polygon boundary. Block separation at Drew Point has been observed to occur both at ice wedge-polygon boundaries and within the permafrost polygon. These results suggest that both locations may be equally possible given homogeneous mechanical properties, but in reality, the location of fracture is probably dependent on which location is weaker. The ice wedge-permafrost polygon boundary typically becomes a preferred pathway for water drainage due to height differences between the permafrost and the ice wedge. Thus in reality, the ice wedge-polygon boundary may be weakened from hydrologic effects, and would become the most likely location for tensile fracture to occur. Observations of block collapse made by team members in the field at Drew Point show it predominantly (but not exclusively) occurs at the ice wedge-polygon boundary. Model predictions are consistent with these observations.

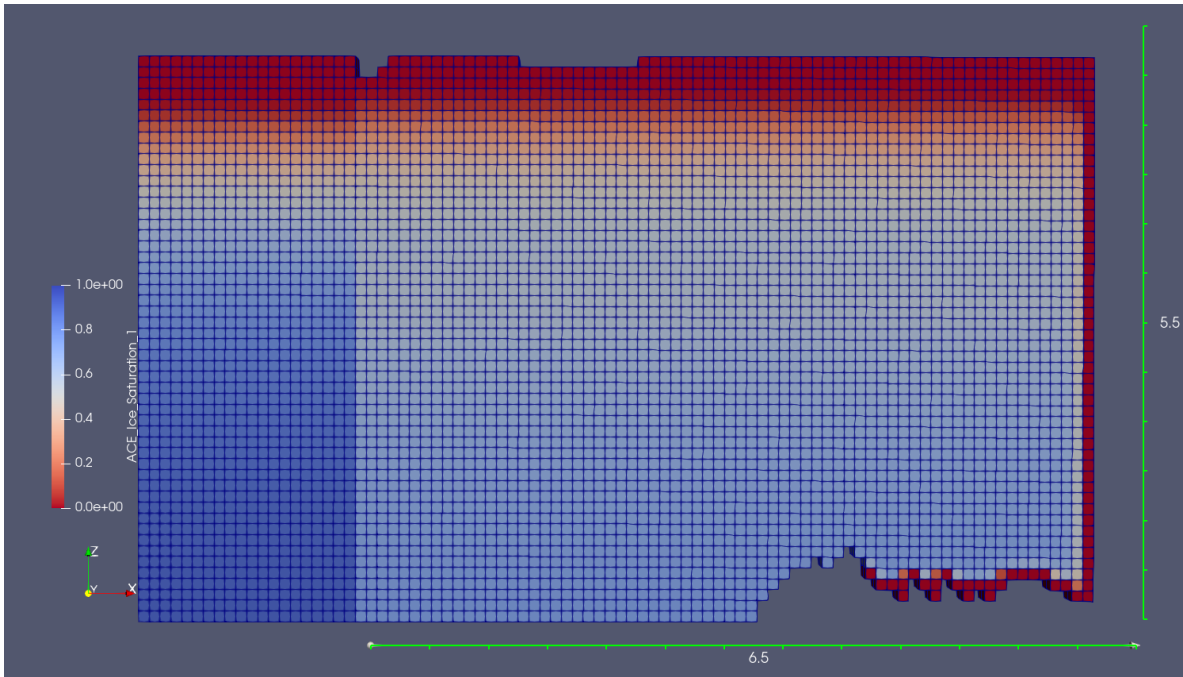


Figure 5.3-12 Ice saturation (blue, 100% and red, 0%) and niche geometry at the time step immediately preceding block collapse. Two potential regions for tension fracture formation can be seen at the surface, $\sim 2/3$ ds of the distance inland from the bluff face and at the ice wedge-permafrost polygon boundary.

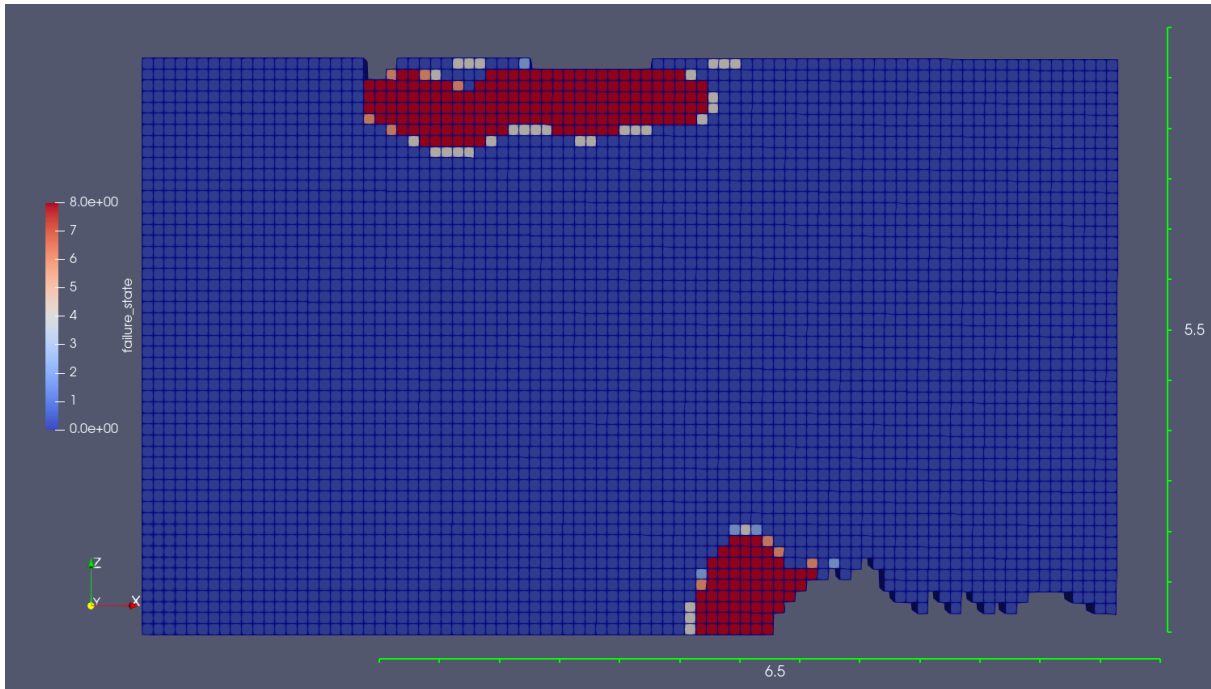


Figure 5.3-13 Grid cell failure state and niche geometry at the time step immediately preceding block collapse. The grid cells with the highest failure state are located in the regions of maximal tension (near the bluff surface behind the niche) and maximal compression (at the back wall of the niche).

Model results in the niche formation demonstration shown here are also consistent with the previously published sensitivity study carried out by Thomas et al. (2020), in which they showed the regions of maximal tensile stress (at the surface of the bluff slightly behind the deepest point of the niche) and maximal compressive stress (at the top of the back wall of the niche) in a 2D cross-section of a permafrost bluff with a prescribed niche geometry (Figure 5.3-14). This can be seen via visual inspection by comparing the red regions in Figure 5.3-13 to the red and blue regions in Figure 5.3-14A/B.

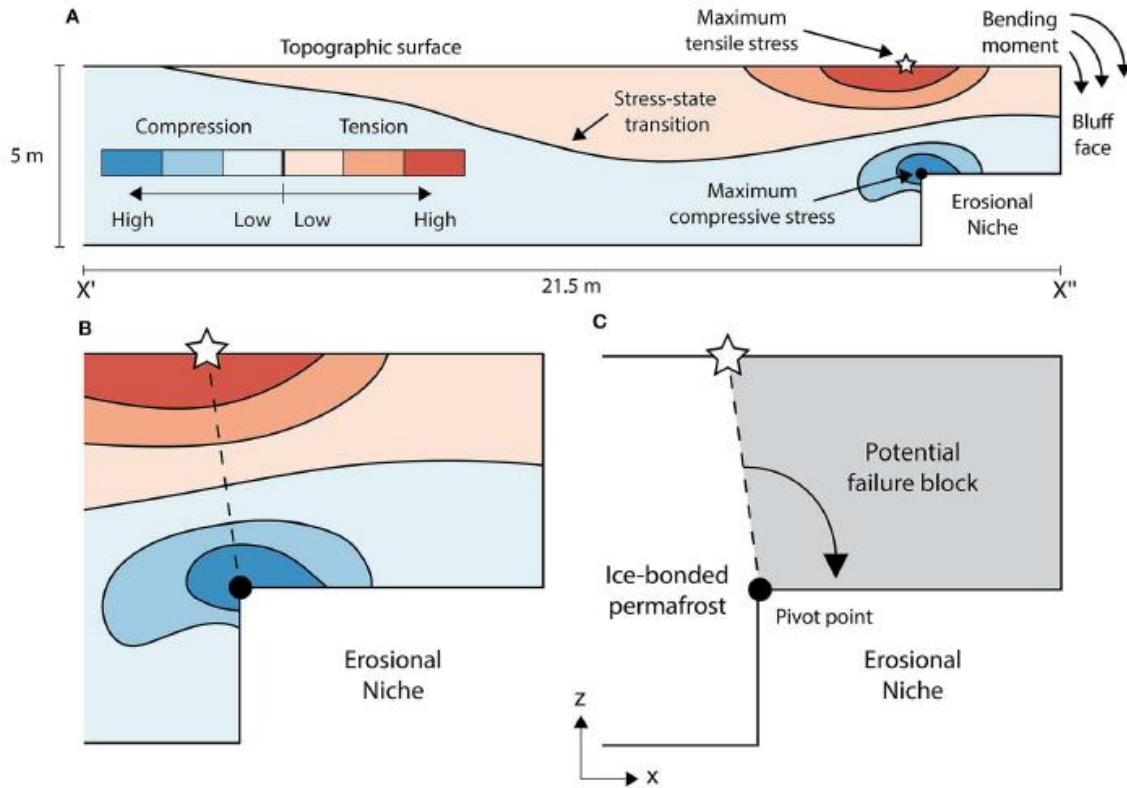


Figure 5.3-14 Conceptual cross section of a bluff with a prescribed niche, showing regions of maximal tensile stress and maximal compressive stress. Adapted from Thomas et al. 2020.

The enhanced salinity diffusion process model is demonstrated in Figure 5.3-15, which shows the salinity field in the permafrost bluff at the time step immediately preceding block collapse. As measured in the field, and described in Section 4.3.1.3, the salinity of the permafrost soil increases with depth and towards the cryopeg layer. Grid cells that have been exposed to the ocean water for a sufficient amount of time increase in salinity, ultimately reaching the salinity value of the ocean water. The newly exposed back wall of the niche has not been exposed long enough to see any considerable increase in the salinity value, however, all of the previously exposed grid cells have elevated salinity (that of the sea water). At this snapshot in time, the sea level height is ~ 0.5 m.

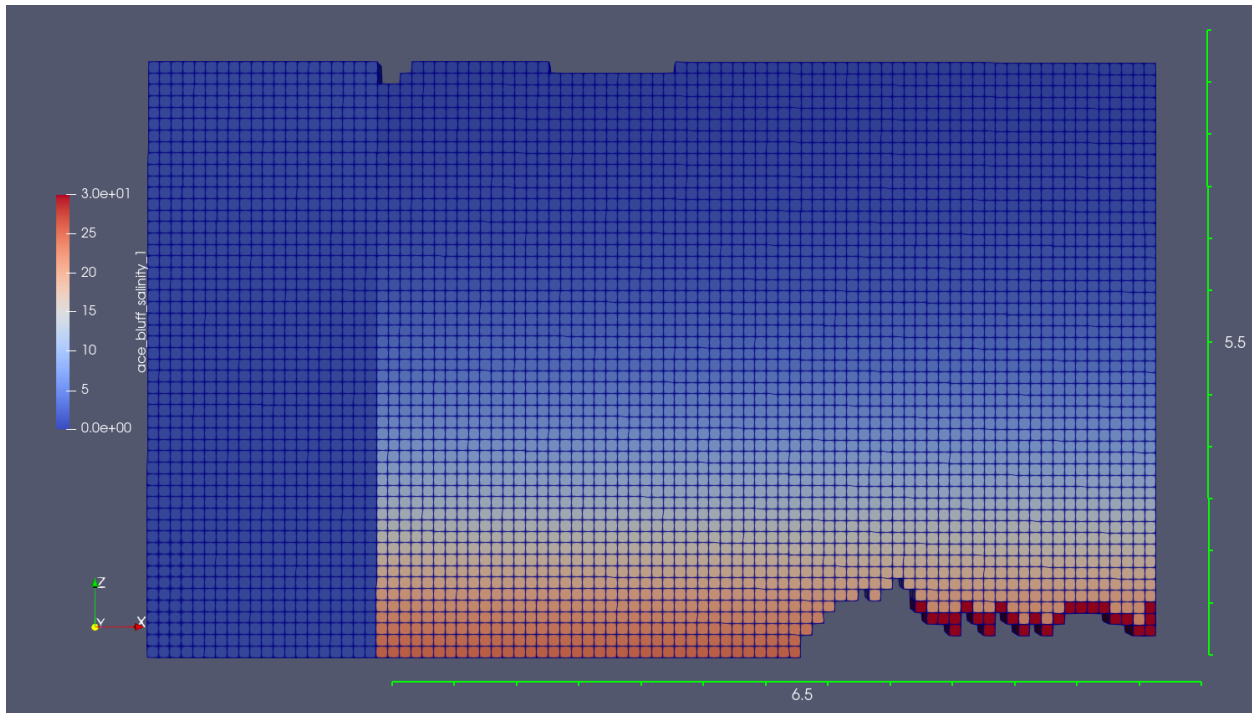


Figure 5.3-15 Bluff salinity field and niche geometry at the time step immediately preceding block collapse. Grid cells that have been exposed to the ocean experience enhanced thaw and diffusion of salt into the permafrost.

Furthermore, the mechanical model also calculates displacement. Not only does the mesh go through adaptation due to erosional material removal, but the mesh can physically deform. This is shown in Figure 5.3-16. Blue color indicates little to no displacement, while red color indicates larger values of displacement, or slumping/rotation as the weight of the bluff and niche incision creates a bending moment. This bending moment is what ultimately leads to block collapse.

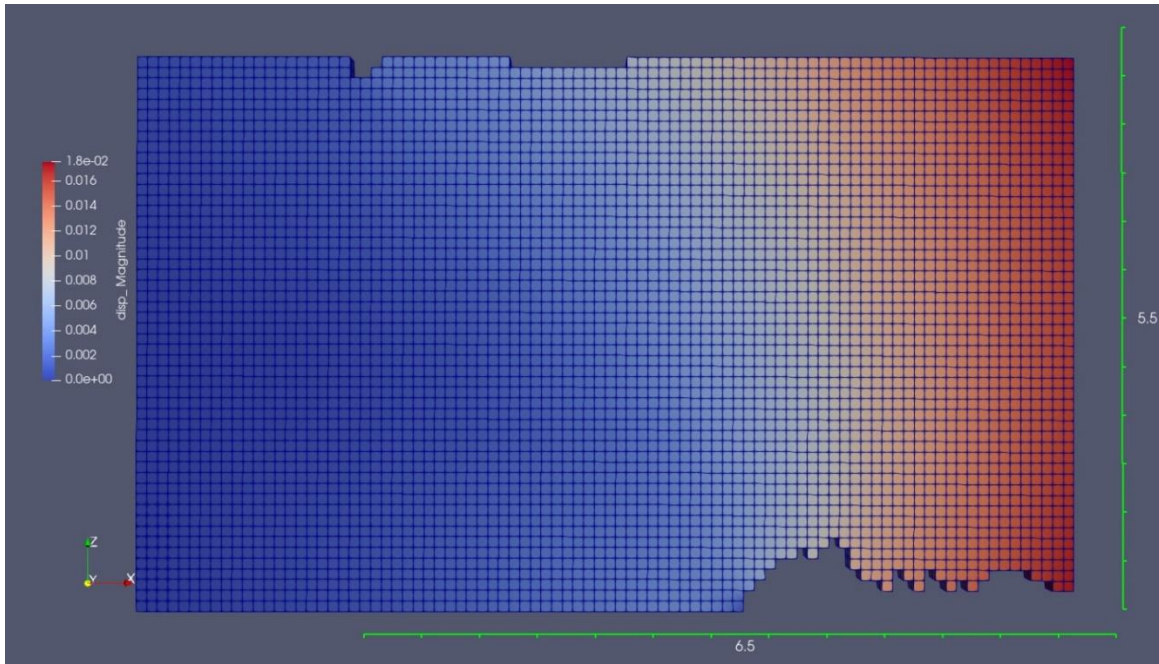


Figure 5.3-16 Bluff displacement and niche geometry at the time step immediately preceding block collapse. Red indicates larger values of displacement, or slumping/rotation as the weight of the bluff and niche incision creates a bending moment.

5.3.3.3. Future Modeling Work

As previously mentioned, while the coupled thermo-mechanical model has been demonstrated to function as designed, there are still some process models which have not been fully incorporated in order to make it realistically represent field conditions. Namely, the dynamic ocean water pressure boundary condition is hypothesized as a critical component, expected to alter the state of stress at the bottom of the bluff exposed to water at a level that is on the same order of magnitude as the experimentally derived values for material yield strength. Without this boundary condition, the stress state is only a result of self-weight, which is not large enough to exceed the experimentally derived values for the yield strength.

Additionally, putting together a model of such complexity required overcoming several numerical challenges, especially for the solvers. Much more work remains to be done to ensure the model's robustness. Along the same lines, time step and grid resolution studies must be thoroughly performed to understand the effects of time step and grid resolution choice on the value/consistency of the output.

In order to gain a much richer knowledge of the original science questions raised in this project, a sensitivity study should be performed which addresses the ranges of environmental input parameters (i.e. air temperature, ocean state) and variation in the geomorphology (i.e. permafrost material properties and geometries).

Finally, as is evident from Section 2, there is a rich and diverse set of field data that has been collected during this project. Calibration and validation studies employing these field data sets will be performed on 3D meshes.

6. ACCOMPLISHMENTS

6.1. Follow-on Work

6.1.1. *InteRFACE*

InteRFACE (Interdisciplinary Research for Arctic Coastal Environments) is a new project for which SNL has a unique and new scientific role, directly leveraging an LDRD investment, with the Earth and Environmental System Sciences division in the office of Biological and Environmental Research within the DOE's Office of Science. Further, this multi-institutional collaboration is led by LANL and is the first time these team members have worked together. Hence, this project has offered inroads to new and important customers as well as creating new partnerships.

InteRFACE aims to quantify and reduce uncertainties in our fundamental understanding of the magnitude, rates, and patterns of change along the Arctic coast by integrating leading expertise and new datasets on Alaska and Arctic social-environmental systems with long-championed DOE leadership in data and model analysis, coupled Earth System model development, and modeling of co-evolutionary pathways of human and natural systems. SNL will be estimating erosional fluxes using the LDRD developed ACE Model by modeling idealized terrestrial coastlines subject to varying oceanographic boundary conditions.

6.1.2. *Air Force Reviewer*

After the initiation of our LDRD at SNL, the Air Force initiated a project to study coastal erosion at two of the Long Range Radar Sites in the North Warning System (NWS) (Barter Island and Oliktok Point). This study was jointly led by University of Alaska Anchorage (UAA) and BEM Systems. During the spring of 2019, leadership from this LDRD worked with UAA, UAF, and USGS Pacific Coastal Marine Sciences Center to explore alterations to the UAA led modeling campaign. This exploration resulted in a few changes to the Air Force coastal erosion study: 1) inclusion of a more mechanistically grounded model (the Hoque & Pollard 2009, 2016) and 2) a review of the modeling work by Sandia National Laboratories. The Air Force timeline did not allow for the LDRD developed ACE Model to be used directly in the modeling campaign, but the review work offered us the opportunity to contextualize how the LDRD developed ACE Model would differ from the approaches pursued by the Air Force.

This opportunity was the first work issued under a newly developed CRADA (No 1949.01.00) with UAA.

6.2. Publications

This modeling project initiated with a comprehensive assessment of the state of Arctic coastal erosion modeling and the development of a new strategy that could accurately predict Arctic coastal erosion (Frederick et al. 2016).

Frederick, J. M., M. A. Thomas, D. L. Bull, C. Jones, and J. Roberts (2016), [The Arctic Coastal Erosion Problem](#), SAND2016-9762, Sandia National Laboratories, NM.

6.2.1. Journal

6.2.1.1. Published or Submitted

Jones, B. M., L. M. Farquharson, C. A. Baughman, R. M. Buzard, C. D. Arp, G. Grosse, D. L. Bull, F. Gunther, I. Nitze, F. Urban, J. L. Kasper, J. M. Frederick, M. Thomas, C. Jones, A. Mota, S. Dallimore, C. Tweedie, C. Maio, D. H. Mann, B. Richmond, A. Gibbs, M. Xiao, T. Sachs, G. Iwahana, M. Kanevskiy, and V. E. Romanovsky. 2018. A decade of remotely sensed observations highlight complex processes linked to coastal permafrost bluff erosion in the Arctic. *Environmental Research Letters* 13: 115001. doi.org/10.1088/1748-9326/aae471.

The ERL paper was also highlighted in a story in the Washington Post on 14 November 2018 <https://www.washingtonpost.com/energy-environment/2018/11/14/watch-warming-ocean-devour-alaskas-coast-this-striking-time-lapse-video/>.

Thomas, M.A., Mota, A., Jones, B.M., Choens, R.C., Frederick, J.M. and Bull, D.L., 2020. Geometric and material variability influences stress states relevant to coastal permafrost bluff failure. *Frontiers in Earth Science*, 8, p.143. doi.org/10.3389/feart.2020.00143.

Bristol, E. M., C. T Connolly, T. D. Lorensen, B. M. Richmond, A. G. Ilgen, R. C. Choens, D. L. Bull, M. Kanevskiy, G. Iwahana, B. M. Jones and J. W. McClelland. *Submitted*. Geochemistry of coastal permafrost and erosion-driven organic matter fluxes to the Beaufort Sea near Drew Point, Alaska. *Frontiers in Earth Science*, section Biogeoscience.

6.2.1.2. In Preparation

Tezaur, I., et al. Development of a strongly-coupled thermo-mechanical model of permafrost for the simulation of Arctic coastal erosion.

Bristol, E. M., et al. Decomposition of organic carbon from coastal permafrost.

Ward Jones, M., et al. High Resolution Observations of coastal permafrost erosion processes and patterns using imagery and in situ probes.

Frederick, J.M., et al. Validation of an Arctic Coastal Erosion Model at Drew Point, Alaska.

6.2.2. Invited Presentations

Thomas, M.A., Mota, A., Jones, B.M., Choens, R.C., Frederick, J.M. and Bull, D.L., 2020 Physics-based simulation can facilitate hypothesis testing for increasingly dynamic coastal permafrost systems. Proposed Session C006: Arctic Coastal Dynamics: Rates, Impacts, Hazards and Implications for the Future. American Geophysical Union Annual (Fall 2020) Meeting, San Francisco, CA.

Thomas, M. 2020 Exploring the mechanics of our retreating arctic coastline. USGS Rocky Mountain Science Seminar, Denver, CO.

McClelland, J.W. 2019. Land-ocean interactions in a rapidly changing Arctic: Consideration of rivers, groundwater, and shoreline erosion. Frontiers in Geoscience seminar series, Los Alamos National Laboratories, Los Alamos.

Thomas, M. 2019. The arctic coastal erosion problem. Colorado School of Mines, Van Tuyl Lecture Series, Golden, CO.

Mota, A., et al. 2019. Strongly-coupled thermo-mechanical model of permafrost for the simulation of Arctic coastal erosion. International Congress on Industrial and Applied Mathematics 2019, July 15-19, Valencia, Spain. SAND2019-7899C.

Bull, D., J. Frederick, B. Jones, C. Jones, J. Kasper, A. Mota, J. Roberts, M. Thomas, J. McClelland, C. Connolly, K. Dunton, (2018) A Predictive Model for Arctic Coastal Erosion. Interagency Arctic Research Policy Committee's (IARPC's) Permafrost & Coastal Resilience Collaborations. February 13th 2018.

6.2.3. Conference Presentations

Mota, A., J. M. Frederick, R. C. Choens, D. Bull, I. Tezaur. (2020). Development of a strongly-coupled thermo-mechanical model of permafrost for the simulation of Arctic coastal erosion, European Seminar on COmputing (ESCO). ~~Pilsen, Czech Republic~~ Online Meeting. June 8-12 2020.

Bull, D. L., J. M. Frederick, A. Mota, M. A. Thomas, B. M. Jones, C. A. Jones, C. Flanary, J. Kasper, R. C. Choens, E. Bristol, J. W. McClelland, S. Namachivayam (2019), Development of a Tightly Coupled Multi-Physics Numerical Model for an Event-Based Understanding of Arctic Coastal Erosion, Abstract C12B-04, presented at the 2019 Fall Meeting, AGU, San Francisco CA, 9-13 December.

Bristol, E., C. Connolly, J. McClelland, T. Lorenson, B. Richmond, A. Ilgen, C. Choens, C. Herrick, D. Bull, M. Kanevskiy, G. Iwahana, B. Jones (2019), Biogeochemistry of eroding soils along the Beaufort Sea coastline: Results from permafrost cores collected at Drew Point, AK. ASLO Aquatic Sciences Meeting. Planet Water in San Juan, Puerto Rico.

Bull, D. L., J. M. Frederick, B. Jones, C. Jones, J. Kasper, A. Mota, J. Roberts, M. A. Thomas, J. McClelland, and K. Dunton (2018), Arctic Coastal Erosion: Development of a Mechanistic Model Designed for Coastal Hazards Evaluation, presented at the 2018 DoD Arctic Science & Technology Synchronization Workshop, Hanover, NH, 16-18 May.

Jones, B., D. Bull, et al. (2018) Seasonal to annual remote sensing of a rapidly eroding segment of coastline in arctic Alaska, presented at 2018 International Symposium: 15th International Circumpolar Remote Sensing Symposium. Sept 11-15th. Potsdam, Germany.

6.2.4. Lectures Series Presentations

D. Bull, et al. 2019. A Predictive Model for Arctic Coastal Erosion. Lecture Series at University of Alaska Fairbanks.

D. Bull, et al. 2019. A Predictive Model for Arctic Coastal Erosion. Lecture Series at University of Alaska Anchorage.

D. Bull, et al. 2019. A Predictive Model for Arctic Coastal Erosion. Presentation to 611th Civil Engineer Squadron of U.S. Air Force. JBER, AK.

6.2.5. Posters

Bristol, E., C.T. Connolly, J.W. McClelland, T.D. Lorenson, B.M. Richmond, A.G. Ilgen, R.C. Choens, D. L. Bull, G. Iwahana, M. Kanevski, B.M. Jones, 2019. Geochemical characterization of costal permafrost and estimation of organic matter fluxes to the Beaufort Sea via shoreline erosion

near Drew Point, Alaska, Abstract C13D-1343, presented at the 2019 Fall Meeting, AGU, San Francisco CA, 9-13 December.

Thomas, M. A., A. Mota, B. M. Jones, R. C. Choens, J. M. Frederick, and D. L. Bull (2019), Bluff Geometry and Material Variability Influence Stress States Relevant to Coastal Permafrost Bluff Failure, Abstract C13D-1339, presented at the 2019 Fall Meeting, AGU, San Francisco CA, 9-13 December.

Jones, B. M., C. E. Tweedie, M. Xiao, V. A. Alexeev, A. Baranskaya, N. Belova, E. Bristol, D. L. Bull, G. Chi, S. Dallimore, L. H. Erikson, L. M. Farquharson, C. Flanary, J. M. Frederick, M. Fuchs, A. Gibbs, J. Graybill, M. Grigoriev, G. Grosse, F. Gunther, K. E. Halvorsen, V. Isaev, A. M. Irrgang, G. Iwahana, A. M. Jensen, C. A. Jones, M. Z. Kanevskiy, J. Kasper, N. Kinsman, O. Kokin, A. Kroon, H. Lantuit, T. C. Lantz, A. K. Liljedah, R. Lubbad, C. Maio, A. Maslakov, J. W. McClelland, A. Mota, I. Nitze, A. V. Novikova, S. A. Ogorodov, J. Overbeck, P. P. Overduin, A. N. Petrov, B. M. Richmond, V. E. Romanovsky, J. C. Rowland, T. Sachs, E. Schuur, N. N. Shabanova, A. Sinitsyn, N. I. Shiklomanov, D. A. Streletskiy, M. C. Strzelecki, D. K. Swanson, and M. A. Thomas (2019), An Emerging International Network Focused on Permafrost Coastal Systems in Transition, Abstract C13D-1351, presented at the 2019 Fall Meeting, AGU, San Francisco CA, 9-13 December.

Flanary, C., C. Jones, S. McWilliams, D. Bull 2019. Arctic Coastal Erosion: Coupled Modeling System for Coastal Hazards Evaluation. American Shore and Beach Preservation Association's (ASBPA) National Coastal Conference in Myrtle Beach, SC, 22-25 October.

Frederick, J. M., D. L. Bull, A. Mota, M. A. Thomas, B. M. Jones, C. Jones, J. Kasper, C. T. Connolly, J. W. McClelland, and J. Roberts 2018, Development of a Tightly Coupled Model for Arctic Coastal Erosion, Infrastructure Risk, and Evaluation of Associated Coastal Hazards, presented at the *2019 Symposium on Arctic Maritime Domain Awareness*, National Geospatial-Intelligence Agency, Springfield VA, 21-22 November.

Frederick, J. M., D. L. Bull, A. Mota, M. A. Thomas, B. M. Jones, C. Jones, J. Kasper, C. T. Connolly, J. W. McClelland, and J. Roberts (2018), Development of a Tightly Coupled Model for Arctic Coastal Erosion, Infrastructure Risk, and Evaluation of Associated Coastal Hazards, Abstract EP23D-2351, presented at the 2018 Fall Meeting, AGU, Washington, D.C., 10-14 December.

Bull, D. L., J. M. Frederick, B. Jones, C. Jones, J. Kasper, A. Mota, J. Roberts, M. A. Thomas, J. McClelland, and K. Dunton (2018), Arctic Coastal Erosion: Development of a Mechanistic Model Designed for Coastal Hazards Evaluation, presented at the 2018 International Symposium: Climate Change Effects on the World's Oceans, Washington, D.C., 4-8 June.

Jones, B., D. Bull, et al., (2018) Observations and implications of an erosional hotspot getting hotter, Drew Point, Alaska DoD Arctic Science & Technology Synchronization Workshop. NORTHCOM Sponsored. May 14th-18th, Hanover New Hampshire.

Frederick, J. M., D. L. Bull, C. Jones, J. Roberts, and M. A. Thomas (2016), Evaluating approaches to a coupled model for Arctic coastal erosion, infrastructure risk, and associated coastal hazards, Abstract EP13C-1043, presented at the 2016 Fall Meeting, AGU, San Francisco, Calif., 12-16 Dec.

6.3. Career Development

Emily Bristol. PhD student University of Texas Austin. 2019-2020.

Rich Buzard. PhD student University of Alaska Fairbanks. Summer 2018.

Craig Connolly. PhD student University of Texas Austin. 2018-2019.

William Eymold. Post-Doctoral Appointee Sandia National Laboratory. 2020-2022.

Melissa Ward Jones. Post-Doctoral Appointee University of Alaska Fairbanks. 2020.

Siddharth Namachivayam. Undergraduate Summer Intern. Pomona College. Summer 2019.

7. CONCLUSIONS

This comprehensive report detailed the ACE model development and execution along with the detailed experimental work underpinning the ACE model.

The Field Work section, Section 2, detailed the terrestrial and oceanographic field campaigns in 2018 and 2019 placed into a longer-term historical context. Measurement details, and in some cases results, were presented. The terrestrial dataset is unique in its high temporal resolution of erosion, its breadth of measurement, and its ability to decipher niche characteristics. The mean annual erosion between 2002 and 2019 is 17.2 m/yr in comparison to a mean annual erosion rate of 8.7 m/yr between 1979 and 2002. Repeat unperson-ed aerial vehicle surveys allowed for differentiation between erosion processes (block failure vs. thaw slumping) at a high temporal resolution (days) in both field work years. This data set paired with other terrestrial measurements, the oceanographic model output, and the ACE model will enable new analyses to quantitatively uncover erosion drivers in the Arctic.

The Arctic Ocean is, in particular, very data sparse due to the seasonal changes it undergoes with ice cover. Hence, collecting bathymetric, wave, inundation, temperature, salinity, water isotope, and seafloor sediment data enables verification analyses normally unavailable in this region. Unique in location, this oceanographic data set facilitated an evaluation of oceanographic model skill in the nearshore environment.

The Permafrost Material Analyses section, Section 3, detailed a coring campaign and the subsequent analyses of active layer and permafrost material. High resolution sampling downcore provided insight on the characteristics of soil/sediments from the tundra surface (elevations reaching 6.8 m) to below sea level. The breadth of ensuing analyses included geochemical characterization of soils and porewaters, estimation of dissolved organic carbon leaching and lability, physical composition (effective porosity, bulk density, grain size, etc.), and strength properties derived from thermally driven geomechanical experiments.

Geochemical data demonstrated that two distinct geomorphic units are eroding into the ocean: organic-rich Holocene-era terrestrial soils (above 3 m elevation) and late-Pleistocene marine sediments (below 3 m elevation). Our estimate of the 21st century erosional total organic flux yr⁻¹ at Drew Point is similar to annual total organic fluxes from the Sagavanirktok and Kuparuk rivers, which rank as the second and third largest rivers draining the North Slope of Alaska. In a laboratory experiment, approximately 25% of dissolved organic carbon leached from active layer and permafrost soils in seawater was bioavailable during a 90 day incubation, suggesting that eroding soils may be an increasingly important source of labile carbon in the coastal environment.

Experimental material strength models were based on unconfined compressive strength relationships between volumetric content of ice and ice saturation to estimate strength assuming failure is controlled by either total ice or remaining ice-sediment interface. Linear relationships between failure strength and either ice volume fraction or ice saturation have been developed over relevant temperature ranges. Average elastic moduli have also been determined from this data set. All tests demonstrate the suitability of an elastic-perfectly plastic rheology for the permafrost soils. These experimentally derived strength models allow for accurate calibration of the material strength numerical model.

The ACE Model Development section, Section 4, details the main components of the numerical model: the boundary conditions, the oceanographic modeling suite, and the terrestrial model. The atmospheric, terrestrial, and oceanographic boundary conditions are obtained from a variety of

reanalysis sources, dynamically downscaled projections developed specifically for the state of Alaska, and also a variety of local sources. The grids, bathymetries, physics, and boundary conditions used in each of the three models (WAVEWATCH III, Delft3D-FLOW, and Delft3D-WAVE) constituting the oceanographic modeling suite were described. The Arctic Ocean scale wave prediction and nearshore hydrodynamic and wave predictions along the bluff face are the highest fidelity treatment of the oceanographic forcing environment for Arctic erosion in literature. The two-way coupling between the nearshore hydrodynamic model (Delft3D-FLOW) and the nearshore wave model (Delft3D-WAVE) accounts for the interaction of waves, current, and storm surges thus producing highly accurate and resolved spatiotemporal knowledge of water contact with the bluff, water temperature, and water salinity.

In the terrestrial model, 3D stress/strain fields develop in response to a plasticity model of the permafrost that is controlled by the frozen water content determined by modeling 3D heat conduction and solid-liquid phase change. The numerical code that we used is Albany LCM, an open-source multi-physics based finite element model that is specifically targeted at solid mechanics applications. Development of a new thermal model governing the 3D heat conduction and solid-liquid phase change in Albany is outlined. The plasticity model, failure criterion, and dynamic remeshing developed in the mechanical model are detailed. The material model detailing the thermally mediated mechanical behavior of ice and permafrost provides the dependency between the models. A sequential thermo-mechanical coupling scheme allows each problem dedicated time integration techniques and also keeps the difference in magnitude between problem variables separate, avoiding ill-conditioned problems. This is the first numerical modeling framework capable of capturing the failure mechanism of coastal permafrost—thermo-abrasion or thermo-denudation—without pre-determined failure planes, critical niche depths, or empirical relationships.

The ACE Model Execution section, Section 5, details the model skill for both the oceanographic modeling suite and the Arctic Coastal Erosion Model. Employed boundary conditions and are specified for the Arctic Coastal Erosion Model. Multiple aspects of the oceanographic modeling suite were verified: bathymetry applicability, offshore spectral wave predictions, nearshore spectral wave predictions, and nearshore water levels. For as data sparse of a region as the Arctic is, the breadth of this verification is extraordinary. Overall the oceanographic numerical modeling suite accurately predicted the measured water levels, wave heights, and wave periods at inshore and offshore locations, providing confidence in the predictions being passed to the terrestrial model.

A unique verification case for the ACE Model was available from the terrestrial field work in which a vertical thermistor string captured the temperature evolution of a bluff and the development of a niche resulting in a block breakage event. The high spatiotemporal boundary conditions revealed that three storms generated and developed the niche over a 5 week period. A quasi-two-dimensional representation of the specific bluff geomorphology was created and material properties experimentally derived and modeled for the location were employed. The model demonstrated successful thermo-mechanical coupling, dynamic remeshing upon exceedance of thermally mediated strength properties, and conditions which would induce block failure.

Combined, this work offers the most comprehensive and physically grounded treatment of Arctic coastal erosion available in literature. The ACE model and experimental results can be used to inform scientific understanding of coastal erosion processes, contribute to estimates of geochemical and sediment ocean fluxes, and facilitate infrastructure susceptibility assessments.

REFERENCES

- Allen, J.I., J.T. Holt, J. Blackford, and R. Proctor. 2007. Error Quantification of a High-Resolution Coupled Hydrodynamic Ecosystem Coastal-Ocean Model: Part 2. Chlorophyll-a nutrients and SPM. *J. Mar. Systems*. 68(3-4):381–404.
- Amante, C., and B.W. Eakins. 2009. ETOPO1 1 Arc-Minute Global Relief Model: Procedures, Data Sources and Analysis. NOAA Technical Memorandum NESDIS NGDC-24. National Geophysical Data Center, NOAA. doi:10.7289/V5C8276M March 30, 2018.
- Arctic Report Card. www.arctic.noaa.gov/Report-Card/ annual report from National Oceanic and Atmospheric Administration (NOAA). In its 13th year of reporting, we reference 2017 2018.
- Arctic Report Card: Update for 2018. Sea Ice Arctic Essay. "The September monthly average trend for the entire Arctic Ocean is now -12.8% per decade relative to the 1981-2010 average." <https://arctic.noaa.gov/Report-Card/Report-Card-2018/ArtMID/7878/ArticleID/780/SeanbspIce>.
- Arduin, F., W. E. Rogers, A. V. Babanin, J. Filipot, R. Magne, A. Roland, A. van der Westhuysen, P. Queffelec, J. Lefevre, L. Aouf, and F. Collard (2010), Semiempirical dissipation source functions for ocean waves. Part I: Definition, calibration, and validation, *J. Phys. Oceanogr.*, 40, 1,917– 1,941.
- Aré, F.E. (1988a). Thermal abrasion of sea coasts (part I). *Polar Geology and Geology*. 12:1. doi: 10.1080/10889378809377343.
- Aré, F.E. (1988b). Thermal abrasion of sea coasts (part II). *Polar Geology and Geology*. 12:2. doi: 10.1080/10889378809377352.
- Arenson, L.U., Springman, S.M., and Segó, D.C. (2007). The rheology of frozen soils. *Applied Rheology*. 17:1, 1-14. doi: 10.1515/arh-2007-0003.
- Atkinson, D.E. 2005 Observed storminess patterns and trends in the circum-Arctic coastal regime *Geo-Marine Lett.* 25(2-3) 98-109.
- Atmospheric Radiation Measurement (ARM) user facility. 2015, updated hourly. Interpolated Sonde (INTERPOLATEDSONDE). 2018-03-01 to 2018-10-31, ARM Mobile Facility (OLI) Oliktok Point, Alaska; AMF3 (M1). Compiled by T. Fairless and S. Giangrande. ARM Data Center. Data set accessed 2020-03-16 at <http://dx.doi.org/10.5439/1095316>.
- Atmospheric Radiation Measurement (ARM) user facility. 2015, updated hourly. Interpolated Sonde (INTERPOLATEDSONDE). 2019-03-01 to 2019-10-31, ARM Mobile Facility (OLI) Oliktok Point, Alaska; AMF3 (M1). Compiled by T. Fairless and S. Giangrande. ARM Data Center. Data set accessed 2020-03-16 at <http://dx.doi.org/10.5439/1095316>.
- Ballinger, T.J.; Rogers, J.C. 2013 Atmosphere and Ocean Impacts on Recent Western Arctic Summer Sea Ice Melt *Geogr. Compass* 7(10) 686-700.
- Barnhart, K. R., Miller, C. R., Overeem, I., & Kay, J. E. 2016 Mapping the future expansion of Arctic open water *Nature Climate Change* 6(3) 280.

- Barnhart, K.R., Overeem, I., and Anderson, R.S. (2014a). The effect of changing sea ice on the physical vulnerability of Arctic coasts. *The Cryosphere*. 8:5, 1777-1799. doi: 10.5194/tc-8-1777-2014.
- Barnhart, K.R., Anderson, R.S., Overeem, I., Wobus, C., Clow, G.D., and Urban, F.E. (2014b). Modeling erosion of ice-rich permafrost bluffs along the Alaskan Beaufort Sea coast. *Journal of Geophysical Research: Earth Surface*. 119:5, 1155-1179. doi: 10.1002/2013JF002845.
- Bell, L.E., Bluhm B.A., Iken K. (2016). Influence of terrestrial organic matter in marine food webs of the Beaufort Sea shelf and slope. *Mar Ecol Prog Ser* 550, 1-24.
- Bieniek, P. A., Bhatt, U. S., Walsh, J. E., Rupp, T. S., Zhang, J., Krieger, J. R., and Lader, R. 2016: Dynamical downscaling of ERA-Interim temperature and precipitation for Alaska. *Journal of Applied Meteorology and Climatology*, 55(3), 635-654.
<https://journals.ametsoc.org/doi/abs/10.1175/JAMC-D-15-0153.1>
- Bird, Kenneth J., Ronald R. Charpentier, Donald L. Gautier, David W. Houseknecht, Timothy R. Klett, Janet K. Pitman, Thomas E. Moore, Christopher J. Schenk, Marilyn E. Tennyson, and Craig R. Wandrey. Circum-Arctic resource appraisal: Estimates of undiscovered oil and gas north of the Arctic Circle. No. 2008-3049. Geological Survey (US), 2008.
- Borgerson, Scott, “The Coming Arctic Boom: As the Ice Melts, the Region Heats Up,” *Foreign Affairs* 92, no. 4 (2013): 76–V.
- Bristol, E. M, C. T Connolly, T. D. Lorenson, B. M. Richmond, A. G. Ilgen, R. C. Choens, D. L. Bull, M. Kanevskiy, G. Iwahana, B. M. Jones and J. W. McClelland. *Submitted*. Geochemistry of coastal permafrost and erosion-driven organic matter fluxes to the Beaufort Sea near Drew Point, Alaska. *Frontiers in Earth Science*, section Biogeoscience.
- Bromwich, D., A. Wilson, L. Bai, Z. Liu, M. Barlage, C. Shih, S. Maldonado, K. Hines, S.-H. Wang, J. Woollen, B. Kuo, H. Lin, T. Wee, M. Serreze, and J. Walsh. 2018: The Arctic System Reanalysis Version 2. *Bull. Amer. Meteor. Soc.* 99:805-828. doi: 10.1175/BAMS-D-16-0215.1.
- Brown, J.; Jorgenson, M.T.; Smith, O.P.; Lee, W. Long- term rates of erosion and carbon input, Elson Lagoon, Barrow, Alaska 2003 In ICOP 2003 Permafrost: Proceedings of the 8th International Conference on Permafrost M. Phillips, S.M. Springman, and L.U. Arenson, (Eds.) A.A. Balkema Publishers, Netherlands pp 101-106.
- Clow, G. D. (2014) Temperature data acquired from the DOI/GTN-P Deep Borehole Array on the Arctic Slope of Alaska, 1973–2013, *Earth Syst. Sci. Data*, 6, 201–218, doi:10.5194/essd-6-201-2014.
- Copernicus Climate Change Service (C3S) (2017): ERA5: Fifth generation of ECMWF atmospheric reanalyses of the global climate . Copernicus Climate Change Service Climate Data Store (CDS), date of access. <https://cds.climate.copernicus.eu/cdsapp#!/home>.
- Cummings, J.A. and O.M. Smedstad. 2013: Variational Data Assimilation for the Global Ocean. *Data Assimilation for Atmospheric, Oceanic and Hydrologic Applications*. Vol. II, chapter 13, 303-343.
- Cummings, J.A., 2005: Operational multivariate ocean data assimilation. *Quart. J. Royal Met. Soc.*, Part C, 131(613), 3583-3604.

- Dallimore, S.R.; Wolfe, S.A.; Solomon, S.M. Influence of ground ice and permafrost on coastal evolution, Richards Island, Beaufort Sea coast, N.W.T. 1996 *Can. J. of Earth Sci.* 33 664-675.
- Danielson, S. L., E. L. Dobbins, M. Jakobsson, M. A. Johnson, T. J. Weingartner, W. J. Williams, and Y. Zarayskaya (2015), Sounding the northern seas, *Eos*, 96, doi:10.1029/2015EO040975. Published on 29 December 2015.
- Danielson, S., E. Curchitser, K. Hedstrom, T. Weingartner, and P. Stabeno (2011), On ocean and sea ice modes of variability in the Bering Sea, *J. Geophys. Res.*, 116, C12034, doi:10.1029/2011JC007389.
- Danielson, S., M. Johnson, S. Solomon & W. Perrie, 1 km Gridded Bathymetric Dataset Based on Ship Soundings: A research tool for the waters of eastern Russia, Alaska & western Canada, 2008, Poster presentation at the 2008 Alaska Marine Science Symposium, Anchorage, Alaska.
- Darrow, M. (2011), Thermal modeling of roadway embankments over permafrost, *Cold Regions Science and Technology*, Vol. 65, 474-487, <https://doi:10.1016/j.coldregions.2010.11.001>.
- Darrow, M., S. Huang, and S. Akagawa (2009), Adsorbed cation effects on the frost susceptibility of natural soils, *Cold Regions Science and Technology*, Vol. 55, pp. 263-277, <https://doi:10.1016/j.coldregions.2008.08.002>.
- Deltares. 2018. Delft3D-FLOW: Simulation of multi-dimensional hydrodynamic flows and transport phenomena, including sediments: User Manual. Deltares, The Netherlands.
- Deltares. 2018. Delft3D-WAVE: Simulation of short-crested waves with SWAN: User Manual. Deltares, The Netherlands.
- Dou, F., Ping C.L., Guo L., Jorgenson, T. (2008). Estimating the Impact of Seawater on the Production of Soil Water-Extractable Organic Carbon during Coastal Erosion. *J Environ Qual* 37, 2368-2374.
- Dunton, K.H., Schonberg S.V., Cooper L.W. (2012). Food Web Structure of the Alaskan Nearshore Shelf and Estuarine Lagoons of the Beaufort Sea. *Estuaries and Coasts* 35:2, 416-435.
- Frederick, J.M., Thomas, M.A., Bull, D.L.; Jones, C.A.; Roberts, J.D. (2016). The Arctic coastal erosion problem. Albuquerque, NM: Sandia National Laboratories SAND2016-9762, 122 p. doi: 10.2172/1431492.
- Fritz, M., Vonk J.E., Lantuit H. (2017). Collapsing Arctic coastlines. *Nat Clim Change* 7:1, 6-7.
- Fuchs, M., Lenz J., Jock S., Nitze I., Jones B.M., Strauss J., Guther F., Grosse G. (2019). Organic carbon and nitrogen stocks along a thermokarst lake sequence in Arctic Alaska. *J Geophys Res: Biogeo.* 124, 1230-1247.
- Gao, X., E. Nielsen, R. Muller, R. Young, A. Salinger, N. Bishop, M. Lilly, and M. Carroll. Quantum computer aided design simulation and optimization of semiconductor quantum dots. *Journal of Applied Physics*, 114:1–19, 2013.
- Gibbs, A.E., and Richmond, B.M. 2015 National assessment of shoreline change—Historical shoreline change along the north coast of Alaska U.S.—Canadian border to Icy Cape: U.S. Geological Survey Open-File Report 2015–1048 96 p., <https://dx.doi.org/10.3133/ofr20151048>.

- Gibbs, A.E., B.M. Richmond, L.J. Erikson, and B.M. Jones 2018 Long-term retreat of coastal permafrost bluffs, Barter Island, Alaska. European Conference on Permafrost, Chamonix, 23 June to 01 July 2018.
- Griffies, S. M., and Coauthors, 2011: The GFDL CM3 Coupled Climate Model: Characteristics of the Ocean and Sea Ice Simulations. *J. Climate*, 24, 3520–3544, <https://doi.org/10.1175/2011JCLI3964.1>.
- Günther, F., Overduin, P.P., Sandakov, A.V., Grosse, G., and Grigoriev, M.N. (2013). Short- and long-term thermo-erosion of ice-rich permafrost coasts in the Laptev Sea region. *Biogeosciences*. 10:6, 4297-4318. doi: 10.5194/bg-10-4297-2013.
- Günther, F.; Overduin, P.P.; Baranskaya, A.; Opel, T.; Grigoriev, M.N. 2015 Observing Muostakh Island disappear: erosion of a ground-ice-rich coast in response to summer warming and sea ice reduction on the East Siberian shelf *The Cryosphere* 9 151-178, doi:10.5194/tc-9-151-2015.
- Harris, C.M., McTigue, N.D., McClelland, J.W. and Dunton, K.H., 2018. Do high Arctic coastal food webs rely on a terrestrial carbon subsidy?. *Food Webs*, 15, p.e00081.
- Hasselmann, K., T. P. Barnett, E. Bouws, H. Carlson, D. E. Cartwright, et al. 1973. Measurements of wind-wave growth and swell decay during the Joint North Sea Wave Project (JONSWAP). Technical Report, Deutsches Hydrographisches Institut.
- Hawkes, I. (1969). Development and evaluation of an apparatus for the direct tensile testing of ice. CRREL Special Report 13, 1-27.
- Haynes, F.D. (1973) Tensile strength of ice under triaxial stresses. CRREL Research Report 312. 1-21.
- Haynes, F.D., and Karalius, J.A. (1977). Effect of temperature on the strength of frozen silt. CRREL Report 77-3, 1-27.
- Haynes, F.D., Karalius, J.A., and Kalafu, J. (1975). Strain rate effect on the strength of frozen silt. CRREL Research Report 350, 1-27.
- Hequette, A., and P. W. Barnes. 1990. Coastal retreat and shoreface profile variations in the Canadian Beaufort Sea. *Marine Geology*, 91, 113-132.
- Heroux, M., R. Bartlett, V. Howle, R. Hoekstra, J. Hu, T. Kolda, K. Long R. Lehoucq, R. Pawlowski, E. Phipps, H. Thornquist A. Salinger, R. Tuminaro, J. Willenbring, and A. Williams. An overview of trilinos. Technical Report SAND2003-2927, Sandia National Laboratories Report, 8 2003.
- Hinkel, K.M., Eisner, W.R., Bockheim, J.G., Nelson, F.E., Peterson, K.M. and Dai, X. (2003). Spatial extent, age, and carbon stocks in drained thaw lake basins on the Barrow Peninsula, Alaska. *Arctic, Antarctic, and Alpine Research*, 35:3, 291-300.
- Holthuijsen, L.H., N. Booij, and R.C. Ris. 1993. A Spectral Wave Model for the Coastal Zone. Proceedings 2nd International Symposium on Ocean Wave Measurement and Analysis, New Orleans, Louisiana, July 25–28, 1993, New York, pp. 630–641.
- Hoque, M.A., and Pollard, W.H. (2009). Arctic coastal retreat through block failure. *Canadian Geotechnical Journal*, 46:10, 1103-1115. doi: 10.1139/T09-058.

- Hoque, M.A., and Pollard, W.H. (2016). Stability of permafrost dominated coastal cliffs in the Arctic. *Polar Science*. 10:1, 79-88. doi: 10.1016/j.polar.2015.10.004.
- Hugelius, G., Strauss J., Zubrzycki S., Harden J.W., Schuur E.A.G., Ping C.L., Schirmermeister L., Grosse G., Michaelson G.J., Koven C.D., O'Donnell J.A., Elberling B., Mishra U., Camill P., Yu Z., Palmtag J., Kuhry P. (2014). Estimated stocks of circumpolar permafrost carbon with quantified uncertainty ranges and identified data gaps. *Biogeosciences* 11:23, 6573-6593.
- Hughes, Z. (2016). Erosion threat are remote military radars decades ahead of schedule. Alaska Public Media. <https://www.alaskapublic.org/2016/07/04/erosion-threat-at-remote-military-radars-decades-ahead-of-schedule/>.
- Humpert, Malte and Raspotnik, Andreas. The Future of Arctic Shipping. The Arctic Institute. October 11, 2012 <https://www.thearcticinstitute.org/future-arctic-shipping/>.
- Irrgang, A. M., Lantuit H., Manson G. K., Günther F., Grosse Gand, Overduin P. P., 2018 Variability in rates of coastal change along the Yukon coast, 1951 to 2015 *J. Geophys. Res.: Earth Sur.* 123 779–800.
- Jakobsson, M., L. A. Mayer, B. Coakley, J. A. Dowdeswell, S. Forbes, B. Fridman, H. Hodnesdal, R. Noormets, R. Pedersen, M. Rebecco, H.-W. Schenke, Y. Zarayskaya A, D. Accettella, A. Armstrong, R. M. Anderson, P. Bienhoff, A. Camerlenghi, I. Church, M. Edwards, J. V. Gardner, J. K. Hall, B. Hell, O. B. Hestvik, Y. Kristoffersen, C. Marcussen, R. Mohammad, D. Mosher, S. V. Nghiem, M. T. Pedrosa, P. G. Travaglini, and P. Weatherall, The International Bathymetric Chart of the Arctic Ocean (IBCAO) Version 3.0, *Geophysical Research Letters*, doi: [10.1029/2012GL052219](https://doi.org/10.1029/2012GL052219).
- Jones, B.M., Hinkel, K.M., Arp, C.D. and Eisner, W.R. (2008). Modern erosion rates and loss of coastal features and sites, Beaufort Sea coastline, Alaska. *Arctic* 61:4, 361-372.
- Jones, B.M., Arp C.D., Jorgenson M.T., Hinkel K.M., Schmutz J.A., Flint P.L. (2009a). Increase in the rate and uniformity of coastline erosion in Arctic Alaska. *Geophys Res Lett* 26:3. doi: 10.1029/2008GL036205.
- Jones, B.M., Arp CD, Beck R A, Grosse G, Webster JM and Urban F E 2009b Erosional history of Cape Halkett and contemporary monitoring of bluff retreat, Beaufort Sea coast, Alaska *Polar Geogr.* 32 129–42
- Jones, B.M., Farquharson L.M., Baughman C.A., Buzard R.M., Arp C.D., Grosse G., Bull D.L., Gunther F., Nitze I., Urban F., Kasper J.L., Frederick J.M., Thomas M., Jones C., Mota A., Dallimore S., Tweedie C., Maio C., Mann D.H., Richmond B., Gibbs A., Xiao M., Sachs T., Iwahana G., Kanevskiy M., Romanovsky V.E. (2018). A decade of remotely sensed observations highlight complex processes linked to coastal permafrost bluff erosion in the Arctic. *Environ Res Lett* 13(11). Doi: 10.1088/1748-9326/aae471.
- Jones, M.C., Grosse, G., Jones, B.M. and Walter Anthony, K. (2012). Peat accumulation in drained thermokarst lake basins in continuous, ice-rich permafrost, northern Seward Peninsula, Alaska. *J Geophys Res: Biogeo* 117. Doi: 10.1029/2011JG001766.
- Jorgenson, M.T., and Brown, J. (2005). Classification of the Alaskan Beaufort Sea Coast and estimation of carbon and sediment inputs from coastal erosion. *Geo-Marine Letters*. 25:2, 1432-1157. doi: 10.1007/s00367-004-0188-8.

- Kanevskiy, M., Shur, Y., Jorgenson, M.T., Ping, C.L., Michaelson, G.J., Fortier, D., Stephani, E., Dillon, M. and Tumskoy, V.E. (2013). Ground ice in the upper permafrost of the Beaufort Sea coast of Alaska, *Cold Regions Science and Technology*. 85, 56–70, doi: 10.1016/j.coldregions.2012.08.002.
- Kobayashi, N. (1985). Formation of thermoerosional niches into frozen bluffs due to storm surges on the Beaufort Sea Coast. *Journal of Geophysical Research*. 90:C6, 11983-11988. doi: 10.1029/JC090iC06p11983.
- Kruse, A., and M. Darrow (2017), Adsorbed cation effects on unfrozen water in fine-grained frozen soil measured using pulsed nuclear magnetic resonance, *Cold Regions Science and Technology*, Vol. 142, 42-54, <https://dx.doi.org/10.1016/j.coldregions.2017.07.006>.
- Kwok, Ron. "Arctic sea ice thickness, volume, and multiyear ice coverage: losses and coupled variability (1958 {2018})." *Environmental Research Letters* 13.10 (2018): 105005.
- Lantuit, H. and W.H. Pollard. 2008b. Fifty years of coastal erosion and retrogressive thaw slump activity on Herschel Island, southern Beaufort Sea, Yukon Territory, Canada. *Geomorphology*, 95, 84-102.
- Lantuit, H., Overduin, P.P., Couture, N., Wetterich, S., Aré, F., Atkinson, D., Brown, J., Cherkashov, G., Drozdov, D., Forbes, D.L., Graves-Gaylord, A., Grigoriev, M., Hubberten, H., Jordan, J., Jorgenson, T., Ødegård, R.S., Ogorodov, S., & Pollard, W.H., Rachold, V., Sedenko, S., Solomon, S., Steenhuisen, F., Streletskaia, I., and Vasiliev, A. (2012). The Arctic coastal dynamics database: a new classification scheme and statistics on Arctic permafrost coastlines. *Estuaries and Coasts*. 35:2, 383-400. doi: 10.1007/s12237-010-9362-6
- Lantuit, H.; Atkinson, D.; Overduin, P.P.; Grigoriev, M.; Rachold, V.; Grosse, G.; Hubberten, H.W. 2011 Coastal erosion dynamics on the permafrost-dominated Bykovsky Peninsula, north Siberia, 1951-2006 *Polar Res* 30 7341
- Lantuit, H.; Overduin, P.P.; Couture, N.; Odegard, R.S. 2008a Sensitivity of coastal erosion to ground ice contents: an Arctic-wide study based on the ACD classification of Arctic coasts. In *NICOP 2008: Proceedings of the 9th International Conference on Permafrost*, D.L. Kane and K.M. Hinkel (Eds.) pp. 1025-1029
- Larsen, PH., Goldsmith, S., Smith, O., Wilson, M.L., Strzepek, K., Chinowsky, P., and Saylor, B. (2008). Estimating future costs for Alaska public infrastructure at risk from climate change. 18:3, 442-457. doi: 10.1016/j.gloenvcha.2008.03.005
- Lee, C. M., S. Cole, M. Doble, L. Freitag, et al. 2012. Marginal Ice Zone (MIZ) Program: Science and Experiment Plan. Applied Physics Laboratory, University of Washington
- Lee, M.Y., Fossum, A., Costin, L.S., and Bronowski, D. (2002). Frozen soil material testing and constitutive modeling. SAND2002-0524. 1-65.
- Leffingwell, E and DE K 1919 The Canning River region, northern Alaska US Geol. Survey Prof. Paper 109 251.
- Lincoln, B. J., Rippeth, T. P., Lenn, Y. D., Timmermans, M. L., Williams, W. J., & Bacon, S. (2016). Wind-driven mixing at intermediate depths in an ice-free Arctic Ocean. *Geophysical Research Letters*, 43(18), 9749-9756.

- Liu, F., Krieger, J.R. and Zhang, J., 2014. Toward producing the Chukchi–Beaufort High-Resolution Atmospheric Reanalysis (CBHAR) via the WRFDA data assimilation system. *Monthly Weather Review*, 142(2), pp.788-805.
- Marsden, J.E. and Ratiu, T.S., 1999. *Introduction to mechanics and symmetry: a basic exposition of classical mechanical systems*. Springer Science & Business Media.
- Martin, P.D., J.L. Jenkins, F.J. Adams, M.T. Jorgenson, A.C. Matz, D.C. Payer, P.E. Reynolds, A.C. Tidwell, and J.R. Zelenak. 2009. Wildlife Response to Environmental Arctic Change: Predicting Future Habitats of Arctic Alaska. Report of the Wildlife Response to Environmental Arctic Change (WildREACH): Predicting Future Habitats of Arctic Alaska Workshop, 17-18 November 2008. Fairbanks, Alaska: U.S. Fish and Wildlife Service. 138 pp.
- McClelland, JW, Holmes RM, Peterson BJ, et al. (2016) Particulate organic carbon and nitrogen export from major Arctic rivers, *Global Biogeochem. Cycles*, 30, 629-643, doi: 10.1002/2015GB005351.
- Mesinger, F., G. DiMego, E. Kalnay, K. Mitchell, P.C. Shafran, W. Ebisuzaki, D. Jović, J. Woollen, E. Rogers, E.H. Berbery, and M.B. Ek. 2006. North American regional reanalysis. *Bull. Amer. Meteor. Soc.* 87(3):343-360.
- Mota, A., I. Tezaur, and C. Alleman. The Schwarz alternating method. *Comput. Meth. Appl. Mech. Engng.*, 319:19–51, 2017.
- Mota, A., I. Tezaur, and G. Philipot. The Schwarz alternating method for transient solid dynamics. *Comput. Meth. Appl. Mech. Engng.* (under review), 2020.
- NCEP reanalysis data provided by NOAA/OAR/ESRL PSD, Boulder, Colorado, available at <https://www.esrl.noaa.gov/psd/>.
- NOAA NDBC Prudhoe Bay, AK station (ID #9497645) <https://tidesandcurrents.noaa.gov/stationhome.html?id=9497645>.
- Ober, C., S. Conde, R. Pawlowski, and R. Pawlowski. Tempus: Time integration package. trilinos.github.io/tempus.html, February 2018.
- Ochi, Michel K. *Ocean waves: the stochastic approach*. Vol. 6. Cambridge University Press, 2005.
- O'Connor, M.T., Cardenas, M.B., Ferencz, S.B., Wu, Y., Neilson, B.T., Chen, J. and Kling, G.W., 2020. Empirical models for predicting water and heat flow properties of permafrost soils. *Geophysical Research Letters*, 47(11), p.e2020GL087646.
- Overduin, P. P., M. C. Strzelecki, M. N. Grigoriev, N. Couture, H. Lantuit, D. St.-Hilaire-Gravel, F. Gunther, and S. Wetterich. 2014. Coastal changes in the Arctic. From: Martini, I. P. and Wanless, H. R. (eds) *Sedimentary Coastal Zones from High to Low Latitudes: Similarities and Differences*. Geological Society, London, Special Publications, 388.
- Overeem, I., Anderson, R.S., Wobus, C.W., Clow, G.D., Urban, F.E. and Matell, N. (2011). Sea ice loss enhances wave action at the Arctic coast. *Geophysical Research Letters*. 38:17. doi: 10.1029/2011GL048681.
- Overland, James, Edward Dunlea, Jason E. Box, Robert Corell, Martin Forsius, Vladimir Kattsov, Morten Skovgaard Olsen, Janet Pawlak, Lars-Otto Reiersen, and Muyin Wang. "The urgency of arctic change," *Polar Science* (2018).

- Partensky, H.-W. 1989. Dynamic Forces due to Waves Breaking at Vertical Coastal Structures". 21st International Conference on Coastal Engineering June 20-25, 1988, Costa del Sol-Malaga, Spain.
- Perovich, D., W. Meier, M. Tschudi, S. Farrell, S. Gerland, S. Hendricks, T. Krumpen, and C. Haas 2017 Sea ice cover [in "State of the Climate 2016"]. Bull. Amer. Meteor. Soc 98 (8) S93-S98doi:10.1175/2017BAMSSStateoftheClimate.I.
- Pierson, W. J. and L. Moskowitz. 1964. A proposed spectral form for fully developed wind seas based on the similarity theory of SA Kitaigorodskii. Journal of Geophysical Research, 69, 24, 5181-5190.
- Ping, C.L., Michaelson G.J., Guo L.D., Jorgenson M.T., Kanevskiy M., Shur Y., Dou F.G., Liang J.J. (2011). Soil carbon and material fluxes across the eroding Alaska Beaufort Sea coastline. J Geophys Res-Bioge 116:G2. Doi: 10.1029/2010JG001588.
- Pribyl, DW. (2010) A critical review of the conventional SOC to SOM conversion factor. Geoderma 156: 75-83.
- Ravens, T.M., Jones, B.M., Jinlin, Z., Arp, C.D., and Schmutz, J.A. (2012). Process-based coastal erosion modeling for Drew Point, North Slope, Alaska. Journal of Waterway, Port, Coastal, and Ocean Engineering. 138:2, 122-130. doi: 10.1061/(ASCE)WW.1943-5460.0000106
- Reynolds, R.W., N.A. Rayner, T.M. Smith, D.C. Stokes, and W. Wang, 2002 An improved in situ and satellite SST analysis for climate J. Climate 15 1609-1625.
- Robertson, E.C., 1988. Thermal properties of rocks. U.S. Geological Survey Open-File Report 88-441.
- Rogers, W.E. and Zieger, S., 2014. New wave-ice interaction physics in wavewatch iii. NAVAL RESEARCH LAB STENNIS DETACHMENT STENNIS SPACE CENTER MS OCEANOGRAPHY DIV.
- Romanovsky, V E, Smith S L, Christiansen H H 2010 Permafrost thermal state in the polar Northern Hemisphere during the international polar year 2007–2009: A synthesis Permafr. and Periglac. Process 21 106-116.
- Russell-Head, D.D. (1980). The melting of free-drifting icebergs. Annals of Glaciology. 1, 119-122. doi: 10.3189/S0260305500017092.
- Salinger, A.G., Bartlett, R.A., Bradley, A.M., Chen, Q., Demeshko, I.P., Gao, X., Hansen, G.A., Mota, A., Muller, R.P., Nielsen, E., Ostien, J.T., Pawlowski, R.P., Perego, M., Phipps, E.T., Sun, W., and Tezaur, I.K. (2016). Albany: Using component-based design to develop a flexible, generic multiphysics analysis code. International Journal for Multiscale Computational Engineering. 14:4, 415-438. doi: 10.1615/IntJMultCompEng.2016017040.
- Sandia National Laboratories. (2017). Sandia's Open Source Software Portal, "Albany," available from: <https://software.sandia.gov/drupal/software/> (accessed 17 January 2020).
- Schrader, F.C. A reconnaissance in northern Alaska across the Rocky Mountains, along the Koyukuk, John, Anaktuvuk, and Colville rivers, and the Arctic coast to Cape Lisburne, in 1901, with notes by W.T. Peters. U.S. Geol. Surv. Prof. Paper 1904, 20, pp. 1-139.

- Schuur, E.A.G., McGuire A.D., Schadel C., Grosse G., Harden J.W., Hayes D.J., Hugelius G., Koven C.D., Kuhry P., Lawrence D.M., Natali S.M., Olefeldt D., Romanovsky V.E., Schaefer K., Turetsky M.R., Treat C.C., Vonk J.E. (2015). Climate change and the permafrost carbon feedback. *Nature* 520:7546, 171-179.
- Smith, S.L., Romanovsky, V.E., Lewkowicz, A.G., Burn, C.R., Allard, M., Clow, G.D., Yoshikawa, K. and Throop, J., 2010. Thermal state of permafrost in North America: a contribution to the international polar year. *Permafrost and Periglacial Processes*, 21(2), pp.117-135.
- Spotz, W., T. Smith, I. Demeshko, and J. Fike. Aeras: A next generation global atmosphere model. *Procedia Computer Science*, 51:2097–2106, 2015.
- Stammerjohn, S., Massom R., Rind D., Martinson D. (2012). Regions of rapid sea ice change: An inter-hemispheric seasonal comparison. *Geophys Res Lett* 39:6. Doi: 10.1029/2012GL050874.
- Steele, M., and S. Dickinson (2016), The phenology of Arctic Ocean surface warming, *J. Geophys. Res. Oceans*, 121, 6847–6861, doi:10.1002/2016JC012089.
- Stein, R. and Macdonald R.M. (2004). *The Organic Carbon Cycle in the Arctic Ocean*. Berlin Heidelberg: Springer.
- Stopa, J. E., F. Arduin, and F. Girard-Arduin. 2016. Wave climate in the Arctic 1992{2014: seasonality and trends. *The Cryosphere*, 10, 1605-1629
- Strauss, J., Schirmermeister, L., Grosse, G., Wetterich, S., Ulrich, M., Herzsuh, U. and Hubberten, H.W., 2013. The deep permafrost carbon pool of the Yedoma region in Siberia and Alaska. *Geophysical Research Letters*, 40(23), pp.6165-6170.
- Sun, W., J. Ostien, and A. Salinger. A stabilized assumed deformation gradient finite element formulation for strongly coupled poromechanical simulations at finite strain. *International Journal for Numerical and Analytical Methods in Geomechanics*, 37:2755–2788, 2013.
- Tanski, G., Wagner D., Knoblauch C., Fritz M., Sachs T., Lantuit H. (2019). Rapid CO2 Release From Eroding Permafrost in Seawater. *Geophys Res Lett* 46. Doi: 10.1029/2019GL084303.
- Tezaur, I., M. Perego, A. Salinger, R. Tuminaro, and S. Price. Albany/felix: A parallel, scalable and robust finite element higher-order stokes ice sheet solver built for advanced analysis. *Geoscientific Model Development*, 8:1–24, 2015.
- Thomas, M.A., Mota, A., Jones, B.M., Choens, R.C., Frederick, J.M. and Bull, D.L., 2020. Geometric and material variability influences stress states relevant to coastal permafrost bluff failure. *Frontiers in Earth Science*, 8, p.143. doi.org/10.3389/feart.2020.00143
- Thomson, J. and W. E. Rogers. 2014. Swell and sea in the emerging Arctic ocean. *Geophysical Research Letters*, 41, 3136-3140.
- Thomson, J., Fan, Y., Stammerjohn, S., Stopa, J., Rogers, W.E., Girard-Arduin, F., Arduin, F., Shen, H., Perrie, W., Shen, H. and Ackley, S., 2016. Emerging trends in the sea state of the Beaufort and Chukchi Seas. *Ocean Modelling*, 105, pp.1-12.
- Timmermans, M.-L. (2015), The impact of stored solar heat on Arctic sea ice growth, *Geophys. Res. Lett.*, 42, 6399{6406, doi:10.1002/2015GL064541.

- Tolman, H. L. 2002, Alleviating the garden sprinkler effect in wind wave models, *Ocean Mod.*, 4, 269–289.
- Tweedie, C. E.; Escarzaga, S. M.; Cody, R. P.; Manley, W. F.; Gaylord, A. G.; Aiken, Q.; Lopez, A. F.; Aguirre, A.; George, C.; Nelson, L.; Brown, J. 2016 Patterns and Controls of Erosion along the Elson Lagoon Coastline, Barrow, Alaska (2003-2016) American Geophysical Union, Fall General Assembly 2016 abstract id. EP12B-02.
- Tweedie, C.E.; Aguirre, A.; Vargas, C.S.; Brown, J. Spatial and temporal dynamics of erosion along the Elson Lagoon Coastline near Barrow, Alaska (2002-2011) 2012 In Proceedings of the Tenth International Conference on Permafrost 425-430.
- United States General Accounting Office (USGAO), 2014. Climate Change Adaptation: DOD can improve infrastructure planning and processes to better account for potential impacts. Report to Congressional Requesters. <http://www.gao.gov/assets/670/663734.pdf>.
- United States Government Accountability Office (2004). Alaska native villages: villages affected by flooding and erosion have difficulty qualifying for federal assistance. Washington, D.C.: U.S. Government Accountability Office, GAO 04-895T, 17 p.
- United States Government Accountability Office. (2009). Alaska native villages: limited progress has been on relocating villages threatened by flood and erosion. Washington, D.C.: U.S. Government Accountability Office, GAO 09-551, 53 p.
- Urban, F.E., and Clow, G.D., 2018, DOI/GTN-P climate and active-layer data acquired in the National Petroleum Reserve–Alaska and the Arctic National Wildlife Refuge, 1998–2017 (ver. 1.1, June 2020), U.S. Geological Survey Data Series 1092, 71 p., <https://doi.org/10.3133/ds1092>. [Supersedes USGS Data Series 1021.]
- Urban, Frank E., and Gary D. Clow 2016 DOI/GTN-P Climate and Active-layer Data Acquired in the National Petroleum Reserve-Alaska and the Arctic National Wildlife Refuge, 1998-2014. US Department of the Interior US Geological Survey 2016.
- Urban, Frank. U.S. Geological Survey, personal communication, March 2020.
- USEPA. 1990. Technical guidance manual for performing waste load allocations, Book III: Estuaries. Chapter 5: Model calibration, validation, and use. EPA-823-R-92-003. U.S. Environmental Protection Agency, Office of Water, Washington, DC.
- Vonk, J.E., Sanchez-Garcia L., van Dongen B.E., Alling V., Kosmach D., Charkin A., Semiletov I.P., Dudarev O.V., Shakhova N., Roos P., Eglinton T.I., Andersson A., Gustafsson O. (2012). Activation of old carbon by erosion of coastal and subsea permafrost in Arctic Siberia. *Nature* 489:7414, 137-140.
- Vonk, J.E., and Gustafsson, O. (2013). Permafrost-carbon complexities. *Nature Geoscience* 6, 675-676.
- Walker, H.J., 1988, November. Permafrost and coastal processes. In Proceedings of the Fifth International Conference on Permafrost (Vol. 3, pp. 35-42).
- Wan, X. and Z. Yang (2020), Pore water freezing characteristic in saline soils based on pore size distribution, *Cold Regions Science and Technology*, Vol. 173, 103030, <https://doi.org/10.1016/j.coldregions.2020.103030>.

- Watanabe, E. and H. Hasumi, 2009: [Pacific Water Transport in the Western Arctic Ocean Simulated by an Eddy-Resolving Coupled Sea Ice–Ocean Model](#). *J. Phys. Oceanogr.*, **39**, 2194–2211, doi: 10.1175/2009JPO4010.1.
- WAVEWATCH III ® Development Group (WW3DG), (2019): User manual and system documentation of WAVEWATCH III ® version 6.07. Tech. Note 333, NOAA/NWS/NCEP/MMAB, College Park, MD, USA, 465 pp. + Appendices.
- Wegner, C., Bennett K.E., de Vernal A., Forwick M., Fritz M., Heikkila M., Lacka M., Lantuit H., Laska M., Moskalik M., O'Regan M., Pawlowska J., Prominska A., Rachold V., Vonk J.E., Werner K. (2015). Variability in transport of terrigenous material on the shelves and the deep Arctic Ocean during the Holocene. *Polar Res* 34. Doi: 10.3402/polar.v34.24964.
- Wendler, G.; Chen, L.; Moore, B. 2012 The First Decade of the New Century: A Cooling Trend for Most of Alaska Open Atmos. Sci. J. 2012 6 111-116.
- White, F.M.; Spaulding, M.L.; and Gominho, L. (1980). Theoretical estimates of various mechanism involved in iceberg deterioration in the open ocean environment. Washington, D.C.: U.S. Coast Guard Technical Service Information Service Publication CG-D-62-8081-20571, 126.
- Willmott, C.J. 1981. On the Validation of Models. *Physical Geography*. 2:184-194.
- Wobus, C., Anderson, R., Overeem, I., Matell, N., Clow, G., and Urban, F. (2011). Thermal erosion of a permafrost coastline: improving process-based models using time-lapse photography. *Arctic, Antarctic, and Alpine Research*. 43:3, 474-484. doi: 10.1657/1938-4246-43.3.474.
- Xu, X., Wang, Y., Zhenhua, Y., and Zhang, H. (2017). Effect of temperature and strain rate on mechanical characteristics and constitutive model of frozen Helin loess. *Cold Regions Science and Technology* (136). 44-51.
- Yamamoto, Y., and Springman S.M. (2017). Three- and four-point bending tests on artificial frozen soil samples at temperatures close to 0° C. *Cold Regions Science and Technology* (134). 20-32.
- Young, I. R. 1999. *Wind generated ocean waves*, Elsevier Publishing.
- Yuanlin, Z., and Carbee, D.L. (1984). Uniaxial compressive strength of frozen silt under constant deformation rates. *Cold Regions Science and Technology* (9). 3-15.
- Yuanlin, Z., and Carbee, D.L. (1987). Tensile strength of frozen silt. CRREL Report 87-15, 1-23.
- Zhou, G., Hu, K., Zhao, X., Wang, J., Liang, H., and Lu, G. (2015). Laboratory investigation on tensile strength characteristics of warm frozen soils. *Cold Regions Science and Technology* (113). 81-90.
- Zhou, Z., Ma, W., Zhang, S., Mu, Y., and Li, G. (2018). Effect of freeze-thaw cycles in mechanical behaviors of frozen loess. *Cold Regions Science and Technology* (146). 9-18.

APPENDICES

DISTRIBUTION

Email—Internal

Name	Org.	Sandia Email Address
Technical Library	01977	sanddocs@sandia.gov

This page left blank

This page left blank



Sandia
National
Laboratories

Sandia National Laboratories is a multimission laboratory managed and operated by National Technology & Engineering Solutions of Sandia LLC, a wholly owned subsidiary of Honeywell International Inc. for the U.S. Department of Energy's National Nuclear Security Administration under contract DE-NA0003525.

ARCTIC COASTAL EROSION APPENDICES

Appendix A. Mechanical Material Model and Adaptive Meshing for the Arctic Coastal Erosion Model	A-1
Appendix B. Coring Campaign—Additional Work.....	B-1

APPENDIX A. MECHANICAL MATERIAL MODEL AND ADAPTIVE MESHING FOR THE ARCTIC COASTAL EROSION MODEL

APPENDIX: Mechanical Material Model and Adaptive Meshing for the Arctic Coastal Erosion Model

Alejandro Mota¹

¹Mechanics of Materials
Sandia National Laboratories
Livermore CA 94550, USA, amota@sandia.gov

September 16, 2020

Abstract

This appendix document describes the mechanical material model and the adaptive meshing for the Arctic coastal erosion project and its implementation in the ALBANY finite element code.

1 Introduction

Although the Arctic coastline comprises one-third of the global coastline length [14], much of our current understanding of coastal landscape evolution is applicable to coasts that are fundamentally different than the Arctic. Current erosion models lack mechanistic processes critical to predicting thermo-abrasive erosion of sedimentary permafrost ground [1]. In the thermo-abrasive process, the parent material at the base of the bluff is warmed by the ocean and eroded by the mechanical action of the ocean. A recess at the base of the bluff, referred to as a niche, progresses inland until the overhanging material fails in a shearing or toppling mode known as block failure (Figure 3, adapted from Hoque and Pollard [12]) [13]. The fallen, ice-bound block thaws in the near-shore environment within a week, suspending the sediment in the ocean [3]. The erosion is a non-linear process; it occurs in discrete events resulting in permanent coastline loss. This event-driven loss is normally forced by a storm with increased wave activity and inundation.

2 Mechanical Material Models

In this section we describe the material models used for capturing the behavior of ice and permafrost.

2.1 Constitutive Model for Ice

Ice is a polycrystalline granular material. Its microstructure can evolve under different stress states due to plastic deformation, recrystallization, and grain boundary migration [7]. Its material response is highly nonlinear, viscoplastic and anisotropic, depending mainly on applied stress, strain-rate, temperature, salinity, grain-size, and anisotropic effects [21]. While mostly brittle under tension, it undergoes transitions to a

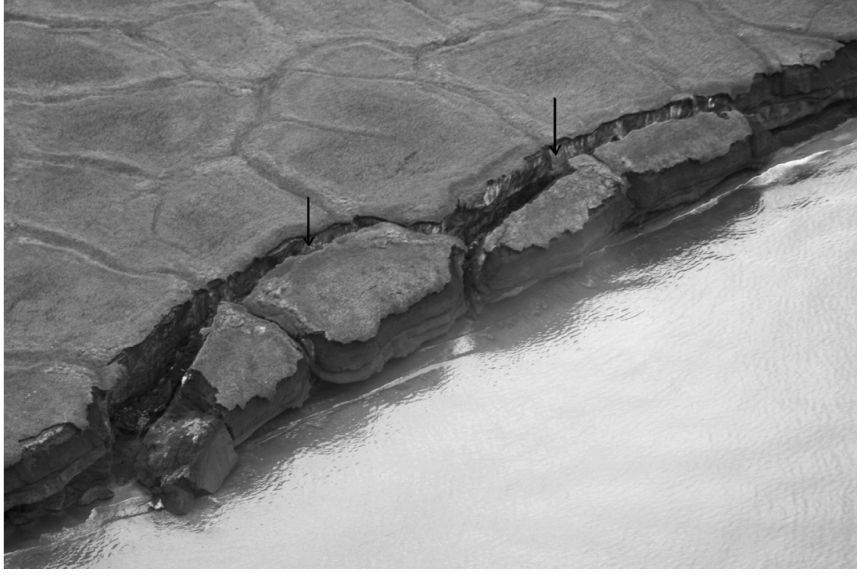


Figure 1: Aerial photograph of block failure along the Arctic coastline. Black arrows point to exposed ice wedges. Bluff height 8 m. Adapted from Hoque and Pollard [12].

ductile material under significant compression. We propose to model the mechanical response of ice using standard J_2 plasticity extended to the large-deformation regime for four reasons:

- Our application space is at a sufficiently large scale, and therefore the micro-structural characteristics of ice are reasonably captured by an isotropic material model.
- It incorporates all mechanisms that lead to the deformation, plastic flow and creep of polycrystalline materials like ice.
- It requires minimal calibration, as most parameters are determined by the known crystalline microstructure of ice.
- It is implemented within the ALBANY code base where our erosion framework will reside.

We start by providing a simple framework for integrating the conventional model of deviatoric plasticity, from J_2 -flow theory, to a model that incorporates the effects of temperature through ice saturation.

The thermo-mechanical response of the solids considered here is characterized by a free-energy density per unit undeformed volume of the form

$$A = A(\mathbf{F}, \mathbf{F}^p, \epsilon^p, T), \quad (1)$$

where \mathbf{F} is the deformation gradient, \mathbf{F}^p is the plastic part of the deformation gradient, $\epsilon^p \geq 0$ is an effective deviatoric plastic strain, T is the absolute temperature, and

$$\mathbf{F}^e = \mathbf{F}(\mathbf{F}^p)^{-1} \quad (2)$$

is the elastic part of the deformation gradient [15].

The plastic deformation rate is assumed to obey the flow rule

$$\dot{\mathbf{F}}^p (\mathbf{F}^p)^{-1} = \dot{\epsilon}^p \mathbf{M} \quad (3)$$

where $\dot{\epsilon}^p$ is subject to the irreversibility constraint

$$\dot{\epsilon}^p \geq 0, \quad (4)$$

and the tensor \mathbf{M} sets the direction of the deviatoric plastic deformation rate, which is assumed to satisfy

$$\text{tr} \mathbf{M} = 0, \quad \mathbf{M} : \mathbf{M} = \frac{3}{2}. \quad (5)$$

The tensor \mathbf{M} is otherwise unknown and is to be determined as part of the solution. The constraint (5) may be regarded as defining the assumed kinematics of plastic deformation. As we shall see, the direction of plastic deformation, as determined by \mathbf{M} , follows from the variational structure of the constitutive update in a manner which generalizes the principle of maximum dissipation [11, 17].

The first Piola-Kirchhoff stress tensor \mathbf{P} follows from Coleman's relations as

$$\mathbf{P} = \frac{\partial A}{\partial \mathbf{F}}, \quad (6)$$

while the thermodynamic force Y conjugate to the internal variable ϵ^p is

$$Y = \frac{dA}{d\epsilon^p} = \sigma - \sigma_c = \mathbf{T} \cdot \frac{\partial \mathbf{F}^p}{\partial \epsilon^p} - \frac{\partial A}{\partial \epsilon^p}, \quad (7)$$

where

$$\sigma = \boldsymbol{\Sigma} \cdot \mathbf{M}, \quad \sigma_c = \frac{\partial A}{\partial \epsilon^p}, \quad (8)$$

are the effective deviatoric stress and the deviatoric flow stress, respectively, and we write

$$\boldsymbol{\Sigma} = \mathbf{T} (\mathbf{F}^p)^T, \quad (9)$$

in which \mathbf{T} is the thermodynamic force conjugate to \mathbf{F}^p , written as

$$\mathbf{T} = -\frac{\partial A}{\partial \mathbf{F}} \cdot \frac{\partial \mathbf{F}}{\partial \mathbf{F}^p} - \frac{\partial A}{\partial \mathbf{F}^p} = (\mathbf{F}^e)^T \mathbf{P} - A_{, \mathbf{F}^p}. \quad (10)$$

Appropriate rate equations for the internal variable ϵ^p must be specified to formulate a complete set of constitutive relations. With a view to ensuring a variational structure, we postulate the existence of a dual kinetic potential $\psi^*(\dot{\epsilon}^p, \mathbf{F}^p, T)$ such that

$$Y = \frac{\partial \psi^*}{\partial \dot{\epsilon}^p}. \quad (11)$$

In addition, for every $t \in [t_1, t_2]$ we introduce the power functional

$$\Phi[\dot{\varphi}, \dot{\epsilon}^p, \mathbf{M}] = \int_{\Omega} (\dot{A} + \text{ * }) dV - \int_{\Omega} \rho \mathbf{B} \cdot \dot{\varphi} dV - \int_{\partial_{\mathbf{T}} \Omega} \mathbf{T} \cdot \dot{\varphi} dS. \quad (12)$$

where \mathbf{F}^p , $\dot{\epsilon}^p$, and \mathbf{M} are now regarded as fields over Ω , and $\dot{\mathbf{F}}^p$ is determined by $\dot{\epsilon}^p$ and \mathbf{M} through the flow rule (3). Using identities (6), (7) and the flow rule (3), (12) may be rewritten as

$$\Phi[\dot{\varphi}, \dot{\epsilon}^p, \mathbf{M}] = \int_{\Omega} (\mathbf{P} : \text{Grad}\dot{\varphi} - Y \dot{\epsilon}^p + \psi^*) \, dV - \int_{\Omega} \rho \mathbf{B} \cdot \dot{\varphi} \, dV - \int_{\partial_T \Omega} \bar{\mathbf{T}} \cdot \dot{\varphi} \, dS, \quad (13)$$

where $\mathbf{F} = \text{Grad}\varphi$ has been introduced. For every $t \in [t_1, t_2]$, the rates $\dot{\varphi}$, $\dot{\epsilon}^p$, and the direction of plastic flow \mathbf{M} follow jointly from the minimization problem

$$\Phi^{\text{eff}}[\dot{\varphi}] = \inf_{\dot{\epsilon}^p, \mathbf{M}} \Phi[\dot{\varphi}, \dot{\epsilon}^p, \mathbf{M}], \quad (14)$$

subject to the constraints (4), (5). Problem (14) additionally defines the reduced power functional $\Phi^{\text{eff}}[\dot{\varphi}]$. The material velocity field $\dot{\varphi}$ finally follows from the minimization problem

$$\inf_{\dot{\varphi}} \Phi^{\text{eff}}[\dot{\varphi}], \quad \dot{\varphi} = \dot{\bar{\varphi}} \text{ on } \partial_{\varphi} \Omega. \quad (15)$$

Since the extended functional $\Phi[\dot{\varphi}, \dot{\epsilon}^p, \mathbf{M}]$ does not depend on spatial derivatives of the fields, the minimization (14) may be effected locally, with the result

$$\Phi^{\text{eff}}[\dot{\varphi}] = \int_{\Omega} [\phi(\text{Grad}\dot{\varphi}) - \rho \mathbf{B} \cdot \dot{\varphi}] \, dV - \int_{\partial_T \Omega} \mathbf{T} \cdot \dot{\varphi} \, dS, \quad (16)$$

where

$$\phi(\dot{\mathbf{F}}) = \inf_{\dot{\epsilon}^p, \mathbf{M}} f(\dot{\mathbf{F}}, \dot{\epsilon}^p, \mathbf{M}), \quad (17)$$

subject to the constraints (4), (5), and

$$f(\dot{\mathbf{F}}, \dot{\epsilon}^p, \mathbf{M}) = \mathbf{P} : \dot{\mathbf{F}} - Y \dot{\epsilon}^p + \psi^*, \quad (18)$$

is a power density per unit undeformed volume. Evidently, by the construction of the power functional the kinetic relation (11) is an Euler-Lagrange equation of the minimum problem (17). The additional Euler-Lagrange equations with respect to \mathbf{M} are

$$\boldsymbol{\Sigma} - \lambda \mathbf{M} = \mathbf{0}, \quad \text{tr}(\boldsymbol{\Sigma}) = 0, \quad (19)$$

where λ is a Lagrange multiplier arising from the constraints (5). Using these constraints, eqs. (19) can be solved for \mathbf{M} , with the result

$$\mathbf{M} = \frac{3 \text{dev}(\boldsymbol{\Sigma})}{2\sigma}, \quad (20)$$

where

$$\sigma = \sqrt{(3/2) \text{dev}(\boldsymbol{\Sigma}) : \text{dev}(\boldsymbol{\Sigma})} \quad (21)$$

is the von Mises effective stress. Using (20) in (3) we obtain

$$\dot{\mathbf{F}}^p (\mathbf{F}^p)^{-1} = \dot{\epsilon}^p \frac{3 \text{dev}(\boldsymbol{\Sigma})}{2\sigma}, \quad (22)$$

which is an extension of the Prandtl-Reuss flow rule into the finite-deformation range.

The power density function $\phi(\dot{\mathbf{F}})$ has the fundamental property [17]

$$\mathbf{P} = \frac{\partial \phi}{\partial \dot{\mathbf{F}}}(\dot{\mathbf{F}}), \quad (23)$$

and, consequently, the Euler-Lagrange equations corresponding to the minimization problem (15) are the equilibrium equations

$$\text{Div} \mathbf{P} + \rho \mathbf{B} = \mathbf{0} \quad \text{in } \Omega, \quad \mathbf{P} \cdot \mathbf{N} = \mathbf{T} \quad \text{on } \partial_T \Omega, \quad (24)$$

where in the latter expression \mathbf{N} is the unit normal to $\partial \Omega$.

2.1.1 Elastic strain-energy density

Assume that the free-energy density (1) has the additive structure

$$A(\mathbf{F}, \mathbf{F}^p, \epsilon^p, T) = W^e(\mathbf{F}^e, T) + W^p(\epsilon^p, T), \quad (25)$$

where $W^e(\mathbf{F}^e, T)$ and $W^p(\epsilon^p, T)$ are the elastic and stored energy densities per unit undeformed volume, respectively. Then σ_c reduces to

$$\sigma_c(\epsilon^p, T) = \frac{\partial W^p}{\partial \epsilon^p}(\epsilon^p, T). \quad (26)$$

Due to material-frame indifference, W^e can only depend on \mathbf{F}^e through the corresponding elastic right-Cauchy Green deformation tensor

$$\mathbf{C}^e = (\mathbf{F}^e)^T \mathbf{F}^e = (\mathbf{F}^p)^T \mathbf{C} (\mathbf{F}^p)^{-1}. \quad (27)$$

Furthermore, the elastic strain-energy density may alternatively be expressed in terms of the logarithmic elastic strain

$$\epsilon^e = \frac{1}{2} \log(\mathbf{C}^e), \quad (28)$$

whereupon W^e takes the form

$$W^e = W^e(\epsilon^e, T). \quad (29)$$

We denote by $\boldsymbol{\sigma}$ the stress conjugate to ϵ^e , namely,

$$\boldsymbol{\sigma} = \frac{\partial W^e}{\partial \epsilon^e}(\epsilon^e, T). \quad (30)$$

In order to obtain a simple form of $W^e(\mathbf{C}^e, T)$ we consider a representative neighborhood in the plastically-deformed or ‘intermediate’ configuration of the material. We assume that the plastic deformation of the ice matrix leaves the elastic properties of the matrix unchanged. This assumption is appropriate for crystalline materials such as ice, whose elastic properties are ostensibly insensitive to isochoric plastic deformation. A simple form of the resulting elastic energy is

$$\begin{aligned} W^e(\epsilon^e, T) &= W^{e,\text{vol}}(\theta^e, T) + W^{e,\text{dev}}(\epsilon^e, T), \\ W^{e,\text{vol}}(\theta^e, T) &= \frac{\kappa}{2} [\theta^e - \alpha(T - T_0)]^2 + \rho C_v T \left(1 - \log \frac{T}{T_0} \right), \\ W^{e,\text{dev}}(\epsilon^e, T) &= \mu \|\text{dev}(\epsilon^e)\|^2, \end{aligned} \quad (31)$$

where $\theta^e = \log J^e$, κ is the bulk modulus, μ is the shear modulus, α is the thermal expansion coefficient, T_0 is a reference absolute temperature, and C_v is the specific heat per unit mass at constant volume.

2.1.2 Stored energy

A simple stored energy function can be formulated by assuming a deviatoric character to the plasticity. This can be modeled simply by a conventional power-law of hardening such as

$$\begin{aligned} W^P(\epsilon^P, T) &= W^{P,\text{dev}}(\epsilon^P, T), \\ W^{P,\text{dev}}(\epsilon^P, T) &= \frac{n\sigma_0(T)\epsilon_0^P}{n+1} \left(1 + \frac{\epsilon^P}{\epsilon_0^P}\right)^{\frac{n+1}{n}}. \end{aligned} \quad (32)$$

In these expressions, n is the hardening exponent, $\sigma_0(T)$ is the yield stress, and ϵ_0^P is a reference deviatoric plastic strain. The yield stress is assumed to depend on temperature through the ice saturation, as follows

$$\sigma_0(T) := f(T)\sigma_Y^{\text{ice}} \quad (33)$$

where $f(T) \in [0, 1]$ is the ice saturation, computed separately by the strongly coupled thermal problem, σ_Y is the yield stress of pure crystalline ice, and $\sigma_0(T)$ is the effective yield stress of the ice wedge material.

2.1.3 Rate sensitivity

For completeness we consider rate sensitivity in the plastic deformation. The deviatoric rate sensitivity may be modeled simply by means of a conventional power-law of hardening. Based on these considerations, and the same approach as in the previous section, we have

$$\begin{aligned} \dot{\epsilon}^P &= \dot{\psi}^{*,\text{dev}}(\dot{\epsilon}^P, T), \\ \dot{\psi}^{*,\text{dev}}(\dot{\epsilon}^P, T) &= \frac{m\sigma_0(T)\dot{\epsilon}_0^P}{m+1} \left(\frac{\dot{\epsilon}^P}{\dot{\epsilon}_0^P}\right)^{\frac{m+1}{m}}. \end{aligned} \quad (34)$$

In these expressions, m is the rate sensitivity exponent, and $\dot{\epsilon}_0^P$ is a reference plastic strain rate.

2.2 Constitutive Model for Permafrost

The mechanical behavior of permafrost at the surveyed sites is mostly characterized by its ice content, and it only shows a significant deviation from elasto-perfectly-plastic behavior near the melting point of ice, according to our experiments [6]. Near the melting point of ice the softening behavior exhibited by the stress-strain relationship may be appropriately modeled by a hardening law such as Voce or power law. For these reasons, we assume that the mechanical behavior of permafrost may also be captured by the same J_2 flow plasticity model we introduced for ice. The yield stress (33), however, is now expressed as

$$\sigma_0(T) := S_s\sigma_Y^{\text{soil}} + \phi f(T)\sigma_Y^{\text{ice}} \quad (35)$$

where $f \in [0, 1]$ is the ice saturation, σ_Y^{soil} is the yield stress of the soil material, S_s is the soil volume fraction, σ_Y^{ice} is the yield stress of pure crystalline ice, and ϕ is the soil porosity.

3 Erosion by Mesh Adaptation

In a simulation that requires the removal of material due to physical phenomena such as erosion, the finite element mesh is initially coherent. As the simulation advances, a failure criterion is computed at each

integration or material point each time a specified number of computational steps have been performed. When the failure criterion is satisfied at a particular integration point or points, the element containing those points is removed from the mesh. The continuous evolution of the topology of the mesh is an inherent feature of mesh adaptation element approaches. This evolution involves complex operations on the mesh, with the result that robust three-dimensional implementations that take into account these changes in topology are difficult to develop. A formal approach for the manipulation of the topology of finite element meshes is thus necessary in order to bring the complexities of these operations to a manageable level, and also to avoid the creation of *ad hoc* algorithms that may result in error-prone and inefficient implementations.

Mesh descriptions often assume one of the following two representations: *full* or *reduced*. According to the full representation, all topological entities in a mesh, such as points, segments or faces, are represented explicitly in the data structure. By contrast, in the reduced representation, one or more classes of topological entities are not represented explicitly, and hence their topological information must be inferred in terms of other entities that exist in the data structure [9]. The most common representation of a finite element mesh is a connectivity list or table. In this representation, each row in the table simply lists the nodes for a particular element according to some ordering convention. The connectivity table, although simple to implement, has proved extremely cumbersome for complex topological manipulations of meshes, such as those imposed by the aforementioned erosion processes.

Most advanced mesh representations are capable of effectively dealing with issues of non-manifold topologies, storage requirements, efficiency of construction, and modification or retrieval of topological information. For instance, the radial-edge data structure introduced by Weiler emphasizes completeness and suitability for the representation of non-manifold topologies. Here, completeness is defined as the ability to generate all topological information from the representation alone, i.e., all adjacency relationships are directly retrievable or derivable from the information contained in the data structure [22, 20, 5]. Specialized topology-based data structures were introduced by Beall and Shephard, with a varying degree of explicitness. Some of the proposed data structures are fully explicit, while the rest offer different levels of implicit representation with the objective of minimizing storage.

Previous efforts to develop a representation of a mesh, in which —possibly radical— topological changes occur, often involve the direct manipulation of finite-element connectivity arrays by means of complex algorithms [19, 18]. While this approach may be effective for relatively small meshes and light computational loads, it ostensibly fails to deal properly with non-manifold topologies and does not scale well to large meshes. Celes et al. developed an implicit data structure that supports fracture and fragmentation. The authors particularly stress storage reduction and the representation of various types of elements, including simplicial ones. A direct comparison with our approach, however, is not possible at this time as the authors do not report performance data for fracture.

In the present work, a *complete* approach for the topological representation of finite element meshes as graphs is developed. By recourse to algebraic topology and graph theory, the original n -dimensional cell complex is reduced to a uni-dimensional simplicial complex in the form of a graph, thus greatly decreasing the complexity of topological manipulations. We show that the graph representation is particularly well-suited for the simulation of erosion.

3.1 Failure Criteria

The first step in defining an erosion algorithm is establishing the failure criterion or criteria that leads to the removal of material from the mesh. Within each time step, the mesh adaptivity infrastructure that we implemented in ALBANY queries the finite element model to determine if any element satisfies the failure criteria. Within the finite element model, each element is checked to see if it satisfies any of the failure criteria.

If so, that element is marked for removal. If the finite element model notifies the mesh adaptivity framework that there are failed elements, the framework proceeds to request the removal of the failed elements from the mesh topology (in the form of the graph representation described in the next section).

The failure criteria currently implemented are two:

- Stress criterion: when the material reaches a critical value of the stress.
- Kinematic criterion: when the material has tilted excessively, it is assumed that has fallen as part of block erosion.

3.1.1 Stress Failure Criterion

This criterion simulates the initiation and propagation of cracks in the bluff due to stresses induced by the advancement of the niche, a failure mechanism that is supported by observations in the field. In lieu of a full-blown loss of ellipticity analysis at each of the integration points, which would be prohibitive from a computational point of view, we determine a value of the critical stress failure criterion f_{stress} as follows,

$$f_{\text{stress}} = \begin{cases} f_{\text{stress}} + 1, & \|\boldsymbol{\sigma} \cdot \boldsymbol{n}\| \geq \sigma_{\text{critical}}; \\ f_{\text{stress}}, & \text{otherwise,} \end{cases} \quad (36)$$

in which $\boldsymbol{\sigma}$ is the Cauchy stress, \boldsymbol{n} is the normal of each of the element faces, and σ_{critical} is a critical value of the stress, in our case $\sigma_0(T)$ from the material model.

3.1.2 Kinematic Failure Criterion

This criterion is used to determine when to remove entire sections of material due to block failure. One way to achieve this is to remove elements when the deformation is large enough that there is a significant rotation of angle of tilt with respect to the reference configuration. The angle of rotation θ for each integration point is determined by first performing the polar decomposition of the deformation gradient \boldsymbol{F} ,

$$[\boldsymbol{R}, \boldsymbol{U}] = \text{polar}(\boldsymbol{F}), \quad \boldsymbol{R} \in SO(3), \quad \boldsymbol{U} \in SPD(3), \quad \boldsymbol{F} \in GL^+(3), \quad (37)$$

and then recovering the angle of rotation from the rotation \boldsymbol{R} as

$$\theta := \cos^{-1}\left[\frac{1}{2}(\text{tr } \boldsymbol{R} - 1)\right], \quad (38)$$

so that the kinematic failure criterion becomes

$$f_{\text{kinematic}} = \begin{cases} f_{\text{kinematic}} + 1, & |\theta| \geq \theta_{\text{critical}}; \\ f_{\text{kinematic}}, & \text{otherwise.} \end{cases} \quad (39)$$

Then we compute a global failure criterion f_{global} as

$$f_{\text{global}} := f_{\text{stress}} + f_{\text{kinematic}}, \quad (40)$$

and mark the element for removal if $f_{\text{global}} > 0$.

3.2 Finite Element Meshes as Graphs

We restrict our definitions to simplicial and geometric cube complexes, as the only meshes that are available to use through ALBANY are triangular or tetrahedral (*simplicial*) and quadrilateral or hexahedral (*geometric cubical*). We define a finite element mesh as a cell complex $K \in \mathbb{R}^N$ of dimension $n \leq N$ such that a cell σ in the $(n-1)$ -skeleton of K , $\sigma \in K^{(n-1)}$, is a face of at least one cell of dimension n .

An oriented cell $+\sigma$ is a cell σ together with a particular ordering of its points and all even permutations thereof. The same cell with all odd permutations of this ordering is said to have an opposite orientation and is denoted as $-\sigma$. A p -chain on K is a function $c : K \mapsto \mathbb{N}$ such that $c(\sigma) = -c(-\sigma)$ and $c(\sigma) = 0$ for all but finitely many oriented p -cells in K [8, 16]. The elementary chain c corresponding to σ is defined as

$$c(\tau) := \begin{cases} 0, & \text{if } \tau \neq \sigma; \\ 1, & \text{if } \tau = \sigma; \\ -1, & \text{if } \tau = -\sigma. \end{cases} \quad (41)$$

The symbol σ is often used to denote both a cell and its elementary chain.

Consider the oriented n -cell $\sigma = [x_0, \dots, x_n]$ in which $x_i \in \mathbb{R}^N$, $i \in [0, \dots, n]$ are its points. We define the *face operator* as

$$d_i(\sigma) := [x_0, \dots, x_{i-1}, x_{i+k}, \dots, x_n], \quad (42)$$

where $k = 1$ for a simplicial complex, and $k = 2^{n-1}$ for a geometric cube complex, and which returns the i^{th} $(n-1)$ -cell that is a *proper face* of the cell σ . It follows that the *boundary operator* can be defined as

$$\partial_n(\sigma) := \sum_{i=0}^n (-1)^i d_i(\sigma). \quad (43)$$

Next consider a pair of cells, $\sigma^p \in K$ and $\sigma^{p-1} \in K$, with $p \in [1, \dots, n]$. If $\sigma^p \cap \sigma^{p-1} = \sigma^{p-1}$, then let x_i be the first of the extra points of σ^p that do not belong to σ^{p-1} . The *incidence number* is defined as

$$[\sigma^p, \sigma^{p-1}] := \begin{cases} 0, & \text{if } \sigma^p \cap \sigma^{p-1} = \emptyset; \\ 1, & \text{if } \sigma^{p-1} = d_i(\sigma^p); \\ -1, & \text{if } \sigma^{p-1} = -d_i(\sigma^p). \end{cases} \quad (44)$$

Let $f : K \mapsto \mathbb{N}$ be an injective map that assigns to each cell in the mesh a non-negative integer. Then let

$$\begin{aligned} V &= \{v \mid v = f(\sigma) \in \mathbb{N}, \sigma \in K\}, \\ E &= \{e \mid e = (u, v), u = f(\sigma^p) \in V, v = f(\sigma^{p-1}) \in V, \sigma^p \in K, \sigma^{p-1} \in K, [\sigma^p, \sigma^{p-1}] \neq 0\} \end{aligned} \quad (45)$$

where $E \subset V \times V$ is the set of integer pairs for which the corresponding cells have a non-zero incidence number. The graph $G = (V, E)$ is used to represent the mesh cell complex, where V is the vertex set and E is the edge set. The map $f : K \mapsto V$ between the cell complex and the vertex set is bijective. Note that f is a *labeling* that has been extended not only to the points but to all cells in K . It follows then that vertices represent cells and edges represent their adjacency, and that by the definition of the incidence number, edges connect vertices that represent a cell and its proper faces. The edges are assumed to be directed, i.e. if $e \in E$, $u = \text{tail}(e)$, $v = \text{head}(e)$ and $\sigma = f^{-1}(u)$, $\tau = f^{-1}(v)$, then $\dim(\sigma) = \dim(\tau) + 1$, which renders the graph *directed, oriented* (i.e. no loops or multiple edges) and *acyclic*.

The *in-degree* of a vertex v is the number of edge heads adjacent to it and is denoted as $d^-(v)$. Conversely, the *out-degree* is the number of edge tails adjacent to v , denoted as $d^+(v)$. The *source vertex set* of a vertex is

defined as $D^-(v) = \{u \mid u = \text{tail}(e) \forall e \text{ s.t. } v = \text{head}(e)\}$, and the *target vertex set* of a vertex is defined as $D^+(v) = \{u \mid u = \text{head}(e) \forall e \text{ s.t. } v = \text{tail}(e)\}$.

A *path* on the graph G is defined as the sequence $P = v_1 e_1 \dots v_i e_i \dots e_{n-1} v_n$ where both the vertices $\{v_1, \dots, v_n\} \subset V$ and the edges $\{e_1, \dots, e_{n-1}\} \subset E$ are distinct. The tail and head vertices of edge e_i are v_i and v_{i+1} , correspondingly, with the initial and terminal vertices of P being $v_1 = \text{init}(P)$ and $v_n = \text{ter}(P)$, respectively. The length of the path from vertex u to vertex v is the number of edges in the path, and a path of length k is denoted as P^k . The distance $d(u, v)$ is the length of the shortest path between the vertices. Note that for the graph G constructed as described above, the length and the distance are equal. Furthermore, if there exists a path between two vertices, their distance is given by

$$d(u, v) = |\dim(\sigma) - \dim(\tau)|, \quad \sigma = f^{-1}(u), \quad \tau = f^{-1}(v). \quad (46)$$

Next consider the cell σ^p . All paths of length p with initial vertex $f(\sigma^p)$ have terminal vertices that correspond to the points that define the cell, i.e.

$$\sigma^p = [f^{-1}(v_0), \dots, f^{-1}(v_i), \dots, f^{-1}(v_p)], \quad v_i \in \{v \mid v = \text{ter}(P^p) \forall \text{init}(P^p) = f(\sigma^p)\}. \quad (47)$$

Now let \mathcal{K} be the collection of all point subsets $\{x_0, \dots, x_p\}$ such that each subset spans a cell in K . The collection \mathcal{K} is known as the *vertex scheme* of K and is a prime example of an *abstract cell complex* [16]. Define \mathcal{S} as the collection of sets $a^p = \{v_0, \dots, v_i, \dots, v_p\}$ with v_i given by Eq. (47) for each of the cells $\sigma^p \in K$. The collection \mathcal{S} is also an abstract cell complex in which the sets $a^p \in \mathcal{S}$ are its cells. Thus, there is a bijective correspondence f mapping the vertex set of \mathcal{K} to the vertex set of \mathcal{S} , and therefore \mathcal{K} and \mathcal{S} are isomorphic [16]. By virtue of this isomorphism, our graph representation is *complete* in the sense of Weiler. The cell complex K is a *geometric realization* of the abstract cell complex \mathcal{S} . Furthermore, the abstract cell complex \mathcal{S} is a *partially ordered set* in which the *covering relation* is defined as $a^{p-1} \subset a^p$. Thus, the graph G is in effect a *Hasse diagram* of the abstract cell complex \mathcal{S} where the representation of the empty set has been omitted.

In addition, the graphs obtained by representing a cell complex in this manner are $(n+1)$ -partite (i.e. they have $n+1$ “levels”, from points to the cell of highest dimension), and are also cell complexes themselves [10, 2].

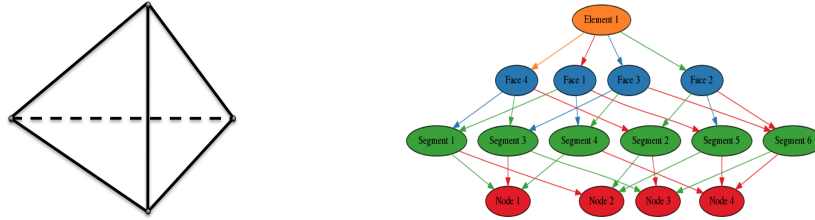


Figure 2: Graph representation of a single tetrahedral element. This representation is necessary to determine and manipulate topological features of the mesh, such as which faces of the bluff are subjected to erosion, and the erosion of material from the mesh.

4 Acknowledgements

Support for this work was received through the Laboratory Directed Research and Development (LDRD) program at Sandia National Laboratories. Sandia National Laboratories is a multimission laboratory man-

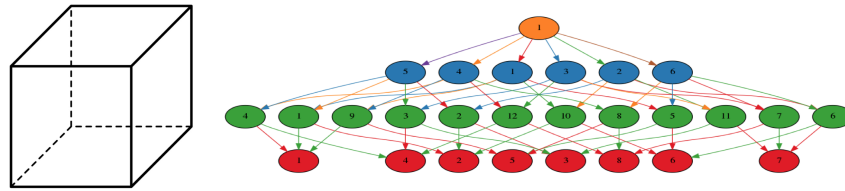


Figure 3: Graph representation of a single hexahedral element. This representation is necessary to determine and manipulate topological features of the mesh, such as which faces of the bluff are subjected to erosion, and the erosion of material from the mesh.

aged and operated by National Technology and Engineering Solutions of Sandia, LLC., a wholly owned subsidiary of Honeywell International, Inc., for the U.S. Department of Energy’s National Nuclear Security Administration under contract DE-NA-0003525.

References

- [1] F. E. Ar’è. “Thermal abrasion of sea coasts (part I)”. In: *Polar Geography and Geology* 12.1 (1988), pp. 1–1.
- [2] J. Bang-Jensen and G. Gutin. *Digraphs: Theory, Algorithms and Applications*. London: Springer-Verlag, 2002.
- [3] Katherine R. Barnhart et al. “Modeling erosion of ice-rich permafrost bluffs along the Alaskan Beaufort Sea coast”. English. In: *JOURNAL OF GEOPHYSICAL RESEARCH-EARTH SURFACE* 119.5 (May 2014), 1155–1179.
- [4] M.W. Beall and M.S. Shephard. “A general topology-based mesh data structure”. In: *Internat. J. Numer. Meths. Engrg.* 40 (1997), pp. 1573–1596.
- [5] W. Celes, G. Paulino, and R. Espinha. “A compact adjacency-based topological data structure for finite element mesh representation”. In: *Internat. J. Numer. Meths. Engrg.* 64.11 (2005). 1529–1556.
- [6] Charles Choens. personal communication. Apr. 2019.
- [7] DM Cole. “The microstructure of ice and its influence on mechanical properties”. English. In: *ENGINEERING FRACTURE MECHANICS* 68.17-18 (2001), 1797–1822. ISSN: 0013-7944.
- [8] S. Deo. *Algebraic Topology: A Primer*. New Delhi: Hindustan Book Agency, 2003.
- [9] R.V. Garimella. “Mesh data structure selection for mesh generation and FEA applications”. In: *Internat. J. Numer. Meths. Engrg.* 55.4 (2002), pp. 451–478.
- [10] J.L. Gross and T.W. Tucker. *Topological Graph Theory*. Mineola, NY: Dover, 2001.
- [11] K. Hackl. “Generalized standard media and variational principles in classical and finite strain elastoplasticity”. In: *J. Mech. Phys. Solids* 45.5 (1997), pp. 667–688.
- [12] Md. Azharul Hoque and Wayne H. Pollard. “Arctic coastal retreat through block failure”. English. In: *CANADIAN GEOTECHNICAL JOURNAL* 46.10 (Oct. 2009), 1103–1115.
- [13] N KOBAYASHI. “FORMATION OF THERMOEROSIONAL NICHES INTO FROZEN BLUFFS DUE TO STORM SURGES ON THE BEAUFORT SEA COAST”. English. In: *JOURNAL OF GEOPHYSICAL RESEARCH-OCEANS* 90.NC6 (1985), 1983–1988.

- [14] Hugues Lantuit et al. “The Arctic Coastal Dynamics Database: A New Classification Scheme and Statistics on Arctic Permafrost Coastlines”. In: *Estuaries and Coasts* 35.2 (Mar. 2012), pp. 383–400.
- [15] E.H. Lee. “Elastic-plastic deformation at finite strains”. In: *J. Appl. Mech.* 36.1 (1969), pp. 1–6.
- [16] J.R. Munkres. *Elements of Algebraic Topology*. Cambridge, MA: Perseus Publishing, 1984.
- [17] M. Ortiz and L. Stainier. “The variational formulation of viscoplastic constitutive updates”. In: *Comput. Method. Appl. M.* 171.3-4 (1999), pp. 419–444.
- [18] A. Pandolfi and M. Ortiz. “An Efficient Adaptive Procedure for Three-Dimensional Fragmentation Simulations”. In: *Eng. Comput.* 18.2 (2002), pp. 148–159.
- [19] A. Pandolfi and M. Ortiz. “Solid modeling aspects of three-dimensional fragmentation”. In: *Eng. Comput.* 14.4 (1998), pp. 287–308.
- [20] J.F. Remacle and M.S. Shephard. “An algorithm oriented mesh database”. In: *Internat. J. Numer. Meths. Engrg.* 58.2 (2003), pp. 349–374.
- [21] P TRYDE. “PHYSICS AND MECHANICS OF ICE”. English. In: *NATURWISSENSCHAFTEN* 67.11 (1980), 556–559. ISSN: 0028-1042.
- [22] K. Weiler. “The Radial Edge Structure: A Topological Representation for Non-Manifold Geometric Boundary Modeling”. In: ed. by M.J. Wozny, H.W. McLaughlin, and J.L. Encarnaç o. North-Holland, 1988, pp. 3–36.

APPENDIX B. CORING CAMPAIGN—ADDITIONAL WORK

Coring Campaign—Additional Work

B.1. Field Work Notes

Table B-1. Sample log and preliminary core descriptions by Misha Kanevskiy for all sites.

Borehole	Date	Depth, cm	Field description (preliminary)	Samples, cm	Notes
DP-1-1	4/10/2018	0-42	Frozen active layer (AL): 0-13 brown peat 13-23 l-brown silt with peat, 20-30% vis.ice 23-26 dry silt 26-42 l-brown silt with peat, no vis.ice	0-42	Old DTLB
		42-127	Peat/silt vertical structure, no vis.ice in peat, lenticular to braided cryostructure (c/s) in silt, vertically oriented, ~30% vis.ice 42-48 Transient layer (TL)??? 41-127 ice vein up to 3 cm wide (<1 cm at depths from 42 to 48)	42-92 92-136	Lacustrine and taberal deposits?
		127-198	Brown-gray to gray ice-rich silt, peat inclusions, reticulate to ataxitic c/s, 40-60% vis.ice; ice belts	136-189	From 127 – undisturbed deposits of the primary surface?
		198-335	Gray ice-rich silt, ataxitic c/s, 60-80% vis.ice; 252-265 ice-poor, from 265 ~50% vis.ice; from 315 – yellow-gray silt with vf sand	189-244 244-301	
		335-350	Silty vf sand, 20-30% vis.ice	301-346	
		350-390	Brown organic silt/silty clay, 10-15% vis.ice, no vis.ice from 384	346-387	
	4/11/2018	390-477	Dark-gray silty clay, 5-10% vis.ice (?)	387-439	
		477-498	Gray sandy silt, no vis.ice	439-493	
		498-510	Dark-gray silty clay, 5-10% vis.ice (?); @505 – lens of light-gray vf sand	493-510	
	4/15/2018	510-515	Half-frozen brown to dark-gray silty clay, almost no vis.ice		JIPRO coring from 510

Borehole	Date	Depth, cm	Field description (preliminary)	Samples, cm	Notes
		515-552	Unfrozen dark-gray to black silty clay	510-552	
		552-560	Half-frozen soil, several thin ice lenses		
		560-685	Unfrozen dark-gray to black silty clay	552-604 604-618 618-669	
		685-710	Unfrozen vf-f silty sand, dark brown-gray (brown with depth)	669-???	
		710-734	Unfrozen dark-gray vf silty sand; from 730 – oxidized f silty sand	???-750	
		734-750	Unfrozen dark-gray silty clay		
DP-2-1	4/11/2018	0-23	Frozen AL: 0-23 brown peat	0-49	Young DTLB
		24-32	TL? Light-brown silt 5% vis.ice		
		32-73	IL? Light-brown org-rich silt, reticulate to ataxitic c/s, ~40% vis.ice; ice belts	49-101	Lacustrine and taberal deposits?
		73-114	Light-brown org-rich silt / y-gray silt (less org. soil from 94), ~10% vis.ice; ice belts		
		114-190	Light-gray to yellow-gray silt, ataxitic (?) c/s, ~50% vis.ice, no distinctive ice belts; ice-poor from 172 (~10% vis.ice)	101-159 159-198	From 114 – undisturbed deposits of the old DTLB?
		190-201	Brown-gray org.silt, ~30% vis.ice, reticulate to braided (?) c/s	198-245	
		201-295	Dark-gray silty clay, braided to layered c/s; ~20% vis.ice (up to 30%?)	198-245 245-296	
		295-360	Yellow-gray silt, oxidized, vertical boundary with silty clay; <10% vis.ice	296-343	

Borehole	Date	Depth, cm	Field description (preliminary)	Samples, cm	Notes
		360-402	Brown silt / l-yellow silty vf sand (horizontal interbedding), almost no vis.ice, ice layer ~1 cm @401-402	343-402	
	4/16/2018	402-415	Black ice-poor silty clay (several thin ice lenses)	402-415	JIPRO coring from 402
		415-458	Unfrozen black silty clay	415-458	
PM-1-1	4/12/2018	0-49	Frozen AL: 0-7 brown peat 7-49 yellow-gray silt, ~7% vis.ice (7-15); dry from 37 to 42	0-54	High (primary) surface
		49-54	TL Silt		
		54-88	Silt, ice rich, ataxitic c/s, ice belts	54-112	
		88-310	Peat/silt vertical structure, ataxitic c/s in silt, from 132 ~70% vis.ice; ice belts – rare?; 223-228 mostly peat	112-167 167-213 213-268 268-320	
		310-478	Mostly gray silt, ataxitic c/s, 50-70% vis.ice	320-371 371-426 426-481	
		478-488	Gray silt, ice poor, ~10% vis.ice		
		488-535	Gray silt, ataxitic c/s (small blocks), ~50% vis.ice	481-532	
		535-633	Brown silty clay / silt interbedding, 5-40% vis.ice (irregularly distributed)	532-568 568-618 618-633	
	4/14/2018	633-738	Unfrozen saline soil: mainly vf to f silty clayey sand / silty clay	633-687 687-738	JIPRO coring from 633

Borehole	Date	Depth, cm	Field description (preliminary)	Samples, cm	Notes
PM-1-2	4/12/2018	0-40	Frozen AL: 0-8 brown peat 8-24 yellow-gray silt, ~5% vis.ice (8-19); 24-35 brown dry peat 35-40 silt / peat, ice poor	0-50	High (primary) surface
		40-46	TL Silt, reticulate c/s		
		46-50	Intermediate layer (IL) silt with some peat, ice rich, ataxitic c/s		
		50-130	Thermokarst-cave ice (mainly) with wedge ice (the core was mostly destroyed)	~130	
PM-1-3	4/13/2018	0-53	Frozen AL: 0-11 brown peat 11-53 brown-gray silt, almost no vis.ice	5-54	High (primary) surface
		53-58	TL Silt, reticulate c/s		
		58-223	Silt with peat inclusions (mostly vertical), more peat from 140, ice rich, ataxitic c/s, ice belts	54-101 101-155 155-207 207-252	
		4/15/2018	223-401	Gray silt with some clay; slightly yellowish from 340; ataxitic c/s 60-70% vis.ice, at 335-383 <50%	252-297 297-344 344-401
DP-1-2	4/15/2018	0-43	Frozen AL: 0-8 brown peat 8-18 silt with m-braided c/s 18-26 dry silt 26-43 silt, no vis.ice	0-55	Old TLB

Borehole	Date	Depth, cm	Field description (preliminary)	Samples, cm	Notes
	4/16/2018 (from 102 cm)	43-178	Brown-gray silt with peat and organic silt inclusions (mainly subvertical [?]); reticulate chaotic c/s with horizontal belts; relatively ice poor; subvertical ice veins up to 1 cm wide	55-102 102-157	Lacustrine and taberal deposits [?]
		178-206	Brown ice-poor org.silt / gray ice-rich min.silt vertical structure, almost no vis.ice in org.silt, ataxitic c/s in gray silt	157-213	From 178 – undisturbed deposits of the primary surface [?]
	4/19/2018 (from 267 cm)	206-314	Gray (to light brown-gray) ice-rich silt, ataxitic c/s, 60-80% vis.ice, decreases to 30-50% with depth;	213-267 267-326	
		314-326	Same silt, braided c/s, ~15% vis.ice		
DP-2'-2	4/17/2018	0-24	Frozen AL: brown peat	0-52	Young TLB, ~300 m (?) from the coastal bluff
		24-38	TL? Silt with peat inclusions, reticulate c/s, 15-20% vis.ice		
		38-59	IL? Silt with peat inclusions, mainly ataxitic c/s, ~70% vis.ice (from 48); ice belts		Lacustrine and taberal deposits [?]
		59-88	Silt, reticulate c/s, 15-20% vis.ice	52-110	
		88-122	Ice wedge / silt boundary		From 88 – undisturbed deposits of the old TLB?
		122-230	Ice wedge (the core was partly destroyed)	110-164 164-242	
		230-242	Ice wedge / frozen silty clay boundary (soil was oxidized along the boundary)		
		242-297	Unfrozen black silty clay, 287-297 – half-frozen, plastic	242-297	JIPRO coring from 242

SUMMARY

Borehole	Depth, cm	Depth to unfrozen soils, cm	Coordinates	Elevation, m	Notes
DP-1-1	750	515		5.2	Old DTLB
DP-1-2	326	–		5.2	Old DTLB
DP-2-1	458	415		4.0	Young DTLB
DP-2'-2	297	242		4.0	Young DTLB
PM-1-1	738	633		6.8	Primary surface
PM-1-2	130	–		6.8	Primary surface
PM-1-3	401	–		6.8	Primary surface
	31.00 m				

The following figures are photographs of the core sections retrieved, including a description of texture.



Figure B-1. Borehole DP-1-1, 20-120 cm.



Figure B-2. Borehole DP-1-1, 190-250 cm.



Figure B-3. Borehole DP-1-1, ice-rich silt with ataxitic cryostructure, 200-220 cm.



Figure B-4. Borehole DP-1-1, silty clay, braided to reticulate cryostructure, 455-470 cm.



Figure B-5. Borehole PM-1-1, subvertical silt/peat structure: almost no visible ice in peat, extremely ice-rich silt with ataxitic cryostructure, 180-200 cm.



Figure B-6. Borehole PM-1-1, unfrozen silty clayey very fine sand, 705-725 cm.



Figure B-7. Borehole PM-1-2, thermokarst-cave ice with vertical frost cracks, ~120-130 cm.



Figure B-8. Borehole PM-1-3, ice-rich silt with ataxitic cryostructure, 250-265 cm.

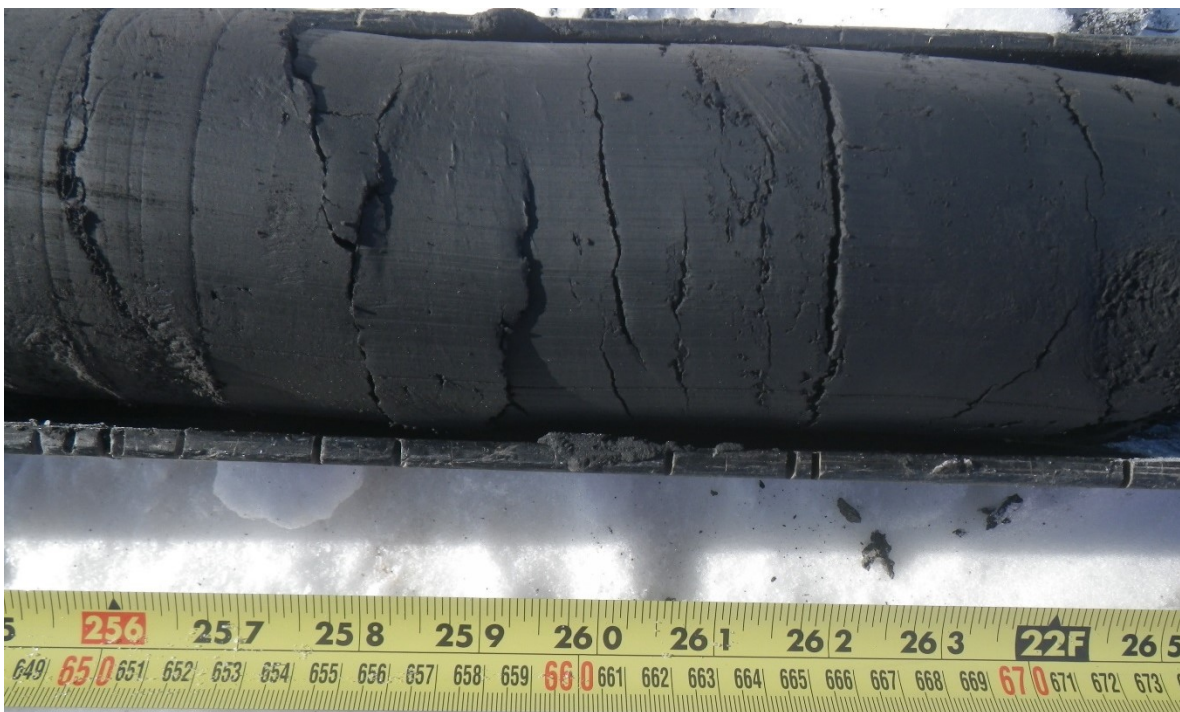


Figure B-9. Borehole DP-1-1, unfrozen silty clay, 650-670 cm.



Figure B-10. Borehole DP-2'-2, silt with reticulate cryostructure, 30-55 cm.



Figure B-11. Borehole DP-2'-2, ice wedge / silt boundary, 110-130 cm.



Figure B-12. Borehole DP-2'-2, ice wedge / silty clay boundary, 230-245 cm.

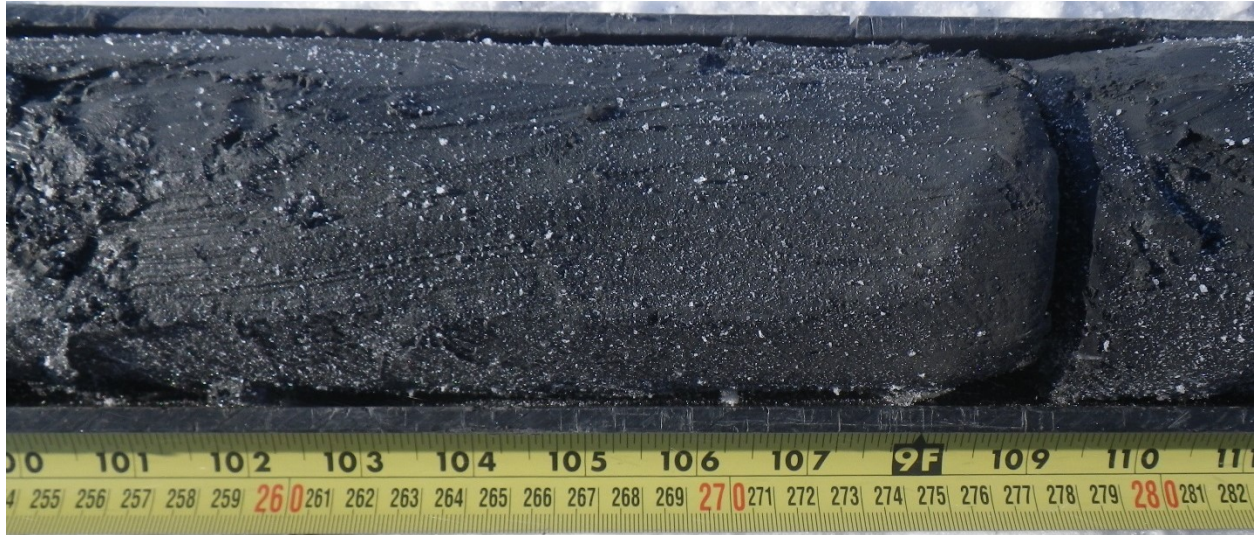


Figure B-13. Borehole DP-2'-2, unfrozen silty clay, 255-280 cm.



Figure B-14. Borehole DP-1-2, ice-rich silt with ataxitic cryostructure, 265-280 cm.

B.2. Permafrost Core Genomics Analysis

Team Member Author: Kylea J. Parchert (Sandia National Laboratories, Albuquerque, NM)

B.2.1. Methods

Small sections of soil were removed from each geochemical sampling location along the DP1-1, DP2-1, and PM1-1 permafrost cores. The mass of samples ranged from 0.5-5g. When permafrost cores were removed from their native locations, drilling and packaging of permafrost core pieces was not done sterilely and the outer surface of each of permafrost core pieces was assumed to be contaminated. To obtain a sample that could reasonably be expected to be free of contaminating microbes, sterilized cork borers were inserted into thawed permafrost core piece. The external most half centimeter of material was discarded. Soil samples were flash frozen in liquid nitrogen and stored at -80C before DNA extraction.

DNA extractions were accomplished using the Qiagen DNeasy Powersoil Kit and extractions were conducted according to the manufacturer's instructions. DNA elutions were amplified using fungal internal transcribed spacer (ITS) primers ITS1 (TCCGTAGGTGAACCTGCCG) and ITS4 (TCTCCGCTTATTGATATGC) and 16S rRNA bacterial primers 27F (AGAGTTTGATCMTGGCTCAG) and 1492R (GGTTACCTTGTACGACTT). The PCR

reactions were accomplished with the Takara Hot Start Taq and reactions included 38.75 µl water, 5 µl 10X Taq buffer, 0.25 µl each of 100uM primers, 4 µl dNTPs, 0.25 µl Hot Start Taq enzyme, and 1 µl of DNA template. The thermocycler protocol was as follows: 95C for 5 min, followed by 34 cycles of 94C for 30s, 57C for 30s, and 72C for 2 min, the final elongation step was 72C for 10min before reactions were cooled to 4C. PCR products were cleaned with the Qiagen QIAquick PCR Purification Kit and DNA elutions were visualized on a 1% agarose gel with a New England Biosystem's 100 bp DNA ladder. Transformation of Top10 competent E. coli cells was accomplished using the TOPO TA cloning kit with the pCR4-TOPO vector. The rapid transformation protocol provided by the manufacturer was followed and competent cells containing vector were screened for on ampicillin (50mg/ml) enriched LB agar plates. After overnight incubation at 37C, individual colonies were selected and grown for 24hr before inoculation into ampicillin (50mg/ml) amended LB broth. Cells were harvested after overnight incubation at 37C with shaking. Cells were pelleted by centrifugation at full speed for 1 min. Pellets were frozen at -20C until DNA was extracted with the ZymoPURE Plasmid Miniprep Kit. All extractions were accomplished according to manufacturer's instructions. Eluted DNA was stored at -20C until amplification with M13 Forward (GTAAAACGACGGCCAGT) and M13 Reverse (AACAGCTATGACCATG) primers. PCR protocols were the same as described above except that only 2 primers were added and an additional 0.5 µl water was included per reaction to keep reaction volumes at 50 µl. Amplicons were visualized on a gel as described above and PCR products were shipped to Eurofins for Sanger sequencing with the T3 (ATTAACCCTCACTAAAGGGA) and T7 (TAATACGACTCACTATAGGG) primers. Returned sequences were edited with Sequencher 5.4.6 to remove low-quality regions and to identify ambiguous bases. Failed sequencing reactions and contaminated sequences were removed. If possible forward and reverse sequences were combined into contigs. Consensus sequences and individual sequences, where contig assembly was not possible, were exported in Fasta format and organisms were identified by comparing sequences to the NCBI Nucleotide BLAST Database.

Table B-2. Number of isolates harvested after transformation of E.coli cells.

DP2-1 Site Locations	Number of Isolates
01	24
02	29
03	29
04	33
05	30
06	32
07	10
08	21
09	26
10	22
11	29

B.2.2. Results

Soil samples were collected from DP1-1, DP2-1, and PM1-1. However, due to time constraints, DNA extractions were only done using the DP2-1 permafrost core. Eleven locations were sampled. In this report these eleven sites will be referred to as 01-11, with site 01 being the surface sample and 11 being the cryopeg. Sample site 04 was submerged in water when the permafrost core sample was thawed, and so even interior portions of this permafrost core sample may have come into contact with contaminating microbes from the exterior of the permafrost core. Approximately 0.25 g of soil from each sampling location was used for the DNA extraction. Amplification of extracted DNA multiplexed bacterial and fungal primers. All sites produced bands at slightly larger than 1000 base pairs (bp) (see Figure B-15). The expected band size for bacterial amplicons was 1500 bp. Additionally at sites 01, 03, and 05, faint bands at 600 bp were observed. The expected amplicon size produced by fungal ITS primers was 600 bp. After PCR clean-up, products were cloned into the pCR4-TOPO vector and inserted into Top10 *E. coli* competent cells. Many clones were obtained on the ampicillin selective media, but due to time constraints 10-33 isolates were collected from each sampling location. A total of 285 isolates were collected from all locations. Table B-2 includes the information about the sampling locations. The vector insert for each isolate has been extracted and sequencing of the insert was attempted.

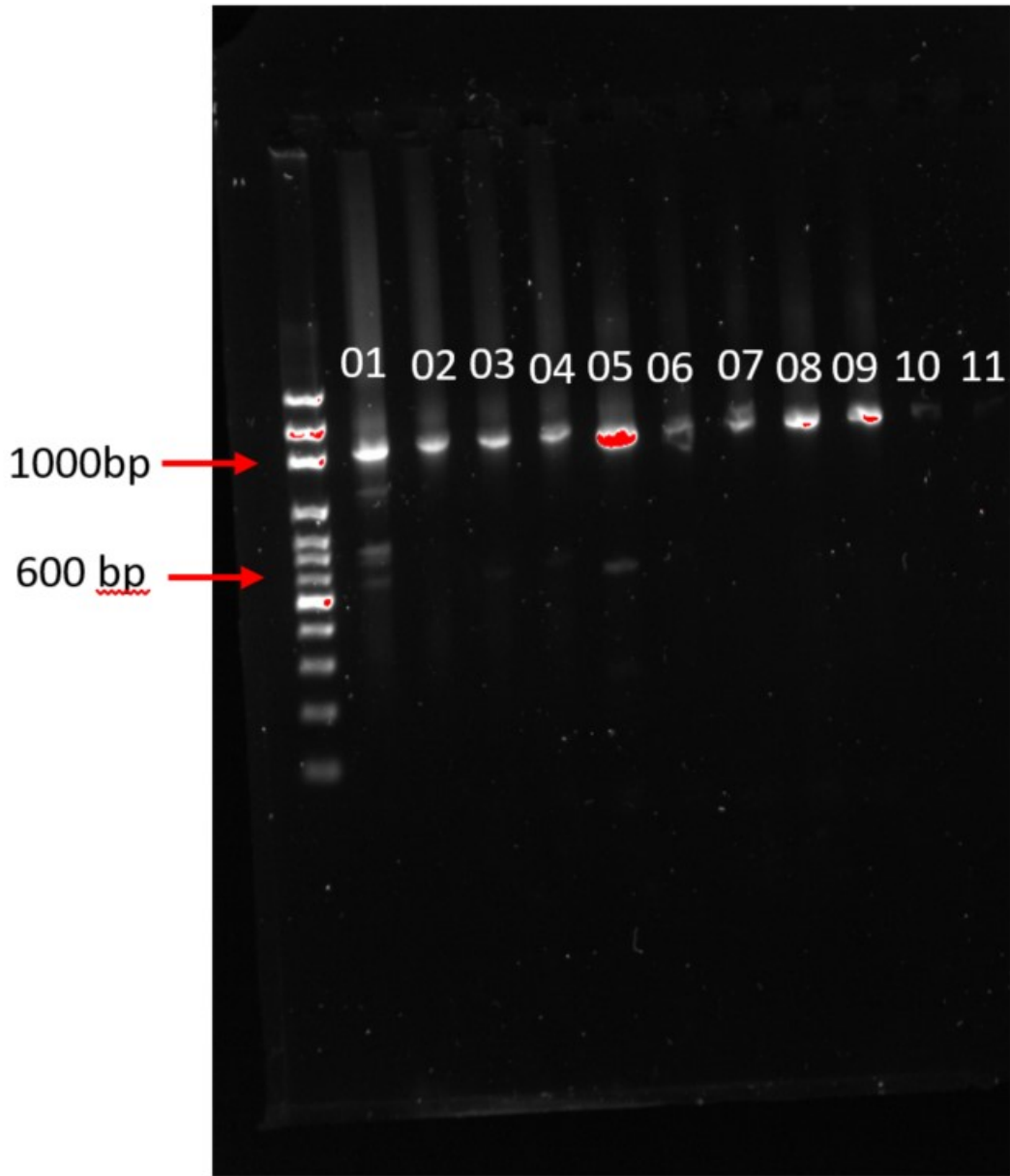


Figure B-15. After PCR clean-up, DNA elutions were visualized on a 1% agarose gel.

Sequencing of the permafrost core clones was attempted twice, but unfortunately the data was unusable both times. The second time, a primer set that was more specific to the plasmid vector containing the DNA from the permafrost core samples was used. However, both times the sequences were identified as *E coli*, which was used as the host for the plasmid vector and did not represent the organisms present in the permafrost cores. This result was very puzzling, especially since the primer change during the second attempt should have avoided this problem. The sequences were also of low-quality and only the forward primer worked. This suggests that either the transformation reaction failed or that the vector was defective or degraded. The transformation reaction was unlikely to have failed because the vector was required for the cells to be able to grow on the ampicillin amended media. An expert at Montana State University, Christine Foreman, who has extensive experience with DNA from frozen samples, has been consulted and we are awaiting

any suggestions she has to address this problem. The manufacturer of the TOPO cloning kit is also being contacted for any tips. The hope is to be able to identify the problem so that if there is additional funding available next year, this work can be continued. All of the remaining material harvested from the permafrost cores, and the extracted DNA are being stored at -80C. The take-away data from this experiment, so far, is that there is DNA at all of the sites on the permafrost cores that were sampled.

B.3. Permafrost Core Bio-Analysis

Team Member Author: Dongmei Ye (Sandia National Laboratories, Albuquerque, NM)

B.3.1. Methods

Two sets of core samples were collected from three permafrost cores: core water and soil. DP2-1 has fewer cuts, is more feasible for analysis to complete in FY18. PM1-1 and DP1-1 have more sections, which resulted in more sample numbers, analysis is pending on time and budget availability in FY19.

Nanoflow-Mass Spectrometry is used to analyze contents in core water and soil. For DP2-1, there are total of 11 core water and 8 soil samples collected. For samples 1, 2 and 4, only core water was collected, but not corresponding soil. Extracted core water was centrifuged at 14,000 RPM for 30 min to remove any insoluble particles. 1g of soil from each cut was soaked into 2 ml of either 0.1 M HCl or 0.1 M NaOH, shake overnight on an end-to-end shaker, centrifuged to remove excess soil, and the supernatant was neutralized to pH=7.0. All samples were analyzed using in-house Nanoflow-MS system.

B.3.2. Results

In core water near surface, a lot of small molecules with a molecular weight (MW) ranging from 400 – 600 were detected. As we go down the core, protein and peptide like compounds with higher MW were detected. In DP2-1 #8, there is a $m/z = 1196$ was identified with signature protein spectrum. Signature protein spectrum disappeared when close to cryopeg, while $m/z = 321$ showed up as the major component. There are a few additional small molecules with similar MW range were identified in HCl and NaOH extracted samples. There is a clear difference in compound identity and distribution through the depth of the core. More effort is needed to further identify compounds of interest as well as their function related to the microorganisms.

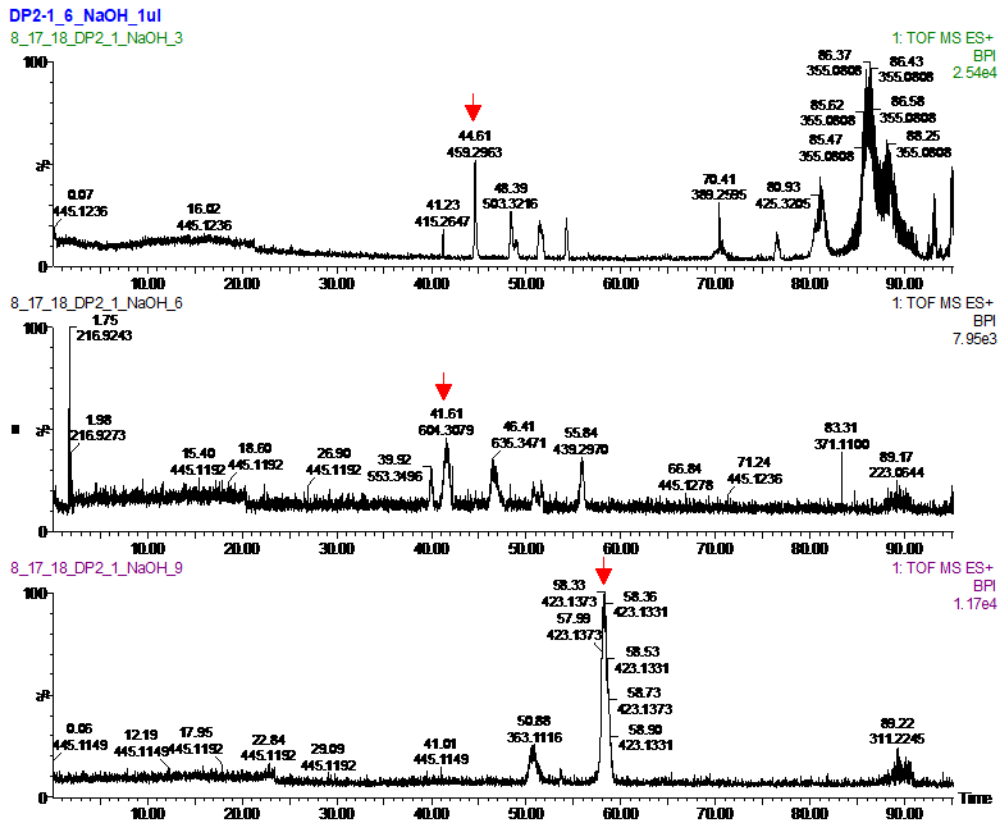


Figure B-18. Signature compounds detected in 0.1 M NaOH extracted soil samples.

B.4. Permafrost Core Trace Element Analysis

Team Member Author: Anastasia Ilgen (Sandia National Laboratories, Albuquerque, NM)

B.4.1. Analytical method

Our scientific goal was to identify what elements can be potentially released into the ocean water from eroding coastal permafrost at Drew Point.

Forty-five water samples were collected from three permafrost cores. After separating from the solids, each aqueous sample was filtered using a 45-micron nylon membrane filter and preserved with 6N ultrapure nitric acid HNO₃ prior to analysis by Inductively coupled plasma mass spectrometry (ICP-MS) to perform trace element analysis. Depending on the concentration of analyte, some samples were diluted at 100x with 2% ultrapure HNO₃. ICP-MS data was acquired using a NexION 350D mass spectrometer (Perkin Elmer) equipped with a collision-reaction cell. Testing for calcium, silicon, strontium, and manganese was done using dynamic reaction cell mode with 0.6 mL/min flow of ammonia gas. Quantitative analyses for iron, titanium, cobalt, nickel, copper, zinc, aluminum, barium, scandium and mercury were done using kinetic energy discrimination mode with helium gas flow set at 5 mL/min. Calibration curves for each element were obtained by running certified standard solutions prior to each analytical run.

B.5. Results

The results are shown in Table B-3 below. The concentrations of elements not included in Table B-3 (titanium, copper, zinc, scandium, and mercury) were below the detection limit (1 ppb) for our

instrument. We observed changes in the aqueous chemistry with sample depth (age). Based on the results shown in Table B-3, calcium (Ca), strontium (Sr), barium (Ba) and silicon (Si) concentrations increase with depth, while highest concentrations of iron (Fe) and manganese (Mn) are observed near the surface at ~ 100 cm depth. There was no measurable mercury (Hg) in any of the water samples.

Table B-3. Summary of aqueous concentrations of trace and some major elements in pore waters separated from three permafrost cores collected at Drew Point, Alaska.

Sample Id	Depth interval, cm	Ca (ppb)	Sr (ppb)	Mn (ppb)	Al (ppb)	Ba (ppb)	Sr (ppb)	Si (ppb)	Fe (ppb)
Core DP1-1									
DP1-1-1	0-10	7977	115	170	210	50	57	7333	1764
DP1-1-1	20-30	3626	87	86	503	33	17	2255	4854
DP1-1-3	42-52	4621	117	128	172	43	17	310	13275
DP1-1-4	60-70	14351	182	320	187	73	48	1137	27291
DP1-1-5	80-92	30010	312	529	172	154	96	1463	84838
DP1-1-6	124-136	42305	276	573	82	262	90	1013	64482
DP1-1-7	182-189	46611	268	125	24	240	179	2549	13259
DP1-1-8	244-259	53632	269	173	8	53	219	1863	156
DP1-1-9	301-308.5	17762	312	151	3	203	272	1270	33
DP1-1-10	338-346	54184	1253	120	8	340	1284	2176	42
DP1-1-11	387-398	130596	3850	207	39	313	4317	2727	190
DP1-1-12	456-468.4	69085	2922	58	6	1221	3168	3537	6117
DP1-1-13	521-531	78873	3800	50	23	2163	4189	4131	5639
DP1-1-14	586-599	122841	5035	53	244	3565	5707	2793	561
DP1-1-15	647-657	137041	4556	42	5	625	5042	4931	9292
DP1-1-16	710-719	146247	3525	124	304	275	3833	2753	80
DP1-1-17	740-750	191901	4854	88	18	493	5378	6955	15389
Core DP2-1									
DP2-1-1	0-12	5099	101	187	25	25	25	1531	4092
DP2-1-2	12-24	9410	132	168	30	69	43	2609	6479
DP2-1-3	24-37	17803	240	369	272	59	70	7933	33307
DP2-1-4	37-49	29977	326	492	254	118	113	9361	56940
DP2-1-5	89-101	86131	440	386	79	305	351	3067	6458
DP2-1-6	170-183	356005	1913	160	5	20	2047	2970	4354
DP2-1-7	235-245	117326	2241	66	23	51	2331	7823	10327
DP2-1-8	290-296	105807	1734	340	5	59	1754	4680	9457
DP2-1-9	343-353	204382	2668	504	4	48	2821	1375	169
DP2-1-10	402-415	210197	3677	124	326	81	4143	1960	1372
DP2-1-11	448-458	89139	3383	48	7	155	3532	4525	2845
Core PM1-1									
PM1-1-1	0-12	9455	93	43	941	72	23	2877	2118
PM1-1-2	12-25	16051	90	180	215	97	29	4648	378
PM1-1-3	25-34	24859	99	621	138	113	37	3676	347
PM1-1-4	54-66	36073	137	79	18	183	47	1738	7603
PM1-1-5	80.5-92	66106	179	42	15	290	96	2453	4647
PM1-1-6	126-138	98428	274	42	10	366	183	1231	5961

Sample Id	Depth interval, cm	Ca (ppb)	Sr (ppb)	Mn (ppb)	Al (ppb)	Ba (ppb)	Sr (ppb)	Si (ppb)	Fe (ppb)
PM1-1-7	154-167	102329	320	45	11	463	223	1722	7672
PM1-1-8	202-213	120046	461	46	15	614	343	1724	12479
PM1-1-9	257-268	275664	1476	101	41	1120	1387	1945	31036
PM1-1-10	310.5-326	350291	2545	201	3	1605	2526	2735	5320
PM1-1-11	363-372	131786	1060	190	bdl	62	951	1059	1072
PM1-1-12	413-426	317131	2172	717	bdl	41	2156	2021	3071
PM1-1-13	456-468	541382	2639	2583	0	17	2895	1793	995
PM1-1-14	633-643	442083	5091	1111	2	24	6105	2255	480
PM1-1-15	687-696	261433	4783	324	5	42	5454	3502	1678
PM1-1-16	726-738	268285	4605	428	11	95	5141	6972	10417
PM1-1-17	522-532	165860	1830	232	2	21	1690	2068	12260

Notes:

bdl = below detection limit